

The Effect of Surface and Loading Conditions on the Corrosion Performance of Stainless Steel Rebar

By

Kyle A. Anders

A thesis
presented to the University of Waterloo
in fulfillment of the
thesis requirement for the degree of
Master of Applied Science
in
Mechanical Engineering

Waterloo, Ontario, Canada, 2009

©Kyle A. Anders 2009

I hereby declare that I am the sole author of this thesis. This is a true copy of the thesis, including any required final revisions, as accepted by my examiners.

I understand that my thesis may be made electronically available to the public.

Abstract

Deterioration of reinforced concrete structures due primarily to chloride induced corrosion of plain carbon-steel reinforcement is a widespread problem, particularly in areas close to marine environments and where de-icing salts are used to keep roadways clear of ice. Replacing plain carbon-steel rebar with highly corrosion resistant stainless steel rebar has been shown to greatly increase the lifespan of concrete structures in harsh environments, and yields favourable life-cycle costs despite high initial costs. In attempt to lower stainless steel rebar's initial cost of processing, this research compared its corrosion resistance in the pickled (mill scale removed) and as-rolled (mill scale intact) surface conditions. Rebar was embedded in highly-chloride contaminated concrete, and corrosion performance between the two surface types was compared in order to determine if conventional pickling of stainless steel rebar is necessary. A second part of this research addressed possible concern of reduced corrosion resistance of pickled stainless steel rebar in concrete exposed to chlorides when subjected to dynamic loading due to micro-motion at the concrete/crack interface.

Microcell corrosion rates and corrosion potentials of pickled and as-rolled 304LN and 316LN, as well as pickled 2205 stainless steel rebars embedded in concrete prisms admixed with 7.5% Cl^- by weight of cement remained stable during the measurement period, indicating that no significant/detectable changes in corrosion states occurred during this time. Microcell corrosion rates for the pickled bars were 10-50 \times lower than the as-rolled bars, though values for the as-rolled bars ($\sim 10^{-3} \text{ A/m}^2$) were still well below those typically observed for actively corroding plain-carbon steel rebar (10^{-2} A/m^2) exposed to much lower chloride levels. Macrocell corrosion rates stabilized to values 10 \times less than the microcell corrosion rates for both surface conditions, with the as-rolled bars exhibiting a decrease in macrocell corrosion rates of over an order of magnitude from the time of casting. Cyclic polarization (CP) curves showed the surface film of the pickled specimens exhibiting an increase in protection from the applied anodic polarization, whereas the as-rolled bars exhibited a steady increase in current densities characteristic of uniform corrosion from applied anodic potential. Nevertheless, CP had no apparent long-term detrimental effect on the corrosion potentials, macrocell current densities or LPR measurements of either surface condition, thus initial passive surface characteristics were regained. Autopsied concrete specimens at the end of testing revealed very little rusting on the pickled stainless steel, with some superficial rusting on the top surface of the as-rolled bars, believed to have formed during the early cement hydration stages when ionic conductivity and subsequent macrocell corrosion rates were higher. Areas of significant corrosion occurred predominantly near

the epoxy-covered ends of the bars where localized corrosion occurred from crevice effects as well as residual knife marks left from applying the epoxy. These “artificial” effects would have had significant contribution to the higher corrosion currents measured on the as-rolled bars. Energy dispersive x-ray spectroscopy of the as-rolled bars revealed chromium depletion levels at the surface of no less than 14 wt% (versus the ~18 wt% in the bulk) over distances of 100-500 nm, and were much smaller than those commonly cited in literature in order to justify the pickling process.

Corrosion current densities, corrosion potentials and cyclic polarization measurements of pickled 316 and 2205 stainless steel rebar embedded in dynamically and statically loaded OPC concrete beams and exposed to salt solution revealed no distinction in corrosion behaviour between the two loading types. However, electrochemical noise measurements taken when cyclic loading of dynamically loaded beams was on revealed much higher fluctuations than both statically loaded beams and dynamically loaded beams when cyclic loading was off. This suggests that, although the passive surface film characteristics of the dynamically loaded bars appear to be restored when cyclic loading is off, during cyclic loading the surface film is susceptible to breakdown and general corrosion.

It was concluded that as-rolled stainless steel rebar in aggressive environments would provide sufficient corrosion resistance for the 75 year lifespan currently specified by the Canadian Bridge Code (CAN/CSA-S6-06, 2006), however it is recommended that monitoring of these specimens be continued to ensure high corrosion rates and/or concrete cracking do not develop. As well, investigation into the effects crevice corrosion cells found in typical concrete structures could have on as-rolled stainless steel rebar’s corrosion resistance should be undertaken. With regard to loading conditions, no significant evidence was found suggesting that pickled stainless steel rebar has reduced corrosion resistance when loaded dynamically versus statically. Therefore pickled stainless steel rebar is recommended for use in dynamically loaded concrete structures if other factors permit. However, the higher electrochemical noise measured during cyclic loading suggests that corrosion behaviour could be influenced largely by frequency of loading, and so further study should be undertaken for applications involving more extreme cyclic loading conditions than those used in this experiment.

Acknowledgements

I would like to thank my supervisor Dr. Hansson for providing me with the opportunity to undertake this research, as well as instilling in me strong critical thinking skills that will be invaluable throughout my life. I hope to adopt her strong work ethic and integrity in my future endeavors.

Thanks to colleagues Heather Austin, Brad Bergsma, Neal Damgard, Md Islam, Shazma Jaffer, Laura Mammoliti, Ramtin Movassaghi, Katherine Olsen, Amir Poursaee, Quan Tan, Khan Tran, and Irene Wijoyo, for all of your support, advice and friendship that made my time at UW such a pleasurable experience. I feel grateful to have been part of a research team of such character and generosity, and I appreciate all you have taught me in the lab, office and of course at our lively research group meetings.

Thanks to Dr. Mustafa Yavuz and Dr. John Medley for their time and assistance as members of my MASc examining committee.

This project would not have been successful without the help of UW technical staff Ken Bowman, Yuquan Ding, Doug Hirst, Richard Morrison, John Potzold, Terry Ridgway, and Norval Wilhelm, as well as the administrative staff Shelley Bacik, Lisa Baxter, Judy Caron, Marlene Dolson, Donna Kellendonk, Jennifer Nicholson, Jian Zou and the many others whom I may not have met personally but who work tirelessly behind the scenes to keep operations at one of the world's premier learning institutions running smoothly.

This project was made possible with the generous grants from our sponsors and the time commitment and help of their contacts, including Frank Pianca of the Ministry of Transportation of Ontario, Paul From of Valbruna Canada Ltd. and Gary Coates of the Nickel Institute. Thanks also to Essroc Canada Inc. for supplying the cement.

Last but not least, thanks to my family, including my parents Cathie and Tom, my brothers Jon and Dave, as well as my fiancé Laura and her family Erin, Pam and Jack. You all have given me so much support and encouragement I cannot thank you enough.

Table of Contents

List of Figures	ix
List of Tables	xiii
Chapter 1 - Introduction.....	1
Chapter 2 Background and Literature Review	2
2.1 Corrosion in Concrete	2
2.1.1 Overview	2
2.1.2 Electrochemistry of Steel in Concrete.....	3
2.1.3 Effect of Chlorides and Other Factors.....	5
2.1.4 Corrosion in Submerged Structures	9
2.2 Stainless Steel Rebar.....	10
2.2.1 Overview	10
2.2.2 Properties of Stainless Steel.....	12
2.2.3 Stainless Steel Performance in Concrete	15
2.2.4 Stainless Steel Bar Fabrication	17
2.2.5 Effect of Surface Conditions	22
2.2.6 Effect of Loading and Cracks	24
2.3 Concluding Remarks.....	25
Chapter 3 Experimental Procedures	27
3.1 Effects of Surface Conditions.....	27
3.1.1 Specimen Design	27
3.1.2 Rebar Types	30
3.1.3 Rebar Preparation.....	31
3.1.4 Concrete Casting.....	32
3.1.5 Exposure Conditions	36
3.1.6 Electrochemical Corrosion Monitoring	36
3.1.7 Pre-cast Metallographic and Chemical Analysis	43
3.1.8 Visual Examination of Autopsied G109 Specimens	45
3.2 Effects of Loading Conditions.....	45
3.2.1 Specimen Preparation.....	45
3.2.2 Loading and Salt Exposure.....	49
3.2.3 Electrochemical Corrosion Monitoring.....	51

Chapter 4 Experimental Results and Discussion	53
4.1 Effects of Surface Conditions	53
4.1.1 Macrocell Corrosion	53
4.1.2 Depolarization Time	58
4.1.3 Microcell Corrosion	59
4.1.4 Metallographic and Chemical Analysis of As-Received Bars.....	72
4.1.5 Visual Examination of Autopsied G109 Specimens	90
4.2 Loading Conditions	99
4.2.1 Crack Widths	99
4.2.2 Linear Polarization Resistance	101
4.2.3 Corrosion Potentials.....	103
4.2.4 Cyclic Polarization.....	104
4.2.5 Electrochemical Noise	106
Chapter 5 Summary, Conclusions & Recommendations	111
5.1 Summary & Conclusions	111
5.1.1 Surface Conditions.....	111
5.1.2 Loading Conditions.....	113
5.2 Recommendations	114
5.2.1 Surface Conditions.....	114
5.2.2 Loading Conditions.....	116
Appendices.....	117
Appendix A Admixed Chloride for Saturated Pore Solution	117
Appendix B G109 Specimen Cast Dates and Engraving Identification	120
Appendix C G109 As-Cast Concrete Data	121
Appendix D Derivation of <i>B</i> Constants from Tafel Slopes	122
Appendix E Loaded Beam Casting Data.....	128
Appendix F Macrocell Current Densities for Individual G109 Specimens	129
Appendix G G109 Bottom Bar Cathodic Exchange Current Densities.....	133
Appendix H Microcell Corrosion Current Densities of Individual G109s	135
Appendix I Corrosion Potentials of Individual G109s	138
Appendix J Additional Top Bar 316P Cyclic Polarization.....	141
Appendix K Energy Dispersive X-ray Spectroscopy of Pickled Rebar	142

Appendix L Loaded Beam Polarized Area	143
References.....	144

List of Figures

Figure 1: Effect of chloride ingress in concrete (Yunovich, Thompson et al., 2001).	2
Figure 2: Potential vs. pH diagram showing the equilibrium potential phases of iron in aqueous solutions (Pourbaix, 1966).....	3
Figure 3: Schematic illustration of microcell corrosion (Hansson, Poursaee et al., 2006).	4
Figure 4: Schematic illustration of macrocell corrosion (Hansson, Poursaee et al., 2006).	5
Figure 5: Submerged concrete structure showing high corrosion risk above water line (Aguilar, Sagues et al., 1990).	9
Figure 6: Stainless steel rebar was first used in Progreso Pier, Yucatan, Mexico (Arminox, 1999)....	11
Figure 7: Effect of alloying additions on stainless steel phase composition (Washko and Aggen, 2002).	12
Figure 8: Schematic of pitting corrosion (Waids, 2008).	15
Figure 9: (a) BSE SEM image and (b) EBSD derived phase map for scale grown on 316L stainless steel at 1200 °C for 4 hours (Higginson, Jepson et al., 2006).....	18
Figure 10: Depth profile of SS304 with ground surface after 100 hours at 600°C (Ostwald and Grabke, 2004).	22
Figure 11: Optical micrographs of microstructure of ribbed 316 and 304 stainless steel bars (García-Alonso(a), M.L.Escudero et al., 2007).	23
Figure 12: Evolution of (a) mass loss and (b) corrosion potential for SS304 with smooth and blank surfaces in HCl at 55°C (Li, Caenen et al., 2005).....	24
Figure 13: Schematic illustration of G109 specimen design, all dimensions in mm (ASTM-G109-99a, 2005).	27
Figure 14: Configurations for different bar sizes in G109 prisms	28
Figure 15: Modified G109 prism with a chloride contaminated upper and chloride-free lower concrete layer.....	29
Figure 16: Embedded Mn-MnO ₂ reference electrode (Klinghoffer).....	30
Figure 17: (a) Prepared rebar end before casting and (b) electrical connections after casting.	32
Figure 18: Formwork used for casting the G109 specimens.	33
Figure 19: As-cast concrete properties for G109 specimens	35
Figure 20: Linear region at polarization curve origin (Corrosion_Doctors, 1999)	37
Figure 21: Plot of polarization curve showing linear anodic and cathodic Tafel regions (Stern, 1957)	38

Figure 22: Experimental setup for microcell corrosion current density measurements (Tran, 2007) ..	39
Figure 23: Applied potential and resulting current plot for potentiostatic LPR	39
Figure 24: Schematic of corrosion potential measurement technique (Gu and Beaudoin, 1998)	40
Figure 25: Potentiodynamic cyclic polarization curve (PAR, 1982).....	42
Figure 26: Hysterisis loop on a potentiodynamic CP curve (PAR, 2008)	43
Figure 27: Dimensional overview of loaded beam.....	46
Figure 28: Schematic of setup for (a) statically loaded beam and (b) dynamically loaded beam	46
Figure 29: Loaded beams cast into formwork.....	47
Figure 30: As-cast concrete properties for loaded beam	48
Figure 31: Illustration of salt solution level during wet cycle (Jaffer, 2007).....	50
Figure 32: Electrode holder for loaded beam LPR measurements (Jaffer, 2007)	51
Figure 33: Short-term macrocell measurements for 304 pickled specimens with bottom black (B) and stainless steel (S) bars.....	53
Figure 34: Short-term macrocell measurements for 304 as rolled specimens	54
Figure 35: Average macrocell current densities over the long-term for 316LN steel type specimens .	55
Figure 36: Average macrocell current densities over the long-term for 304LN steel type specimens .	56
Figure 37: Average macrocell current densities over the long-term for 2205 steel type specimens	56
Figure 38: Depolarization profile of top and bottom 304P and 304A bars with time.	58
Figure 39: Average microcell corrosion current densities for (a) 316, (b) 304 and (c) 2205 steel type specimens.....	60
Figure 40: Microcell corrosion current densities of select top bars when polarized (macrocell connected for ≥ 24 hrs) compared with average values for top bar when depolarized (macrocell disconnected ≥ 24 hrs).....	62
Figure 41: Average corrosion potentials of top bars in G109 specimens	63
Figure 42: Corrosion potentials for certain bottom black steel bars.....	65
Figure 43: Corrosion potentials for certain bottom stainless steel bars	65
Figure 44: Potentiodynamic cyclic polarization curves for the top bars of (a) 316P, (b) 304P, (c) 2205P, (d) 316A and (e) 304A.....	68
Figure 45: Macroscopic images of each stainless steel rebar type before casting.....	72
Figure 46: Images of the different steel and surface types using optical microscopy	75
Figure 47: Optical micrographs of longitudinal cross-sections of 316 and 304 rebar microstructures	77
Figure 48: Optical micrographs of transverse cross-sections of the 316 and 304 rebar	78

Figure 49: Surface images of the different steel types and surface conditions using scanning electron microscopy	81
Figure 50: EDS analysis of the mill scale – base metal interface of 316A rebar	83
Figure 51: EDS analysis of the mill scale – base metal interface of 304A rebar	84
Figure 52: EDS analysis of the mill scale for 316A rebar	86
Figure 53: EDS analysis of the mill scale for 304A rebar	86
Figure 54: Raman analysis of 316A rebar surface	88
Figure 55: Raman analysis of 304A rebar surface	89
Figure 56: Surface images of 316A G109 bars before and after exposure	91
Figure 57: Surface images of 316P G109 bars before and after exposure.....	92
Figure 58: Surface images of 304A G109 bars before and after exposure	93
Figure 59: Surface images of 304P G109 bars before and after exposure.....	94
Figure 60: Surface images of 2205P G109 bars before and after exposure.....	94
Figure 61: Top surface of 304A B4 top bar upon removal from concrete.	96
Figure 62: Bottom surface of 304A B4 top bar upon removal from concrete	96
Figure 63: Appearance and depth loss analysis of 304A B4 specimen after removing corrosion products	97
Figure 64: Crack width measurement using a crack comparator	99
Figure 65: Corrosion current densities of 316 steel type loaded beams obtained by LPR	101
Figure 66: Corrosion current densities of 2205 steel type loaded beams obtained by LPR	102
Figure 67: Corrosion potentials of the 316 steel type loaded beams	103
Figure 68: Corrosion potentials of the 2205 steel type loaded beams	104
Figure 69: Cyclic polarization curves for 316 steel type loaded beams	105
Figure 70: Cyclic polarization curves for 2205 steel type loaded beams	105
Figure 71: ECN measurements for 316 steel type loaded beams at 150 days after casting.....	107
Figure 72: ECN measurements for 2205 steel type loaded beams at 150 days after casting.....	107
Figure 73: Standard deviation of ECN noise measurements at 150 days after casting	108
Figure 74: ECN measurements of dynamically loaded beams with cyclic loading applied at 200 days after casting.....	109
Figure 75: Standard deviation of dynamically loaded beam ECN measurements at 200 days with cyclic loading applied.....	109

Figure 76: Magnification of ECN measurements of dynamically loaded beams with cyclic loading applied at 200 days after casting	110
Figure 77: (a) Schematic diagram (Barneyback and Diamond, 1981) and (b) photograph of pore solution extraction chamber	118
Figure 78: Chloride content in pore cement paste pore solution with varying amounts of admixed chlorides.....	119
Figure 79: Tafel slopes and trendlines for select G109 bottom bars	134
Figure 80: Additional potentiodynamic cyclic polarization curves for 316P top bars	141
Figure 81: Energy dispersive x-ray spectroscopy of outer bulk metal of (a) 316P and (b) 304P	142

List of Tables

Table 1: Electrochemical reactions of steel in concrete	4
Table 2: Alloying additions in stainless steels	12
Table 3: Chemical composition of stainless steel grades for concrete reinforcement, maximum chemical composition values (ASTM-A955, 2004).....	13
Table 4: Mechanical properties of stainless steel rebar (Sedriks, 1996; ASTM-A955, 2004; Tullmin, 2006).	14
Table 5: Pitting resistance equivalent equations and values (BSSA, 2007).	15
Table 6: Steel materials and nomenclature used in modified G109 prisms	30
Table 7: Rebar chemical composition provided by Valbruna.....	31
Table 8: G109 concrete mix design.....	33
Table 9: Corrosion potentials for black steel in concrete (ASTM-C876-91, 1991).....	41
Table 10: Concrete mix design for loaded beams	47
Table 11: Loaded beam pair nomenclature.....	49
Table 12: Schedule of exposure condition changes to loaded beams.....	50
Table 13: Characterization of Raman peaks	89
Table 14: Maximum crack widths of loaded beams at the end of measurement period.....	99
Table 15: Chloride analysis data from extracted pore solution.....	118
Table 16: Oxygen exchange current densities of different G109 bottom bar types	134
Table 17: Loaded Beam Polarized Area Data.....	143

Chapter 1 - Introduction

Deterioration of reinforced concrete structures due to chloride-induced corrosion of plain-carbon steel reinforcement is a significant problem due to the increased use of de-icing salts on roads, construction near coastal areas, and ageing infrastructure. Many methods have been proposed and implemented to address this problem; however, few show as much promise in terms of long-term structural durability in aggressive environments as does the use of stainless steel reinforcement, due to its inherently high corrosion resistance. The main drawback of stainless steel is its high initial cost, despite the fact that the life-cycle costs are predicted to be significantly lower than alternative rebar materials. One way to reduce the initial cost is to forego the expensive and environmentally hazardous pickling process, whereby the mill scale formed on the steel surface during hot rolling and annealing is removed by first abrasive blasting the steel and then pickling it in a mix of nitric and hydrofluoric acids. Removal of these outer surface layers has conventionally been specified in part for aesthetic reasons, but also for concern of chromium depletion at the surface that could result in higher pitting corrosion susceptibility. One objective of this study is to investigate whether the pickling process is necessary for stainless steel concrete reinforcement, by comparing the corrosion resistance of pickled and as-rolled (non-pickled) stainless steels embedded in highly chloride contaminated concrete. Another objective of this study is to investigate the effect, if any, that dynamic loading has on the corrosion resistance of pickled stainless steel rebar in cracked concrete compared with static loading. This is thought to be a potential risk since, in a previous study (Mendoza, 2003) of dynamically loaded plain-carbon steel reinforced beams, corrosion of a stainless steel stirrup was observed at the location of the crack, and was believed to develop from the micro-motion occurring between the concrete/steel interfaces during cyclic loading.

Chapter 2

Background and Literature Review

2.1 Corrosion in Concrete

2.1.1 Overview

Corrosion of reinforced concrete structures due to the ingress of chlorides from de-icing salts and marine conditions is a major source of infrastructure deterioration. As of 2001, the annual direct cost attributed to the corrosion of highway bridges in the U.S.A. alone is an estimated \$8.3 billion, with indirect costs associated with traffic delays and lost productivity totaling approximately ten times this amount (Yunovich, Thompson et al., 2001). The main cause of bridge deterioration is attributed to chloride-induced corrosion, in which chlorides diffuse through the concrete or more directly through cracks in the concrete and proceed to attack the surface of the plain carbon-steel rebar. Plain carbon-steel comprises the overwhelming majority of reinforcement in service today, and its susceptibility to chloride attack has left over 30,000 bridges in Canada and 200,000 bridges in the US in need of repair (Newhouse and Weyers, 1996; Smith and Tullmin, 1999). Other structures including parking garages where salts are carried in from cars, as well as offshore structures, are also affected by chloride-induced corrosion, though direct costs associated with these structures are less easily determined. As illustrated in Figure 1, once chlorides migrate down towards the surface of the rebar and facilitate corrosion, the resulting corrosion products take up a volume of 2-3 times that of the original steel (Marcotte and Hansson, 2007), and the expansion forces produced cause cracking and spalling of the concrete. This makes concrete reinforcement corrosion a significant economic as well as safety concern.

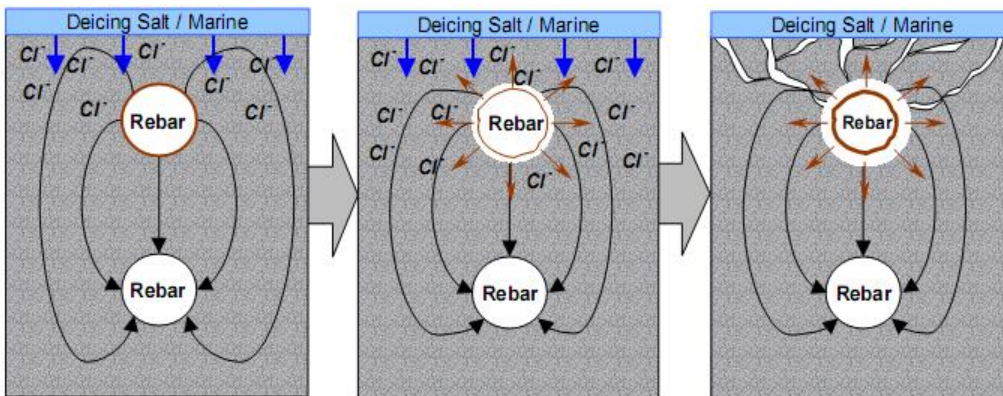


Figure 1: Effect of chloride ingress in concrete (Yunovich, Thompson et al., 2001)

2.1.2 Electrochemistry of Steel in Concrete

The pore fluid of good quality concrete, composed primarily of NaOH, KOH and to a lesser extent $\text{Ca}(\text{OH})_2$, provides a high pH environment of ~ 13.5 that favours the formation of a thin tightly adhering protective oxide layer on the steel surface, comprised of an inner dense spinel phase ($\text{Fe}_3\text{O}_4/\gamma\text{-Fe}_2\text{O}_3$) and an outer layer of $\alpha\text{-FeOOH}$ (Glasser and Crentsil, 1989). Under these conditions carbon steel rebar is passive and protected from active corrosion. However, if the film is disturbed due to reduction of the pH and/or altering of electrochemical potential, non-protective oxides can result, leading to active corrosion of the steel. The electrochemical potential is a thermodynamic property describing the free energy available for electron transfer and is dictated by conditions at the steel-concrete interface. Generally more oxidative species near the steel surface (e.g. oxygen, metallic ions) produces a more positive electrochemical potential with respect to a standard reference potential. The equilibrium phases of steel as a function of pH and potential versus standard hydrogen electrode are illustrated in Figure 2.

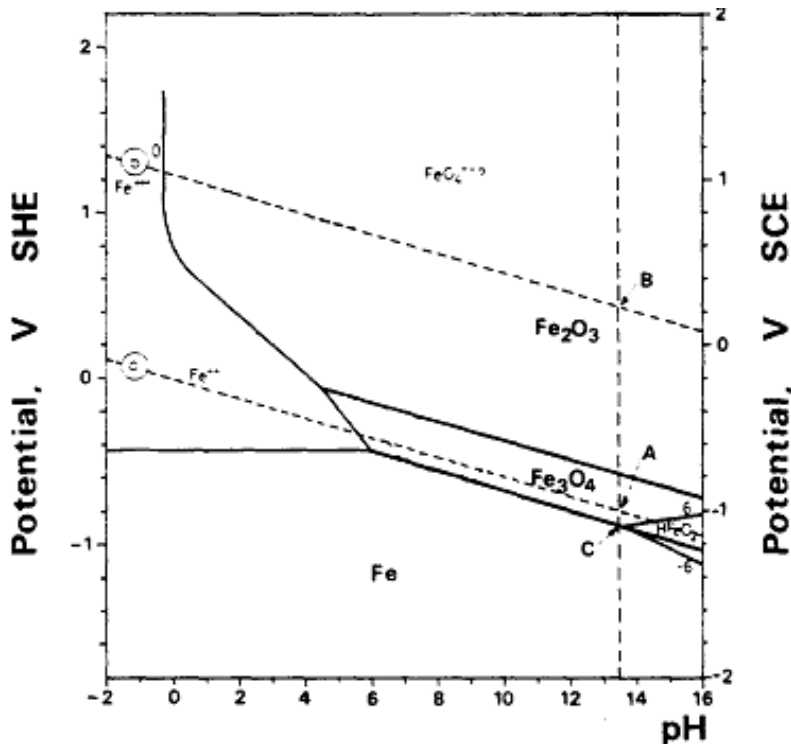


Figure 2: Potential vs. pH diagram showing the equilibrium potential phases of iron in aqueous solutions (Pourbaix, 1966)

The electrochemical reactions of interest for steel embedded in concrete, dictated by the pH and oxygen availability, are shown in Table 1. The first two anodic conditions are favoured in passive conditions and produce an iron oxide, while the last two anodic reactions favour active corrosion conditions and lead to the dissolution of iron into ions. The first and second cathodic reactions are favoured in high and low pH conditions, respectively (Hansson, 1984).

Table 1: Electrochemical reactions of steel in concrete

Anodic	Cathodic
$3\text{Fe} + 4\text{H}_2\text{O} > \text{Fe}_3\text{O}_4 + 8\text{H}^+ + 8\text{e}^-$	$2\text{H}_2\text{O} + \text{O}_2 + 4\text{e}^- > 4\text{OH}^-$
$2\text{Fe} + 3\text{H}_2\text{O} > \text{Fe}_2\text{O}_3 + 6\text{H}^+ + 6\text{e}^-$	$2\text{H}^+ + 2\text{e}^- > \text{H}_2$
$\text{Fe} + 2\text{H}_2\text{O} > \text{HFeO}_2^- + 3\text{H}^+ + 2\text{e}^-$	
$\text{Fe} > \text{Fe}^{2+} + 2\text{e}^-$	

The process of corrosion requires a complete circuit between the anodic and cathodic sites to allow the transfer of electrons and ions as shown in Figure 3. The electron is moving from the anodic site, where metal is dissolving, to an adjacent cathodic site where oxygen is reduced, and this electrochemical exchange occurring closely together on a single rebar is called microcell corrosion.

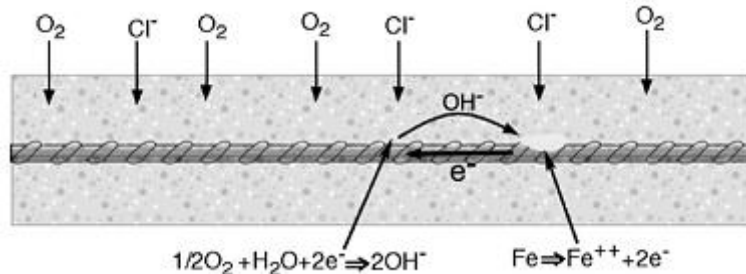


Figure 3: Schematic illustration of microcell corrosion (Hansson, Poursaei et al., 2006)

The corrosion current generated between these two sites is called the corrosion current, I_{corr} , and is directionally proportional to the mass reacted, m , through Faraday's Law as follows:

$$m = \frac{I_{corr} t a}{nF}, \quad (1)$$

where F is Faraday's constant (96,500 coulombs/equivalent), n the valence number, a the atomic weight, and t the time. The corrosion current density, i_{corr} , is defined as the corrosion current I_{corr}

divided by the corroded area, and has units of A/m^2 . Corrosion current density is used throughout this report and, for iron, has an equivalent depth of removal of $10^{-3} A/m^2 \approx 1.16 \mu m$ per year. In the absence of chlorides, the corrosion current density of passive (non-corroding) plain carbon-steel is in the range of 10^{-4} to $10^{-3} A/m^2$. Active corrosion typically proceeds at values greater than $10^{-2} A/m^2$, in which case depth loss is greater than $10 \mu m/year$ and rapid, premature failure can occur (Hansson 1984; Newhouse and Weyers 1996; Alonso, Andrade et al. 2000; García-Alonso(a), M.L.Escudero et al. 2007).

A significant limiting factor of the corrosion current in concrete is its ionic resistance. This is important not only in microcell corrosion where ions diffuse through concrete pore solution between adjacent sites on a single rebar, but also in macrocell corrosion, where electrochemical interactions occur between anodic and cathodic sites which are well separated and may be on separate rebars, as shown in Figure 4. An uneven distribution of chloride ions typically occurs in bridge decks, with larger concentrations of chlorides present near the upper rebar mat as they diffuse down from the road. This can promote a galvanic effect where the top rebar layer behaves anodically with respect to the bottom and, thus, an additional macrocell current is applied to the top rebar in addition to the microcell corrosion taking place.

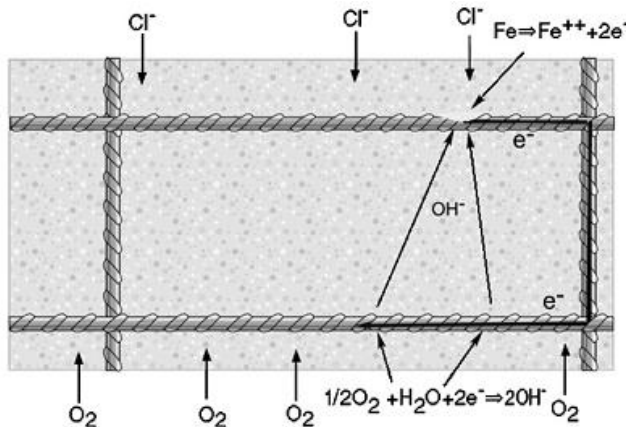


Figure 4: Schematic illustration of macrocell corrosion (Hansson, Poursaei et al., 2006)

2.1.3 Effect of Chlorides and Other Factors

The detrimental effect of chlorides to carbon-steel reinforcement is well documented, and they promote corrosion in the following ways (Hunkeler, 2005):

- Destroy the passive film thus allowing oxidative species access to bare steel surface

- Increase the moisture content and thus oxidative reactant concentration near the surface of the rebar due to salt's hygroscopic (water-absorbing) properties
- Increase conductivity of the concrete thus increasing corrosion kinetics

2.1.3.1 Chloride threshold

The amount of chloride contamination necessary to initiate corrosion varies depending on a number of factors, such as concrete quality (in particular the amount of chloride-binding alumina phase present), moisture content, concrete cover (i.e. oxygen availability, pH) and temperature (Hussain, Rasheeduzzafar et al., 1995; Oh, Jang et al., 2003; Hunkeler, 2005). Nevertheless, several studies have been carried out to determine general guidelines or threshold levels at which active corrosion develops in plain carbon-steel reinforced concrete. Studies on admixed sodium chloride thresholds in OPC concrete have found large ranges of chloride thresholds from 0.35-3.08% by mass of cement, depending on alumina (C_3A) content as well as the technique used to determine the transition point from passive to active corrosion (Hussain, Rasheeduzzafar et al., 1995; Alonso, Andrade et al., 2000; Oh, Jang et al., 2003). It should be noted that thresholds for chlorides admixed into fresh concrete are known to be higher than those for chlorides diffusing into hardened concrete, and is attributed to the chlorides in fresh concrete being more readily bound in the cement matrix by the C_3A (Whiting, 1978; Hussain, Rasheeduzzafar et al., 1995; Oh, Jang et al., 2003). The American Concrete Institute and Federal Highway Administration for instance have set permissible chloride levels in pre-existing concrete structures to 0.1 and 0.15% by mass of cement, respectively (Locke, 1986; Virmani and Clemena, 1998).

The Cl^-/OH^- ratio is another common chloride threshold used, since, at lower pH, the surface film is less protective and the steel more vulnerable. However, values for these ratios also vary considerably, with some reporting 1.17-3.98 (Alonso, Andrade et al., 2000) and others reporting much lower values of 0.16-0.26 (Oh, Jang et al., 2003) for OPC admixed with sodium chloride. Free chloride content in the pore solution is a threshold believed by many to be more meaningful since it is able to moderate the influence of the cement's chloride-binding C_3A content (Hansson and Soerensen, 1990). Again though, a large range of free chloride thresholds exists in literature of 0.1-1.16% by mass of cement for OPC concretes admixed with sodium chloride and containing varying amounts of C_3A (Hussain, Rasheeduzzafar et al., 1995; Alonso, Andrade et al., 2000; Oh, Jang et al.,

2003). The Cl^-/OH^- ratio and free chloride thresholds may hold limited advantage over total chloride content thresholds since bound chlorides can represent a corrosion risk if they are released, where a lack of $\text{Ca}(\text{OH})_2$ exists, as well as the fact that OH^- concentration is only one of the inhibitive alkalis present in cement (Glass and Buenfeld, 1997). An ideal threshold value would, thus, take into account total chlorides as well as the alkaline reserve of the concrete.

Once active corrosion has initiated, the role of chloride content in propagating corrosion is debatable, with some reporting the chloride content having a minor influence on the corrosion process (Hunkeler, 2005), while other observing a linear trend of corrosion current versus chloride concentration when plotted on a logarithmic scale (Alonso, Andrade et al., 2000). Once initiated, the propagation of corrosion is likely influenced strongly by other factors including concrete resistivity, porosity, pH, moisture content and availability oxygen (Hansson, Froelund et al., 1985).

2.1.3.2 Concrete Characteristics

The concrete can affect the susceptibility of the rebar indirectly by influencing the ease at which chlorides can penetrate to the reinforcement. A highly porous concrete in a moist environment will provide an effective route for chloride transport to the rebar and, if allowed to dry while corrosion has already begun, a porous concrete can exacerbate corrosive conditions by allowing oxygen with more access to the rebar surface.

Porosity of concrete is influenced by many things, including the type of cement and aggregate as well as the proportions of components specified in the mix design. High performance concrete made with fine and pozzolanic cementing materials such as silica fume will have denser structure and, thus, higher resistivity compared to concretes made with ordinary Portland cement. A ratio of lower water to cement in the mix design will have a similar effect, though this also raises the pH and increases the critical chloride concentration required to break the passive film by saturating the pore solution. Longer moist curing times after casting will increase hydration in the concrete and thus reduce porosity. This explains the linear relationship observed between increasing the period of moist curing and time for initiation of corrosion (Hansson and Soerensen, 1990).

Both age and environmental conditions influence corrosivity in concrete. An older concrete will have a lower moisture content and thus higher resistivity (Hope, Ip et al., 1985), however consistent rain and/or moisture from marine conditions will ensure enough conductivity to keep corrosion a

concern. Temperature and seasonal fluctuations are another factor, with corrosion accelerated during high temperature seasons with adequate moisture and decreased during colder times of the year when the kinetics of the electrochemical reactions are slower (Hussain, Rasheeduzzafar et al., 1995; Newhouse and Weyers, 1996).

2.1.3.3 Surface Effects

The influence of surface effects on the initiation and propagation of corrosion of plain-carbon steel rebar have been studied. One study (Hansson and Soerensen, 1990) found that during 100 days exposure to 1M NaCl solution, ribbed and pre-rusted rebar embedded in concrete initiated corrosion later than sand-blasted and smooth steel bars, indicating the rust had a positive effect on the corrosion properties at lower chloride levels. However, another study (Mammoliti, Brown et al., 1996) found depassivation to initiate more readily on carbon steel having rougher surfaces in synthetic pore solution of pH 13.3 containing gradual additions of chlorides once 5% Cl⁻ was reached, suggesting the amount of chlorides need to initiate corrosion is less for rougher surfaces. A further study (Esmailpoursaee, 2007) showed as-received carbon-steel rebar with mill scale having twice the corrosion rate of sand blasted after 300 hours in pore solution, though both values were passive, and for rebar in mortar both the corrosion potentials and corrosion rates exhibited were indistinguishable.

One issue that needs consideration is adhesion between the steel and concrete. One study (Yonezawa, Ashworth et al., 1988) found that, when breaking steel bars out of mortar and immersing them in chloride containing pore fluid, bars that were cast with filter paper interposed between them and the mortar initiated corrosion more quickly than bars cast without the paper that were allowed to develop good adhesion and passivate first in the mortar. It is thought that the Ca(OH)₂ crystals at the bar's surface are able to dissolve and act as an alkali reservoir to restrain the initiation of chloride pitting attack that locally reduces the pH. Lack of adhesion reduces the nearby alkali available, and the presence of voids allows greater pore fluid and oxygen concentration, thus increasing the ionic conductivity in the region.

2.1.4 Corrosion in Submerged Structures

Submerged structures are susceptible to corrosion not only due to the high chloride content often found in marine environments but also due to the ideal mix of high moisture content and access to oxygen encountered near the tidal zone, or water line. Submerged concrete is saturated with water while regions near the top are dry, and this moisture gradient causes an upwards flow of liquids. The upward flowing water eventually evaporates, leaving behind a residue of chlorides that accumulate just above the water-line which can reach concentrations of twice that found in the submerged regions. This mix of high chloride, moisture and oxygen content combines synergistically to cause a significant corrosion risk just above the water line (Weiermair, Hansson et al., 1996), shown in the shaded region in Figure 5.

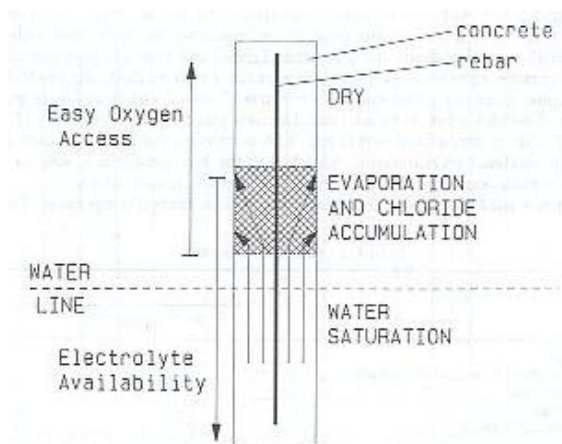


Figure 5: Submerged concrete structure showing high corrosion risk above water line (Aguilar, Sagues et al., 1990)

In one study (Aguilar, Sagues et al., 1990) carbon steel rebar in concrete beams exhibited a shift in corrosion potential from -100 to -400 mV vs. SCE after 100 days of being submerged in water containing 9100 ppm Cl^- , indicating a transition from active to passive corrosion. The earliest depassivation occurred, as expected, just above the water line. The submerged region also became susceptible to corrosion in beams containing a single, electrically continuous rebar along the entire length (as opposed to separate portions of embedded reinforcement); the submerged region's lack of oxygen made it anodic with respect to the well aerated upper portion. Accelerated corrosion in the submerged region is likely to occur only if it already had corrosion present from the water level been below this region for a period of time to allow the ingress of oxygen. Corrosion in a submerged

region that was always underwater with little oxygen access to initiate corrosion would be unexpected.

2.2 Stainless Steel Rebar

2.2.1 Overview

Reinforced structures are currently being specified to last over 75 years (CAN/CSA-S6-06, 2006) and, given the increased use of de-icing salts and construction near coastal areas, several methods to prevent or remediate the corrosion of reinforced concrete structures have been suggested and applied over the years to varying degrees of success. Use of corrosion inhibitors, concrete sealants, and high performance concrete mixes all act to change the rebar's surrounding environment and reduce the amount of corrosive agents near its surface (Smith and Tullmin, 1999). However, in addition to concrete's porosity, it is also highly prone to cracking due to its brittle nature, and since cracks act as rapid transportation routes for chlorides, changing the rebar itself is often the method of choice. Cathodic protection, where the rebar is supplied with an external current or is connected to a sacrificial anode, keeps the bar's electrochemical potential at a more noble (-) value away from the active corrosion regime. This method can be disadvantageous though for large structures, requiring significant ongoing power input, surveillance and/or supply of sacrificial anodes (Andrade, Holst et al., 1991; Smith and Tullmin, 1999). Epoxy-coated rebar was commonly specified throughout the 1970's and 1980's in attempt to insulate the steel surface from the concrete environment. Enthusiasm for this approach has waned in recent years in light of studies showing epoxy coating's susceptibility to scratches and breakdown, as well as moisture absorption and subsequent de-lamination from the steel substrate, both of which have resulted in localized corrosion of the rebar in chloride-contaminated concrete (Rasheeduzzafar, Dakhil et al., 1992; Weyers, Pyc et al., 1998). Galvanized rebar, where plain-carbon steel rebar is coated with zinc to provide a cathodically protective outer layer that is preferentially consumed instead of the steel, is a commonly specified to delay the onset of corrosion, though studies have found its corrosion resistance in heavily chloride-contaminated concrete to be insufficient (Treadway, Cox et al., 1989; Rasheeduzzafar, Dakhil et al., 1992).

The mainstream use of stainless steel rebar has been relatively recent, though it possesses many advantages over the above options. It has inherently good corrosion resistance with no coatings that can degrade or cut ends to cover. From a structural viewpoint, stainless steel also offers good

strength, ductility and, depending on the grade, weldability (Nuernberger, Beul et al., 1993; Smith and Tullmin, 1999). Its primary disadvantage is the high initial cost for currently specified stainless steel types. Though the price ratio of stainless steel to carbon steel is roughly 6-9:1, depending on steel type, the increase in total construction costs is 5-20% (Cochrane, 1995; Smith and Tullmin, 1999; Yunovich, Thompson et al., 2001; Steel, 2008), and even less if used selectively in the more susceptible areas. These costs are easily justified in aggressive environments due to stainless steel rebar's expected lifespan of 75-120 years (MTO, 2001; Yunovich, Thompson et al., 2001). This translates into excellent life cycle costs since future maintenance replacement costs are reduced, as well as indirect disruption costs such as lost productivity, wasted fuel, and loss of trade (NIDI, 2004).

Perhaps the best example of stainless steel rebar's durability is its first use as concrete reinforcement in Progreso Pier, a bridge built with AISI 304 reinforcement during 1937-1941 off the Gulf Coast near Yucatan, Mexico. Shown in Figure 6, Progreso Pier has managed to withstand the aggressive saline environment without any major maintenance despite being cast in relatively porous concrete. A 1999 survey showed no serious signs of corrosion and predicted at least another 20-30 years of maintenance-free service (Arminox, 1999). Its performance is all the more impressive when compared to the neighbouring pier, whose remnants are shown adjacent in Figure 6. Built in 1972 with plain carbon steel reinforcement, it managed to survive only 11 years of service before deteriorating from reinforcement corrosion (Markeset, Rostam et al., 2006). Further studies showing stainless steel rebar's superior corrosion performance compared to galvanized, epoxy-coated and plain carbon-steel rebar are well summarized in literature (Nuernberger, 1996).



Figure 6: Stainless steel rebar was first used in Progreso Pier, Yucatan, Mexico (Arminox, 1999)

2.2.2 Properties of Stainless Steel

2.2.2.1 Alloy Composition and Designations

Stainless steels are comprised of a group of 180 different alloys having chromium content in the range of 11-30% by weight to provide increased corrosion resistance. Table 2 lists a number of additional alloying elements used in stainless steels and their function (Sedriks, 1996):

Table 2: Alloying additions in stainless steels

Alloying Element	Function
Cr, Ni, N, Mo	Corrosion resistance
C, Mo, N, Ti, Al, Cu	Strength
S, Se	Machine ability
Ni	Formability and toughness

The phase composition of stainless steel varies depending on the composition of alloying elements, with different elements stabilizing the formation of either austenite or ferrite. The Schaeffler diagram in Figure 7 illustrates this, showing the degree in which nickel, carbon and nitrogen promote austenite formation while chromium, molybdenum, silicon and niobium promote ferrite formation.

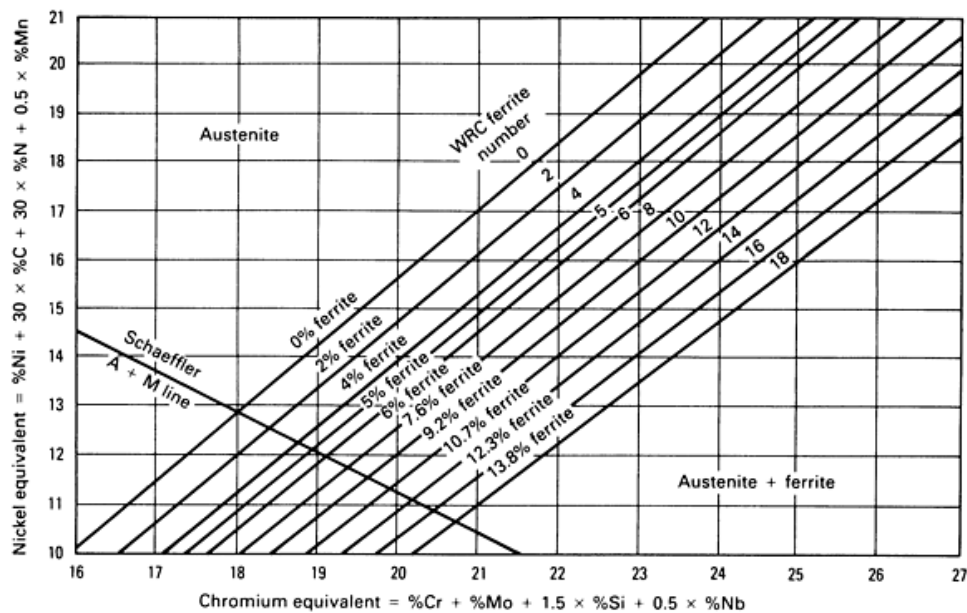


Figure 7: Effect of alloying additions on stainless steel phase composition (Washko and Aggen, 2002)

Stainless steels are designated by AISI as three digit numbers, with wrought austenitic grades in the 200 and 300 series. Duplex alloys containing both ferrite and austenite do not have AISI designations and are instead known by compositional abbreviations and trademarks. For example, duplex steel type 2205 signifies 22% Cr and 5% Ni by weight. Table 3 lists the stainless steel types used in this project, with duplex 2205 among them as well as two austenitic types. These three steel types are most commonly specified for reinforcement applications.

Table 3: Chemical composition of stainless steel grades for concrete reinforcement, maximum chemical composition values (ASTM-A955, 2004)

Steel Type	Cr	Ni	C	Mn	Si	P	S	Mo	N
304LN	18.00-20.00	8.00-10.50	0.03-0.08	2.00	1.00	0.045	0.030	-	0.10-0.16
316LN	16.00-18.00	10.00-14.00	0.03-0.08	2.00	1.00	0.045	0.030	2.00-3.00	0.10-0.16
2205	21.00-23.00	4.50-6.50	0.03	2.00	1.00	0.045	0.020	2.50-3.50	0.08-0.20

The ‘L’ signifies low carbon while the N signifies nitrogen addition. Low carbon prevents the formation of chromium carbides after welding or high temperature exposure, improving intergranular corrosion resistance, and nitrogen is added to compensate for the loss of strength incurred by the reduction in carbon as well as improve crevice and pitting corrosion resistance. Molybdenum gives 316 improved pitting resistance over 304, nickel improves the stress corrosion and high temperature corrosion resistance, and chromium improves the latter (Sedriks, 1996).

2.2.2.2 Mechanical Properties

Typical mechanical properties of each stainless steel type are shown in Table 4 with duplex 2205 having a distinct strength advantage over the austenitic types, enabling less of it to be used for structural applications. Similar strengths to those of the austenitic types are specified for plain carbon-steel rebar (ASTM-A615, 2007).

Table 4: Mechanical properties of stainless steel rebar (Sedriks, 1996; ASTM-A955, 2004; Tullmin, 2006)

Grade	Tensile Strength (MPa)	Yield Strength (0.2% Offset) (MPa)	Elongation (%)	Hardness Rockwell B
Austenitic	550-860	205-500	30-60	80-85
Duplex	570-1000	330-560	25-40	-

2.2.2.3 Corrosion Properties

Stainless steel is well known for its excellent corrosion resistance in many environments, particularly austenitic and duplex types. The key behind this as mentioned above are the alloying elements, notably chromium, nickel, molybdenum and nitrogen, all of which contribute to the formation of a complex passive film on the steel's surface that provides a greater protection from aqueous, chloride-induced corrosion compared with plain carbon-steel. The exact structure and formation mechanism of the complex film is the subject of much research, though the general structure is a thin layer of chromium oxides, with a thickness of ~1.5 nm (Olefjord, Brox et al., 1985). Some have reported the layer to be a duplex structure consisting of an inner barrier oxide film and outer hydroxide or salt film deposit (Clayton and Olefjord, 1995). Though chromium oxide is a reasonable electronic conductor, the layer achieves its protective properties from its low ionic conductivity (Hoar, 1959).

Stainless steels are not immune from corrosion, however, and are particularly susceptible to a localized form known as pitting. Local breakdown of the passive film can occur either due to mechanical imperfections on the surface (e.g. scratches or inclusions), or from local attack of chemical species such as chlorides or other halides. As shown in Figure 8, the pit's base becomes deprived of oxygen relative to the bulk surface, and the resulting aeration cell creates a net current flow accelerating oxidation within the pit and reduction on the surrounding surface. The attraction of chloride anions to metallic cations at the pit's base and the subsequent hydrolysis of the metallic chlorides decrease the pH in the pit and create an autocatalytic corrosion process.

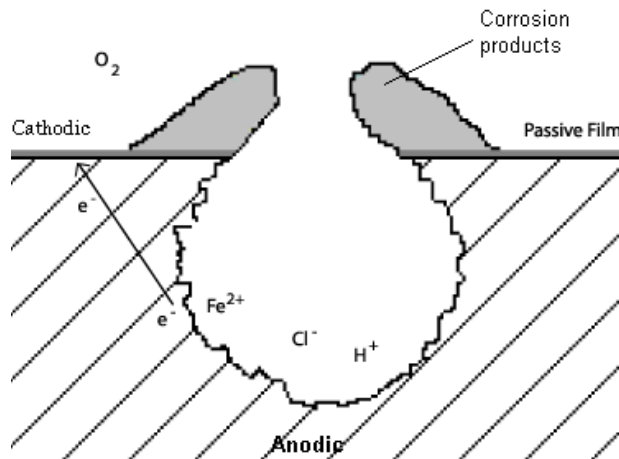


Figure 8: Schematic of pitting corrosion (Waidis, 2008)

A value based on an alloy's chemical composition can be calculated to determine its relative pitting resistance, and is known as the pitting resistance equivalent (PREN)(BSSA, 2007). Table 5 summarizes the PREN equations and values of the alloys used in this project, indicating 2205 to be the most resistant, followed by 316LN then 304LN. These formulas were derived with both commercial and laboratory-produced alloys using various standard test methods (i.e. critical pitting temperature, pitting potential) and in various media (0.6 M NaCl + 0.1M NaHCO₃, to 6% FeCl₃); however, inconsistencies between PREN values and relative real-world corrosion performances among stainless steels have been observed (Cleland, 1996), and evaluating stainless steels, particularly within the same family or grade, based on their PREN carries significant risk.

Table 5: Pitting resistance equivalent equations and values (BSSA, 2007)

Steel Phase	Equation	Steel Type	PREN
Austenitic	PREN = %Cr + 3.3(%Mo) + 30(%N)	304LN	18.9-23.0
		316LN	25.0-30.3
Duplex	PREN = %Cr + 3.3(%Mo) + 16(%N)	2205	30.8-38.1

2.2.3 Stainless Steel Performance in Concrete

The high corrosion resistance of austenitic stainless steel has made the observance of its active corrosion in concrete hard to come by, though its pitting potential has shown more negative values with decreasing alloying content and increasing chloride content (Nürnbergger and Beul, 1999; García-

Alonso(a), M.L.Escudero et al., 2007). Many recent studies have confirmed its superior performance to that of plain carbon-steel. In a long-term study (Cochrane, 1995), SS316 reinforced concrete prisms admixed with 3.2% Cl⁻ by weight of cement were broken open after 22 years to reveal no sign of rusting on the bar's surface. In contrast, the same structures reinforced with carbon-steel were very badly corroded and essentially crumbled when moved. Other studies have found corrosion rates for stainless steel rebar in concrete contaminated with ~ 4 % Cl⁻ by weight of cement to be lower than for carbon steel rebar in Cl⁻ free concrete after 2 years of exposure (Gu, Elliott et al., 1996; García-Alonso(a), M.L.Escudero et al., 2007).

Duplex and austenitic stainless steels perform reasonably similarly in high pH, chloride contaminated environments, with one study (Hope, 2001) showing both exhibiting corrosion currents typical of passive carbon steel in concrete of $10^{-4} - 10^{-3}$ A/m² at Cl⁻ levels that increased from 0-15% over the course of a few months in a simulated concrete pore solution of saturated Ca(OH)₂. The austenitic types 304 and 316 have shown similar corrosion current corrosion performance as well, exhibiting corrosion rates of $10^{-3} - 10^{-4}$ A/m² in concrete containing 4% Cl⁻ by weight of cement over 800 days (García-Alonso(a), M.L.Escudero et al., 2007). These fared much better than the plain carbon-steel rebar in this study which exhibited corrosion rates of ~ 10^{-2} A/m² under equivalent exposure conditions. Lower admixed chloride contents of 1% by weight of cement have caused similarly high corrosion rates of black steel in concrete of $5 \times 10^{-3} - 1.3 \times 10^{-2}$ A/m² after 400 days of exposure (Mammoliti and Hansson, 2007).

In terms of chloride threshold, a test (Trejo and Pillai, 2004) involving the rapid diffusion of chlorides into mortar containing stainless rebar found mean critical chloride thresholds of 4.6 and 10.8 kg/m³ for SS304 and SS316, respectively. These were significantly higher than the 0.4 kg/m³ obtained for plain-carbon steel rebar using the same method (Trejo and Pillai, 2003).

2.2.3.1 Macrocell Corrosion/Coupling

As mentioned in Section 2.1.2, the formation of a macrocell can exacerbate the corrosion of plain carbon-steel (black) rebar. Since the lower rebar layers are less at risk of chloride-induced corrosion, the application of stainless steel rebar was typically favoured solely for the more at-risk top layer. However, there has been concern over the connection of two different steel types in concrete due to the implications of possible galvanic corrosion that may ensue, adding to the already present

macrocell effect of uneven chloride distribution in concrete. Until 2001, the Ontario Ministry of Transportation had specified the use of plastic sleeves to separate the black and stainless steel at all points of contact (Hope, 2001) to avoid this risk of galvanic corrosion, a practice recommended by industry (NIDI, 2004), though surely a time-consuming and expensive process.

Further research has shown that connecting stainless steel rebar to black steel rebar poses no additional risk to the macrocell currents already occurring, whether or not chlorides are present and the plain carbon-steel is in the active or passive state (Abreu, Cristobal et al., 2002; García-Alonso(b), González et al., 2007). If anything, the corrosion of carbon steel when attached to stainless steel is lower due to the slower cathodic reaction kinetics (i.e. oxygen exchange current density) that occurs on stainless steel's surface (Hope, 2001). One study found the cathodic reduction current on stainless steel to be less than half that on passive carbon steel (Qian, Qu et al., 2006). It is speculated by the author to be partially attributed to the smoother surface typically found on stainless steel rebar, which, unlike plain-carbon steel, has its outer layer of mill scale removed after hot rolling, a topic to be discussed in this next section. This smoother surface may contain less actual surface area over a given amount of apparent geometric surface area upon which the cathodic reaction can occur.

2.2.4 Stainless Steel Bar Fabrication

2.2.4.1 Hot Rolling and Annealing

The fabrication of austenitic stainless steel bar involves a series of heating, forming and surface treating processes. The material is first cast into large billets, and then hot rolled into narrower bar diameters, typically a ribbed profile in the case of concrete reinforcement. The work hardened steel is then annealed to achieve a uniform grain size and restore formability. Annealing temperatures are typically around 1150°C, but have been known to reach up to 1260°C (Covino, Scalera et al., 1984; Li and Celis, 2003).

During this high temperature processing, a continuous oxide scale forms on the steel's surface, commonly referred to as 'mill scale'. The conditions in annealing furnaces vary between different manufacturers, and the structure of these oxides for a given steel is not consistent since they depend on both the furnace atmosphere (typically ranging from 11-14% CH₄), schedule of temperature exposures and rolling intensity (Rau, 1988; Li and Celis, 2003).

The oxygen in the annealing atmosphere reacts preferentially with chromium, forming a thin layer of chromium oxide (Cr_2O_3) at the steel's surface because of its low ionic conductivity, while leaving a layer of chromium depleted bulk metal underneath (Covino, Scalera et al., 1984). Other oxides that have been found to form on stainless steel at these high temperatures are Fe_2O_3 , $(\text{Fe,Cr})_3\text{O}_4$ spinel, FeO , Fe_3O_4 , NiFe_2O_4 , and $(\text{Fe,Cr})_2\text{O}_3$ (Wood, 1962; Rau, 1988; Li and Celis, 2003). Cr_2O_3 is adherent and protective, while the iron oxides are generally less adherent, porous and non-protective. Smaller grain sizes are believed to produce mill scale with higher chromium content and, thus, more depletion due to greater grain boundary area for chromium diffusion (Li and Celis, 2003).

Figure 9 shows scanning electron microscope (SEM) backscattered (BSE) and electron backscatter diffraction (EBSD) images of a cross section of surface oxide on SS316L that has been exposed to 1200°C for 4 hours in air, revealing a multi-layered or stratified structure. The inner part of the scale consists of two chromium oxides with either spinel or corundum-like structures. The middle layer is an iron and nickel-rich spinel, while the outer layer consists of Fe_2O_3 . Another study (Wood, 1962) found a similar stratified structure forming after long exposure times: at 1000°C an Fe-14.4% Cr alloy formed a thin chromium oxide layer during the first five minutes which, when left for over an hour, was broken through by iron oxides that formed a stratified structure over the Cr_2O_3 . This process has been reported elsewhere as well (Whittle, Wood et al., 1967; Hobby and Wood, 1969). After 7 hours, a $30\ \mu\text{m}$ thick stratified iron oxide scale resulted consisting from the inside to the outside of $\text{FeFe}_{(2-x)}\text{Cr}_x\text{O}_4$, FeO , Fe_3O_4 and Fe_2O_3 , with a $\sim 1\ \mu\text{m}$ thick chromium oxide remaining at the interior.

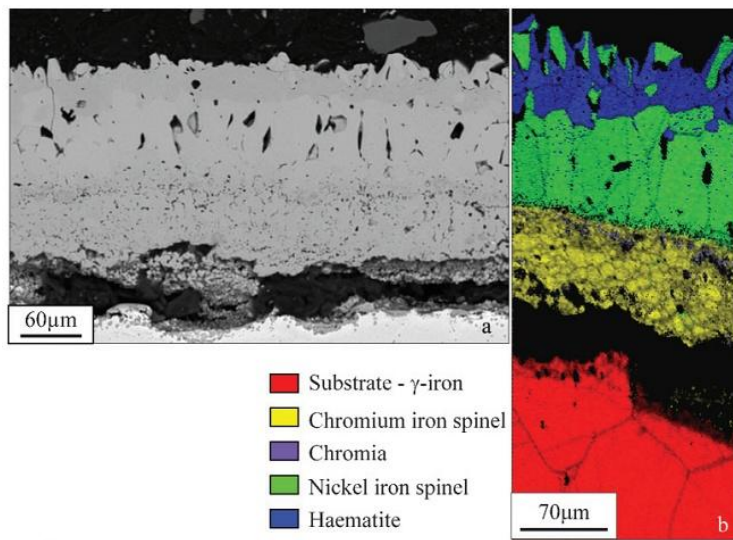


Figure 9: (a) BSE SEM image and (b) EBSD derived phase map for scale grown on 316L stainless steel at 1200°C for 4 hours (Higginson, Jepson et al., 2006)

Another study (Stott and Wei, 1989) found the same maximum scale thickness at 1000°C after 1000 hours for SS310 (25% Cr). However, SS321 (18% Cr) experienced break-away scale growth up to 400 µm after 1000 hours, indicating how crucial the chromium is for limiting the oxidation rate. At 800°C both alloys formed a thicker scale of 50 µm, suggesting as others have found (Betz, Wehner et al., 1974) that the increased kinetics at higher temperatures favour the formation of a more protective chromium oxide scale. These scales are much larger than those encountered on annealed rebar, and the steel types are not the same as those used for this project, but the evolution of high-temperature scale on Fe-Cr alloys is worth examining.

2.2.4.2 Surface Treatment

Standard industry practice has been to treat annealed stainless steel's surface by: (1) removing the mill scale to give the product a shiny and visually aesthetic appearance and (2) removing a thin layer of underlying steel believed by many, as discussed in the next section, to be significantly depleted in chromium, compared to the bulk. This chromium depletion, in theory, reduces the steel's corrosion resistance, and is formed by the preferential diffusion of chromium up to the surface during annealing as mentioned in the last section. Although the improved aesthetics of having the mill scale removed in step (1) adds little value to concrete reinforcement, the removal of the chromium depleted layer in step (2) is believed to be an important consideration for this application. Industry has, to date, strongly recommended the pickling of stainless steel rebar to minimize the risk of any premature corrosion (NIDI, 2004; ASSDA, 2008), and many municipalities including the Ontario Ministry of Transportation have followed these recommendations (MTO 2001; Pianca, 2005).

The mill scale is typically removed by blasting the bar's surface with stainless steel or silica abrasive (Covino, Scalera et al., 1984; NIDI, 2004; Pianca, 2005). The velocities of the abrasive are optimized to crack/loosen the scale without cold-working the steel's surface, and this process can produce surface defects with thickness variations of up to 200µm (Li and Celis, 2003).

Once the outer mill scale has been removed and/or loosened, the material is immersed in large 12-18 meter-long pickling baths typically consisting of a mix of hydrofluoric and nitric acids (Li, Caenen et al., 2005; ASSDA, 2008), where the high reactivity of the Cr-depleted zone underneath causes rapid surface dissolution until the bulk composition is reached. The emissions and effluents from this

process are environmentally hazardous, and their safe handling/disposal adds significant cost to stainless steel rebar's fabrication. An estimated 40 million gallons of waste HNO_3 -HF pickling acid is produced each year in the U.S. alone. Pickling costs, including the disposal method of neutralizing with lime, dewatering the resulting sludge containing iron, nickel and chromium, then land-filling the waste, is approximately \$5000/ton of stainless steel, and its elimination would have saved the Ontario Ministry of Transportation \$1.2 million in 2007 (Price and Horter, 1994; Mammoliti and Hansson, 2007).

The mechanism of pickling involves attacking the steel's passive surface with H^+ , NO_3^- ions which produces metallic cations, NO and water (Li and Celis, 2003). Free fluorides from the HF solution also play a key role in dissolving the chromium from the depleted regions (Price and Horter, 1994). An estimated 1-5 μm of material is removed between the outer oxide scale and the bulk metal (Covino, Scalera et al., 1984). What is not well known however is the depth and magnitude of the Cr-depleted layer, as well as its contribution in controlling the pickling rate. Ideally the pickling solution easily penetrates the remnants of the oxide and rapidly dissolves the Cr-depleted layer, while affecting only a small layer of the bulk steel. However due to the myriad of factors including temperature, time of immersion, dissolved metal concentration, agitation, acid ratio, etc, results can be inconsistent, and in some cases pickling has been shown to cause intergranular corrosion of the base metal (Li and Celis, 2003).

2.2.4.3 Chromium Depletion at High Temperatures

Little data are available on the depth and magnitude of chromium depletion that occurs near the surface of stainless steels during annealing, and they are mostly related to high temperature applications with lengthy exposure times such as encountered in the power generation sector. Studies that advocate removing the chromium depleted layer in stainless steels through pickling (Li and Celis, 2003; Scully and Hurley, 2007) typically refer to research based on these long exposure times (Evans and Lobb, 1984; Stott and Wei, 1989). A challenge is determining which studies are relevant when the actual annealing data of stainless steel rebar are not disclosed by the steel manufacturers. Nevertheless, it is useful to gain an understanding of the degree of chromium depletion encountered in previous studies and under what conditions. The following lists a brief summary:

- No chromium depletion was found in SS304 when heated at 1140°C for 2.5 minutes in a 6% O₂ atmosphere, using a profile spot count across the interface of 50 nm intervals (Hilden, Virtanen et al., 2001).
- A drop in Cr was found for an Fe-20Cr-25Ni alloy from 20 wt% bulk to 12.6% and 16.2% when heated for 10,000 and 6000 hours, respectively, at 1400°C in a CO₂ atmosphere. The thickness of the Cr-depleted region was not provided (Evans, Hilton et al., 1976; Evans, Hilton et al., 1980).
- A drop in Cr was found for SS310 from 26.3 wt% bulk to 22% extending 16 μm into steel substrate after 100 hr at 1000°C, and to a value of 21% after 1000 hr at 800°C. For SS321, a drop in Cr from 18.3 wt% to 10% over a depth of 20μm was exhibited after 1000 hr at 800°C, and to a value of 13% over a depth of 38μm after 100 hr at 1000°C (Stott and Wei, 1989). This suggests that oxides forming below 1000°C or forming on alloys with lower Cr content are less protective.

An interesting study (Ostwald and Grabke, 2004) compared the interfacial chromium concentration of several stainless steels with different initial surface roughnesses. After oxidizing at 600°C for 100 hours in H₂-H₂O, the more deformed surfaces (sandblasted and ground) exhibited a much shallower Cr depletion as well as a more robust, high-Cr content mill scale than smooth (polished) surfaces. It is believed that the surface deformation, which extended 1-2 μm into the surface, leads to better interconnected network of fast diffusion paths in the bulk metal phase, thus allowing concentration gradients to be relieved more quickly. Increased surface area from the deformation may be another factor. It may be worth specifying that stainless steel rebars have adequate surface roughness before annealing to form a more protective film with a less abrupt depletion in chromium underneath which, as the study reports, is a method favoured for stainless steel applications in the power industry. Another consideration when preparing steel for pre-annealing treatment is the grain size; a smaller grain size resulting from lower temperature and more intense rolling will form a more protective chromium oxide due to the greater availability of diffusion paths along grain boundaries for chromium to travel (Covino, Scalera et al., 1984), though the resulting magnitude of chromium depletion from this method is uncertain. The chromium depletion that took place in Ostwald's study for SS304 having a ground surface preparation (600 grit SiC paper) is shown in Figure 10, with a drop in Cr from 18 wt% bulk to just above 10% over 250 nm. In contrast, the electro-polished

SS304, which exhibited a diffusion coefficient two orders of magnitude lower near the surface, formed no dense oxide film under the similar exposure conditions.

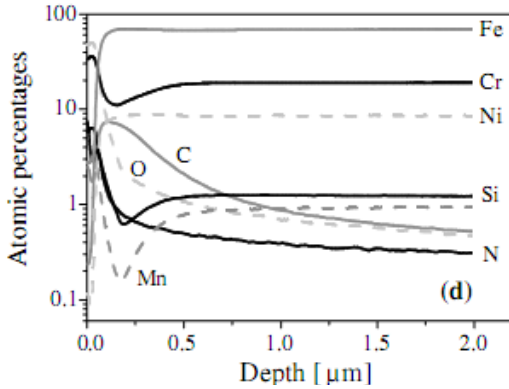


Figure 10: Depth profile of SS304 with ground surface after 100 hours at 600°C (Ostwald and Grabke, 2004)

2.2.5 Effect of Surface Conditions

There has been limited study on the corrosion performance of stainless steel rebar in concrete with different surface conditions. This is worth investigating since the whole point of surface treating stainless steel rebar is ensuring its high corrosion resistance, with aesthetics being a trivial matter. If negligible reduction of the rebar's cross-section and/or corrosion product build-up in chloride-contaminated concrete results from initial roughness or pre-pitting at the surface, then the shot-blasting and pickling processes essentially contribute no value to stainless steel rebar.

An accelerated chloride threshold test in mortar (Pillai and Trejo, 2005) found that when comparing the corrosion performance of different surface conditions, not only did plain-carbon steel show superior chloride threshold values in the “as-rolled” condition versus the polished condition (0.5 vs. 0.3 kg Cl/m³ concrete), but SS316 showed superior performance in the as-rolled versus polished condition as well (10.8 vs. 7.3 kg Cl/m³ concrete), while SS304 as-rolled exhibited slightly inferior performance (5 vs. 6.2 kg Cl/m³ concrete). Important to note however is that this study's as-rolled stainless was still pickled (just not polished), and thus not truly representative of an as-rolled surface. The comparison is still significant though since it provides a somewhat analogous comparison of surface roughness performance one might encounter when comparing pickled versus as-rolled rebar.

A recent study (Scully and Hurley, 2007) of SS316 in saturated Ca(OH)₂ containing chlorides compared the chloride threshold for as-rolled versus pickled surfaces by applying a constant potential

of +200 mV vs. SCE. The as-rolled surface, simulated by heating pickled rebar in air at 1050°C for one hour, exhibited active corrosion ($i_{\text{corr}} > 10^{-2}$ A/m²) at a lower Cl⁻/OH⁻ ratio than pickled (0.3 vs. 30). This may however be due to the as-rolled” bar being placed directly into pore solution containing chlorides without giving the surface time to passivate normally as it would have in concrete structures where chlorides diffuse in over time. As well, saturated Ca(OH)₂ solution has a lower and, thus, less protective pH of 12.6 than the 13.5 typically found in concrete (Mammoliti, Brown et al., 1996).

A study (García-Alonso(a), M.L.Escudero et al., 2007) of pickled rebar in concrete slabs containing 4% Cl⁻ by weight of cement showed SS316’s corrosion rate to be almost 10 times higher than SS304. This contradicts previous findings (Nuernberger, 2005) as well as SS316’s higher PRE mentioned Section 2.2.2.3 which, based on its higher alloy content, predict it would perform better. This behavior was attributed to differences in surface conditions and, as shown in Figure 11, large axial grooves and crevices were present on 316’s surface, whereas 304’s surface was relatively smooth. The surface irregularities were believed to be caused by the rolling process; however another explanation could be over-pickling of the SS316 which induces intergranular corrosion, a phenomenon mentioned in Section 2.2.4.2.

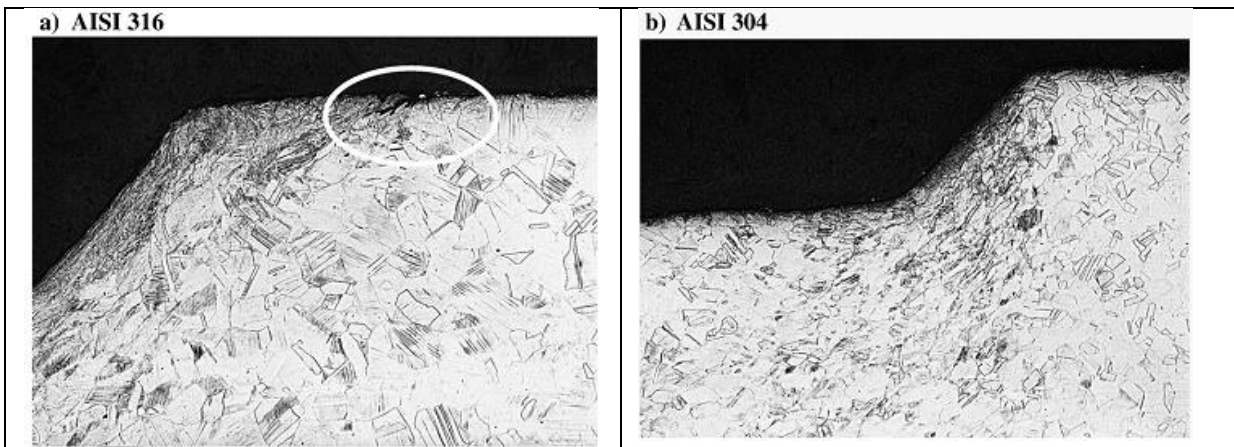


Figure 11: Optical micrographs of microstructure of ribbed 316 and 304 stainless steel bars (García-Alonso(a), M.L.Escudero et al., 2007)

A recent study (Mammoliti and Hansson, 2007) compared the performance of as-rolled versus pickled SS316 and SS2205 in concrete containing 5% Cl⁻ by weight of cement coupled to plain carbon-steel in chloride free concrete, inducing additional corrosion currents via the macrocell

connection. After 60 weeks, values for pickled steels were on average $5 \times 10^{-4} \text{ A/m}^2$, whereas the values for both as-rolled steels were just two times higher at around 10^{-3} A/m^2 . Both values were within the range of passive plain-carbon steel reinforcement, despite exposure to the extremely high chloride concentration. No distinguishable trend in corrosion potentials was observed, with the values all falling in the range of -100 to -300 mV vs. SCE.

While comparing surface conditions of stainless steel in concrete is most beneficial for this project, it may also be worth noting studies comparing their performance in other environments. One study (Li, Caenen et al., 2005) compared SS304 strips with as-rolled and smooth (pre-pickled) surfaces during a number of alternative pickling processes. Exposure to HCl at 55°C produced a lower mass loss rate for the as-rolled than for the smooth strips, as shown in Figure 12. It was suggested that the mill scale suppressed corrosion via concentration polarization by blocking oxidizing reactants' access to the steel's surface. The corrosion potential evolution is also noteworthy, since the oxidized corrosion potential is consistently -30 mV more negative despite a seemingly lower corrosion rate.

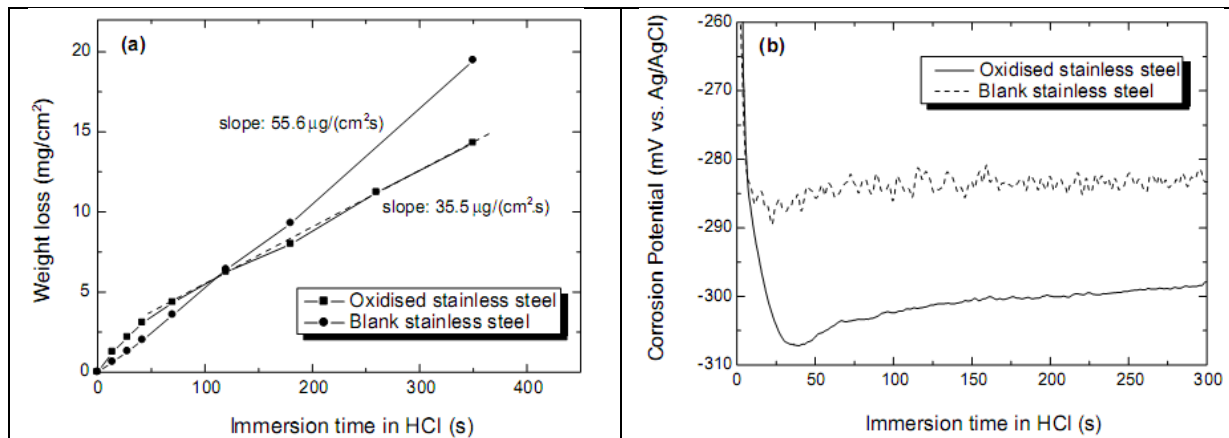


Figure 12: Evolution of (a) mass loss and (b) corrosion potential for SS304 with smooth and blank surfaces in HCl at 55°C (Li, Caenen et al., 2005)

2.2.6 Effect of Loading and Cracks

The effect of loading on stainless steel rebar's corrosion resistance has received very little attention to date. One study (Mendoza, 2003) involving the dynamic loading of carbon-steel reinforced beams immersed in 3% Cl⁻ solution, found corrosion occurring on 5mm ø SS316 stirrups near a crack interface. Cyclic loading opened the crack between 0.1-0.2mm at a frequency of 1 Hz. The abrasion

created by the crack motion may have perpetuated an erosion corrosion process whereby the steel's passive layer was constantly being removed to expose a fresh layer of steel underneath, leading some material loss. One can easily imagine how stainless steel rebar could be susceptible to this same process in structures exposed to similar cyclic loading.

A study (Nürnberg and Beul, 1999) of rebar in cracked, but unloaded, concrete beams exposed outdoors to salt spray for 2.5 years found SS316 pickled stainless steel rebar to remain passive over the duration of testing, despite crack widths of up to 1 mm and chloride contamination at 4% Cl⁻ by weight of cement near the steel surface. Corrosion potentials were around -200 mV vs. SCE at the end of testing. In contrast, unalloyed steel rebar depassivated after 1-3 months, with active corrosion found at the steel intersected by crack widths exceeding 0.1mm. Others have found chloride penetration in concrete to increase rapidly at these at these crack widths (Wang, Jansen et al., 1997; Ismail, Toumi et al., 2004), with cracks widths of < 50 µm having negligible effect on Cl⁻ penetration.

Corrosion originating at cracks in plain carbon-steel reinforced beams has been found in other studies as well. One comparison (Mendoza, 2003) of dynamically and statically loaded plain carbon-steel reinforced beams exposed to 3% Cl⁻ solution found strong corrosion at the cracks occurring within the first few weeks of exposure for both types of loading, though corrosion rates were less on the statically loaded (50 µm/year) than on the dynamically loaded (200 µm/year) beams. This was attributed to the possibility of more micro-cracks forming in the dynamic beams as well self healing mechanisms such as progressive hydration and/or corrosion product blockage in the static beam cracks. Another study (Jaffer and Hansson, 2008) found corrosion occurring *only* at the cracks of plain carbon-steel reinforced beams exposed to 3% Cl⁻ solution, with loading causing significant de-bonding between the steel and concrete near the cracks. This likely intensified the corrosion processes at these locations by providing more chloride accumulation and resulting in increased ionic conductivity at the steel surface.

2.3 Concluding Remarks

While it is clear that stainless steel rebar's corrosion resistance is far superior to that of plain carbon-steel rebar in concrete exposed to chlorides, the need for pickling stainless steel rebar in order to achieve this enhanced corrosion resistance is unknown. Limited data exists on the extent of chromium depletion that occurs at stainless steel's surface during fabrication, with none available for

the case of rebar, and yet the costly practice of pickling stainless steel rebar continues because of this very concern. Another aspect is the effect that dynamic loading may have in removing pickled stainless steel rebar's passive film through micro-motion at the crack-concrete interface, leading to decreased corrosion resistance and possibly premature failure under certain loading scenarios. While this has not been observed in practice, recent observation of corrosion of stainless steel stirrup wire at the crack of dynamically loaded concrete suggests this may be a risk. The objective of this research was to compare the corrosion resistance of pickled and as-rolled (non-pickled) stainless steels of different grades embedded in highly chloride contaminated concrete, as well as investigate the effect, if any, that dynamic loading has on the corrosion resistance of pickled stainless steel rebar in cracked concrete compared with static loading.

Chapter 3

Experimental Procedures

3.1 Effects of Surface Conditions

3.1.1 Specimen Design

The specimen design used to evaluate the effects of surface conditions is a modified version of the ASTM G109 concrete prism design shown in Figure 13. Three bars were cast in a concrete prism: one at the top, two on the bottom, and a ponding well inserted above the top rebar. The two bottom bars were connected electrically, and a 100Ω electrical connection was placed between the top and bottom bars.

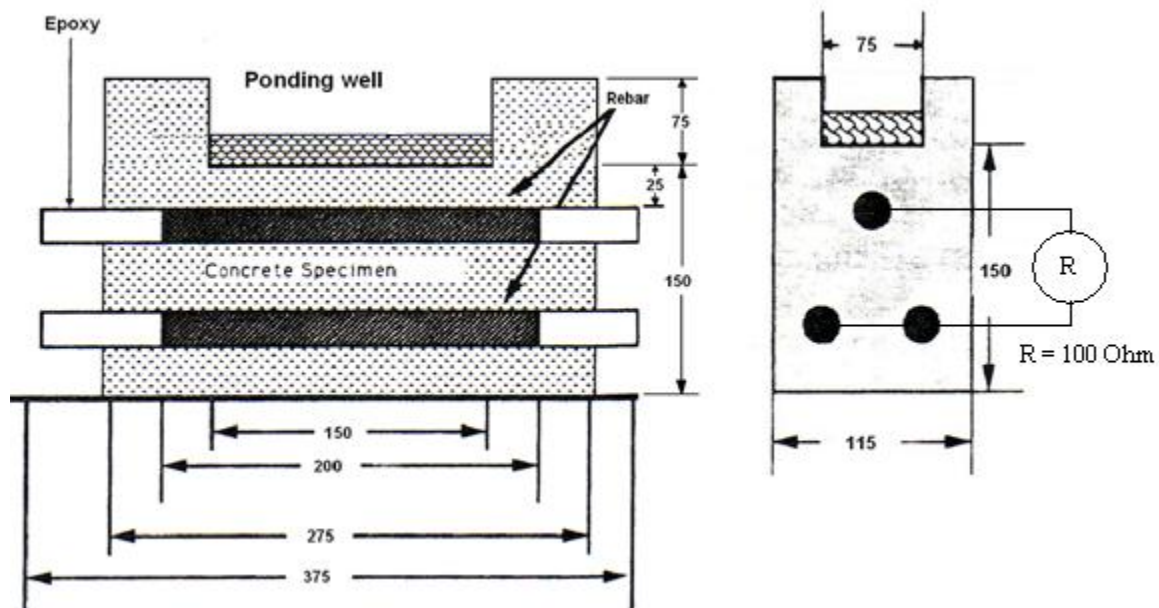
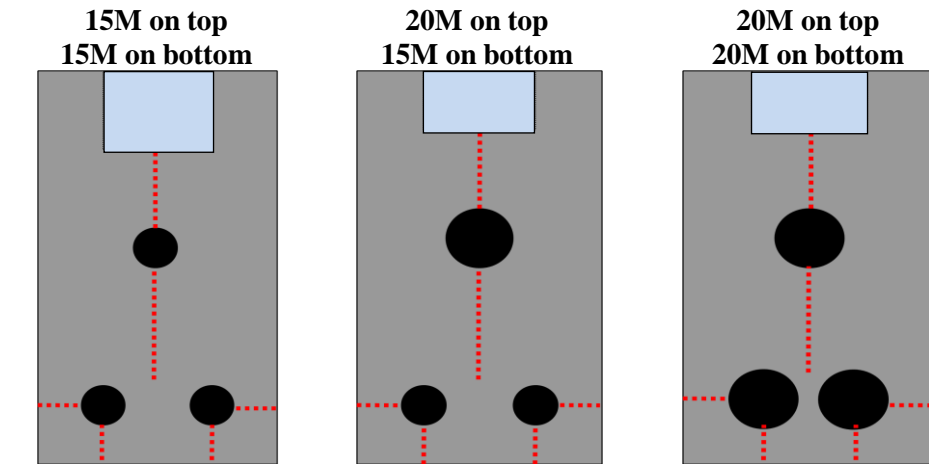


Figure 13: Schematic illustration of G109 specimen design, all dimensions in mm (ASTM-G109-99a, 2005)

The design is meant to simulate multiple reinforcement layers typically found on a bridge deck. The electrical connectivity between these layers, as discussed in Section 2.1.2, can result in the exchange of macrocell currents that accelerate corrosion of the bars near the structure's surface exposed to higher chloride concentrations while decreasing corrosion of the bars further away from the surface where chlorides are usually at lower concentrations.

The reinforcements were all 38 cm in length; however two different diameters were supplied: 15M and 20M, whose nominal diameters are 16.0 and 19.5 mm, respectively. In an attempt to minimize discrepancies in the results attributed to this, a consistent concrete cover depth of 25 mm on each side of the bottom bars was established in order to keep constant the distance required for external oxidative species (i.e. oxygen, water, chlorides) to diffuse to the rebar surface. Since all prisms had equal widths however, this resulted in less concrete between the larger bottom bars than the smaller bottom bars, though this likely had negligible influence on results given that two bars in the same environment would have negligible electrochemical interaction with one another. The cover depth between the ponding well and the top bar was decreased from 25 mm in the G109 standard to 19 mm in order to intensify corrosive conditions at the top bar by providing a shorter diffusion path for oxidative species (i.e. oxygen, water, chlorides) to the bar's surface. Distances between top and bottom rebars were also kept equal by changing the ponding well depth. Schematic diagrams of the various configurations for different bar sizes and the dimensions that were kept equal are shown in Figure 14.



*Distances kept the same for all specimens denoted by

Figure 14: Configurations for different bar sizes in G109 prisms

To further enhance the corrosive conditions of the G109 design, which was originally intended for testing much less corrosion resistant plain carbon-steel rebar, the prisms were modified by casting them as two separate layers of concrete: a chloride contaminated upper layer, and a chloride free lower layer, as shown by the two different shades of concrete in Figure 15.

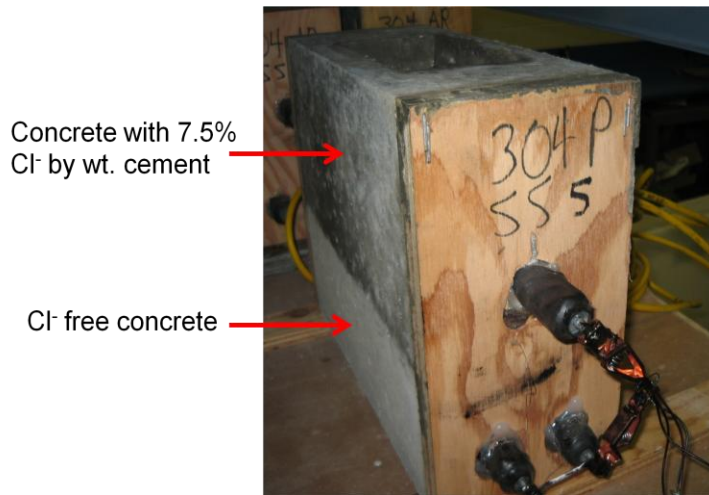


Figure 15: Modified G109 prism with a chloride contaminated upper and chloride-free lower concrete layer

Chloride in the form of NaCl was admixed in the upper layer at a concentration of 7.5% Cl⁻ by mass of cement, determined experimentally to be the minimum amount required to achieve pore solution in the mature concrete which is saturated with chlorides. In other words, 7.5% Cl⁻ by mass of cement is the minimum amount of admixed chlorides that exposes the rebar to the maximum concentration of free chlorides in concrete. Appendix A presents the admixed chloride analysis in further detail.

Manganese-manganese oxide reference electrodes (model: ERE 20 supplied by FORCE Technology), shown in Figure 16, were embedded equidistant from the top and bottom rebars of one 304PS and one 304AS prism by fixing them into place in the forms. This allowed for corrosion potentials of both top and bottom bars to be measured in-situ simultaneously, both with (polarized) and without (depolarized) the connection between the bars. This was helpful in determining the time required to depolarize the bars once the macrocell was disconnected so that equilibrium corrosion potentials were reached before taking microcell corrosion measurements.



Figure 16: Embedded Mn-MnO₂ reference electrode (Klinghoffer)

3.1.2 Rebar Types

The stainless steel was supplied by Valbruna Canada Ltd., and the plain carbon-steel for the bottom bars, referred to in this project as ‘black steel’, was supplied by Albrecht Reinforcing Inc. The surface conditions, steel types and diameters, bottom bar types, nomenclature and quantity of modified G109 prisms incorporating each of these variables are shown in Table 6. The black steel rebar was supplied as-rolled, with a bar size of 15 M (nominal 16.0 mm diameter).

Table 6: Steel materials and nomenclature used in modified G109 prisms

Surface Condition	Top Bar Steel Type/Size	Bar Size (metric/nominal diameter in mm)	Bottom Bar Type	Specimen Nomenclature	# of each
Pickled (P)	304LN	20/19.5	304LN (P)	304P S	5
			Black	304P B	
	316LN	15/16.0	316LN (P)	316P S	
			Black	316P B	
	2205	15/16.0	2205 (P)	2205P S	
			Black	2205P B	
As-Rolled (A)	304LN	20/19.5	304LN (A)	304A S	
			Black	304A B	
	316LN	20/19.5	316LN (A)	316A S	
			Black	316A B	

The chemical compositions provided by Valbruna for their 304LN and 316LN and 2205 steel types are shown in Table 7. These values are in agreement with those specified by standards for stainless steel concrete reinforcements (ASTM-A955, 2004) listed in Table 3.

Table 7: Rebar chemical composition provided by Valbruna

Element (%)	C	Si	Mn	Cr	Mo	Ni	P	S	N
304LN	0.018	0.56	1.27	18.24	-	8.59	0.034	0.009	0.13
316LN (20M)	0.015	0.62	1.09	17.94	2.05	10.50	0.033	0.023	0.12
316LN (15M)	0.018	0.54	1.48	17.17	2.09	10.56	0.028	0.030	0.15
2205	0.028	0.43	1.49	22.63	2.76	5.52	0.030	0.001	0.14

3.1.3 Rebar Preparation

Electrical contacts on the rebars were necessary both for establishing macrocell contact between neighbouring bars as well as for electrochemical corrosion measurements. The contacts were established by drilling, tapping and inserting stainless steel screws into one end of each rebar. The stainless steel bars were drilled with 4.1 mm carbide drill bits, and the black steel bars were drilled with #20 high-strength tool steel. Each bar was then tapped to a depth of 1.25 cm and a #10-32 stainless steel screw was inserted to form an electrical contact on the bar's end.

To isolate the ends of the rebar (not including the electrical contact) from the atmosphere and leave a surface length of 200 mm in the bar's middle exposed to the concrete, the ends were covered by applying three coats of two-part Sikafloor 261^{CA} epoxy, leaving each coat to dry for 24 hours. A light fourth coat was applied, immediately after which heat-shrink rubber tubing was sealed over the wet epoxy with a heat gun. To provide extra protection around the screw-rebar interface and avoid galvanic corrosion between the two metals, hot glue was applied liberally around the base of the screw. The prepared rebars before casting are shown in Figure 17 (a).

After the bars were embedded in concrete as described in the following section, electrical connections were made between the screws of neighbouring bars using crocodile clips and/or electrical wire wound around the leads as shown in Figure 17 (b). Carbon conductive grease was applied at the screw-clip-wire interfaces to reduce the risk of corrosion between dissimilar metals and enhance electrical conductivity. The electrical connections between each pair of bars were initially measured on all specimens to ensure the resistance was $< 1\Omega$ between the bottom two bars and within 95-105 Ω between the top and bottom bars across the 100 Ω resistor. Connections were checked periodically throughout the experiment and repaired if and when measurements became erratic.

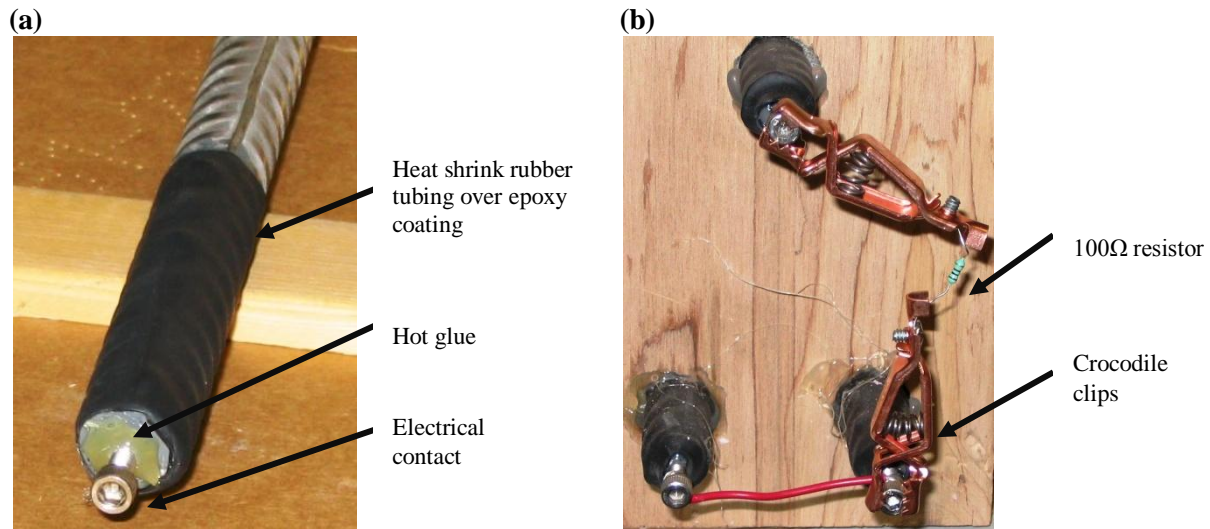


Figure 17: (a) Prepared rebar end before casting and (b) electrical connections after casting

3.1.4 Concrete Casting

3.1.4.1 Formwork

Formwork for casting the specimens consisted of a ply-wood structure with the capacity to cast ten G109 specimens at a time, as shown in Figure 18. High density Styrofoam cubes were fixed to the bottom formwork planks to act as ponding well inserts, and were subsequently removed from the prisms after casting. To accommodate the ponding well inserts, the G109 prisms were cast upside down, with the concrete flowing around the ponding well insert at the bottom. Wooden end boards were individually machined to size and drilled with three holes to act as supports for the rebar, and were left intact at the ends of the prisms after casting since they were fixed to the rebars with hot glue.

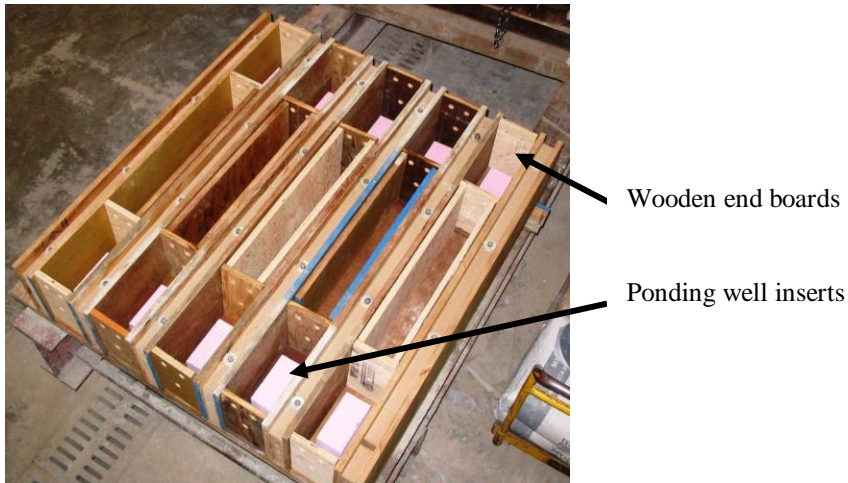


Figure 18: Formwork used for casting the G109 specimens

3.1.4.2 Concrete Mix Design and Procedure

The mix design used for the upper concrete layer containing 7.5% CI by mass of cement is shown in Table 8. The mix design used for the lower CI free concrete layer was the same as in Table 8 except without NaCl. Both concrete layers had a water/cement ratio of 0.5. The cement was Type 1 general purpose Portland cement manufactured by Essroc, the water was from the tap, the coarse aggregate and sand were supplied by Dufferin Concrete, the NaCl was of 99% minimum purity and manufactured by EMD Chemicals, and the air-entraining agent was CATEXOL AE 360 manufactured by Axim Concrete Technologies.

Table 8: G109 concrete mix design

Ingredient	Amount (kg/m³)
Cement (Type 1 OPC)	355
Water	177
Coarse aggregate (ø max. 13 mm)	1070
Sand	770
NaCl	44
Air-entraining agent	0.340

The concrete was mixed in-house using a shear mixer. Due to the limitations of the mixer capacity, casting was done in separate batches for each steel/surface/prism layer combination. This resulted in 10 separate concrete batches mixed, 5 with and 5 without chlorides. Before each batch, the mixer was rinsed to provide similar moisture conditions for all mixes.

For each set of 10 prisms, a concrete batch with chlorides was mixed as per standard mixing schedule: all ingredients were mixed for 3 minutes (water and air-entraining agent mixed together beforehand), followed by 3 minutes of rest, then an additional 2 minutes of mixing (ASTM-C192, 2005). The mixed concrete was then poured into the prisms to a level beyond the first rebar layer, approximately 10 cm from the top of the formwork. In addition to the G109 prisms, 4 replicate cylinders measuring 100 by 200 mm were filled for each batch for compressive strength measurements. After pouring the first concrete layer into the formwork, the vibrating table upon which the formwork sat was activated for 1-1.5 minutes to compact the concrete. The chloride-free concrete batch was mixed immediately thereafter and poured into the formwork to make up the other layer of each prism, in addition to 4 more replicate cylinders. The formwork was vibrated for only 20-30 seconds after this pour in order to minimize mixing between the separate concrete layers. The distinct concrete layers can be seen in Figure 15, with the darker concrete containing chlorides on top poured first, and the lighter, chloride-free layer on the bottom poured second.

The exposed wet concrete surface of each prism was engraved with an identification symbol in addition to the marker nomenclature already written on the end-boards. The prisms were then covered with wet burlap and plastic tarp to cure for 48 hours, with re-wetting of the burlap done after 24 hours to maintain moisture. After curing, the prisms were removed from the formwork within 1-2 days, at which point they were stored permanently at ambient conditions in the lab. The casting procedure was repeated on separate dates for all 5 steel/surface type prisms, and the casting schedule and engraved identifications are shown in Appendix B.

Slump loss, air content and compressive strength for each concrete batch were measured to document the consistency among different batches. The slump loss, a measure of the concrete's workability, was measured once for each batch immediately after casting in accordance with standard methods (ASTM-C143, 2005). The air content, a measure of the microscopic air bubbles in concrete and an indicator both the concrete's resistance to freeze/thaw damage as well as workability and bleeding tendency (PCA, 2008), was measured once for each batch immediately after casting using a Chace indicator in accordance with AASHTO T 199. The compressive strength was measured 46

days after casting for three of the 100 by 200 mm replicate cylinders from each batch in accordance with standards (ASTM-C39, 2003) using a Forney Testing Machine Model QC50DR. An exception to the ASTM standard was that the Forney machine applied compressive stress at a constant rate of displacement rather than a constant rate of loading. The as-cast concrete properties are shown in Figure 19, with more detailed data shown in Appendix C.

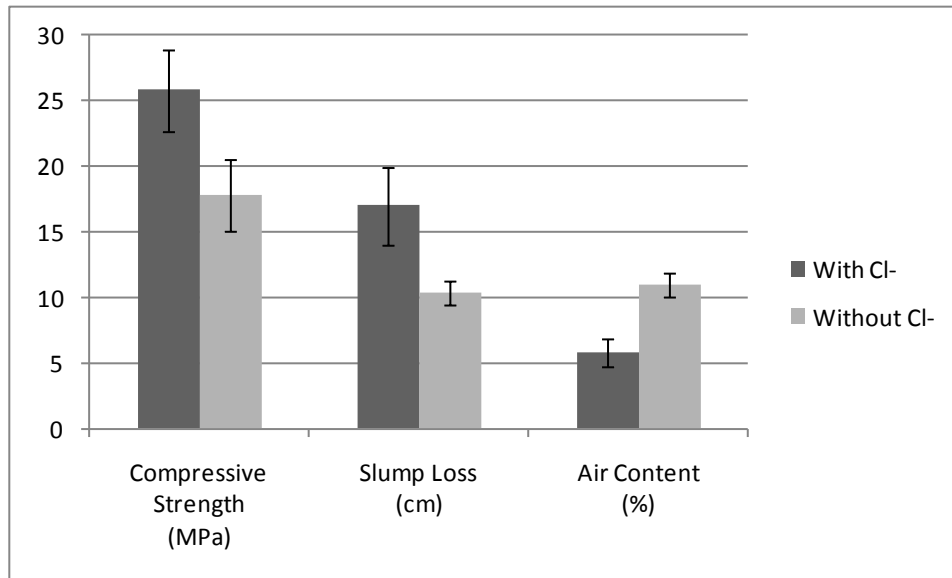


Figure 19: As-cast concrete properties for G109 specimens

Although properties varied among all batches, the general trend showed the concretes with chlorides to have greater workability, lower air content and enhanced strength than those without chlorides. Subsequent testing of concretes using a new compressive testing machine revealed the machine used for this test significantly underestimates strengths (by ~ 40%), and therefore the compression strength values should be considered relative rather than absolute. The air-entraining admixture addition for the concrete with chlorides gave air content within the target range of 3-7.5% recommended by the Portland Cement Association (PCA, 1998). Therefore the same dose was used for the concrete batch without chlorides. Clearly the chlorides had a diminishing effect on the air entrainment. The mix without the chlorides was not discarded, however, because it was considered important to place the second mix very soon after the first to avoid a cold joint. It was decided after the first batch to keep the mix design the same for all subsequent batches in order to keep the concrete properties as consistent as possible. The slump loss for both the chloride contaminated and chloride-free concrete was greater than the minimum of 5cm specified by the ASTM G109 standard.

3.1.5 Exposure Conditions

As mentioned above, the G109 specimens were all initially kept in the laboratory at ambient conditions after 48 hours of curing. Alternate filling and draining of the ponding well on top of the prisms with NaCl aqueous solution consisting of 9 wt% Cl began three months after casting. The salt solution was left in the ponding well for two weeks, and then vacuumed off to allow the prisms to dry for two weeks, in an attempt to simulate the alternate wetting and drying experienced by a reinforced concrete structure in outside conditions. During the wetting cycle, plastic sheet was placed over top of the ponding wells to minimize evaporation of the solution. The wetting cycle provides moisture required to facilitate the corrosion process, as well as replenish any chlorides in the upper concrete portion that may have diffused to the lower, chloride-free concrete; the drying cycle provides external oxygen with greater access to reach the top bar.

3.1.6 Electrochemical Corrosion Monitoring

3.1.6.1 Macrocell Measurements

Macrocell corrosion current densities were obtained by measuring the potential, E_{macro} , across the 100Ω resistor between the top and bottom bars using a high impedance voltmeter (model: Keithley 2750 Multimeter from National Instruments), and dividing that by the top bar's surface area, $A_{top\ bar}$, and 100Ω to give the macrocell current density, i_{macro} (A/m^2), as follows:

$$i_{macro} = \frac{E_{macro}}{100\Omega \times A_{top\ bar}} \quad (2)$$

Measurements were taken daily via data acquisition software (LabVIEW 6.1), although the initial measuring dates varied among specimen types. Measurements of the 316LN and 2205 specimens started beyond 75 days after casting, whereas measurements for the 304P and 304A specimens began much sooner after casting (4 and 5 days, respectively) in order to examine any differences in macrocell corrosion behavior that may occur earlier on.

3.1.6.2 Potentiostatic Linear Polarization Resistance

Linear polarization resistance (LPR) is a common technique used for rapid in situ measuring of instantaneous corrosion rates. It takes advantage of the approximately linear correlation that exists

between potential and current at the origin of a polarization curve (i.e. at the corrosion potential) as shown in Figure 20.

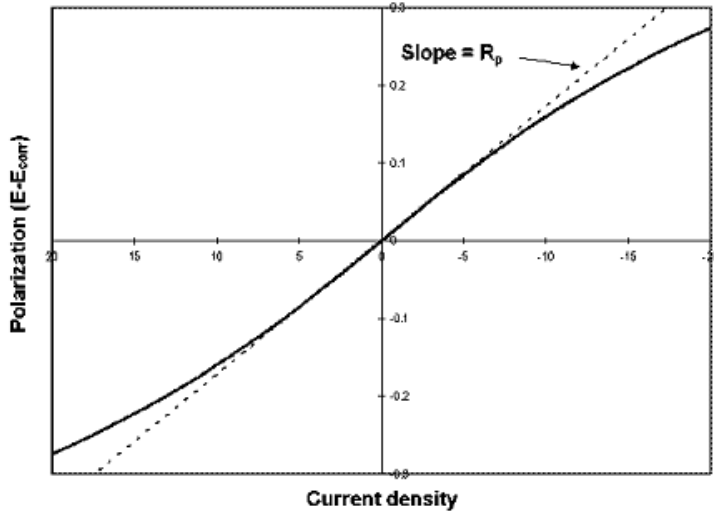


Figure 20: Linear region at polarization curve origin (Corrosion_Doctors, 1999)

This linear region extends a few millivolts in either direction of the origin, and its slope, the polarization resistance, R_p ($\Omega \cdot \text{m}^2$), is inversely proportional to the corrosion current density, i_{corr} (A/m^2), as follows:

$$R_p = \frac{B}{i_{corr}} = \left[\frac{\Delta E}{\Delta i} \right]_{\Delta E \rightarrow 0} \quad (3)$$

where B (V) is a proportionality constant that can be calculated from the anodic and cathodic Tafel slopes, β_a and β_c , in the following equation (Stern and Geary, 1957):

$$B = \frac{\beta_a \beta_c}{2.3(\beta_a + \beta_c)} \quad (4)$$

The Tafel slope values depend on the rate determining step of the electrochemical reaction mechanisms, and are a function of material, electrolyte, temperature and time. Depending on whether the reaction is under charge transfer control, diffusion control, or the metal is in a passive state, the values can range from 30 to ∞ mV/decade (Mansfeld, 1976), and can be obtained from the linear portion of a plot of overvoltage vs. log of current density, shown in Figure 21. The linear portion typically occurs at overvoltages greater than ± 50 mV and, for accurate estimates, should extend over a current density range of at least one order of magnitude (Fontana, 1986).

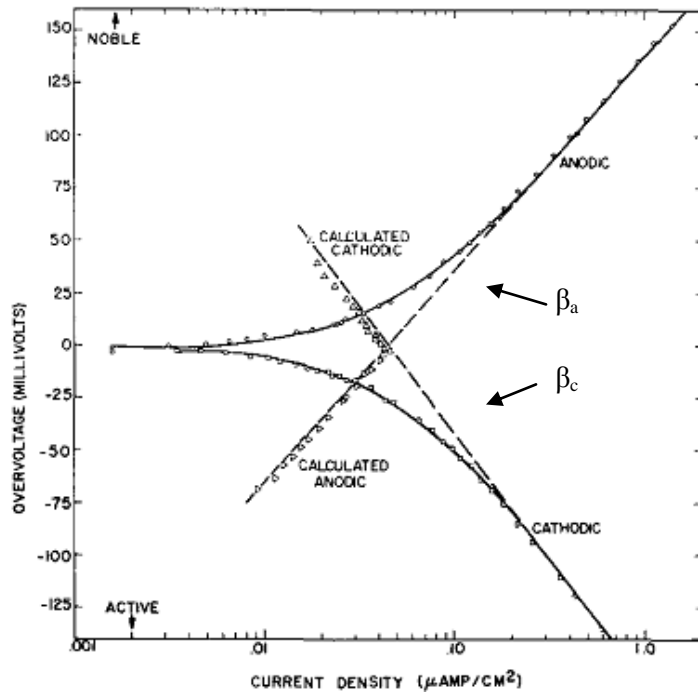


Figure 21: Plot of polarization curve showing linear anodic and cathodic Tafel regions (Stern, 1957)

Given the $30 - \infty$ mV/decade range of Tafel slope values, B values in the range of 6.5 to 52.1 mV can be obtained (Mansfeld, 1976), though estimates for corrosion rates of plain carbon-steel in concrete have found B values of 26mV for active corrosion and 52 mV for passive corrosion (Andrade, Castelo et al., 1986). Sensitivity of the calculated corrosion rates to the B values is minor, with one study (Stern and Weisert, 1959) finding a maximum error of two when approximating with mid-range B values, which is well within the scatter of typical corrosion measurements where orders of magnitude are of more concern. Different B values were used for each steel type in this project based on the Tafel slopes obtained from their respective cyclic polarization curves, a technique to be covered in Section 3.1.6.4. Derivations of the B values for each steel type are shown in Appendix D.

Every four weeks, at the end of each ponding cycle just before draining, the top bar was disconnected from the bottom bar and allowed to depolarize for 24 hours. Monitoring of the potentials with respect to the embedded referenced electrode confirmed that 24 hours was sufficient for depolarization, as shown later in Section 4.1.2. Potentiostatic LPR measurements were then performed on the top bar of all specimens. The experimental setup used a stainless steel counter electrode and a saturated calomel reference electrode (+241mV vs. standard hydrogen electrode)

immersed in the ponding well solution, and connected as shown in Figure 22 to a potentiostat (model: PARSTAT 2263 from Princeton Applied Research).

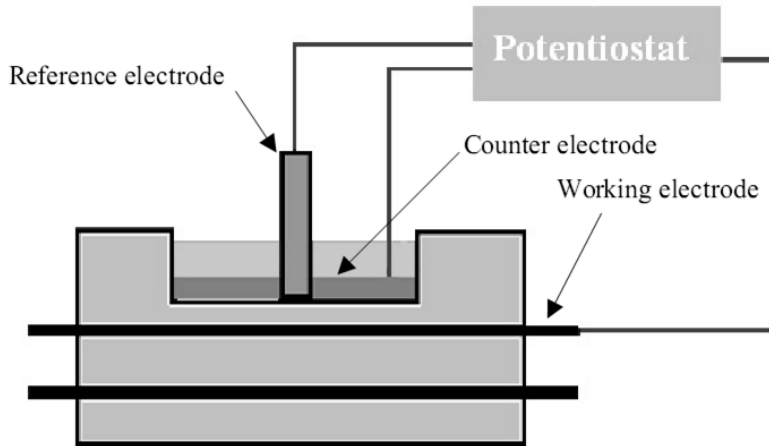


Figure 22: Experimental setup for microcell corrosion current density measurements (Tran, 2007)

A constant potential of $\pm 20\text{mV}$ vs. E_{corr} was applied to the top rebar for 150 seconds per potential shift (absolute potential change between shifts, $\Delta E = 40\text{ mV}$), with the resulting steady-state currents recorded via data acquisition software (PowerSuite 2.51 by Princeton Applied Research) to obtain ΔI , as shown in Figure 23. The corrosion current density, i_{corr} (A/m^2), was then calculated using the following equation, with the total exposed rebar area assumed to be the corroding area, A_{bar} .

$$i_{\text{corr}} = \frac{B \times \Delta I}{40\text{mV} \times A_{\text{bar}}} \quad (5)$$

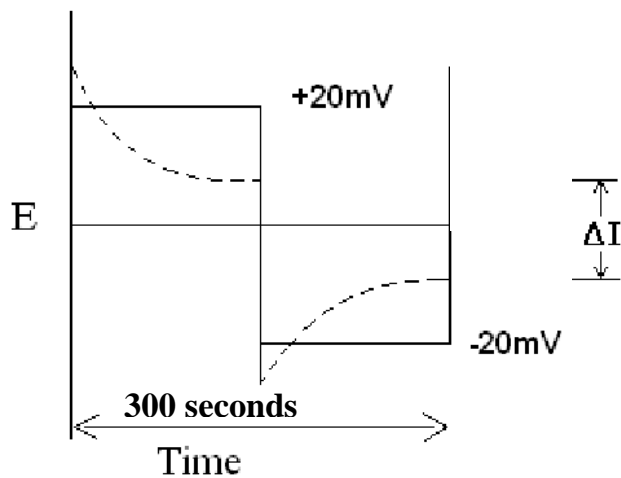


Figure 23: Applied potential and resulting current plot for potentiostatic LPR

3.1.6.3 Corrosion Potential

First employed to evaluate bridge corrosion in California in the 1950's (Stratfull, 1957), corrosion potential measurements are commonly used, due to their speed, simplicity, and lack of external power source requirements, to determine if reinforced concrete structures are actively corroding or are passive. All that is needed is a high impedance voltmeter of at least 10 M Ω (ASTM-C876-91, 1991) with the working lead attached to the reinforcement and the ground lead attached to a reference electrode which is in electrolytic contact with the reinforcement through the concrete pore solution, as shown in Figure 24.

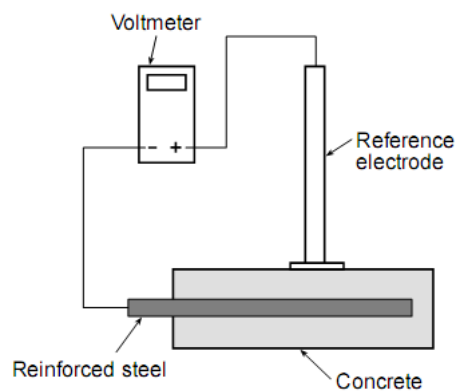


Figure 24: Schematic of corrosion potential measurement technique (Gu and Beaudoin, 1998)

The disadvantage of corrosion potential measurements is they only relay thermodynamic information, or the probability of corrosion, rather than an actual corrosion rate. They can be influenced by other factors in the concrete such as concrete resistivity, cover depth, and oxygen availability. Greater moisture presence (i.e. high humidity, rain, marine conditions, etc) creates a negative shift in potentials due to decreased oxygen availability, whereas dry conditions provide greater diffusivity of oxygen to the rebar surface and thus create more positive potentials. Dry conditions can however increase concrete resistivity which, in turn, increases the potential difference between the reference electrode and the rebar. So, in addition to placing the reference electrode as close to the reinforcement as possible, the concrete surface should be moistened before measuring for optimum accuracy, typically done with a sponge (Stratfull, 1957; ASTM-C876-91, 1991).

Despite the various factors that influence corrosion potentials, significant differences and/or changes/gradients in corrosion potentials are helpful in determining changes in corrosion states, such as when passive to active corrosion transition occurs, particularly in a laboratory setting where non-corrosion related fluctuations are less prevalent. While the guidelines for interpreting stainless steel

rebar corrosion potentials have yet to be established, for black steel rebar, corrosion potentials in terms of probabilities for active corrosion are shown in Table 9 versus the copper-copper (II) sulfate reference electrode (CSE), which is +314 mV vs. standard hydrogen electrode (SHE). Equivalent guidelines for stainless steel rebar have yet to be established.

Table 9: Corrosion potentials for black steel in concrete (ASTM-C876-91, 1991)

Corrosion Potentials (mV vs. CSE)	Active Corrosion Probability (%)
>-200	<10
-350 > -200	Uncertain
< -350	>90

Corrosion potentials were measured roughly every two weeks for the top bar of each G109 prism in the depolarized state (bars disconnected for ~ 24 hrs). The tip of the saturated calomel reference electrode (SCE) was placed in the ponding well, either in solution during the ponding cycle or against a moist sponge on the ponding well's bottom surface during the dry cycle. In the latter case, the moist sponge was left to wet the surface for ~ 15 minutes before measuring. The reference electrode was attached to the ground lead of a high impedance voltmeter (model: Fluke 87 V True RMS Multimeter) and the working lead attached to the top bar. The resulting voltmeter reading, once stabilized to within ± 1 mV, was recorded as the corrosion potential, and this value was then converted to the copper-copper(II) sulfate scale (CSE) by subtracting 77 mV from the SCE reading in order to compare with corrosion potentials from other literature and standards.

The corrosion potential of one bottom bar per steel/surface type was also measured every two weeks in the depolarized state for comparison to the values of the top steel. Though originally immersed in chloride-free concrete at the time of casting, chloride diffusion from the top to the bottom concrete layer may have occurred over time; therefore the bottom bar corrosion potentials are likely representative of steel in low chloride concentrated concrete rather than the original chloride-free concrete. Measuring a bottom bar's corrosion potential involved fastening a moist sponge to the prism's outer side wall directly adjacent to the bottom bar with a rubber band, and leaving it to soak against the concrete surface for ~ 15 minutes before pressing the reference electrode tip up against the sponge and taking the measurement.

3.1.6.4 Cyclic Polarization

Cyclic polarization (CP) is an electrochemical corrosion evaluation technique using the same experimental setup as for LPR shown in Figure 22, but in which the potential is shifted dynamically over a much larger range, and the resulting current is recorded. The potential and current density values are typically used to plot a CP curve presented as potential (V) versus log of current density ($\log A/m^2$), as shown in Figure 25. By forcing the material from its steady-state potential and monitoring the current response, this curve provides valuable information not only on the corrosion current, but also on the behaviour of a metal's passive film, its susceptibility to pitting attack, and any diffusion limitations.

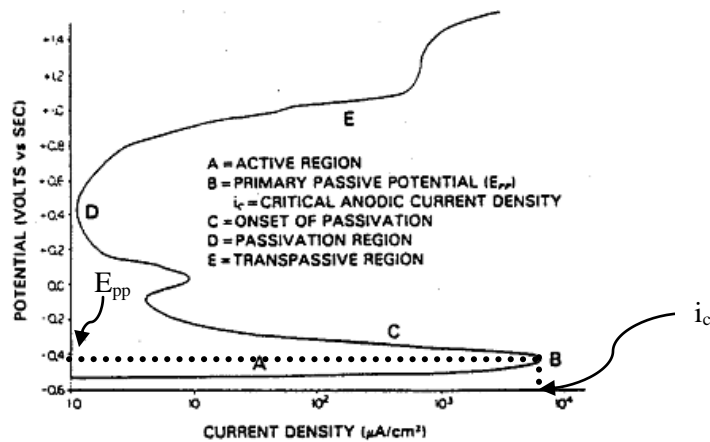


Figure 25: Potentiodynamic cyclic polarization curve (PAR, 1982)

The more noble the potential at which anodic current increases rapidly, shown as E_{pit} in Figure 26, as well as the more electropositive the potential at which the hysteresis loop is completed, E_{pro} , the less susceptible the alloy is to initiation of localized corrosion (ASTM-G61-86, 2003). CP has been used many times in the study of corrosion in concrete of black steel rebar (e.g. Saremi and Mahallati, 2002; Mahallati and Saremi, 2006; Esmailpoursae, 2007; Marcotte and Hansson, 2007; Tran, 2007; Jaffer and Hansson, 2008) as well as stainless steel rebar (García-Alonso(a), M.L.Escudero et al., 2007).

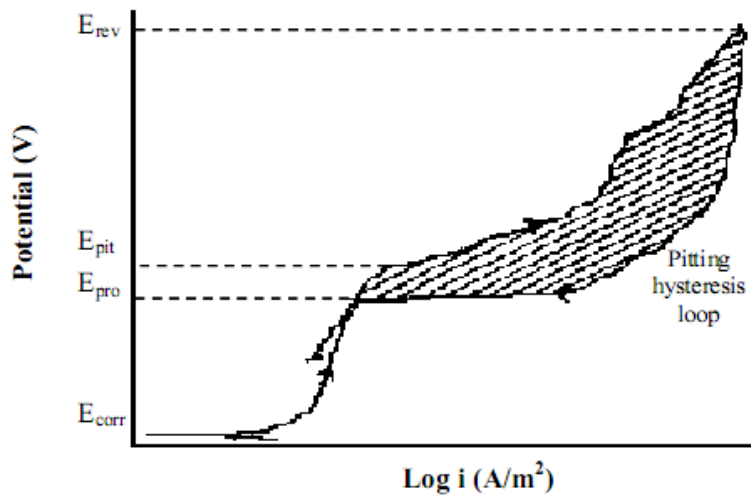


Figure 26: Hysteresis loop on a potentiodynamic CP curve (PAR, 2008)

Cyclic polarization was performed in this experiment by shifting the potential from E_{corr} to +500 mV vs. SCE in order to capture the passivation portion of the curve, then reversing the potential to -100 mV vs. E_{corr} in order to bring the electrochemical conditions at the steel's surface close to its equilibrium state. In order for the true corrosion behaviour at these higher potentials to be observed, it is important to set the potential scanning rate (mV/s) low enough so that steady-state conditions at the steel's surface are maintained. Too high of a scan rate will result in higher currents due to the effect of double layer capacitance charging at the steel's surface (Mansfeld and Kendig, 1981). A scan rate of 0.025mV/s was used in this project since it gave results in agreement with LPR measurements, and lower scan rates showed negligible change in values. Furthermore, 0.025mV/s was well below the conservative scan rates of 0.25-0.5 mV/s used for CP of passive iron-nickel based alloys by others (Silverman).

3.1.7 Pre-cast Metallographic and Chemical Analysis

These analyses were all conducted, in collaboration with B.P. Bergsma, on rebar that had not been exposed to the concrete.

3.1.7.1 Optical Microscopy

Both the outer surfaces as well as the longitudinal and axial cross-sections of the bars were observed using optical microscopy. Specimens for both views were prepared by machining and sectioning with

an abrasive SiC cut-off wheel and stainless steel hacksaw. The specimens used for the cross-sectional views were then prepared by hot-mounting in epoxy resin, grinding with 220, 320, 400 and 600 grit size SiC paper, polishing with 5, 1.0, 0.3 and 0.05 μm alumina powder, and etching for ten minutes using a mixture of HCl, HNO₃ and distilled H₂O at a ratio of 2:1:1, in order to reveal the distinct grain structure of each of each steel type. The cross-sectional and surface views were then positioned under an Olympus optical microscope and photographed at various magnifications. Differences between each steel, surface, and bar size were observed and documented.

3.1.7.2 Scanning Electron Microscopy and Energy-Dispersive X-ray Spectroscopy

The surface of each bar type was observed under a scanning electron microscope (Model: JEOL JSM-6460) with a 20keV beam. The SEM images provided information on how the surface morphology varied among the different surface conditions and steel types, and provided further insight into their respective corrosion behaviours.

Semi-quantitative chemical analyses of the mill scale – bulk steel interface on the as-rolled rebar as well as near the surface on the pickled bar were performed with the aid of the energy-dispersive x-ray spectroscopy (EDS) (model: INCA x-sight 7573 by Oxford Instruments) attachment to the SEM. The purpose was to determine if any chromium was depleted near the surface of the as-rolled bars from the hot rolling and annealing process as discussed in Section 2.2.4.3 and, if so, to determine magnitude and extent of depletion. The presence of a chromium depleted region is used to justify the conventional removal of the outer layers of as-rolled stainless steel rebar via abrasive blasting and pickling as discussed in Section 2.2.4.2, so this analysis was done to provide supporting evidence, or lack thereof, for the need to carry out these costly and environmentally hazardous procedures. The pickled bars were analyzed to provide a relative compositional comparison since EDS is only semi-quantitative.

3.1.7.3 Raman Spectroscopy

Qualitative analysis of the compounds that comprise the as-rolled rebar mill scale was performed by Raman spectroscopy. A Renishaw 1000 Ramascope system with an Olympus optical microscope, a Peltier-cooled charge coupled device detector, and spectrograph analysis software (GRMS/32) were used. After placing the rebar specimen on the microscopy stage and focusing in on an area of typical mill scale appearance, a 35 mW HeNe laser with 632.8 nm wavelength was emitted and reduced by the system's optics to 9 mW, where it was scanned over the bar's surface to obtain 2-4 accumulations

of intensity peaks for 20 seconds per accumulation. The accumulations of intensity peaks over a frequency range of 70-1600 cm^{-1} were then plotted by the spectrograph software. Plots of intensity peaks versus Raman shifts (cm^{-1}), or Raman spectra, from three different regions on the surfaces of both the 316LN and 304LN as-rolled bar were superimposed, and the peaks that were found to be consistent among the scans were correlated with similar peaks from known Raman spectra to identify the compounds present in the mill scale.

3.1.8 Visual Examination of Autopsied G109 Specimens

Near the end of the project, at ~600 days after casting, one G109 specimen of each steel/surface/bottom bar configuration, ten in total, was broken open and the bar surfaces were immediately photographed to document their appearance and any corrosion products present.

3.2 Effects of Loading Conditions

3.2.1 Specimen Preparation

Two types of stainless steel reinforcement were used for this experiment, 316LN and 2205, both in the pickled surface condition and both with a metric bar size of 15M (16 mm nominal diameter). As for the G109 specimens, the reinforcement was supplied by Valbruna Canada Limited.

Beam dimensions of the specimens used to investigate the effect of loading conditions on the corrosion performance of pickled stainless steel rebar are illustrated in Figure 27, noting that the rebar ends shown in black were sealed with epoxy and rubber heat-shrink tubing to expose 1 m of the bar length to the concrete, and an electrical contact was screwed into the end of the bar protruding from the concrete, as described in Section 3.1.3 for the G109 prisms. This setup provided a concrete cover depth of 27 mm.

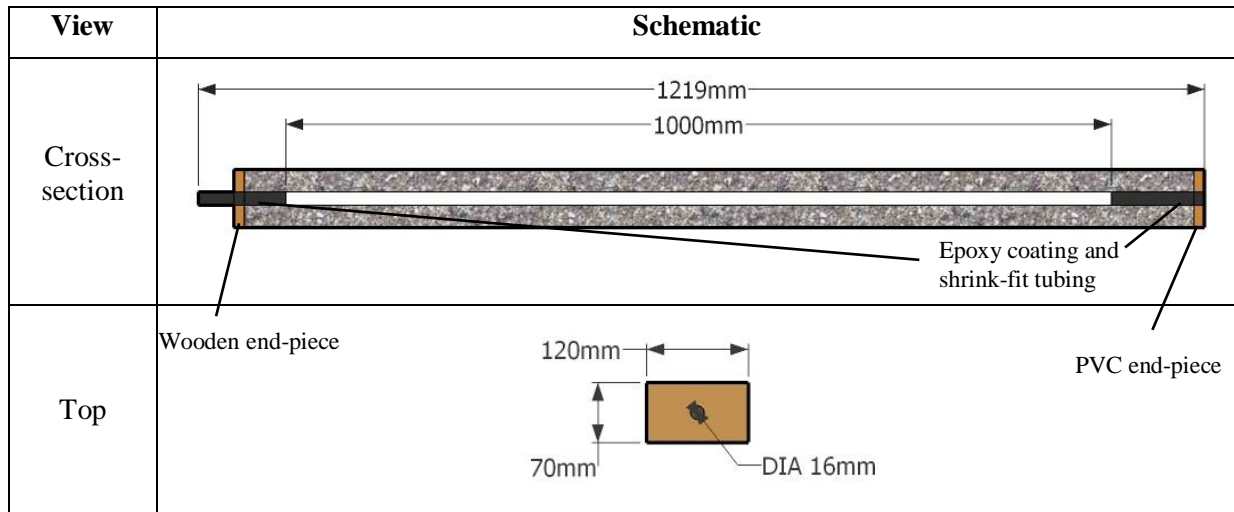


Figure 27: Dimensional overview of loaded beam

Pairs of the singularly reinforced concrete beams were connected together under 3-point bending, with the bottom ends fixed together in place, a fulcrum placed at the pair's mid-section and loading applied to the top ends. The static load was applied by tightening a bolted joint configuration, and the dynamic load was applied using a compressed air actuated cylinder that was cyclically pulsed, as illustrated in Figure 28 (a) and (b), respectively. The loading induces cracks on the outside edge at the mid-section (opposite the fulcrum).

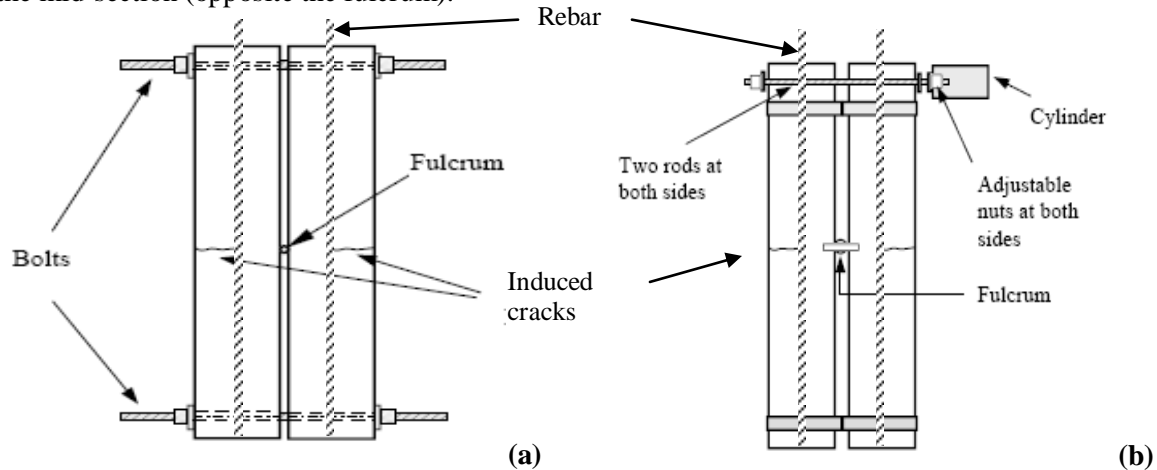


Figure 28: Schematic of setup for (a) statically loaded beam and (b) dynamically loaded beam

Formwork used for casting the beams consisted of a ply-wood structure, shown in Figure 29 with the beams already cast into place. Wooden end boards for the tops of the beams and PVC end-boards

for the bottoms were individually machined to size and drilled with one hole in the middle to hold the rebar in place during casting. They were left intact at the ends of the beams after casting since they were fixed to the rebar with hot glue. PVC end-boards were used on the ends to be exposed to salt solution for better durability.



Figure 29: Loaded beams cast into formwork

The concrete mix design for the beams, shown in Table 10, was similar that used for the G109s except it used a lower but variable water/cement ratio of 0.45-0.5, no sodium chloride was admixed, and water reducer was added (CATEXOL 1000N, manufactured by Axim Concrete Technologies).

Table 10: Concrete mix design for loaded beams

Ingredient	Amount (kg/m³)
Cement	355
Water	160-180
Coarse Aggregate (ϕ max. 13 mm)	1070
Sand	770
Air-Entraining Agent	0.340
Water Reducer	0.710

Concrete for the beams was mixed and cast using the same procedure as for the G109s in Section 3.1.4.2. Casting was done in four separate batches this time, with four beams cast per batch for a

total of 16 beams. Due to the limited capacity of the mixer, two batches (8 beams) were cast at a time, with a week in between the two casting sessions.

Slump loss, air content and compressive strength of each batch was measured using the same procedure as for the G109s in Section 3.1.4, except the compressive strength was measured 28 days after casting as per standard (ASTM-C39, 2003) rather than 46, using a different testing machine (Model: ELE Compression Tester 36-3088/02) which applied compressive stress at a constant load rate as per ASTM standard rather than a set displacement rate which the Forney machine used. The as-cast concrete properties are shown in Figure 30, with more detailed data as well as the casting dates provided in Appendix E.

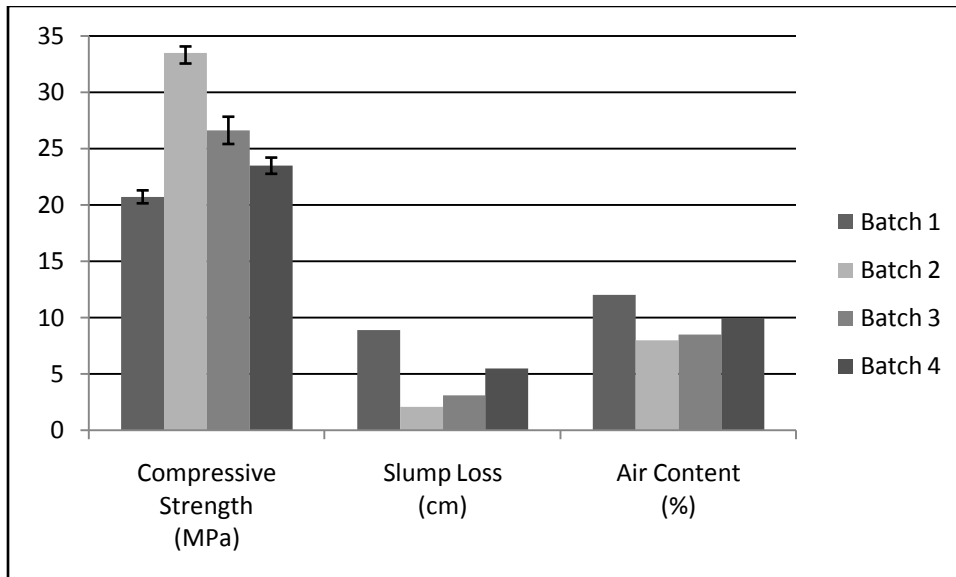


Figure 30: As-cast concrete properties for loaded beam

Though concrete properties varied among batches, a consistent trend exists with those having lower slump loss and air content showing higher compressive strengths and vice versa. It should be noted that different scales were used to measure the dry ingredients, and despite attempts at minimizing differences by ensuring each was properly calibrated, the consistency of the measurements may have been compromised by the differences in precision of each scale. Also, it was felt necessary to add extra water to batches 3 and 4 (up to 180 kg water/m³ concrete) at the time of mixing to increase the workability, as shown by their low slump loss values. Batches 1 and 2 in contrast used 160 kg water/m³ concrete, though batch 2 also had low workability.

As expected from the discussion of underestimated G109 compressive strengths in Section 3.1.4, the compressive strengths of the beams, measured with the new testing machine gave, on average, higher values than the former, though this difference would also be attributed to the loaded beams' lower water/cement ratios. Based on the variable concrete strengths, it was decided to expose the highest and lowest strength beams, batches 1 and 2, to dynamic loading, and the intermediate strength beams, batches 3 and 4, to static loading, in case the corrosion resistance of rebar under dynamic loading was significantly different depending on the strength of the concrete and the resulting crack morphology. Although the effect of the concrete strength on the corrosion and loading characteristics was not known, all beams were to be loaded beyond the point of concrete cracking, and, therefore, the majority of the load would be placed on the rebar. Thus the concrete strength would likely only be an indication of concrete microstructure characteristics and crack morphology rather than the beams' resistance to loading.

The 8 beams from batches 1 and 2 were loaded dynamically, while the 8 from batches 3 and 4 were loaded statically. Of the 4 beams from each batch, two were reinforced with 316LN and 2 were reinforced with 2205; the 2 beams of the same batch and steel type were loaded together in pairs, so that the deflection under load would be shared equally among the partner beams. The nomenclature for the loaded beam pairs is shown in Table 11, with the concrete strength designation meant to differentiate which of the two batches used in each loading condition had relatively higher or lower strength.

Table 11: Loaded beam pair nomenclature

Concrete Batch	Concrete Strength	Loading Type	Steel Type	Nomenclature	# of beams
1	Low	Dynamic	316LN	316 DL	2
			2205	2205 DL	
2	High	Dynamic	316LN	316 DH	
			2205	2205 DH	
3	High	Static	316LN	316 SH	
			2205	2205 SH	
4	Low	Static	316LN	316 SL	
			2205	2205 SL	

3.2.2 Loading and Salt Exposure

Approximately 10 weeks after casting, the loaded beams were placed vertically in tubs, and exposed to salt water containing 3% Cl by mass of solution in the form of commercial de-icing salt. The salt

water was filled to just above the beam mid-section, as shown in Figure 31, to allow chlorides to diffuse into the cracks created near the fulcrum region. The salt solution was drained and filled every two weeks to expose the lower part of the beams to ambient air and increase the accessibility of oxygen to the steel.

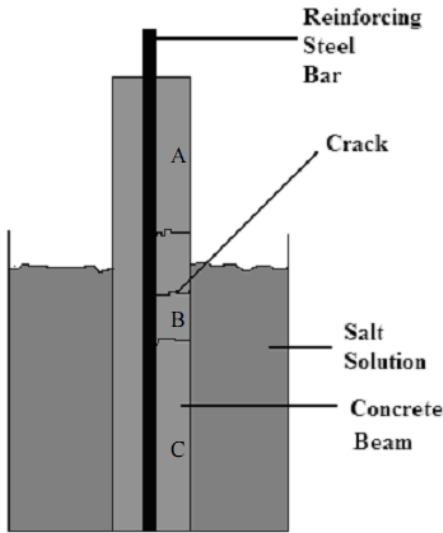


Figure 31: Illustration of salt solution level during wet cycle (Jaffer, 2007)

The top ends of the dynamically loaded beams were subjected to a cyclic (square wave) load of 150 kPa for two hours per day at a frequency of 0.5 Hz, which provided a deflection of ~1.5mm to the electrical contact screws protruding from the beams' top ends. The statically loaded beams were loaded permanently with a deflection of 1.5 mm applied to electrical contact screws.

Loading and salt water concentration was increased throughout the experiment to further intensify exposure conditions and promote localized corrosion initiation near the cracks. Table 12 shows the schedule of exposure condition changes. The chloride concentration of the salt solution was measured with a chloride ion specific electrode (model: Orion 9617 BNWP Ionplus Sure-Flow, with Orion 250A digital readout). A pH of 8.2 was measured for the salt solution at ~40 weeks after beam casting using an autotitrator (model: TIM800 Titration Manager from Radiometer-Copenhagen) and pH reference electrode.

Table 12: Schedule of exposure condition changes to loaded beams

Weeks After Casting	% Chloride in Ponding Solution (by mass)	Loading	
		Dynamic	Static
10	3.0	150 kPa/1.5 mm	1.5 mm

		displacement, 2 hours/day	displacement
36	5.6	-	-
40	-	270 kPa/3 mm displacement	3 mm displacement
42	-	Duration increased to 4 hours/day	-
51	7.2	-	-

3.2.3 Electrochemical Corrosion Monitoring

The electrochemical measurements were performed as described for the G109s in Section 3.1.6.2, with the addition of a special attachment to hold the sponge, counter and reference electrode in place at the beam's mid-section, shown in Figure 32. The attachment was placed directly at the beam's mid-section in the vicinity of cracks, with the working electrode lead of the potentiostat connected to the rebar's electrical contact at the top end of the beam. Measurements on the dynamically loaded beams were performed when cyclic loading was off to prevent the electrodes from being disconnected.

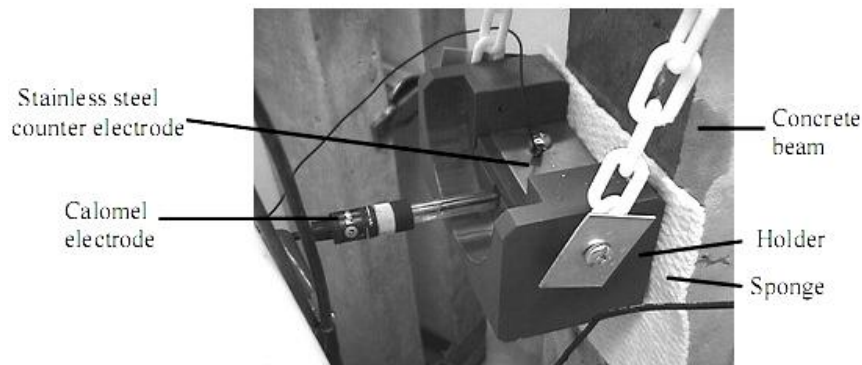


Figure 32: Electrode holder for loaded beam LPR measurements (Jaffer, 2007)

Potentiostatic LPR was used to monitor the instantaneous corrosion current density at the mid section of each beam every month just before draining the salt solution.

Corrosion potential of each beam was measured every two weeks at the end of both wet and dry cycles. The same technique was used as described for the G109s in Section 3.1.6.3.

At various times throughout the exposure period, cyclic polarization (CP) was performed on certain loaded beams as described in Section 3.1.6.4 for the G109 specimens. As was done with the LPR

measurements, the CP scans performed on the dynamically loaded beams were done while cyclic loading was off to prevent the electrodes from being disconnected.

The electrochemical current noise technique (ECN) measures small fluctuations in corrosion currents interacting between two metals. The rate of anodic and cathodic reactions on two “identical” specimens in two “identical” environments is not always equal, and ion dissolution at the surface of each may be different at any given instant. The small current transients measured by ECN represent the initiation, and in some cases subsequent repassivation, of localized corrosion pits at the microscopic level, and the ability of a metal’s surface film to repassivate may be evaluated on a comparative basis with the ECN method (Legat and Dolecek, 1995). An advantage of ECN is that it is a non-perturbative measurement since no external current or voltage is applied and, thus, the metals are kept near equilibrium conditions excluding the polarization that is occurring between the two metals being measured.

ECN is typically measured between bars within a single concrete structure (Weiermair, Hansson et al., 1996; Jaffer, 2007); however since the salt solution in which the beams were immersed for this project provided a low resistant electronic and ionic bridge, measurement between the two beams of each loaded pair was attempted. Measurements were conducted periodically throughout the experiment between both the statically loaded and dynamically loaded beam pairs, with the cyclic loading on the latter both on and off. ECN measurements were performed using a CML corrosion monitoring apparatus.

Chapter 4

Experimental Results and Discussion

4.1 Effects of Surface Conditions

4.1.1 Macrocell Corrosion

4.1.1.1 Short-Term Measurements

Short-term macrocell current density measurements for 304 pickled and as-rolled G109 specimens began 5 days after their casting at intervals of approximately 24 hours in order to observe the macrocell corrosion characteristics early on during the cement's hydration and how they might differ from those exhibited later. Average values over the short-term for 304 pickled and 304 as-rolled are shown in Figure 33 and Figure 34, respectively, with B and S denoting black steel and stainless steel bottom bars, respectively. Data for the individual specimens are plotted in Appendix F.

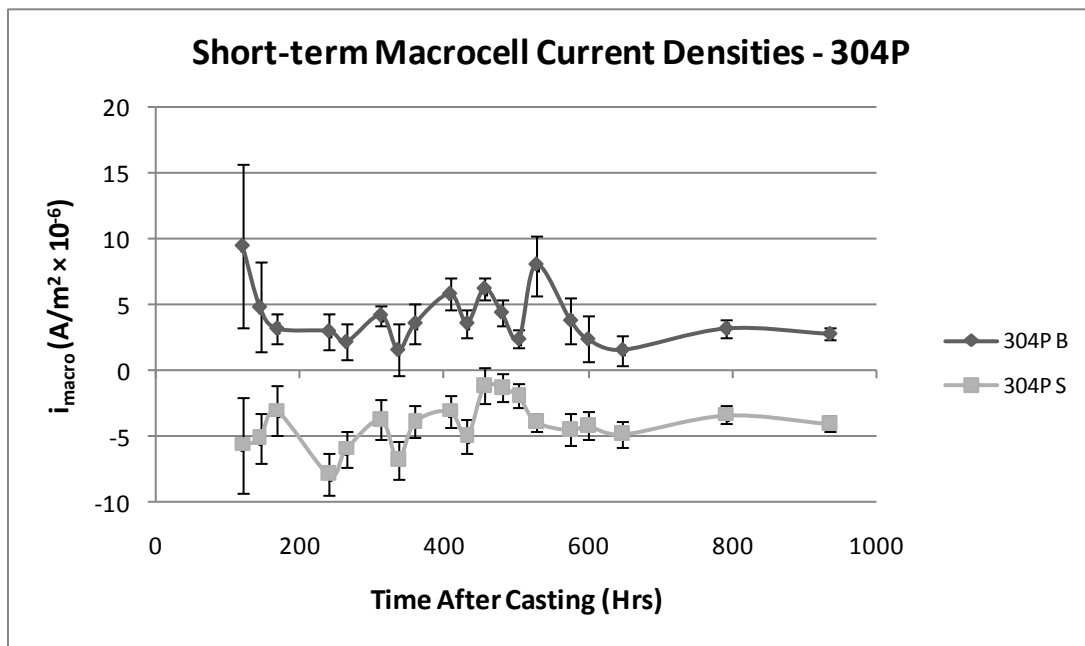


Figure 33: Short-term macrocell measurements for 304 pickled specimens with bottom black (B) and stainless steel (S) bars

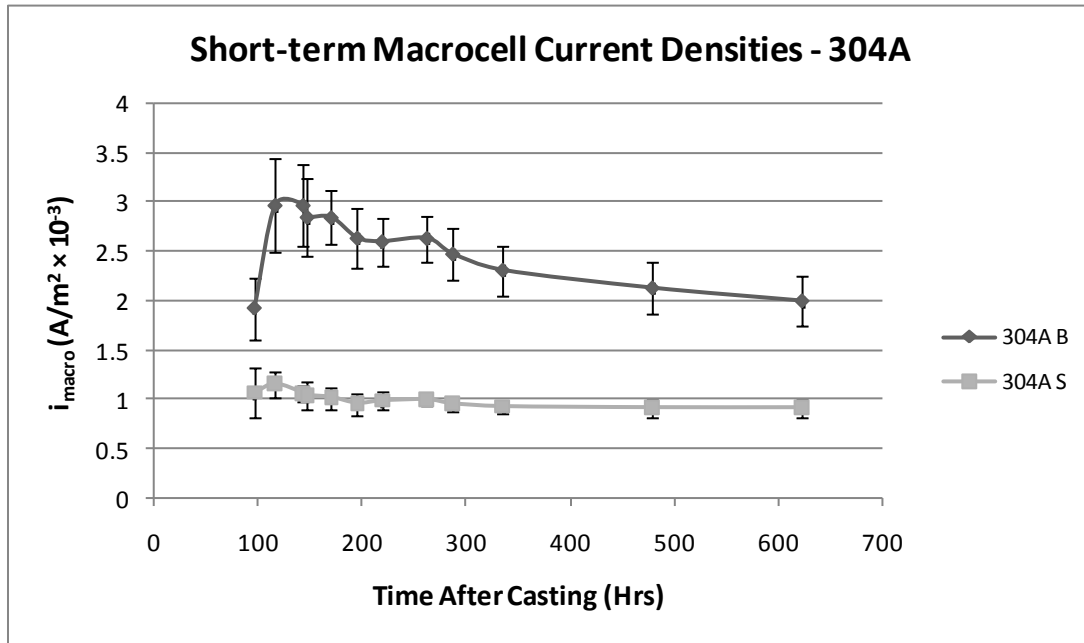


Figure 34: Short-term macrocell measurements for 304 as rolled specimens

Being sure to note the different vertical scales used for the above figures, the pickled specimens in Figure 33 exhibited relatively stable macrocell current densities that differed little with time and were very low, on the order of 10^{-6} A/m². The polarizing behaviour of the 304PS began in reverse of what was expected, where the bottom stainless steel bar in the chloride free concrete had a slightly more negative potential than the top bar and thus behaved as the anode, or corroding bar. This behaviour was eventually reversed as shown by the long-term macrocell current densities presented next.

The as-rolled specimens in Figure 34 began with much higher macrocell current densities than those of the pickled bars. This plot shows the highest measured current densities throughout the entire project of $\sim 3 \times 10^{-3}$ A/m², which were exhibited at the initial measurements just after 100 hours after casting by the specimens with black steel on the bottom. These values then drifted down towards, but not reaching at the time the short-term measurements were ended, those exhibited by the specimens with stainless steel bottom bars of $\sim 10^{-3}$ A/m². The bottom bar types have different macrocell influences on the top bars due to their characteristic oxygen exchange current densities, a subject that is addressed in the next section. The fact that a peak in macrocell current densities occurred earlier and then decreased is important to keep in mind, particularly in this experiment where rebar is immediately immersed in highly chloride contaminated concrete, unlike the more realistic situation where the rebar is gradually exposed to chloride and is in well matured concrete of

relatively low conductivity. This sudden “shocking” of the steel surface when immersed in an aggressive environment may at first overwhelm its ability to form a passive film, requiring time to develop a more protective surface layer.

4.1.1.2 Long-Term Measurements

Average macrocell current densities over the long-term for 316, 304 and 2205 steel type specimens are plotted in Figure 35, Figure 36 and Figure 37, respectively. Data from specimens 316P B4 and 304P B4 were omitted from these plots since their values were considerably higher ($\sim 5\times$) than the population’s and were thus excluded as outliers. These high values may have been the result of black steel or rust contamination on the top bar’s surface before casting that corroded completely over time, since the macrocell current densities of these specimens did eventually declined to those of the general population. Macrocell current densities shown for the individual specimens are shown in Appendix F.

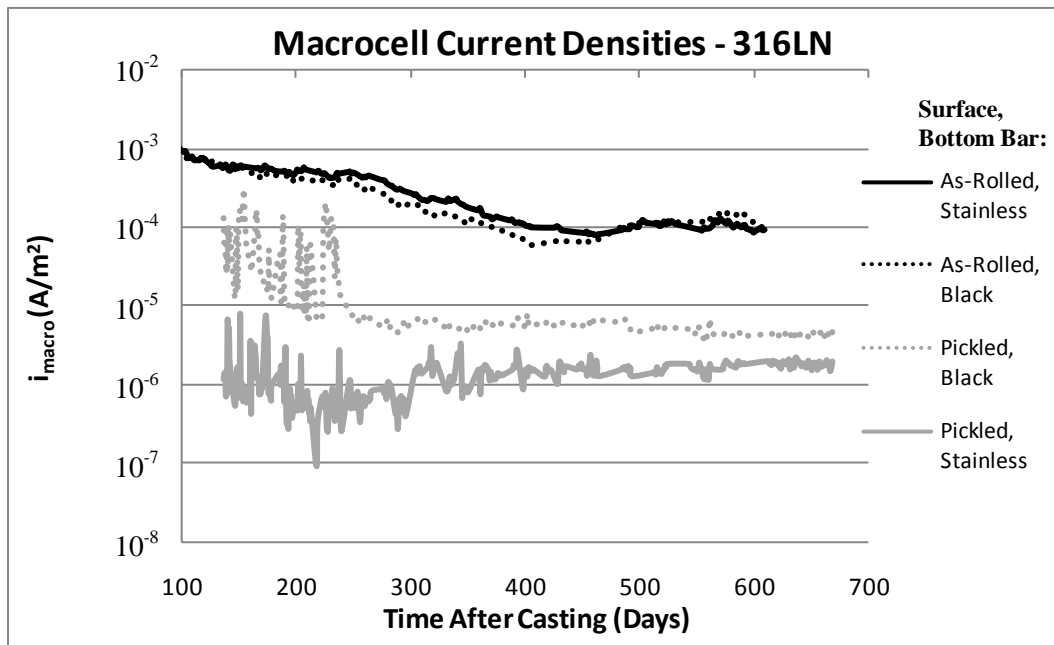


Figure 35: Average macrocell current densities over the long-term for 316LN steel type specimens

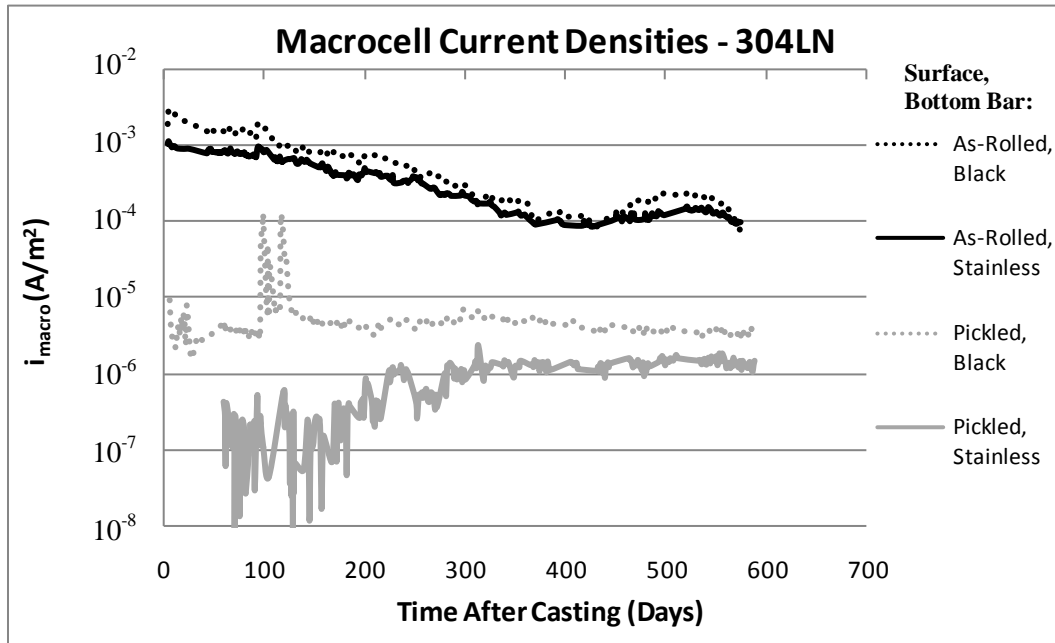


Figure 36: Average macrocell current densities over the long-term for 304LN steel type specimens

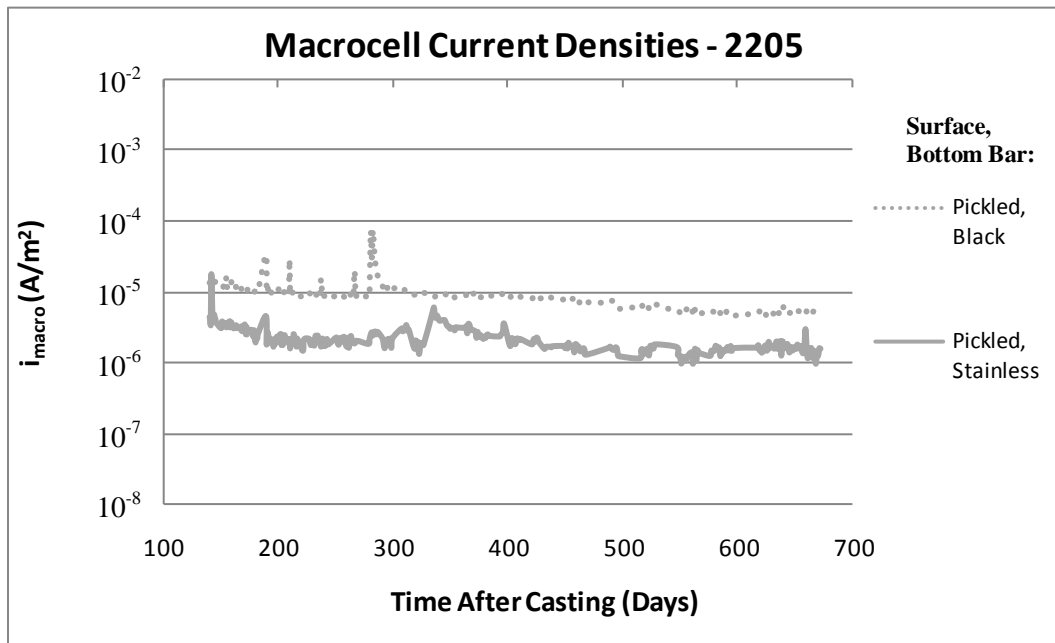


Figure 37: Average macrocell current densities over the long-term for 2205 steel type specimens

The 316 and 304 as-rolled specimens behaved similarly, exhibiting macrocell current densities of $\sim 10^{-3} \text{ A/m}^2$ at 100 days after casting which then gradually decreased and settled to values of $\sim 10^{-4}$

A/m² at 400 days after casting. This decrease is likely attributed to maturing of the concrete: as the concrete hardens with time, its porosity decreases due to hydration of cement particles and the concrete's ionic resistance increases, thus decreasing ionic conductivity between the top and bottom bar (Holly, Reardon et al., 2007). Very little difference was observed between the different bottom bar configurations of the as-rolled specimens, suggesting that both the as-rolled stainless and black steel bars behave similarly in the initially chloride free concrete. Both bottom bar surfaces in this case are coated in mill scale so, by accounting for surface roughness there is likely a similar amount actual surface area across a given amount of apparent geometric surface area for the cathodic reaction (oxygen reduction) to take place. Similar compositions of both mill scales would be another contributing factor. In contrast, the pickled surface has a much smoother profile and, therefore, less actual surface area on a given amount of apparent geometric surface area to host the reaction. The reaction kinetics on a bottom bar are dictated by that surface's oxygen exchange current density, i_o , which is the reversible rate of the oxygen redox reaction at equilibrium (Fontana, 1986). Oxygen exchange current densities of the pickled stainless steel, as-rolled stainless steel and black steel bottom bar surfaces were determined by extrapolating their cathodic Tafel slopes to the oxygen evolution potential, denoted by the upper dashed line in Figure 2, at a pH of 13.5 (see Appendix G). As to be expected given their similar effect on macrocell behaviour, the values for the as-rolled stainless and black steels were similar at $\sim 10^{-6}$ A/m², though the black steel values were slightly higher which explains the variance in short-term macrocell currents for the as-rolled specimens in Figure 34; in contrast, those for the pickled stainless steel were significantly lower at $\sim 10^{-7}$ A/m², consistent with the lower macrocell corrosion rates generated when it is on the bottom concrete layer.

The macrocell current densities of all pickled stainless steel specimens experienced little change over time, all settling to values between $10^{-6} - 10^{-5}$ A/m². The higher fluctuations shown early on are in part due to the nature of the log scale and limited sensitivity of the instrument, but also due to transient development of the pickled steel's surface film once exposed to the new environment of high pH and high chlorides, away from its passive state when exposed to the atmosphere. Higher macrocell currents were exhibited by the specimens coupled to black steel on the bottom than by those coupled to stainless steel on the bottom which, as discussed above, is consistent with black steel's higher oxygen exchange current density, and is in agreement with the findings of other studies discussed in Section 2.2.3.1.

Despite the as-rolled specimens exhibiting values as high as $3 \times 10^{-3} \text{ A/m}^2$ at the beginning of monitoring, at over 600 days after casting both as-rolled and pickled specimens had stabilized to relatively low macrocell corrosion rates below the commonly accepted lower value for passive black steel in concrete of 10^{-4} A/m^2 ($\sim 0.1 \mu\text{m/year}$) as discussed in Section 2.1.2. In contrast, previous research (LeClaire, Zoob et al., 1985) on black steel rebar in concrete contaminated with 2.1% soluble Cl^- by mass of cement found the rebar to exhibit average macrocell corrosion current densities of 10^{-2} A/m^2 , becoming severely corroded and cracking the concrete during the 48 week test period.

4.1.2 Depolarization Time

The time required, upon removing the macrocell connection, for the top and bottom rebars in the G109 prisms to be depolarized from each other was determined by taking potential measurements of the top and bottom rebars versus the embedded Mn-MnO₂ reference electrodes at short time intervals for the 304P S5 and 304A S5 specimens. The depolarization profiles of the top and bottom bars in each specimen, plotted in Figure 38, confirm that 24 hours was sufficient time for allowing the bars to depolarize and reach their equilibrium corrosion potential before performing microcell corrosion measurements. Note that these potentials, rather than presented vs. SCE, are presented with respect to the Mn-MnO₂ reference electrodes, determined to be $\sim +100\text{mV}$ vs. SCE at the time of measuring.

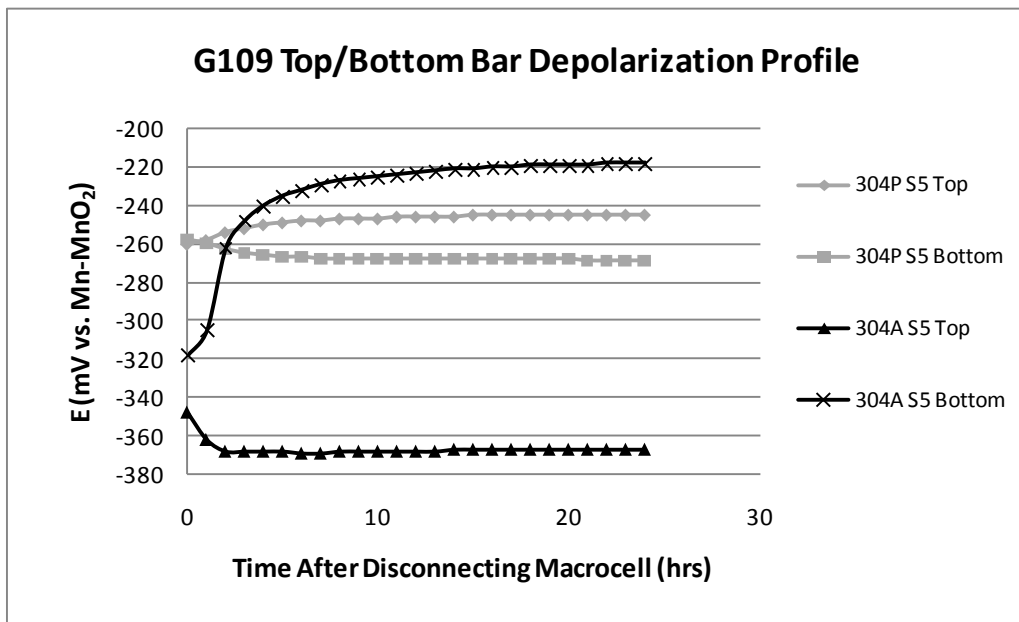
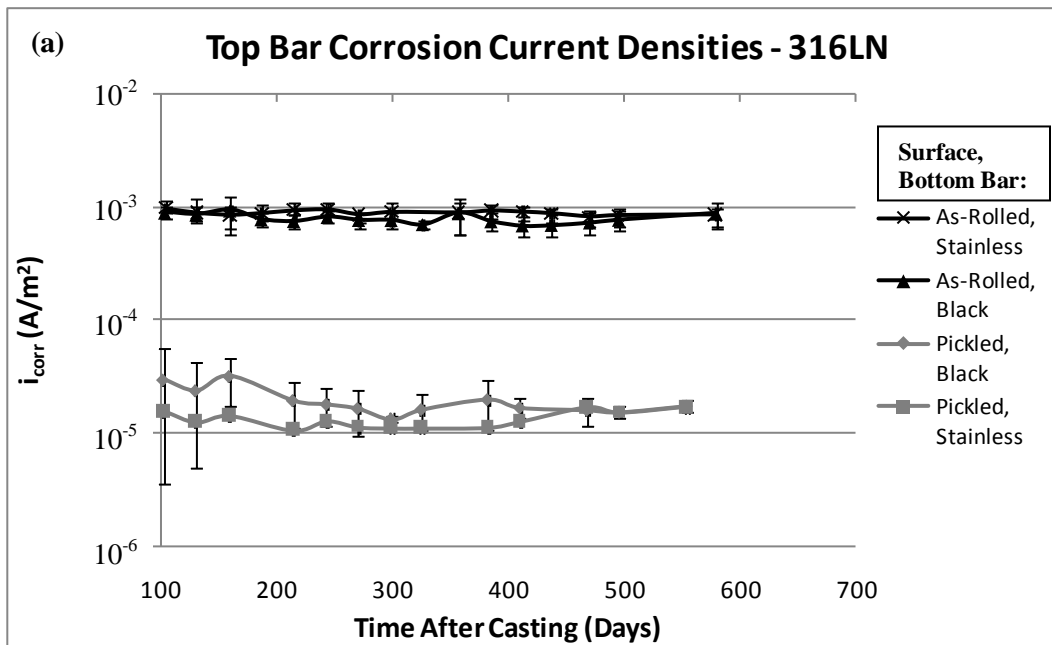


Figure 38: Depolarization profile of top and bottom 304P and 304A bars with time

4.1.3 Microcell Corrosion

4.1.3.1 Linear Polarization Resistance

Average microcell corrosion current densities, i_{corr} , obtained using the linear polarization resistance technique, are shown for the depolarized top bars (macrocell disconnected for ≥ 24 hours) of the 316, 304 and 2205 steel type specimens in Figure 39 (a), (b) and (c), respectively. Unlike for the macrocell corrosion rates in 4.1.1.2, specimens 316P B4 and 304P B4 were included in these averages since their microcell corrosion current densities did not differ significantly from the rest of the population's. Microcell corrosion current densities of individual specimens are plotted in Appendix H.



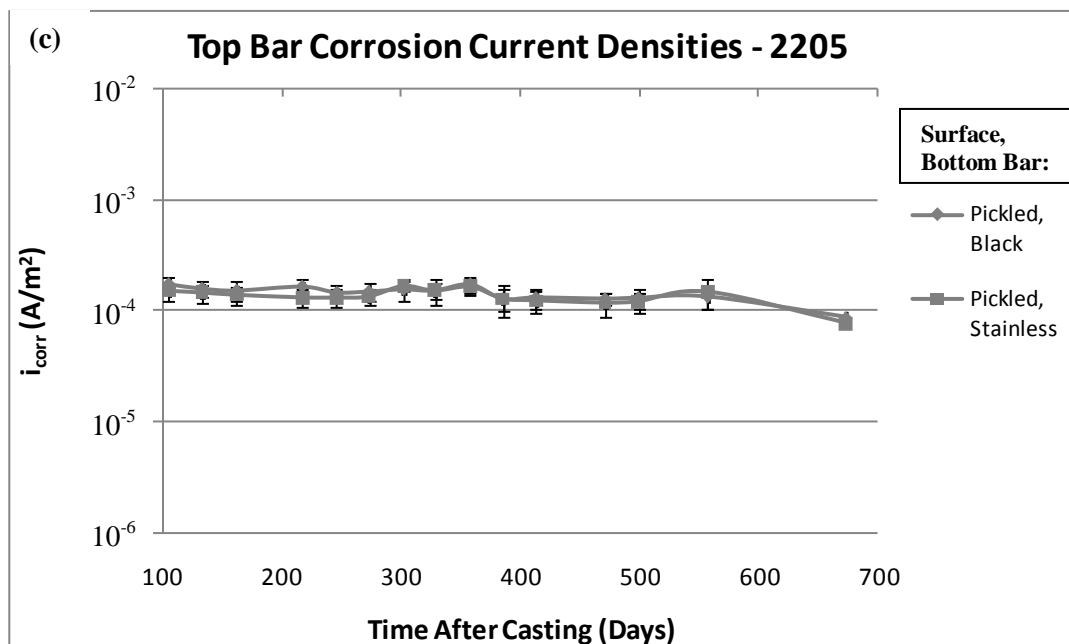
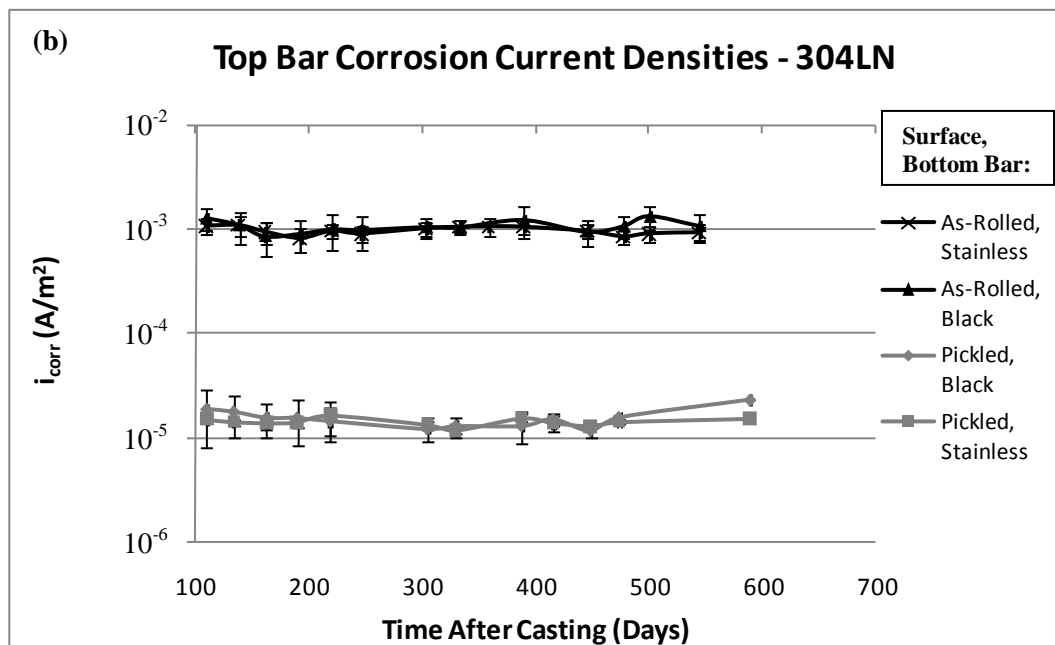


Figure 39: Average microcell corrosion current densities for (a) 316, (b) 304 and (c) 2205 steel type specimens

During the 600 days after casting, the microcell corrosion current densities, measured initially every 4 weeks, remained relatively constant for all steel and surface types with the exception of a small decrease in values for the 316P specimens. The 316 and 304 as-rolled specimens consistently

exhibited microcell corrosion current densities of $\sim 10^{-3}$ A/m², which is near the upper limit of the commonly accepted range for passive black steel in chloride free concrete as discussed in Section 2.1.2 and found in previous work (García-Alonso(a), M.L.Escudero et al., 2007). The pickled specimens exhibited lower values, with the duplex stainless steels at just above 10^{-4} A/m² and the austenitic stainless steels just above 10^{-5} A/m². Similar microcell corrosion rates for as-rolled 316 rebar in concrete admixed with 5% Cl⁻ by mass of cement were found in a previous study (Mammoliti and Hansson, 2007), although the same study reported $\sim 10\times$ greater corrosion rates for pickled 316 and 2205 rebar.

All microcell corrosion rates, beyond 100 days after casting, were higher than the macrocell corrosion rates by as much as $50\times$, indicating that over time microcell corrosion becomes the more dominant corrosion path by virtue of the macrocell currents decreasing. The dominance of microcell corrosion is similar to that observed in other studies on black steel rebar in concrete, with one study (Hansson, Poursaee et al., 2006) showing microcell corrosion rates of black steel in HPC concrete to be $10\times$ higher than macrocell corrosion rates, and another study (Berke, Shen et al., 1990) showing microcell corrosion rates to be up to $10\times$ higher. This can be attributed to the lower ionic resistance path in concrete between two adjacent microcell sites on a single rebar compared with the relatively large depth of concrete separating two macrocell sites on different rebar layers.

The higher passive currents found for the duplex (2205) pickled compared to the austenitic (304 and 316) pickled types is counter-intuitive to 2205's conventionally stronger pitting resistance as dictated by its higher PREN discussed in Section 2.2.2.3. However, these passive current conditions should be differentiated from those invoking active pitting for which the PREN is meant to evaluate. It is possible that when exposed to a higher oxidizing environment, as shown later Section 4.1.3.3, the electrochemical reactions would accelerate on the austenitic surface relative to duplex. A number of metallurgical reasons could explain the higher passive current densities exhibited on duplex, one being its tendency to form high temperature Cr₂N precipitates during processing that can act as initiation sites for pitting (Pozansky, Nalborne et al., 1983). Other locations for possible corrosion initiation are sigma and chi phases, as well as inclusions such as sulphides, delta ferrite, and chromium-depleted zones around precipitated carbides (Sedriks, 1996).

It should be stated that deriving a corrosion rate from the measured polarization resistance is not precise for the simple reason that the actual corroding area of the rebar in concrete is impossible to determine, and as a result incorrect areas are often used.

Measuring microcell corrosion rates in the depolarized state was important for comparing with data from other studies that do not use a macrocell setup; however, the more realistic situation in bridge deck service conditions is where a macrocell is present and the top and bottom bars are connected together. Near the end of the project, linear polarization resistance was performed on the top bar of certain specimens with the macrocell connected (i.e. polarized by the bottom bar for ≥ 24 hrs), and the results are shown in Figure 40 compared with the average values with the macrocell disconnected from Figure 39. The corrosion current densities for the pickled 304 and 316 specimens when polarized by connecting to the bottom bars were 3-9 \times higher, while those for the as-rolled 304 and 316 as well as the pickled 2205 specimens exhibited relatively little change. This is consistent with previous work (Mammoliti and Hansson, 2007) showing a $\sim 6\times$ increase in microcell corrosion rates for pickled 316 in Cl^- -contaminated concrete when connected to a pickled 316 rebar in relatively Cl^- free concrete. The overall message of these findings clearly indicates that under more realistic conditions with the macrocell connected, microcell corrosion rates of the as-rolled and austenitic pickled rebars would differ by only $\sim 10\times$ rather than the $\sim 50\times$ shown by the depolarized values in Figure 39.

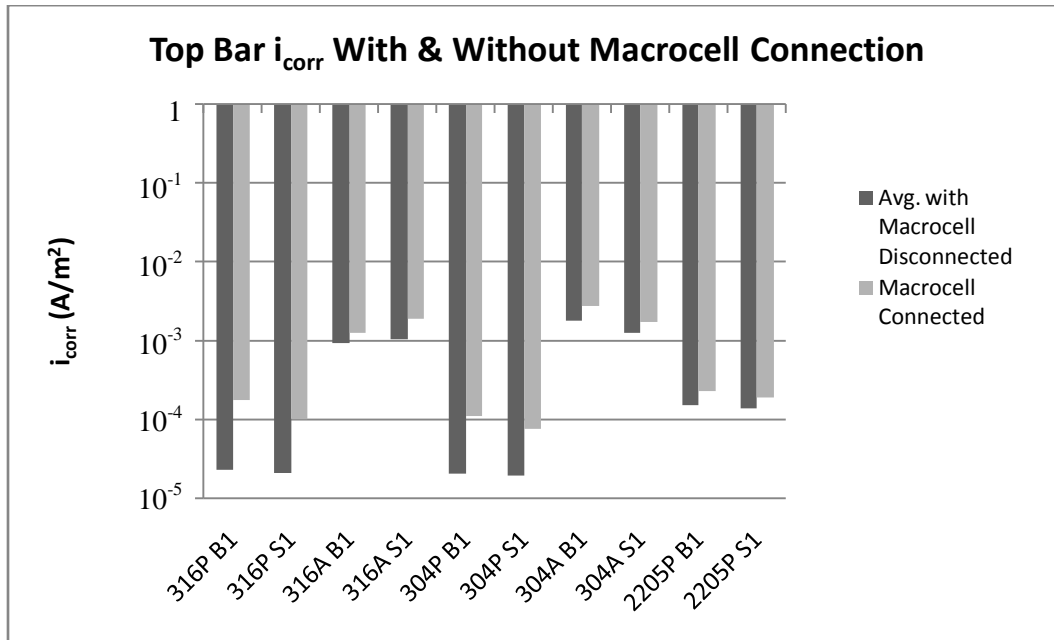


Figure 40: Microcell corrosion current densities of select top bars when polarized (macrocell connected for ≥ 24 hrs) compared with average values for top bar when depolarized (macrocell disconnected ≥ 24 hrs)

4.1.3.2 Corrosion Potentials

Average corrosion potentials of the top bars are presented in Figure 41 versus the copper-copper (II) sulfate reference electrode (CSE = +314 mV vs. SHE) rather than SCE. Corrosion potentials are typically measured versus CSE in field measurements and, thus, presenting in this way is more convenient for comparing with other sources, such as the standard corrosion potential guidelines for black steel in concrete outlined by ASTM-C876. As was done in Section 4.1.1.2 for the macrocell corrosion current measurements, specimens 316P B4 and 304P B4 were not included in these averages since their corrosion potentials were consistently more negative by 50-100 mV than the rest of the population's and, thus, were considered outliers. Corrosion potentials of individual bars, including the outliers, are plotted in Appendix I.

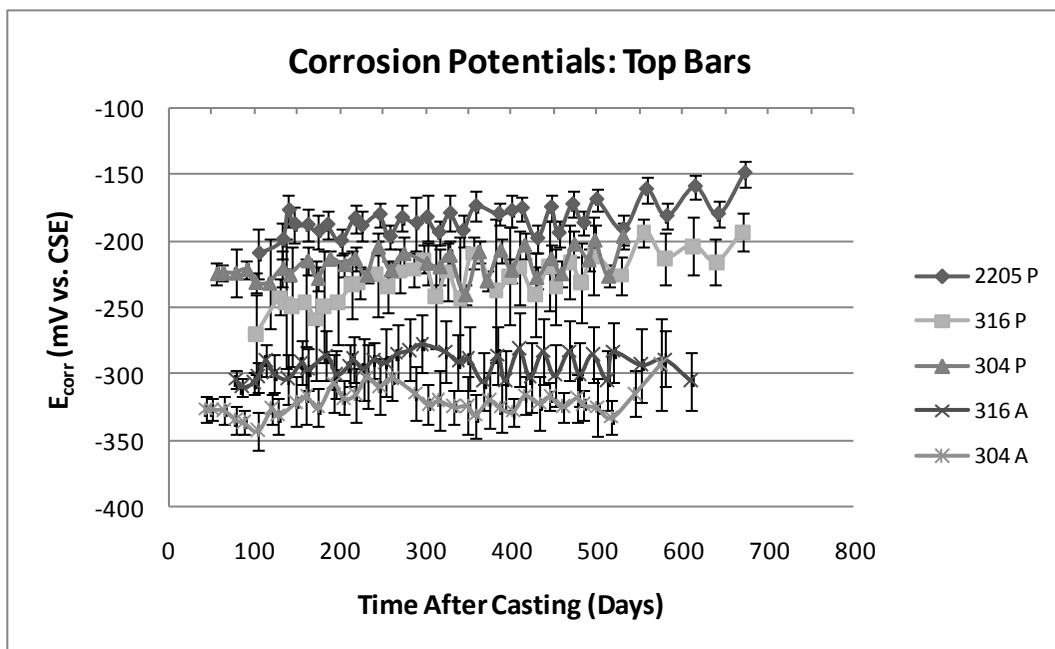


Figure 41: Average corrosion potentials of top bars in G109 specimens

Corrosion potentials of all top bars stayed relatively constant over the ~600 day measurement period, and if anything experienced a slight positive drift over time. The constant fluctuations in values are from the wet/dry exposure cycle, where measurements taken at the end of ponding are more positive due to the drop in ionic resistance across the concrete between the reference electrode and the rebar, as opposed the more negative potentials measured at the end of the dry cycle across the

dry concrete of higher ionic resistance. It is worth noting the relative stability of the corrosion potentials, with no large negative shifts in potential that are characteristic of metals transitioning from passive to active corrosion. This indicates that electrochemical conditions, or corrosion states, of all specimens over the measurement period of 75-600 days after casting experience little change.

Both the as-rolled 316 and 304 specimens exhibited more negative potentials (-275 to -325 mV) than their pickled austenitic counterparts (-200 to -250 mV), with the pickled 2205 exhibiting the most positive corrosion potentials (-150 to -200 mV) despite having higher microcell corrosion rates than the austenitic pickled steels. The more negative potentials of the as-rolled specimens are consistent with their higher corrosion current densities. Standard guidelines (ASTM-C876-91, 1991) for corrosion probabilities of black steel in concrete indicate that the more negative potential, the greater the risk of active corrosion, with black steel having a 90% risk of corrosion at potentials more negative than -350 mV vs. CSE. Excluding the 316P B4 and 304P B4 outliers in the beginning, the corrosion potentials of all specimens stayed more positive than -350 mV. In contrast, a separate study (Mammoliti and Hansson, 2007) found black steel in concrete containing 1% Cl⁻ by weight of cement to exhibit corrosion potentials in the range of -520 to -730 mV vs. CSE. Standard corrosion probability guidelines have yet to be developed for stainless steel in concrete, so no definitive conclusions from these corrosion potentials can be drawn. However, previous work (Mammoliti and Hansson, 2007; Hansson, Jaffer et al., 2008) found austenitic stainless steel rebar in both the pickled and as-rolled surface condition in chloride contaminated high pH environments exhibiting corrosion potentials more negative than -350 mV vs. CSE while still maintaining passive conditions, suggesting that the ASTM C876 guidelines are not suitable for stainless steels, and that they exhibit a more negative threshold beyond which active corrosion becomes probable.

Corrosion rates of black steel in concrete admixed with just 4% Cl⁻ by weight of cement have been found (García-Alonso(a), M.L.Escudero et al., 2007) to be 1.0×10^{-2} A/m² after 400 days, with a corrosion potential of -480 mV vs. CSE. Another study by the same author (García-Alonso(b), González et al., 2007) using mortar specimens admixed with 5% Cl⁻ by weight of cement found corrosion rates of black steel to be $\sim 10^{-1}$ A/m² at high humidity. In concrete containing just 1% Cl⁻ by weight of cement, black steel corrosion rates of $5 \times 10^{-3} - 1.3 \times 10^{-2}$ A/m² after 400 days have been observed (Mammoliti and Hansson, 2007), with corrosion potentials of -530 to -730 mV vs. CSE.

Corrosion potentials measured for selected bottom black and stainless steel bars in the depolarized state (macrocell disconnected for ≥ 24 hours) are shown in Figure 42 and Figure 43, respectively.

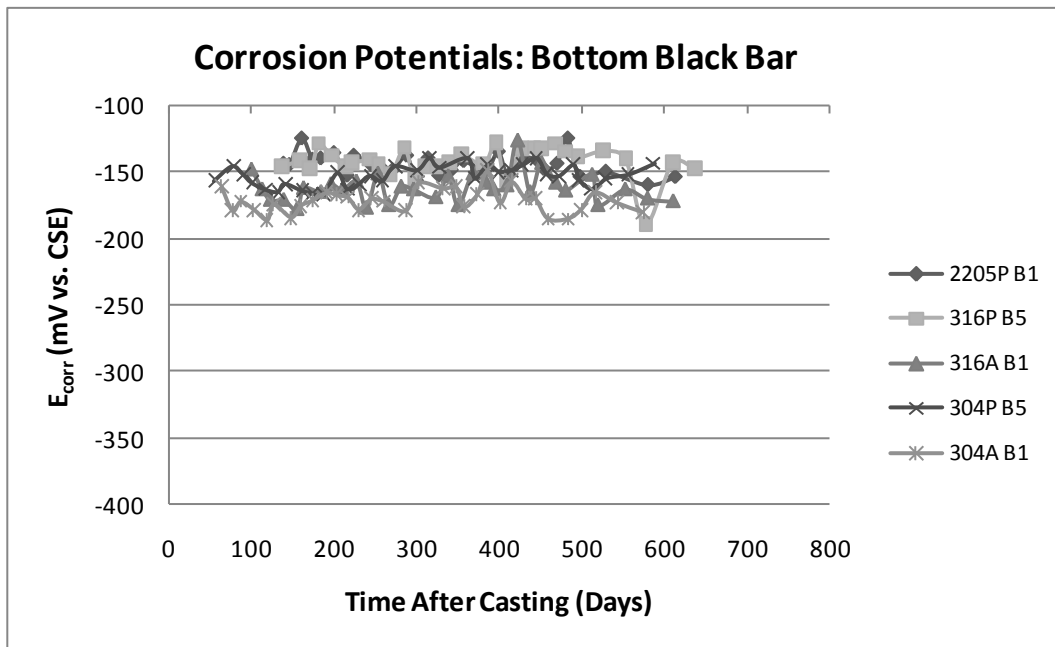


Figure 42: Corrosion potentials for certain bottom black steel bars

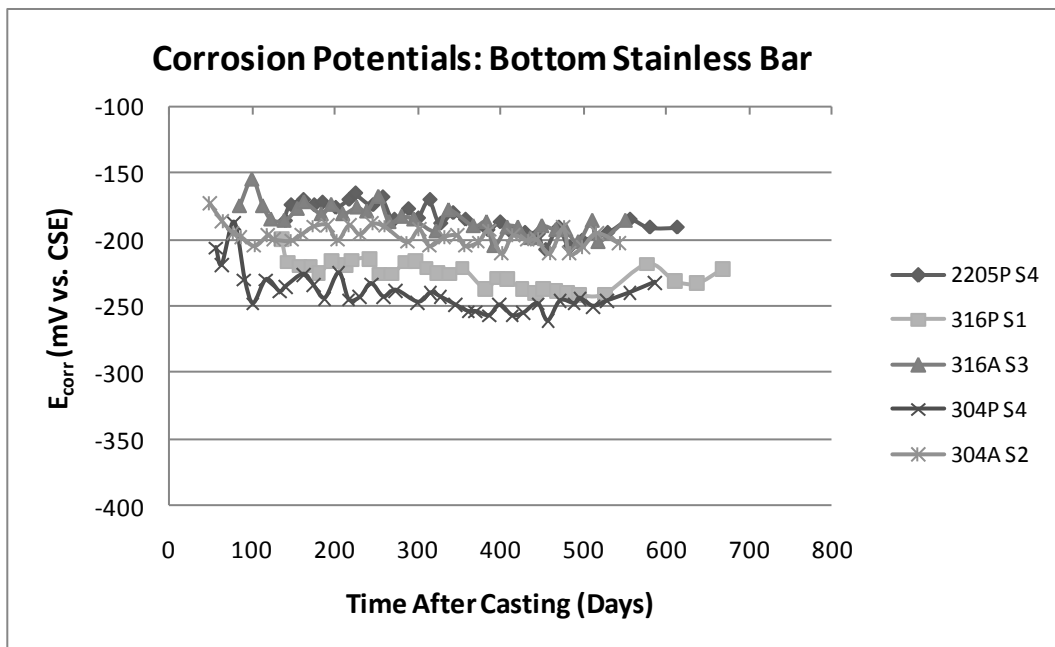


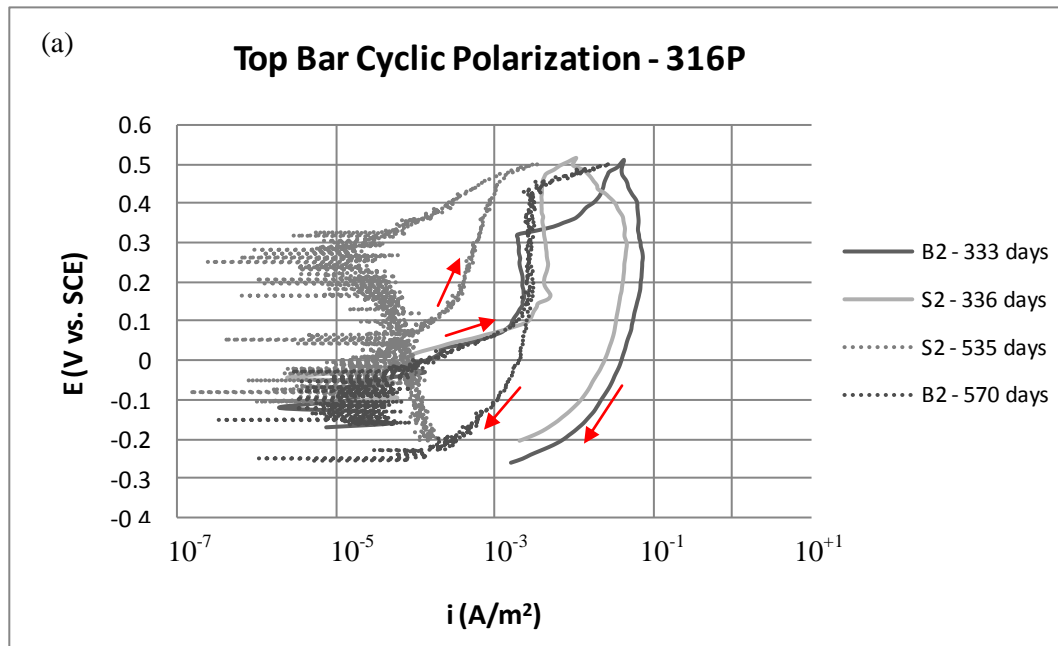
Figure 43: Corrosion potentials for certain bottom stainless steel bars

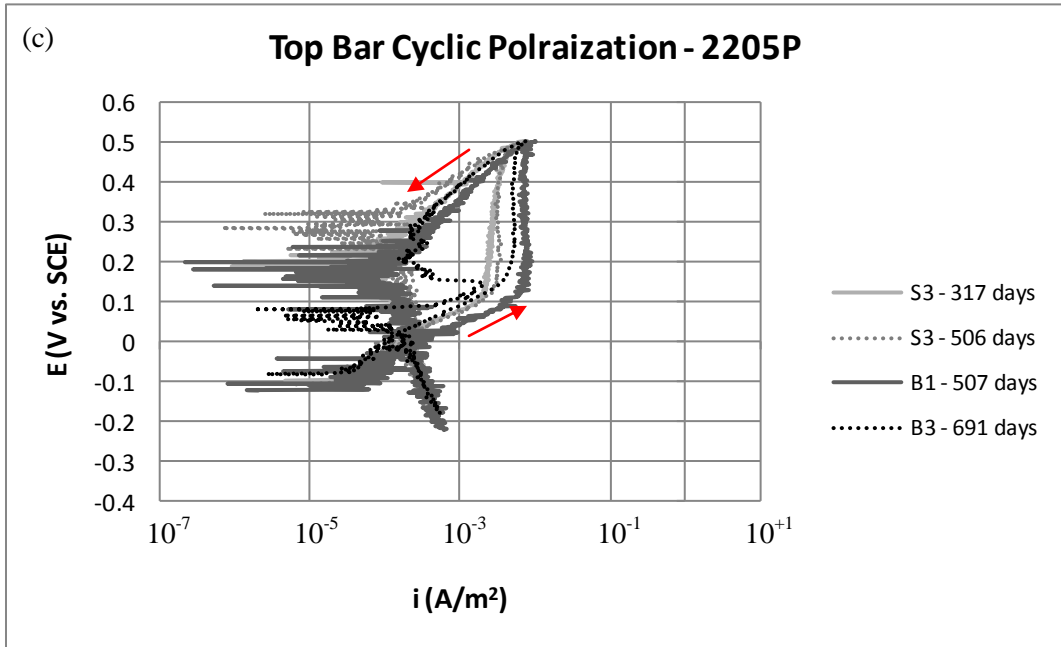
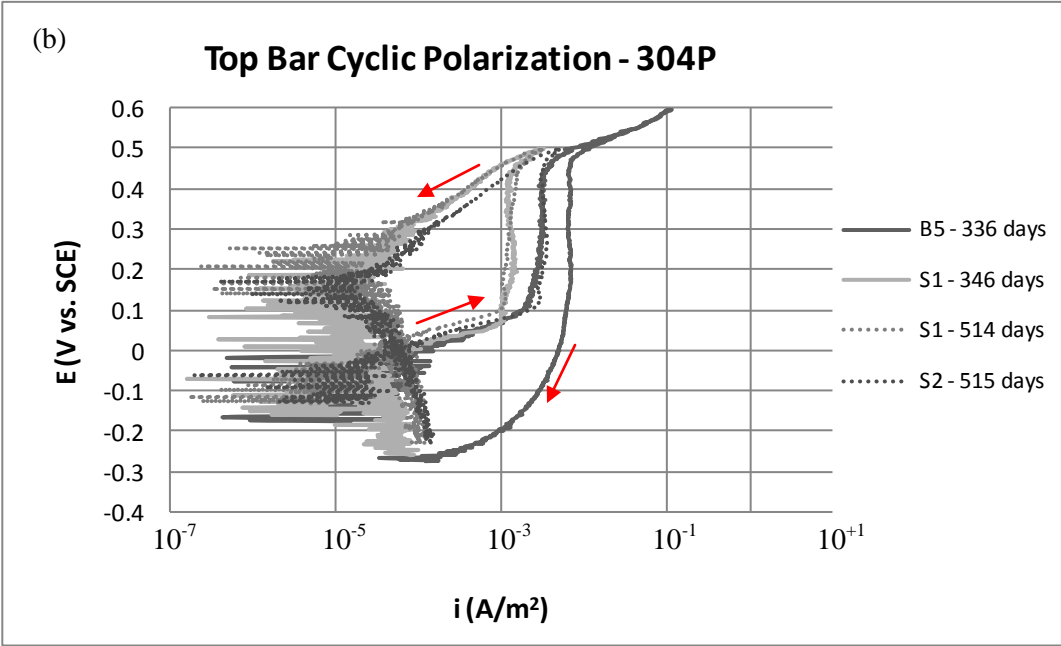
As expected, there is very little difference in corrosion potentials among the bottom black steel bars in Figure 42, since they are essentially comprised of the “same” material and surface condition, and generally exhibit values in the -125 to -175 mV vs. CSE range. In contrast, the bottom stainless steel

bars in Figure 43 exhibit a wider range of corrosion potentials owing to each of their different chemical compositions and surface conditions. The pickled austenitic (316 and 304) specimens exhibited more negative corrosion potentials (between -200 and -250 mV) than the pickled duplex (2205) and as-rolled austenitic steels, which generally exhibited corrosion potentials more positive than -200 mV and closer to those of the black steel. This is likely an effect of their higher oxygen exchange current densities as discussed in Section 4.1.1.2. The corrosion potentials of all bottom bars changed little over time, indicating that the oxidative conditions of the concrete pore solution stayed relatively constant and chlorides did not diffuse from the upper concrete to the bottom rebar surface during the measurement period in sufficient concentrations to disrupt the passive conditions of the bottom steels.

4.1.3.3 Cyclic Polarization

Cyclic polarization (CP) curves for the top bars of various G109 specimens at various points throughout the project are shown for 316P, 304P, 2205P, 316A and 304A steel types in Figure 44 (a), (b), (c), (d) and (e), respectively. Each CP curve was generated by polarizing from E_{corr} to +500 mV vs. SCE than back down to -100 mV vs. E_{corr} , with the arrows next to the curves representing the direction of the potentiodynamic scan.





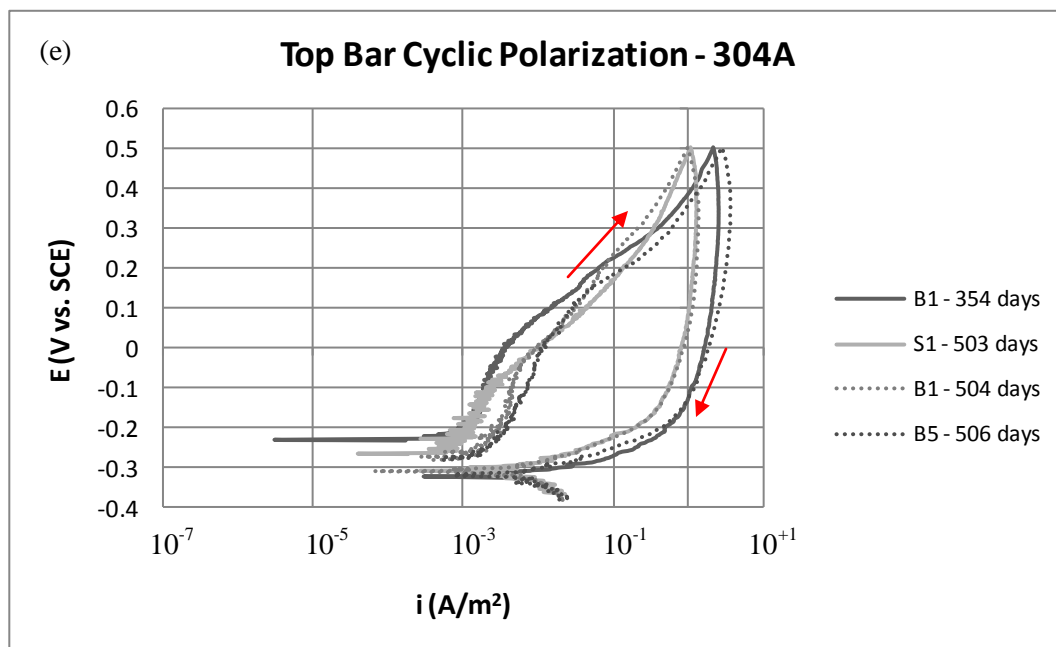
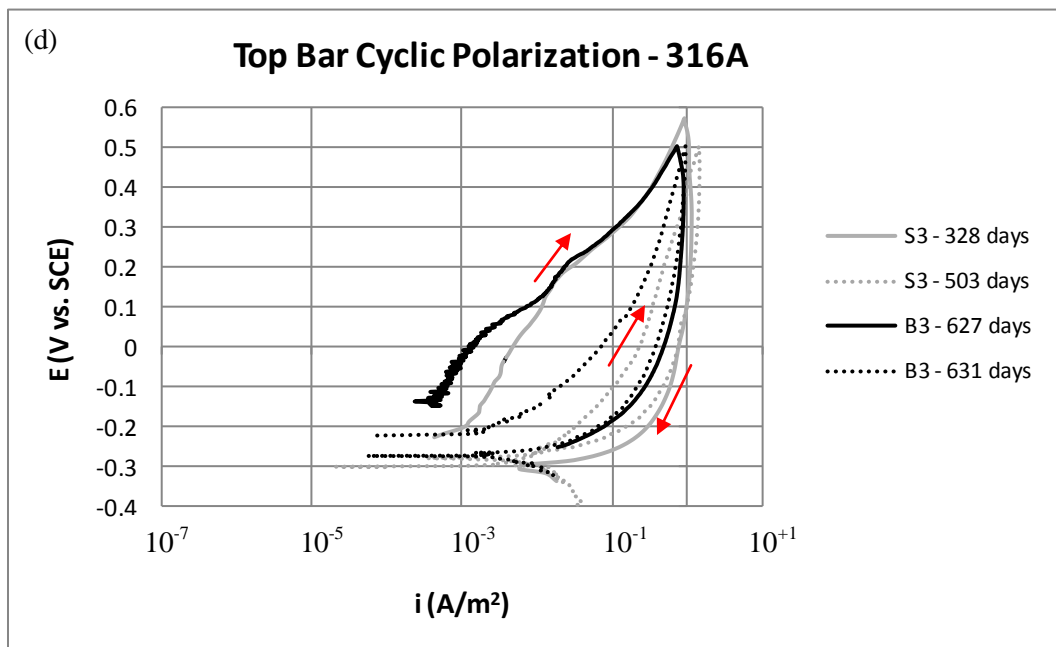


Figure 44: Potentiodynamic cyclic polarization curves for the top bars of (a) 316P, (b) 304P, (c) 2205P, (d) 316A and (e) 304A

All CP curves exhibited consistent corrosion current densities with those obtained from LPR in the Section 4.1.3.1, exhibiting values within the same order of magnitude at E_{corr} (i.e. origin of the upward scan). The 316P curves in Figure 44 (a) all began with rapidly increasing currents during the

initial portion of the upward anodic sweep. A study (Beverkog and Puigdomenech, 1999) that derived the E/pH diagram for the Cr-Ni-Fe ternary system found a solubility limit for Cr_2O_3 at -200 mV vs. SCE at pH of 13.5, above which it is no longer thermodynamically stable. It is believed by the author that the rapid increase in current during the initial portion of the upward anodic scan represents dissolution of the Cr_2O_3 . As the current increase lessens substantially above $\sim +100$ mV vs. SCE, it is believed that the Fe/Ni spinel Fe_2NiO_4 , found in the above study to be thermodynamically stable up to +450 mV vs. SCE at pH of 13.5, becomes the protective species. This spinel film appears to be more conductive than the normally present Cr_2O_3 passive film due to the relatively high current densities exhibited at these potentials, and it is, therefore, not accurate to classify the Fe_2NiO_4 as a passive film. Above +450 mV vs. SCE, all curves exhibit transpassive behaviour, with a sudden acceleration in currents (except for the earlier 316P B2 specimen, which exhibited this behaviour at lower potentials). It is believed that this current increase results from a combination of the dielectric breakdown of the Fe_2NiO_4 film as well as oxygen evolution which, as determined in Appendix G and shown on the E vs. pH diagram in Figure 2, occurs at potentials above +190 mV vs SCE for pH of 13.5.

Different hysteresis loops and current densities were exhibited among the 316P specimens, indicating mixed surface film behaviour, though a common trend can be deduced, based on whether previous CP scans were applied for a single specimen. For instance, the initial scans performed on samples 316P S2 and B2, denoted by the solid curves in Figure 44 (a), exhibited higher current densities on the downward scan, indicating that the transpassive activity has resulted in removal of the protective surface film. In contrast, subsequent scans on the same specimens, denoted by the dashed curves, exhibited smaller currents on the downward scan, indicating a less damaged surface film than with the prior scan or, in the case of S2, the development of an even more protective surface film from the applied anodic potential. CP curves were performed on additional 316P top bars, shown in Appendix J, that confirm the trend of decreasing currents with multiple scans. An alternative hypothesis one could make is that current densities of the CP scans generally decrease with the number of days after casting from when they are taken (i.e. change of the steel's surface film from maturing of the concrete and/or evolution of chloride attack), however this is unlikely since the initial scan for 316P S3 (see Appendix J) showing more positive hysteresis and higher current densities (less protective surface film) was taken well after the second scans of other 316P specimens (i.e. B2 and S2) that exhibit negative hysteresis and lower current densities (more protective surface film).

Based on the 316P results, CP scans likely do have a long-term effect on the surface film properties, though it is uncertain why the surface film on 316P becomes more protective with time or with multiple cyclic polarization scans. There may have been surface impurities or left-over heterogeneities not completely removed from the final pickling processes (note the rougher, more tarnished surface appearance of the 316P compared to the 304P and 2205P in Figure 45) that, once oxidized away during the first CP scan, left a more uniform surface that tended to form a stronger surface film during subsequent polarization. The higher sulphur content of the 316LN versus the 304LN steels used in this experiment (0.030 versus 0.009% by mass, respectively, as shown in Table 7) may provide a greater number of sites to initiate localized corrosion on the 316LN due to the presence of sulphide inclusions. Previous study (Suleiman and Newman, 1994) of two 316 steels having different sulphur contents (0.004 and 0.018% by mass) and polarized anodically in deaerated 0.5M NaCl solution (though not at high pH levels) observed breakdown of the surface film at much lower potentials for the steel of higher sulphur content. Manganese sulfides have received significant attention in their role of pit initiation in stainless steels (Sedriks, 1983). Another study of SS rebar in chloride contaminated concrete (García-Alonso(a), M.L.Escudero et al., 2007) that found 316P to exhibit inferior surface film protection during CP compared with 304P, attributed this to differences in microstructure from cold-working, since separate corrosion measurements involving stainless steel rebar of identical compositions only in mortar and machined down to equal diameters (i.e. both surfaces were smooth) exhibited no distinction in corrosion characteristics. Despite affecting the shape of the CP curves themselves however, multiple CP scans in the present project did not change the corrosion potentials or microcell and macrocell corrosion rates in any noticeable way over the long-term from the values exhibited by other 316P specimens not exposed to cyclic polarization. Previous study (García-Alonso(a), M.L.Escudero et al., 2007) has also observed restoration of corrosion current densities after cyclic polarization of stainless steel rebar in chloride-contaminated concrete, though original corrosion current densities were not restored on all stainless steel types, with microstructure defects from the forming processes thought to be a determining factor. It is therefore quite probable that, for application as concrete reinforcement, these defects are not critical to the steel's long-term corrosion performance.

The 304P and 2205P CP scans in Figure 44 (b) and (c) gave much more consistent curves, showing similar slowing of the current density increase at potentials near +100 mV vs. SCE, as well as consistent negative hysteresis curves and thus more protective surface films on the downward scan. The slightly higher currents at all locations for 2205P compared with 304P are consistent with the

former's higher microcell corrosion current densities from LPR. One outlier curve was for specimen 304P B5 that was mistakenly polarized by an additional 100 mV to +600mV vs. SCE and exhibited positive hysteresis and thus a less protective surface film on the downward scan. The large increase in current in the 500-600 mV range is likely not a sign of localized corrosion but of uniform corrosion in the transpassive or oxygen evolution region (ASTM-G61-86, 2003) via oxidation of hydroxyl ions (600 mV vs. SCE being significantly above the oxygen equilibrium line of the E vs. pH diagram in Figure 2). The formation of corrosion cells in practice that would provide such high potentials is highly improbable, and evaluating metals based on their performance at these high potentials may not be practical.

The 316A and 304A CP curves in Figure 44 (d) and (e) were of distinctly different shape than those for the pickled steels. Rather than exhibiting a rapid increase in current density from E_{corr} on the upward scan up to +100 mV vs. SCE followed by a region of approximately constant current, the curves for the as-rolled steels exhibited a constant positive slope on the upward scan characteristic of uniform corrosion. The downward scans exhibited positive hysteresis, indicating a breakdown of the surface film during the upward scan and a propagation of general corrosion on the downward scan. The current densities for the as-rolled CP curves were higher than for the pickled, particularly in the downward scan where values of up to 1-2 A/m² were reached. In contrast, the highest current densities achieved by the pickled CP scans were for 316P S3 on the downward scan of ~0.1A/m² (see Appendix J). However, as what happened for the pickled specimens, subsequent corrosion potentials as well as microcell and macrocell corrosion rate measurements did not vary over the long-term from those of the as-rolled specimens not subjected to cyclic polarization; therefore, despite the significant surface film breakdown demonstrated by the as-rolled CP scans at high potentials, the original protective surface conditions were restored.

Additional CP scans on the same bar of 316A specimens, shown by the dashed plots in Figure 44 (d), exhibited a more exponentially curved upward scan that began with a shallow slope and ended nearly vertical between 300 and 500mV vs. SCE. An explanation for this could be that during the first scan, the surface layer is being uniformly oxidized on the upward scan (and further destroyed on the downward scan), and during additional scans the absence of that original film allows the corrosion current to initially increase much more rapidly, but the rate of current increase gradually slows and the current is not able to exceed the maximum ~1A/m² reached during the initial scan. As with the variable CP behaviour exhibited by 316P, time after casting does not appear to influence this trend,

since 316A B3 was initially scanned much later than the second scan for 316A S3, but still exhibited a curve similar to the first 316A S3 scan. 304A exhibited little change in CP behaviour with subsequent scans as shown by the similarly shaped CP curves for specimen B1 taken ~150 days apart.

4.1.4 Metallographic and Chemical Analysis of As-Received Bars

A macrograph of one bar of each stainless steel type before being embedded in concrete is shown in Figure 45 to provide a baseline reference for the micrographs of the bar surfaces shown in this section.

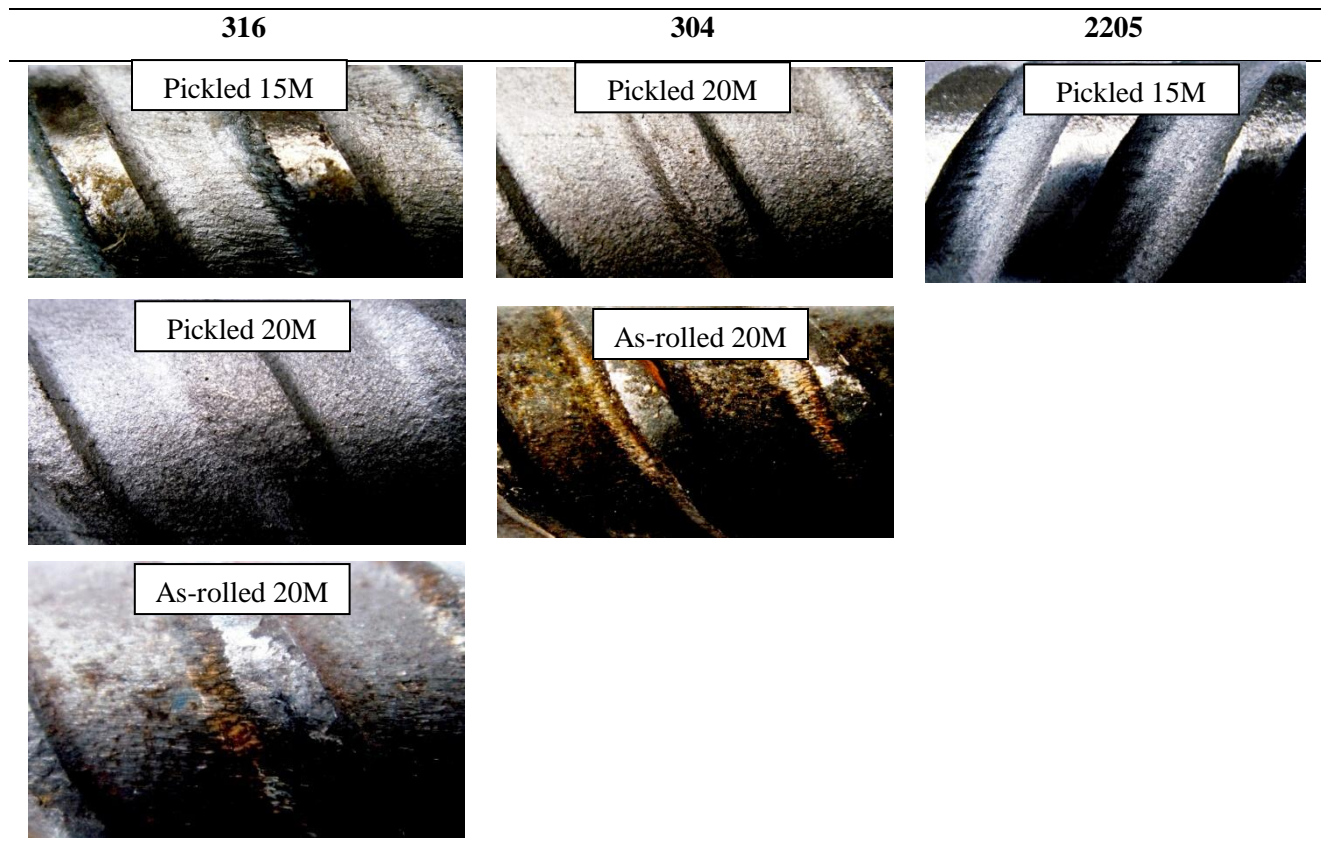


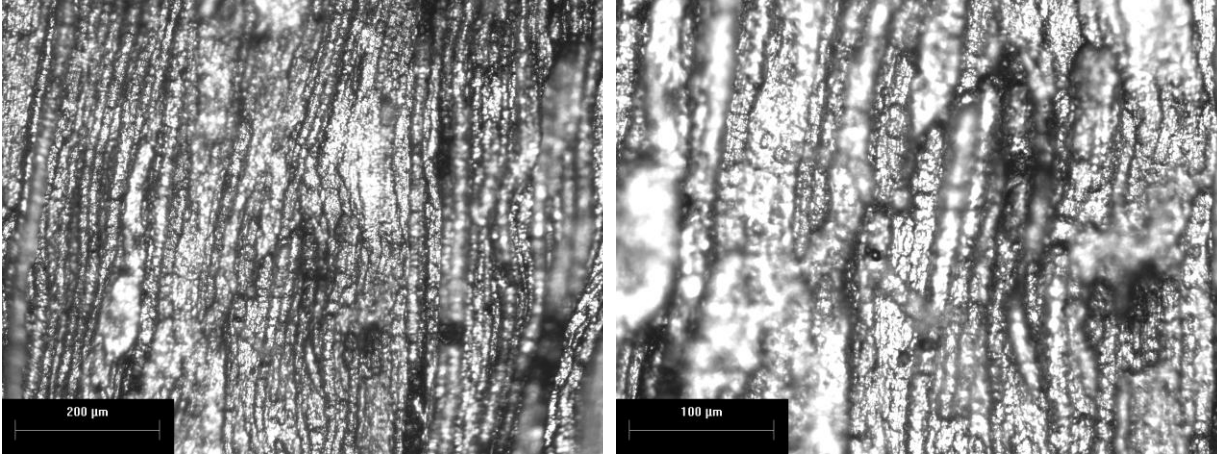
Figure 45: Macroscopic images of each stainless steel rebar type before casting

4.1.4.1 Optical Microscopy

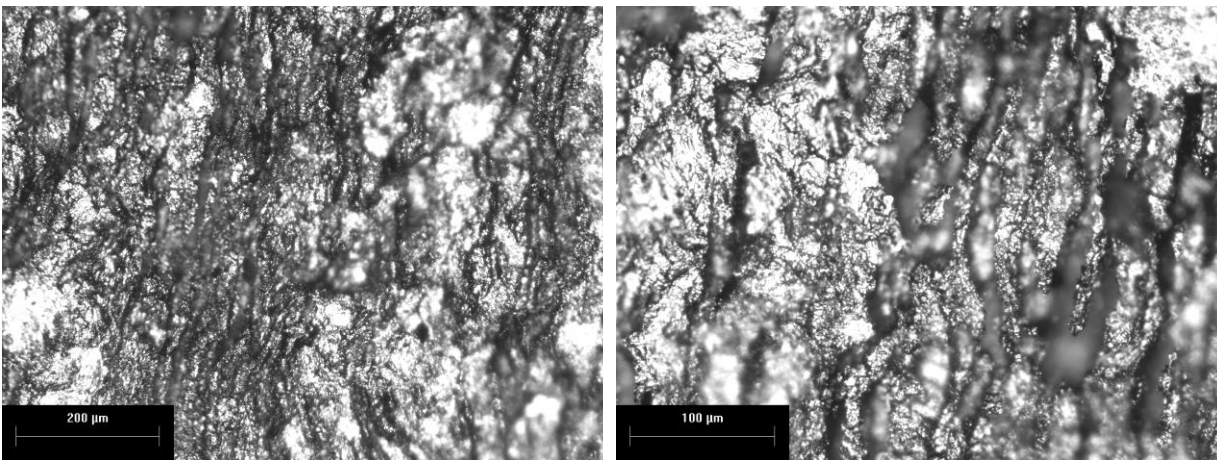
Optical micrographs of the external surface of a rebar for all steel types and surface conditions are shown in Figure 46. The images show two magnifications per bar type, and an additional rebar type

not used in the G109s, 20M 316P from Valbruna, is also shown for comparison with the 15M 316P to observe any differences from processing between two bars of identical surfaces and compositions.

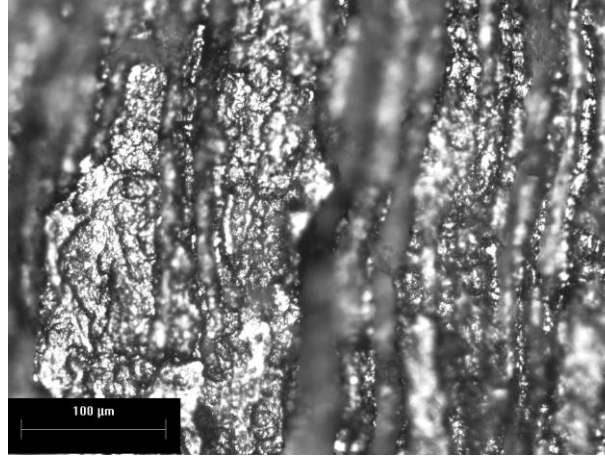
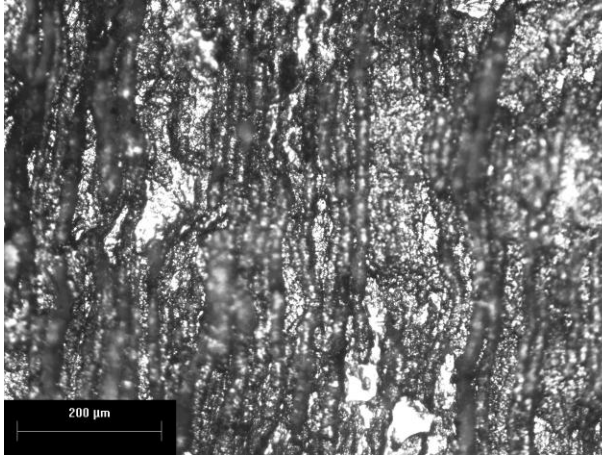
316P (15M)



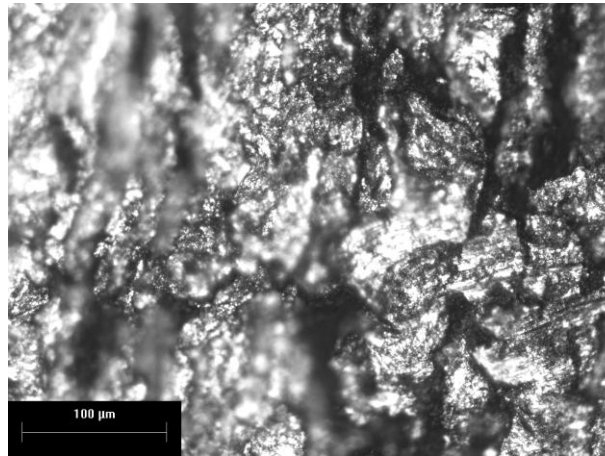
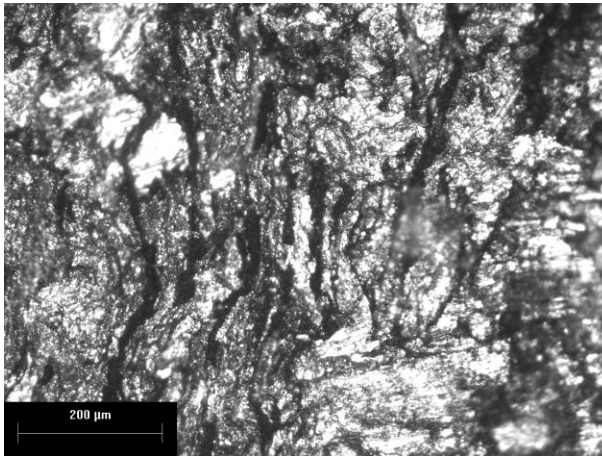
316P (20M)



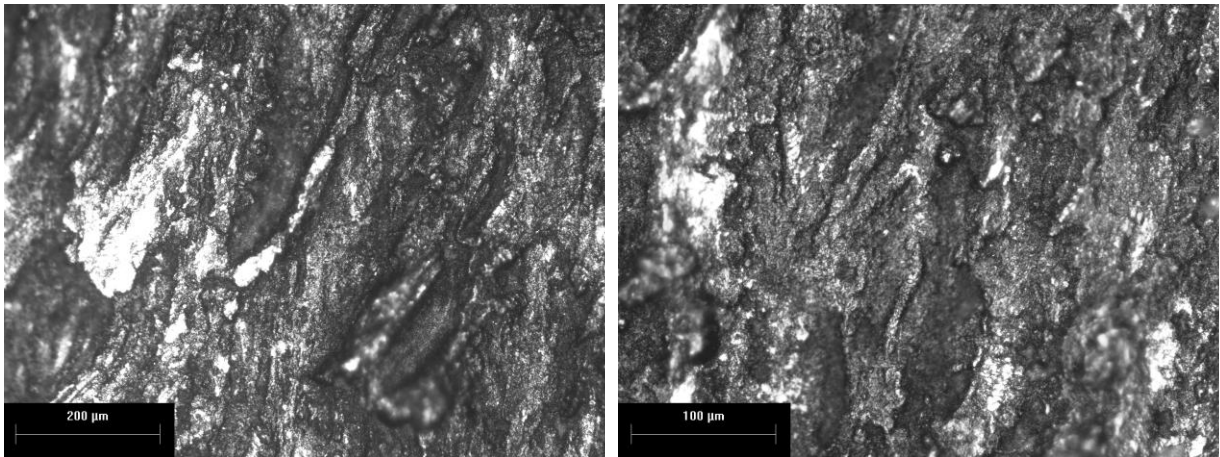
304P (20M)



2205P (15M)



316A (20M)



304A (20M)

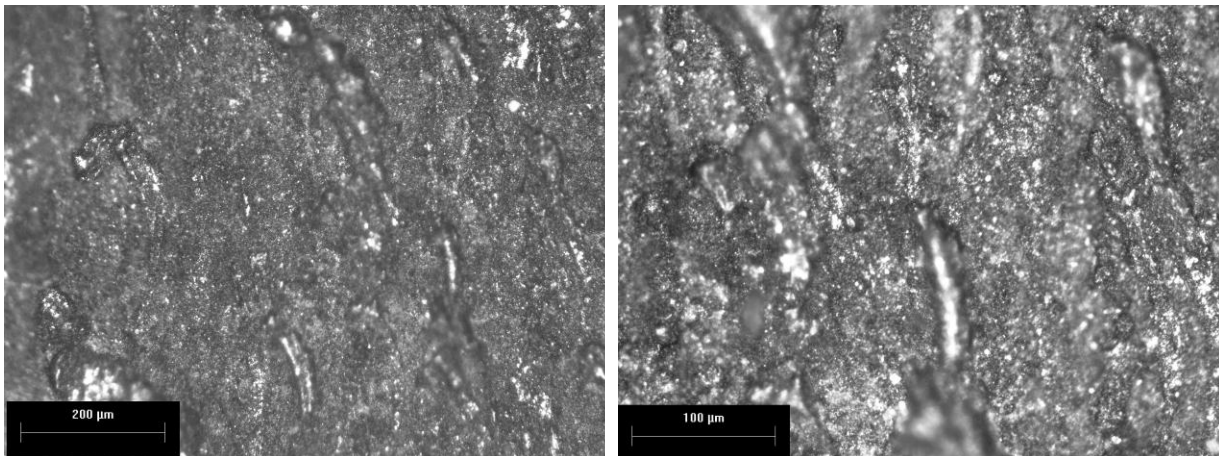


Figure 46: Images of the different steel and surface types using optical microscopy

The 15M 316P surface exhibits distinct parallel ridges running longitudinally that are likely left over from the forming process. All other pickled surfaces exhibit ridges that are more subtle and less discreet, uniform and narrow. The 20M 316P and 304P appear very similar, particularly at higher magnification, whereas the 2205P surface looks the most disordered of all the pickled surfaces. The different appearance between the 15M austenitic (316) versus the two 20M austenitics (316 and 304)

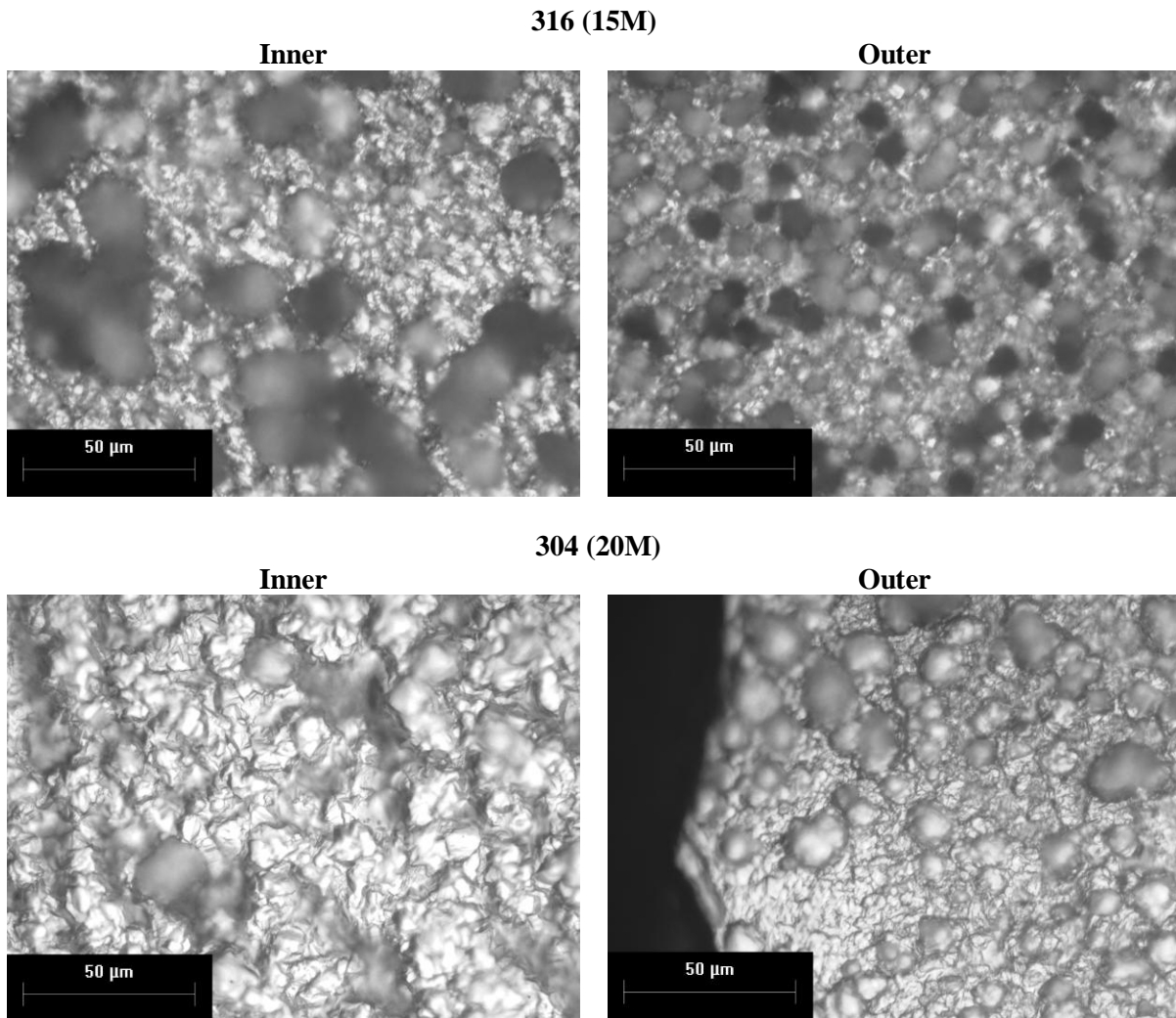


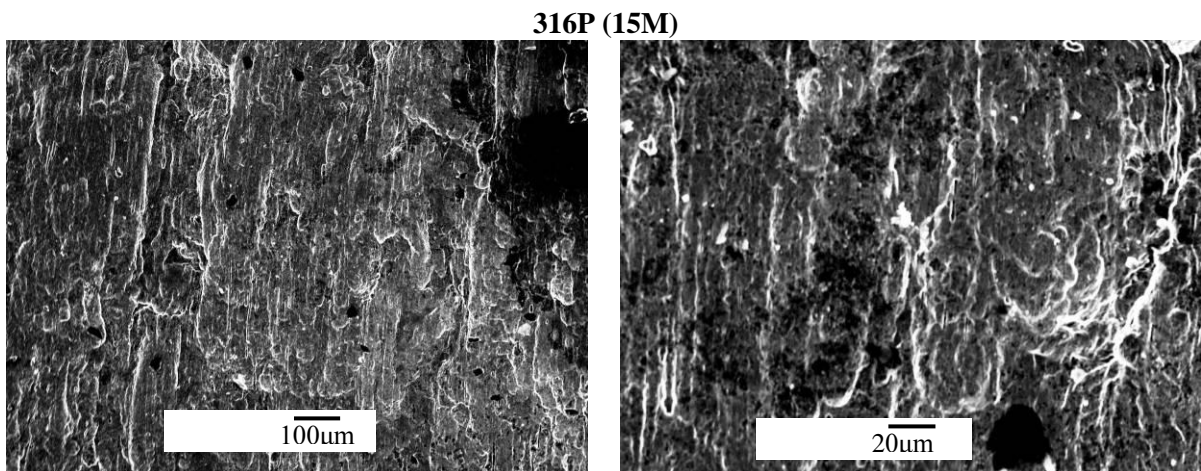
Figure 48: Optical micrographs of transverse cross-sections of the 316 and 304 rebar

The optical micrographs in Figure 47 revealed elongated grain structure oriented along the rebar axis, a result of the rolling process during the bar's manufacture. Both steel types have a noticeably larger grain size in interior of the bar than near the surface, which is also shown in the transverse cross-sections in Figure 48. This is also a result of the hot rolling, where higher deformation as well as higher rates of heat loss experienced at the outer surfaces impedes grain growth in those areas. The 15M 316 has a slightly smaller grain size than the 20M 316 and 304, due to the greater extent of

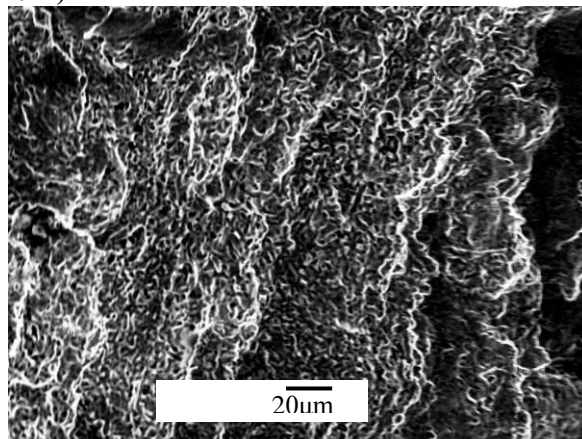
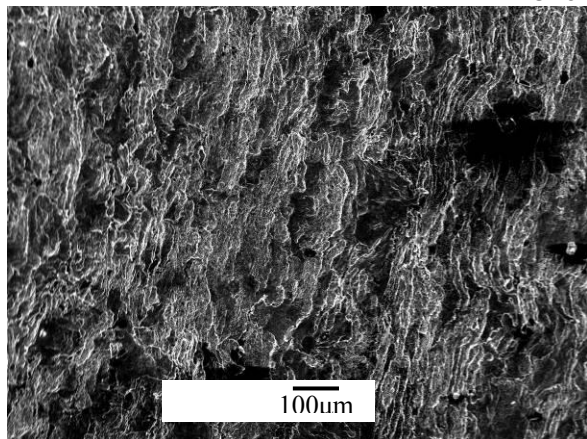
deformation required for its smaller size. The 20M 316 in turn has a slightly smaller grain size than the 20M 304, and given their equal sizes this difference maybe be accounted for rather by different heat treatments. As previously reported (Covino, Scalera et al., 1984), stainless steels of smaller grain size form mill scales of higher chromium content, and thus greater chromium depletion underneath, due to the greater availability of grain boundaries across which chromium can diffuse from the bulk to the outer surface during hot rolling and annealing. This may have led to the 15M 316P's greater susceptibility to over-pickling as shown by its more tarnished surface appearance in Figure 45, which in turn would account for its inferior surface film protection, exhibited by the CP curves in Figure 44, compared with the other pickled steels.

4.1.4.2 Scanning Electron Microscopy

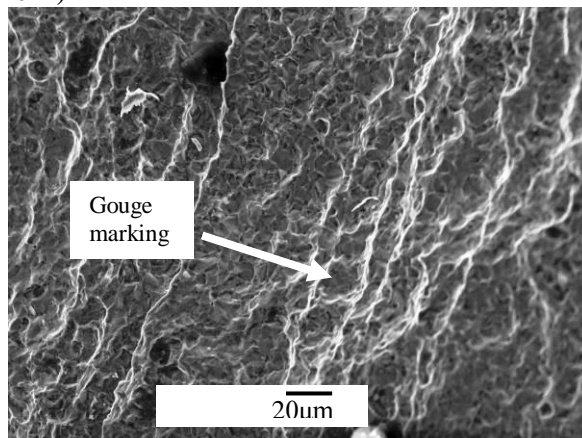
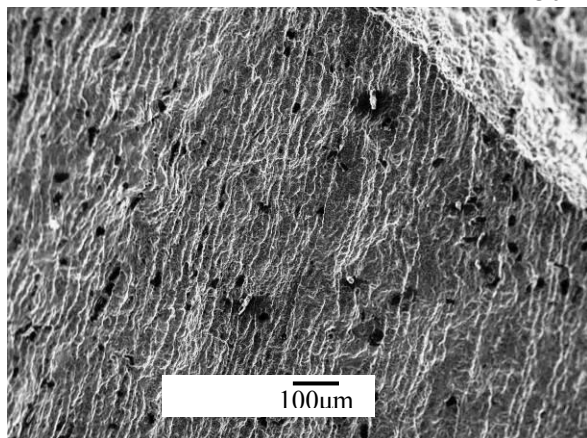
Scanning electron micrographs of the outside surfaces of all steel types and both surface condition are shown in Figure 49. Micrographs are taken at two magnifications, and again, 20M 316P from Valbruna is also shown in order to compare with the 15M 316P and observe any processing differences that may exist between two bars of "identical" surfaces and compositions.



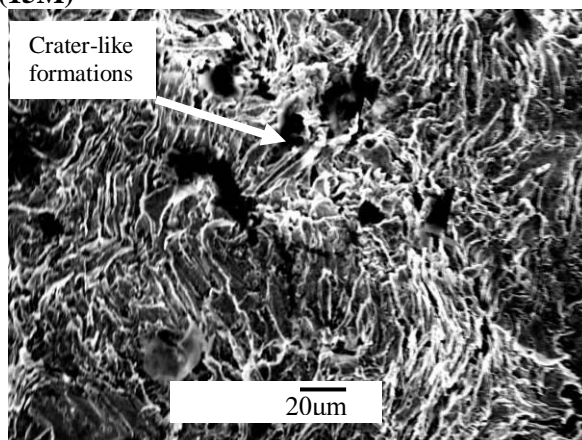
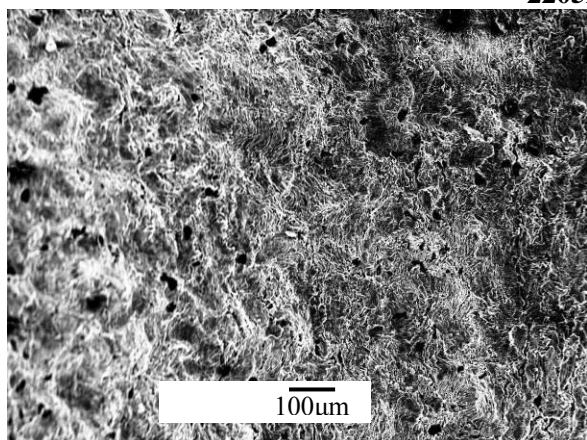
316P (20M)



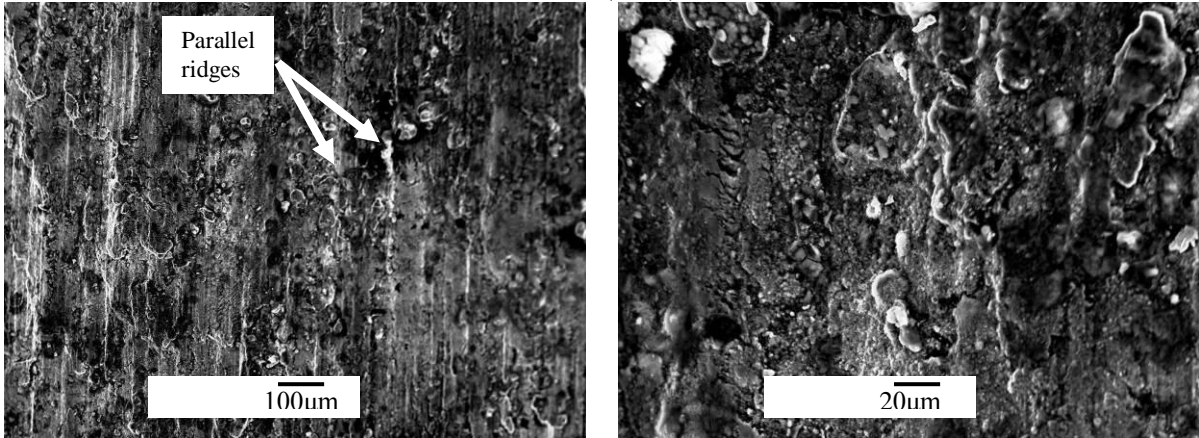
304P (20M)



2205P (15M)



316A (20M)



304A (20M)

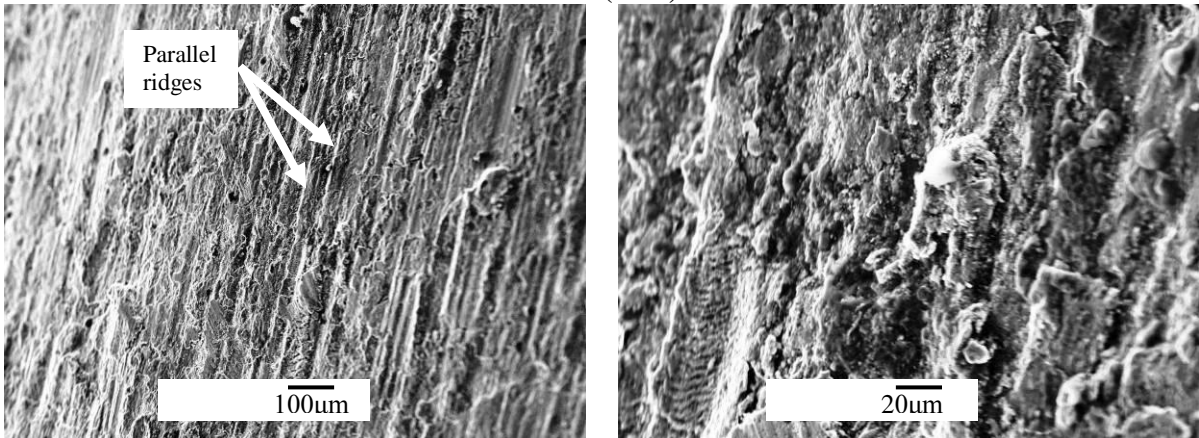


Figure 49: Surface images of the different steel types and surface conditions using scanning electron microscopy

The rougher surface morphology of the 2205P compared with the austenitic pickled types may be a factor in its higher microcell corrosion current densities measured by LPR in Figure 39. The crater-like formations on its surface may act as pit initiation sites and increase the number of current exchanges occurring over a given surface area. Despite not exhibiting these deep crater-like formations, 15M 316P shows a relatively heterogeneous surface appearance similar to its as-rolled counterpart. In contrast, 304P's surface differs significantly from that of 304A, exhibiting a network

of distinct, gouge-like markings which indicate signs of grain dissolution from pickling (the gouge diameters are within the same order of magnitude as the grain sizes seen in Figure 47 and Figure 48). The 15M 316P on the other hand does not exhibit this fine network, suggesting that its surface was not pickled as extensively.

The as-rolled surfaces both exhibit parallel ridges running along the axis of the rebar left over from forming, as well as globular nodules resulting from mill scale's heterogeneous growth at high temperatures. This uneven morphology provides greater ability for electrochemical reactions to occur, whether on the microcell level where crevices under the nodules and adjacent exposed areas can create corrosion cells, or on the macrocell level where, as the bottom bar, the greater surface area per unit length generates higher oxygen exchange current densities, thus increasing macrocell corrosion rates of the attached top bar.

4.1.4.3 Energy Dispersive X-Ray Spectroscopy

Semi-quantitative chemical analysis was performed on the interface between the mill scale and base metal in order to determine the composition and extent of the chromium depleted region of the 316A and 304A bars using energy dispersive X-ray spectroscopy (EDS). Two separate regions of each steel type were analyzed, and cross-sectional images of these regions as well as the composition profiles are shown in Figure 50 and Figure 51. The chemical contents of the interfacial region were plotted in weight %, with the Cr content of bulk metal, confirmed by EDS analysis of the bulk pickled specimens to be approximately 18.8% for 316A and 18.3% for 304A (see Appendix K), included on the plots as a solid line for reference.

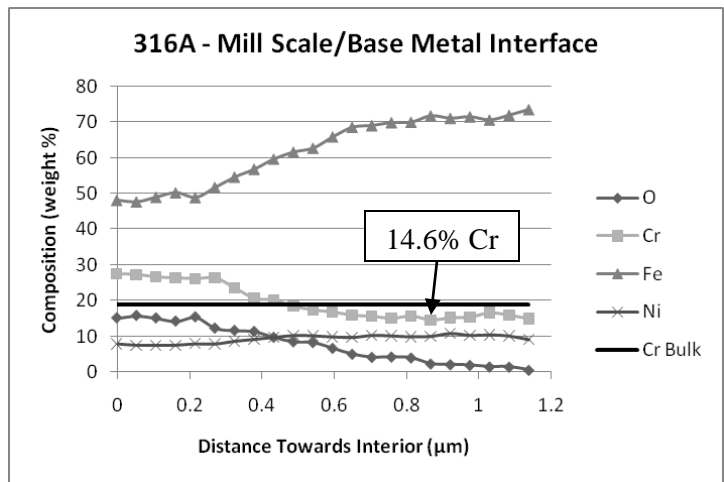
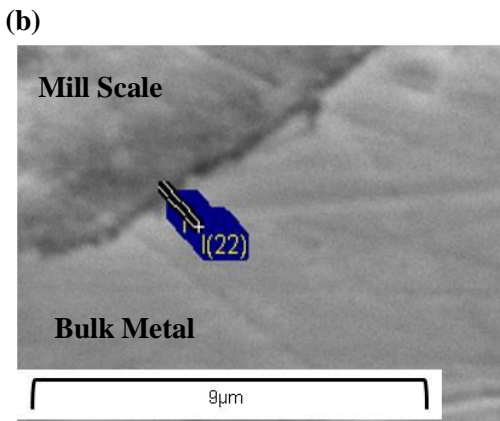
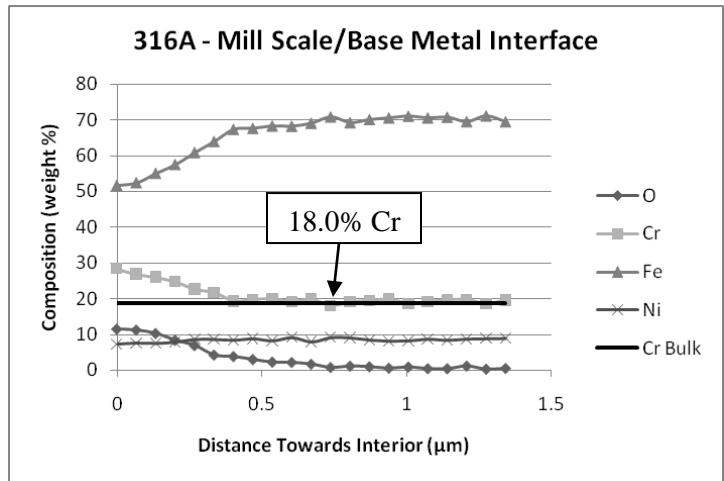
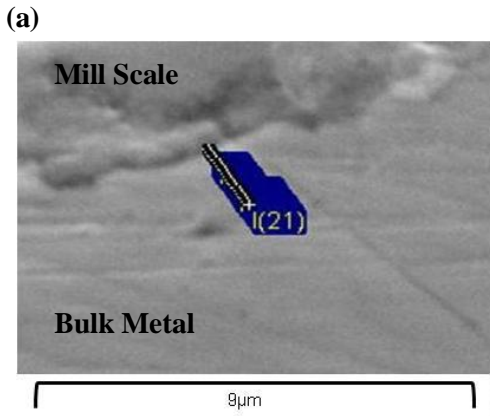
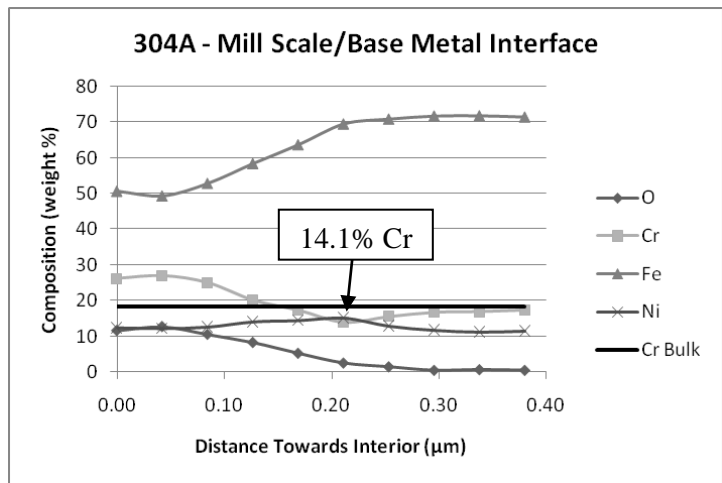
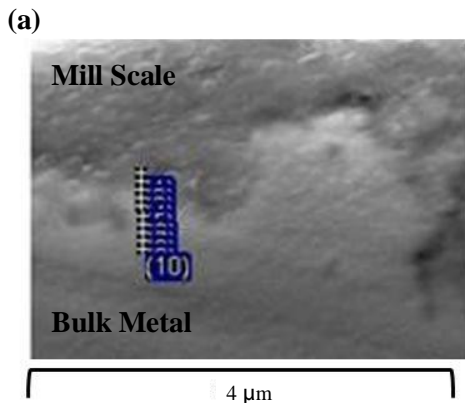


Figure 50: EDS analysis of the mill scale – base metal interface of 316A rebar



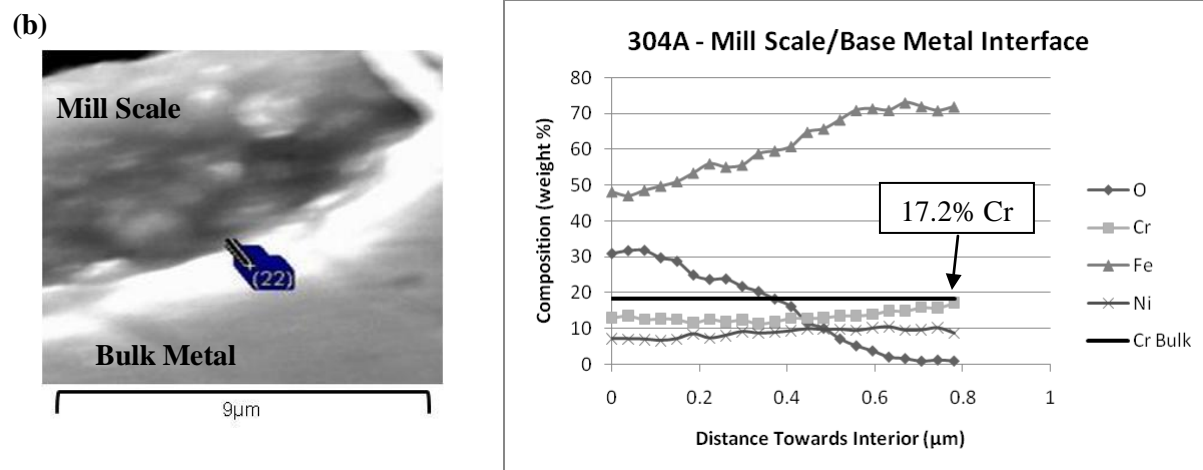


Figure 51: EDS analysis of the mill scale – base metal interface of 304A rebar

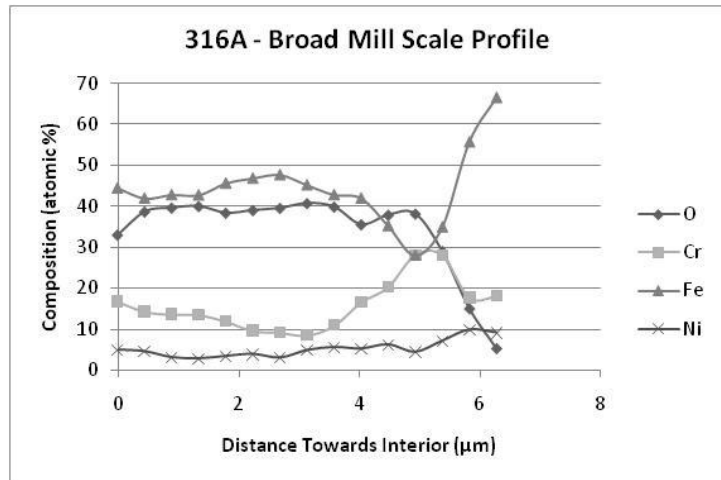
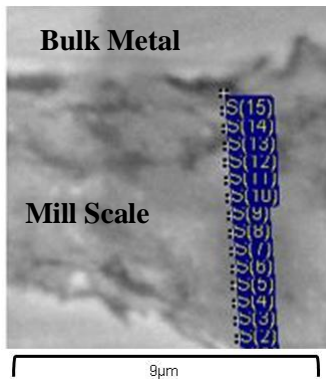
Analysis of the 316A interface in Figure 50 (a) shows negligible Cr-depletion over increments of 60 nm across the mill-scale/bulk-metal interface, with values only as low as 18% detected. Another region analyzed in Figure 50 (b) does show some chromium depletion over a distance of ~400 nm, reaching a low of 14.6% Cr before recovering back to bulk values. Analysis of 304A in Figure 51 (a) revealed a ~100 nm depth of Cr depletion that reached a low of 14.1% Cr before recovering back to bulk content. It should be noted that the cross-section of this sample was mounted at 65° from the horizontal during its analysis in order to obtain higher magnification. It is unlikely that this significantly influenced the data; given that the EDS sampling depth is on the order of 1-2 μm, the only effect would be that the compositions detected would truly reflect points slightly offset towards the outer surface rather than their apparent positions as shown on the scanning electron micrograph. Another 304A region in Figure 51 (b) shows something different, where, rather than dropping off from a high Cr content in the mill scale, the Cr content gradually increases from a low content in the mill scale towards bulk metal values without exhibiting a dip at the interface. It is evident that little depletion occurs in the bulk metal here since Cr content is near bulk values at the point where the oxygen content drops off to low levels.

These EDS analyses show inconsistent chemical compositions present at the mill scale/bulk metal interface for both steel types, with each exhibiting some Cr depletion in one area and negligible Cr depletion in another area. It is believed that the inconsistent chemical profiles are largely due to the rolling processes taking place while the mill scale is forming, causing what would otherwise be more distinct and orderly chemical gradients to be formed into a less uniform, more random pattern. It is uncertain exactly how detrimental is the Cr depletion that was found; however, to provide some

context, 12 wt% is commonly acknowledged as the minimum chromium necessary for the formation of the Cr_2O_3 passive film in unpolluted atmospheres (Binder and Brown, 1946). While Cr contents as low as 12 wt. % may not provide sufficient corrosion resistance in chloride-contaminated concrete, the depth of depletion is another factor requiring consideration, since there must be a maximum depth below which pitting is unable to propagate. Either way, the maximum level and depth of Cr depletion found in both steel types is not nearly as large as the 18 to 10% depletion over a distance of 20 μm observed by Stott (1989) that is often referred to in literature (Li and Celis, 2003; Scully and Hurley, 2007) in order to justify the pickling process, and which occurred after 1000 hours at 800°C.

EDS analysis of the mill scale for 316A and 304A rebar was also performed, as show in Figure 52 and Figure 53, respectively. In order to determine the atomic ratios and possible compounds present within the mill scale, the chemical contents were plotted in atomic %.

(a)



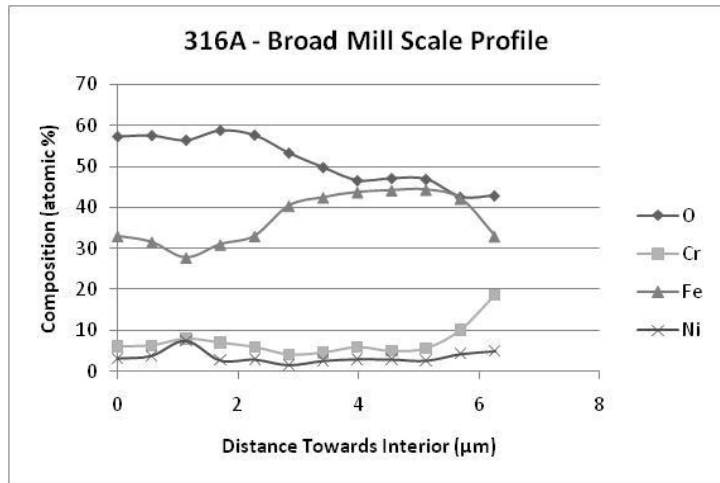
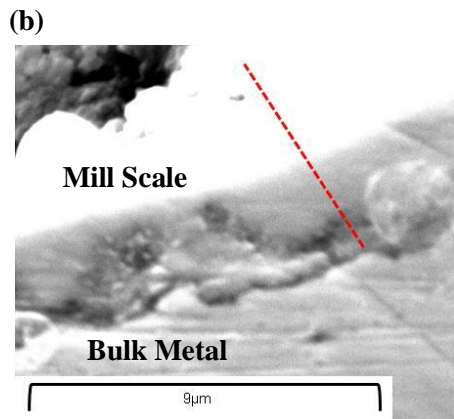


Figure 52: EDS analysis of the mill scale for 316A rebar

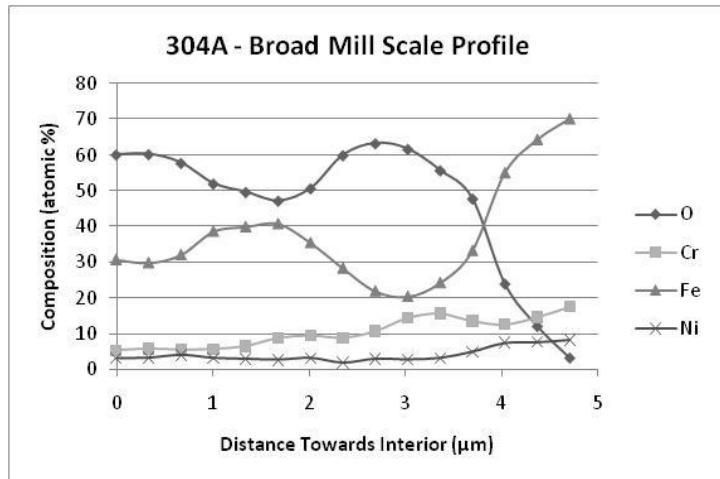
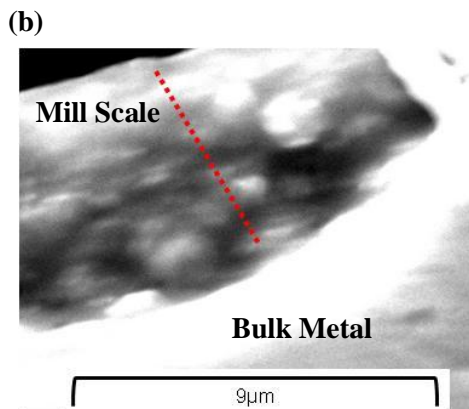
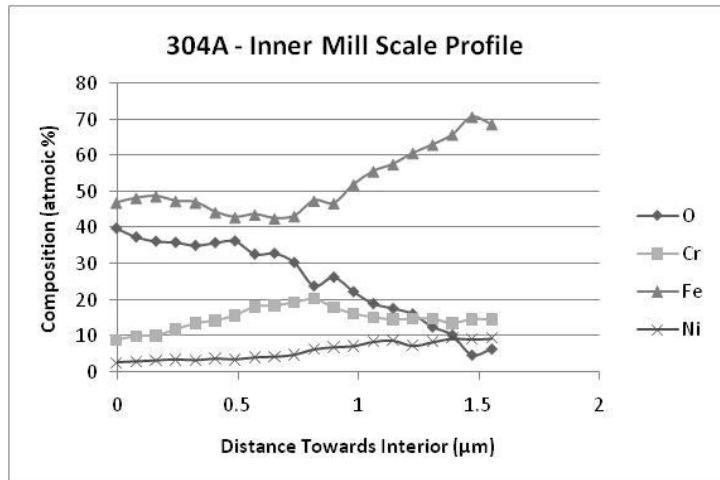
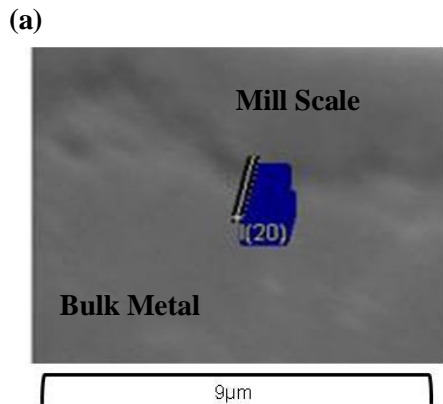


Figure 53: EDS analysis of the mill scale for 304A rebar

The mill scale for the 316A region analyzed in Figure 52 (a) shows high Fe and low Cr in the outer mill scale, with a dip in Fe and spike in Cr to 30% at the inner scale over a $\sim 1\mu\text{m}$ depth from the bulk metal, representing the Cr-rich oxide layer that accounts for the Cr depletion in the base metal. This same characteristic was also seen at the other 316A region analyzed in Figure 53 (b), though the profile was unfortunately not extended as far in towards the bulk metal in order to capture the full depth of the chromium oxide. Both regions showed mostly oxygen and iron at the outer mill scale, with Cr generally below bulk level except within the small chromium oxide region, and Ni at consistently low levels of ≤ 5 atomic %. The compounds making up the outer scale are thus likely comprised predominantly of a series of iron oxides as well as some spinel of $(\text{Fe}, \text{Cr})_2\text{O}_3$, though the inconsistent ratios of elements throughout the profiles of both regions examined prevents any general progression of compounds from being identified. Mill scale thickness observed on the 316A rebar ranged from 4.5-9 μm .

The mill scale for the 304A region analyzed in Figure 53 (a) shows similarly high Fe and O contents at the outer mill scale, with Fe continually increasing towards the interior and oxygen continually decreasing. The presence of Cr in small amounts indicates a spinel of $(\text{Fe}, \text{Cr})_2\text{O}_3$ similarly exhibited by the 316A, with consistently low Ni presence (< 5 atomic%) until the base metal is reached. The 304A region analyzed in Figure 53 (b), which captures a broader length of mill scale, shows a fluctuating pattern of Fe and O contents, representing distinct transitions of compounds. Judging by the ratios of elements measured, the progression appears to be from an Fe_2O_3 at the outer scale to an Fe_3O_4 at the mid-region, transitioning then to a spinel of $(\text{Fe}, \text{Cr})_2\text{O}_3$ near the inner scale as the Cr content increases. Both 304A regions show relatively low Cr levels throughout most of the scale, exhibiting a gradual rise to form a wider, less concentrated (< 20 atomic %) Cr-rich region at the inner mill scale than that exhibited for the 316A. This lower Cr content in the 304A mill scale is interesting to note and could be the result of its larger grain size (shown in the optical micrographs in Figure 47 between the pickled 20M 304 and 316 bars) providing less grain boundary area for Cr diffusion. The lack of difference in chromium depletion levels observed at the mill scale/base metal interface between the two steels in Figure 50 and Figure 51 does not support this trend, however further EDS measurements of the mill scale/base metal interface would be needed to confirm. Mill scale thickness observed on the 304A rebar ranged from 1.5-7.5 μm .

In general the compositions of both the 316A and 304A mill scale were found to be primarily Fe and O based, with only localized regions of relatively high Cr content near the inner mill scale. This indicates how little Cr was lost from the bulk metal, and explains the low levels of Cr-depletion found by the EDS analyses of the bulk metal/mill scale interfaces in Figure 50 and Figure 51.

4.1.4.4 Raman Spectroscopy

Qualitative chemical analysis was performed on the 316 and 304 as-rolled rebar surfaces using Raman spectroscopy, with the resulting Raman spectra of each shown in Figure 54 and Figure 55, respectively. Characterization of the Raman peaks is shown in Table 13.

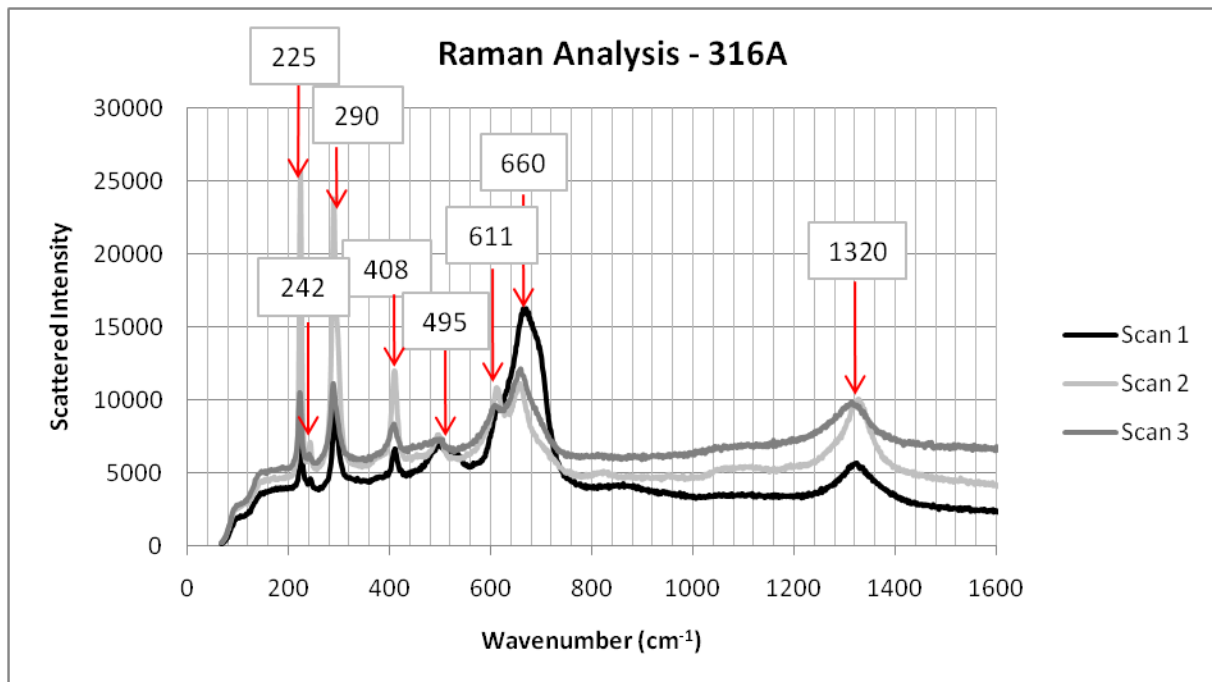


Figure 54: Raman analysis of 316A rebar surface

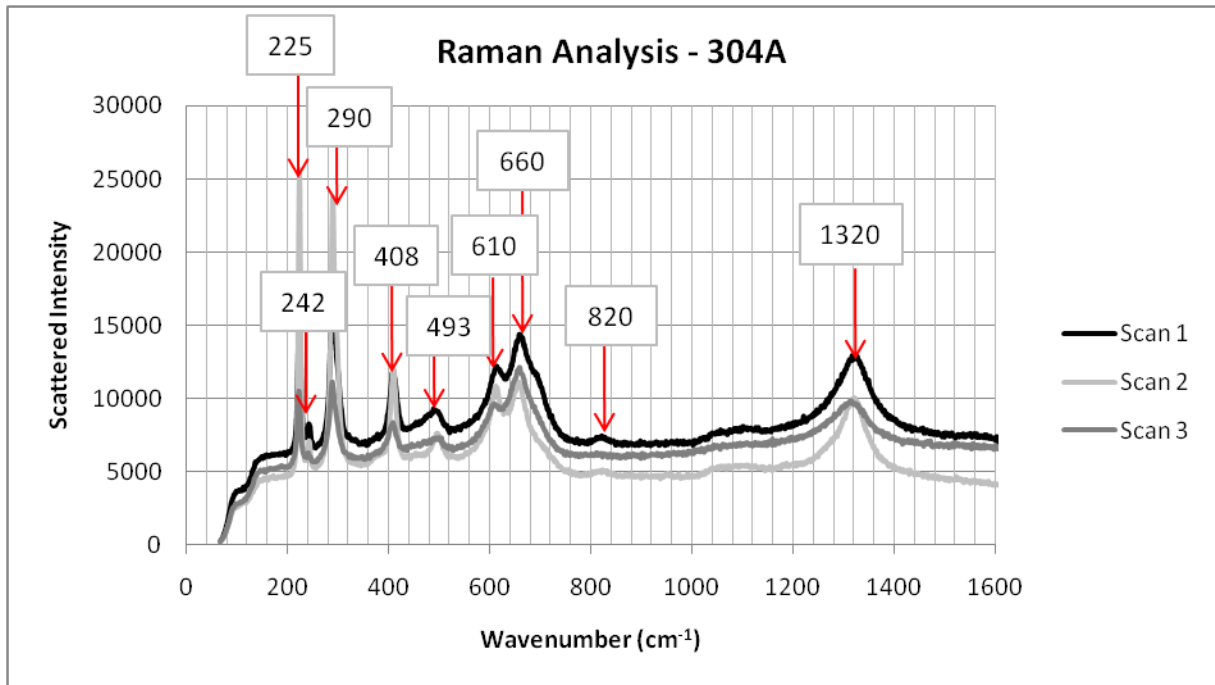


Figure 55: Raman analysis of 304A rebar surface

Table 13: Characterization of Raman peaks

Steel Type	Compound	Peak (cm ⁻¹)	Peak in Reference (Reference)
316A	Haematite (α - Fe ₂ O ₃)	225	226 (Oh, Cook et al., 1998), 227 (Thibeau, Brown et al., 1978), 225 (Ritter, Odziemkowski et al., 2002)
		242	245 (Thibeau, Brown et al., 1978; Oh, Cook et al., 1998; Ritter, Odziemkowski et al., 2002)
		290	292 (Oh, Cook et al., 1998), 293 (Thibeau, Brown et al., 1978), 295 (Ritter, Odziemkowski et al., 2002)
		408	411 (Oh, Cook et al., 1998), 414 (Thibeau, Brown et al., 1978), 415 (Ritter, Odziemkowski et al., 2002)
		611	612 (Oh, Cook et al., 1998), 612 (Thibeau, Brown et al., 1978), 615 (Ritter, Odziemkowski et al., 2002)
		1320	1320 (Ritter, Odziemkowski et al., 2002)
	Feroxyhite (δ -FeOOH)	495	unlabeled (Ohtsuka, 1996)
	Lepidocrocite (γ -FeOOH)	660	660 (Thierry, Persson et al., 1991)
	Maghemite (γ -Fe ₂ O ₃)	660	660 (Boucherit, Delichere et al.,

			1989)
	Cr ₂ O ₃	495	495 (Vuurman, Stufkens et al., 1990)
		611	609 (Beattie and Gilson, 1970)
304A	Haematite (α - Fe ₂ O ₃)	225	226 (Oh, Cook et al., 1998), 227 (Thibeau, Brown et al., 1978), 225 (Ritter, Odziemkowski et al., 2002)
		242	245 (Thibeau, Brown et al., 1978; Oh, Cook et al., 1998; Ritter, Odziemkowski et al., 2002)
		290	292 (Oh, Cook et al., 1998), 293 (Thibeau, Brown et al., 1978), 295 (Ritter, Odziemkowski et al., 2002)
		408	411 (Oh, Cook et al., 1998), 414 (Thibeau, Brown et al., 1978), 415 (Ritter, Odziemkowski et al., 2002)
		610	612 (Oh, Cook et al., 1998), 612 (Thibeau, Brown et al., 1978), 615 (Ritter, Odziemkowski et al., 2002)
		1320	1320 (Ritter, Odziemkowski et al., 2002)
	Feroxyhite (δ -FeOOH)	493	unlabeled (Ohtsuka, 1996)
	Lepidocrocite (γ -FeOOH)	660	660 (Thierry, Persson et al., 1991)
	Maghemite (γ -Fe ₂ O ₃)	660	660 (Boucherit, Delichere et al., 1989)
	Cr ₂ O ₃	493	495 (Vuurman, Stufkens et al., 1990)
		610	609 (Beattie and Gilson, 1970)

The Raman spectra for both the 316A and 304A surfaces were very similar, showing primarily iron oxides and hydroxides, with possibly some chromium oxide as well. Bearing in mind that Raman sampling depth is generally $\leq 1 \mu\text{m}$, this agrees with the predominant Fe and O composition of the outer mill scale found from the EDS analysis in the previous section.

4.1.5 Visual Examination of Autopsied G109 Specimens

One G109 specimen of each steel/surface/bottom bar type (ten in total) was broken open at 500-600 days after casting to autopsy the embedded bars and examine their surface conditions. Upon removing them from the concrete, they were immediately photographed in order to document any corrosion products before given the chance to react and transform in the atmosphere (i.e. black rust

oxidizing to brown rust). Surface images of the bars before exposure, and the top/bottom sides of the top bar as well as the bottom bars after exposure are shown for 316A, 316P, 304A, 304P and 2205P in Figure 56, Figure 57, Figure 58, Figure 59 and Figure 60, respectively.





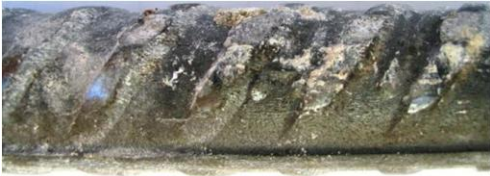

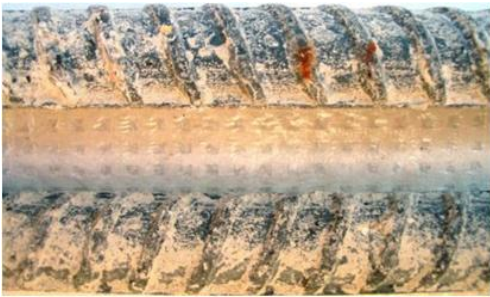
316A Before Exposure		
Specimen	316A S1	316A B4
Top of Top Bar After Exposure		
Bottom of Top Bar After Exposure		
Bottom Bars After Exposure		

Figure 56: Surface images of 316A G109 bars before and after exposure

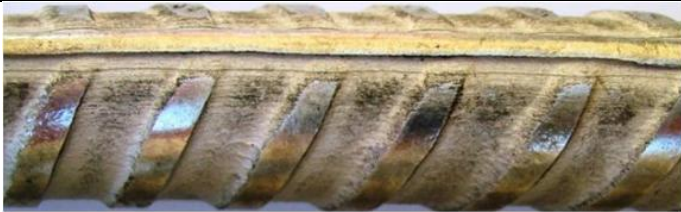
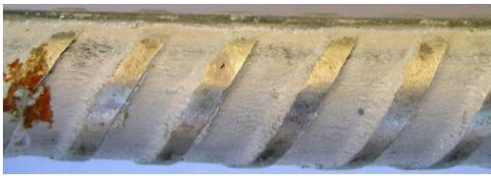




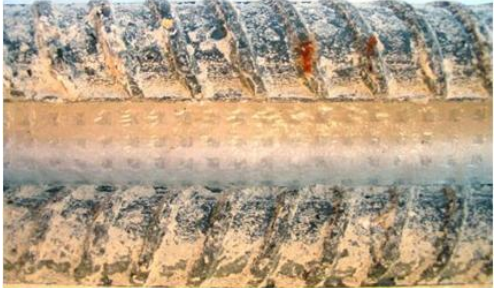



316P Before Exposure		
Specimen	316P S2	316P B5
Top of Top Bar After Exposure		
Bottom of Top Bar After Exposure		
Bottom Bars After Exposure		

Figure 57: Surface images of 316P G109 bars before and after exposure

304A Before Exposure		
Specimen	304A S2	304A B4
Top of Top Bar After Exposure		










Bottom of Top Bar After Exposure		
Bottom Bars After Exposure		

Figure 58: Surface images of 304A G109 bars before and after exposure

304P Before Exposure		
Specimen	304P S3	304P B1
Top of Top Bar After Exposure		
Bottom of Top Bar After Exposure		

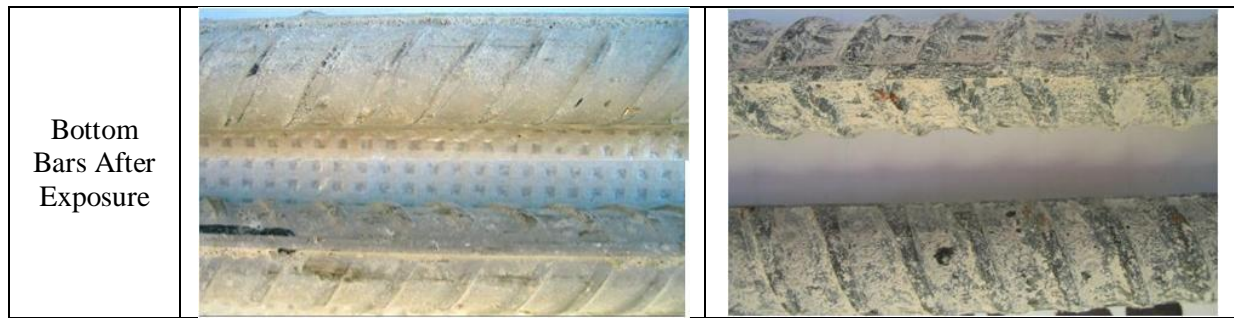


Figure 59: Surface images of 304P G109 bars before and after exposure

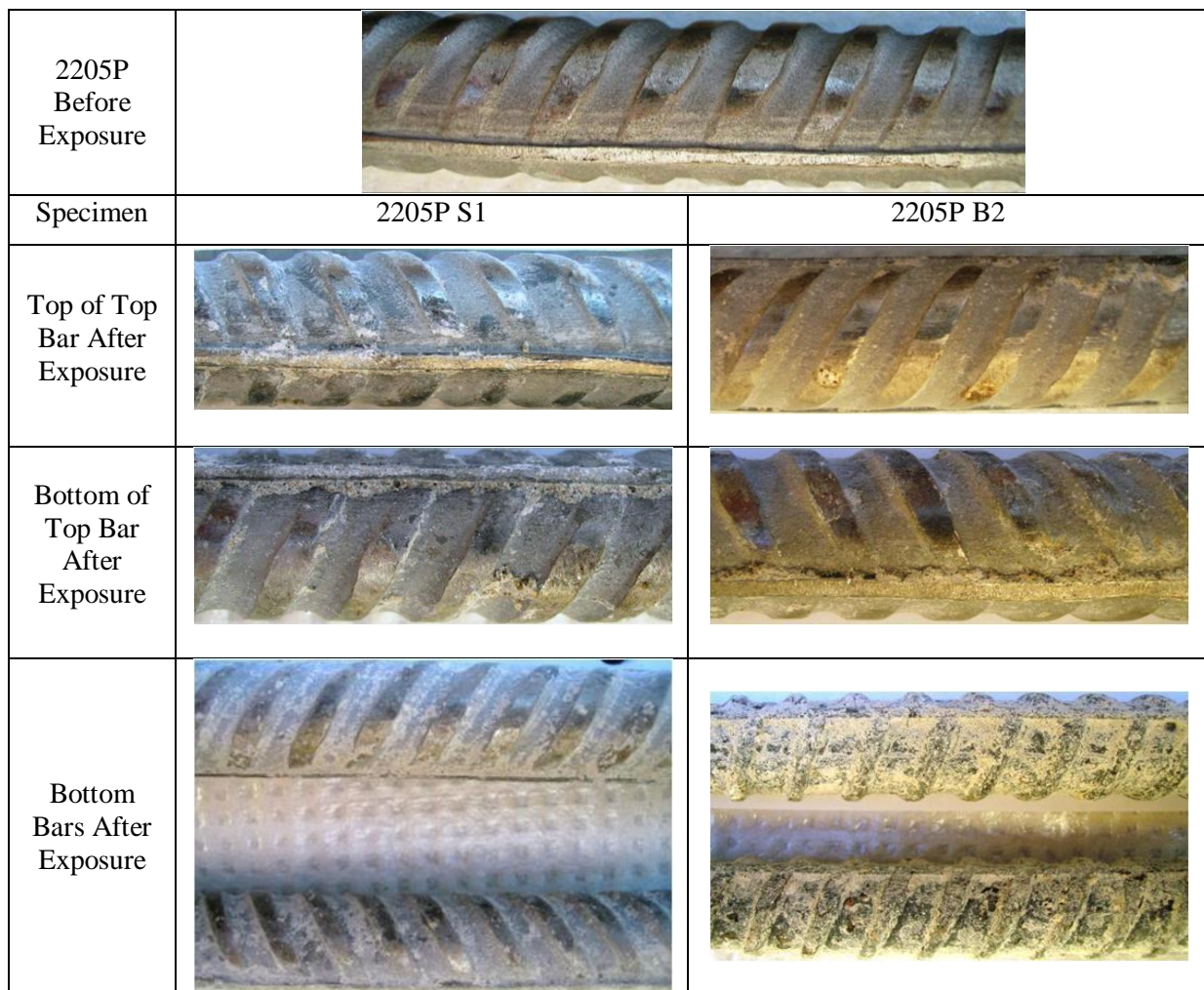


Figure 60: Surface images of 2205P G109 bars before and after exposure

The as-rolled top bars exhibited noticeable superficial rusting along just their top surfaces (i.e. closest to the ponding well), whereas the bottom surfaces of the top bars exhibited no signs of rust

despite being surrounded by the same highly chloride contaminated concrete. Previous study (Mammoliti and Hansson, 2007) of as-rolled rebar in concrete contaminated with 5% Cl⁻ by weight of cement (compared with 7.5% in this study) did not show the development of any corrosion products on the surface after exposure for ~550 days. The limitation of the corrosion strictly on the top half of the top rebar was due to greater moisture presence at this region, which in turn was due the bleeding of the concrete. After concrete mixing and once the concrete is cast into place, the higher density cement and aggregate particles tend to sink, leaving a larger proportion of the water near the upper surfaces, including directly below reinforcement surfaces. Given that the G109 specimens were cast upside down, a higher water/cement ratio would thus be present at the top surface of the top bar, increasing chloride concentration and decreasing the ionic solution resistance along that surface. While the 7.5% admixed Cl⁻ by weight of cement is much higher than the threshold for corrosion of black steel in concrete of ~0.5-2% admixed Cl⁻ by weight of cement reported found in literature (Glass and Buenfeld, 1997), if 7.5% does in fact exceed the chloride threshold of the as-rolled stainless steel bars in concrete than this may be an indication that, under extremely aggressive environments, pickling of the rebar is necessary. While no known studies have been found to report such high chloride concentrations in existing in structures, core samples taken from the oldest stainless steel reinforced structure, Progreso Pier in Yucatan, Mexico, were found to contain 0.6-1% Cl⁻ by dry weight of concrete after 60 years of exposure to the aggressive marine conditions in the Gulf of Mexico (Arminox, 1999). Assuming the concrete mix proportions were equivalent to those used in this project, this equates to 4-6% Cl⁻ by weight of cement. As discussed in Section 2.1.3.1, chlorides such as these that have diffused in over time are more detrimental to rebar compared to an equivalent admixed amount because of chlorides binding to the C₃A in freshly mixed concrete. As a result, the free chlorides in the Pier Progreso concrete pore solution could very well be near levels of chloride saturated pore solution used in this project. The high chloride levels measured here are subject to skepticism however, since it has been shown (Byfors, Hansson et al., 1986) that over long periods, concrete pore solution composition and external environmental composition should reach equilibrium, which could only bring the pore solution concentration to the levels in the ocean of ~3% Cl⁻. Furthermore, chloride contents in concrete structures in Ontario that have been exposed to de-icing salts typically reach no higher than 0.43% Cl⁻ by weight of concrete (McCormick_Rankin_Corporation, 2008), which translates to 2.9% Cl⁻ by weight of cement assuming equivalent concrete mix proportions. Just from the superficial corrosion observed on the as-rolled bars in this project it is not entirely clear if, in fact, the chloride threshold was exceeded, and

certain factors must be considered. Though the corrosion rates measured for the as-rolled bars were high in comparison with pickled, they were not as high as $\sim 10^{-2}$ A/m² typically found for actively corroding black steel in concrete of lower chloride levels, as discussed in Section 2.2.3.

The autopsied 304A B4 top bar was further examined by removing the corrosion products in a solution of 1:10 dilute nitric acid at 60°C (ASTM-G1-03, 2003), and measuring the depth loss at the most damaged areas. The top and bottom surfaces of the 304A B4 top bar upon being removed from the concrete (before corrosion products were removed) are shown in Figure 61 and Figure 62, respectively, and the top surface of the bar after removing the corrosion products, along with the depth loss analysis, is shown in Figure 63.

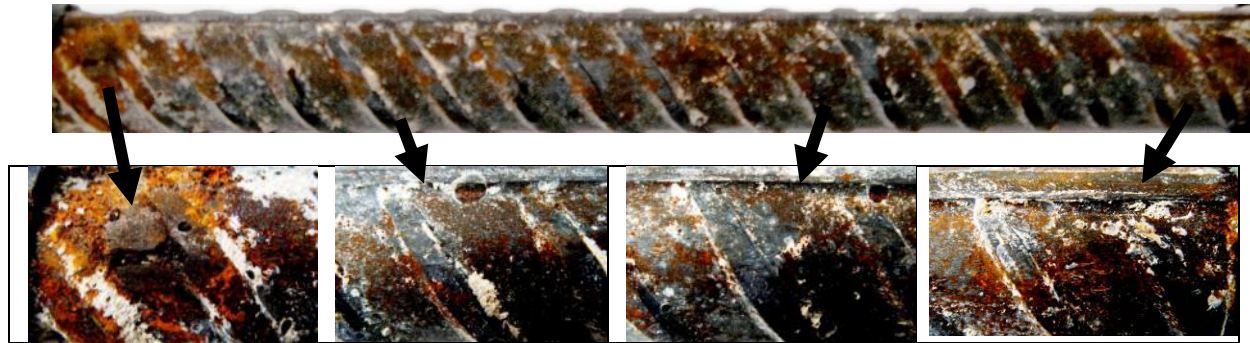


Figure 61: Top surface of 304A B4 top bar upon removal from concrete.

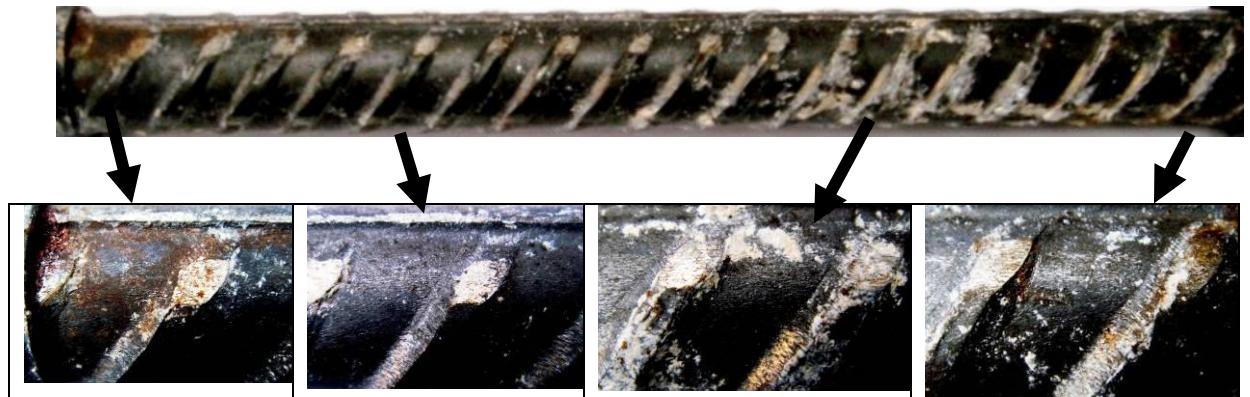


Figure 62: Bottom surface of 304A B4 top bar upon removal from concrete

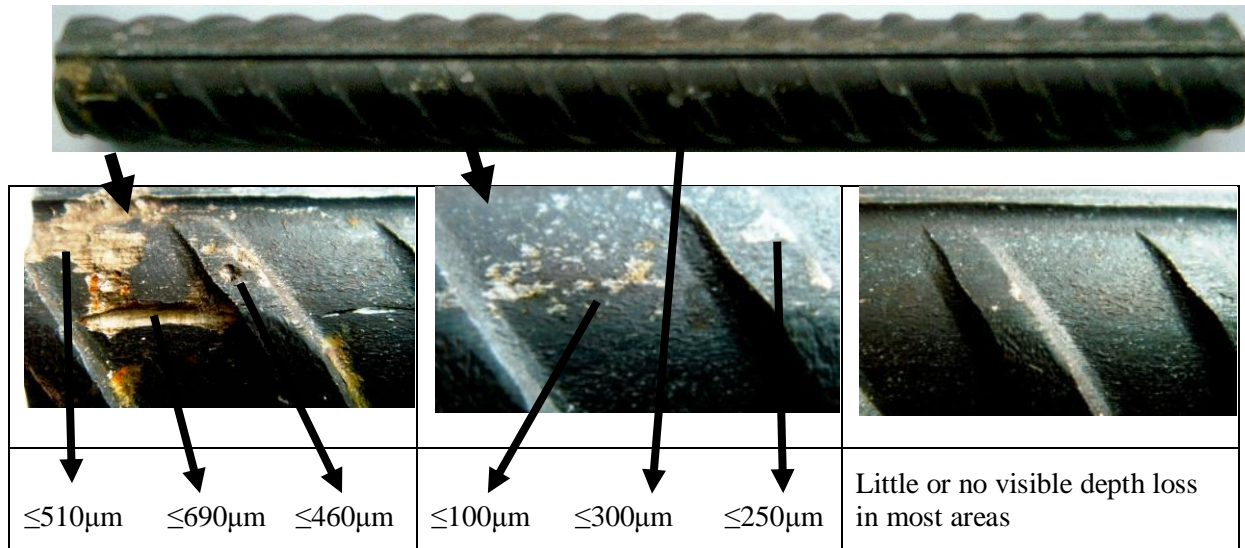


Figure 63: Appearance and depth loss analysis of 304A B4 specimen after removing corrosion products

The removal of the corrosion products revealed only a select few spots across the entire bar of noticeable depth loss, shown in Figure 63, with the majority of the bar appearing undamaged. Of the damaged areas, the regions of highest depth loss occurred at the bar's end near the epoxy interface. The majority of corrosion products observed on all other as-rolled bars that were autopsied were found in this region as well. The crevice corrosion cell formed between the epoxy/steel interface would have initiated the corrosion found here, and the fact that this situation would not be encountered in a real structure skews the as-rolled rebar corrosion rates measured in this project. Given that bar ends show the regions of highest corrosion, the corrosion rates to be expected without the crevice effect of the epoxy coating would be significantly lower and the difference in corrosion rates between the as-rolled and pickled bars would be much less. The long, narrow gouge in the left-most region of Figure 63 originated from a knife mark left on the bar's surface during its preparation before casting. The mark was originally smaller like the parallel mark directly to its right, but the surface imperfection was large enough to act as a preferred initiation site in forming a crevice corrosion cell with the adjacent steel, and resulting in relatively large depth loss. The middle of the bar encountered very little visible depth loss in comparison, with two crater-shaped inclusions originating at the ribs having a maximum depth loss of 250-300 μm , and a region of localized corrosion having a maximum depth loss of 100 μm . Given the rebar's original 20 mm diameter, the non-crevice-induced corrosion at the bar's mid-section caused maximum cross-sectional loss of 1.5%. Note that this was localized, with the majority of the bar's length experiencing no detectable cross-

sectional loss. To put this amount into context, one study (Treadway, Cox et al., 1989) observed local cross-sectional losses of 10% and 25% for black steel rebar in concrete admixed with 0.96 and 3.2% Cl by weight of cement, respectively, after only one year of exposure (compared with the 7.5% used in the present project and a period of two years).

Another consideration is that the brown corrosion products observed on the top rebar underwent no change in colour upon breaking open the specimens, as typically occurs on actively corroding rebar when removed from concrete (i.e. black or green rust to brown), indicating that these products may have formed earlier at higher corrosion rates, gradually subsiding over time. This seems especially true when considering the lack of change and/or more passive development of the corrosion currents and potentials over time, with the highest corrosion currents measured also being the initial measurements taken across the macrocell connection at 5 days after casting, and eventually decreasing over an order magnitude by 400 days. This is the opposite of what one would expect to see in a real structure, where as chlorides gradually diffuse to the rebar surface over time, an increase in corrosion currents would occur. The initially high macrocell currents may be the result of an initially high ionic conductivity in the concrete after casting, which gradually decreases as cement proceeds to hydrate and remove the “free” water (Holly, Reardon et al., 2007). A peak in corrosion rates of stainless steel rebar in chloride contaminated concrete at the beginning of exposure has also been observed in previous research (García-Alonso(a), M.L.Escudero et al., 2007).

Very little corrosion was observed on the pickled specimens, except for some isolated superficial rust spots initiating at the ribs, such as those shown for pickled 316 in Figure 57. Preferential initiation of corrosion at these spots likely occurs due to their irregular geometry that promotes the formation of corrosion cells, and also since these areas experiences the largest degree of deformation, a greater likelihood of stress cells exists. Another cause for small isolated corrosion spots would be the propagation of localized corrosion cells at imperfection and/or contamination sites present on the rebar surface prior to casting. The white, bubble-like formations shown on the 304P S3 top bar in Figure 59 as well as the whitish-grey residue on several other bars is adhered cement paste.

No significant rusting was observed on the bottom bars, except for a few small isolated spots on the as-rolled and black steel bars originating at the ribs. The cement paste adhered to the black steel surface to a much greater degree than to either the pickled or as-rolled stainless, similar to previous observations (Mammoliti and Hansson, 2007). It is believed by the author that the rougher surfaced black steel provides greater surface heterogeneities that allow for better absorption of the cement

paste onto its surface as opposed to the smoother stainless steel surface that provides less irregular surface features for the cement paste to bond to.

4.2 Loading Conditions

4.2.1 Crack Widths

At the end of the measurement period, the maximum observable crack widths of all beams were measured for comparison using a crack comparator, as shown in Figure 64, and the results are shown in Table 14. The crack widths of the dynamically loaded beams were measured with loading disengaged. The fluctuation of the crack widths on the dynamically loaded beams during cyclic loading was not measured, but given the relatively larger sized cracks already present on these beams when unloaded, this felt unnecessary.

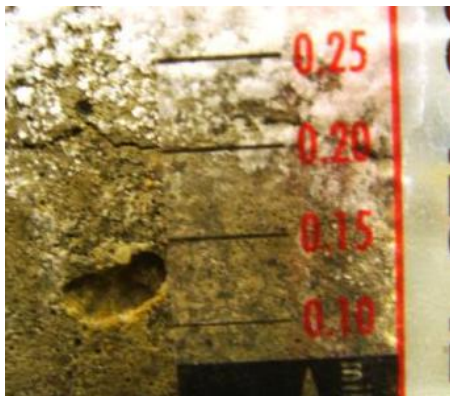


Figure 64: Crack width measurement using a crack comparator

Table 14: Maximum crack widths of loaded beams at the end of measurement period

Specimen		Max. Crack Width (mm)	Crack Location
2205SL	a	0.15	Salt covering fulcrum, crack measured above
	b	0.2	Salt covering fulcrum, crack measured above
316SL	a	0.2	Fulcrum
	b	0.3	Fulcrum
2205SH	a	-	Salt covering fulcrum, no cracks >100µm
	b	0.3	Fulcrum
316SH	a	0.3	Fulcrum
	b	0.1	Salt covering fulcrum, crack measured above

2205DL	a	0.3	Fulcrum
	b	0.3	Fulcrum
316DL	a	-	Salt covering fulcrum, no cracks >100µm
	b	1.0	Fulcrum
2205DH	a	0.3	Fulcrum
	b	0.35	Fulcrum
316DH	a	0.6	Fulcrum
	b	0.8	Fulcrum

The majority of the maximum crack widths were located directly at the fulcrum region (beam's mid-section), however many beams were covered with thick, strongly adherent salt residue in this area on account of the salt solution being filled to the fulcrum during the wet cycle. As a result, the view of this region on many beams was obstructed, with cracks only observable in other areas, as specified in the crack location of Table 14. The maximum crack widths should therefore be distinguished as the maximum *observable* crack widths, since the fulcrum of many beams likely contains larger cracks hidden by the strongly adherent salt deposits. In any case, most beams exhibited crack widths above the 0.1 mm obtained in the study by Mendoza (2003) on the corroding 316 stirrup wire, as well as above 0.05 mm which, as discussed in Section 2.2.6, the rate of chloride diffusion into concrete rapidly increases; therefore the crack widths sizes were sufficient to allow rapid chloride penetration to the rebar surfaces. Only two beams exhibited no observable crack widths >100 µm, though they were likely hidden beneath the adherent salt deposits at the fulcrum.

Larger cracks were observed in the dynamically loaded beams compared with the statically loaded beams. Previous study (Raju, 1970) has found greater numbers of micro-cracks to develop under conditions of the former compared to the latter, which would provide greater probability for large cracks to develop under similar deflection magnitudes. Other research has also found larger crack widths in concrete beams to form under dynamical loading compared with static loading (Jaffer and Hansson, 2008). Cracks in statically loaded beams also are also capable of self-healing when exposed to water for extended periods of time due to filling of the cracks with hydration products, corrosion products and/or debris (Jacobsen, Marchand et al., 1996), which would further account for the difference in observable crack sizes between the statically and dynamically loaded beams.

4.2.2 Linear Polarization Resistance

Corrosion current densities obtained by LPR for 316 and 2205 steel type loaded beams are shown in Figure 65 and Figure 66, respectively. Values for the dynamically loaded beams are plotted in black and for statically loaded beams plotted in grey. The solid plots indicate concretes of relatively lower strength versus the dashed plots indicating higher strength concretes. The area used for the current densities was found by determining the polarized length of the beam when applying 20 mV at the beam's mid-section (i.e. the distance from the mid-section at which the beam is no longer polarized represents area not affected by the LPR measurements and thus should not be include in the current densities). The length/area of polarized beam was found to be 0.66 m/0.033 m², assuming uniform polarization around the bar's circumference, and the analysis is shown in Appendix L.

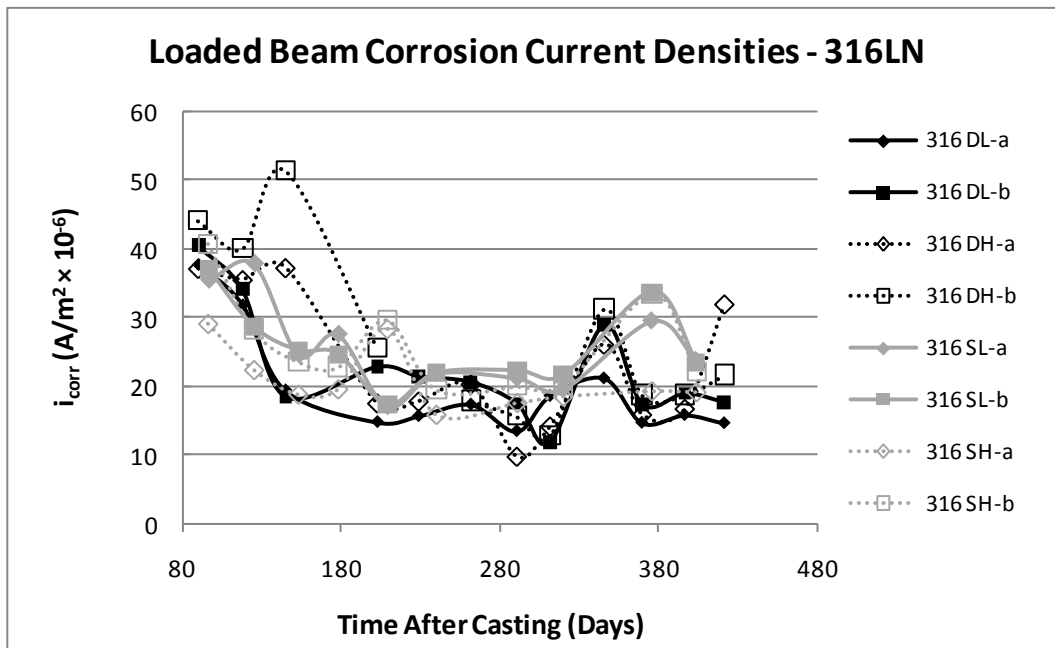


Figure 65: Corrosion current densities of 316 steel type loaded beams obtained by LPR

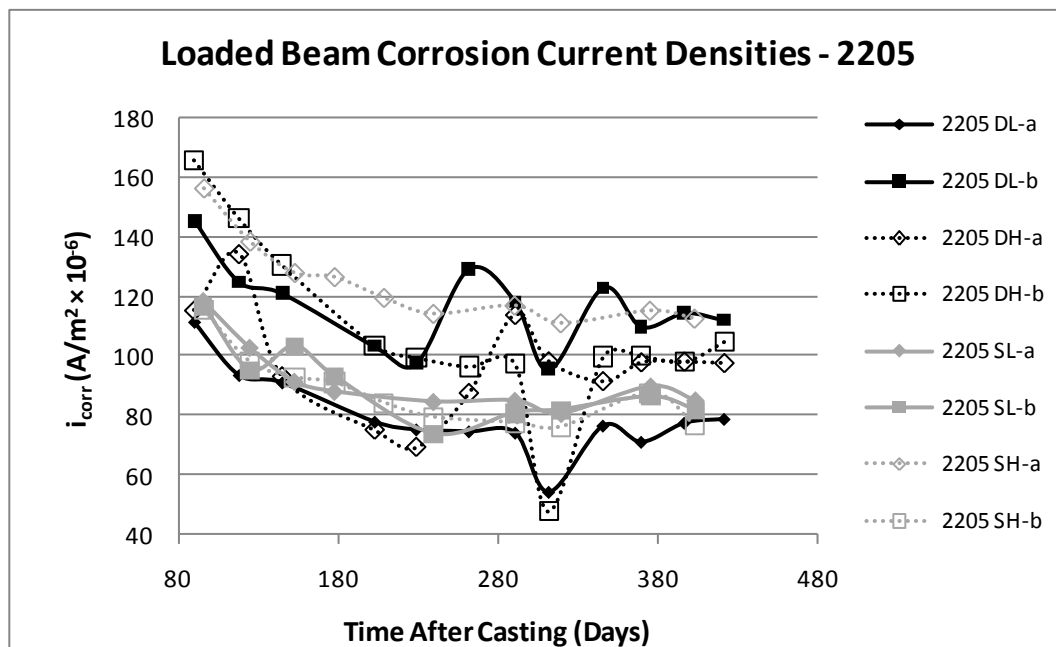


Figure 66: Corrosion current densities of 2205 steel type loaded beams obtained by LPR

The corrosion current densities obtained for both 316 and 2205 bars were very low, on the order of 10^{-5} to 10^{-4} A/m², and were similar to those obtained for the pickled bars in the G109 prisms. As with the G109 specimens, the 2205 specimens exhibited approximately 5× higher corrosion current densities than the 316 bars, indicating the relative passive corrosion characteristics of pickled 316 and 2205 in chloride contaminated concrete are not overly influenced by the degree of chloride contamination or specific characteristics of the concrete. There is no clear distinction in corrosion current densities between the different loading types of either steel, especially considering the scale used to present these results is linear and, thus, not wide-ranging in the context of significant differences in corrosion rates (i.e. all corrosion rates shown in these scales are very low). Jaffer (2008) found a similar lack of distinction in the corrosion performance of black steel rebar in concrete under different loading types. Also no clear distinction in corrosion rates between the different concrete strengths used in the present project were found; however this should not be confused with the case of OPC versus HPC concretes, for which corrosion rate differences of embedded rebar between the two have been well documented (Hansson, Poursaee et al., 2006; Jaffer and Hansson, 2008).

Difficulty has been reported (Feliu, Gonzalez et al., 1996) in providing accurate estimates of low corrosion rates in passive reinforcement of relatively large reinforced structures, due to the tendency

of the current to spread far away from the application point as a result of the high polarization resistance it encounters. In contrast, a metal of low polarization resistance that is actively corroding can efficiently confine the current to the corroding surface area. While the loaded beam in this experiment has an exposed rebar area much larger than that in the G109 prisms, the fact that both specimens types gave similar corrosion current densities for the same steels confirms that the amount of polarized area determined in Appendix L is reasonable and that the loaded beams are not too large for obtaining accurate corrosion rate measurements.

4.2.3 Corrosion Potentials

Results of the corrosion potential measurements for the 316 and 2205 steel type loaded beams are shown in Figure 67 and Figure 68, respectively.

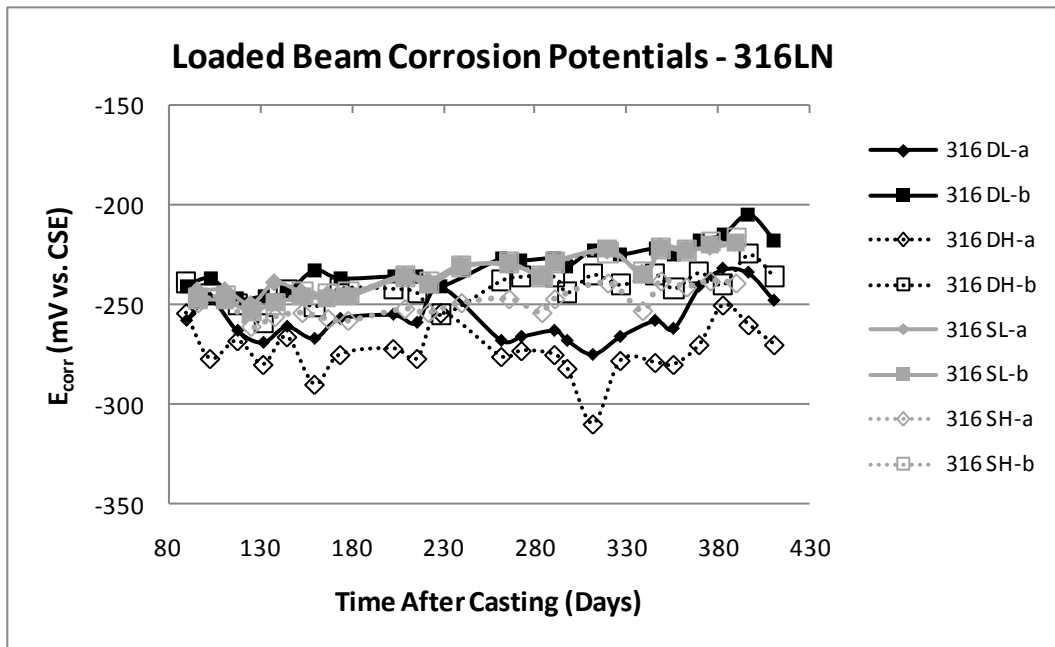


Figure 67: Corrosion potentials of the 316 steel type loaded beams

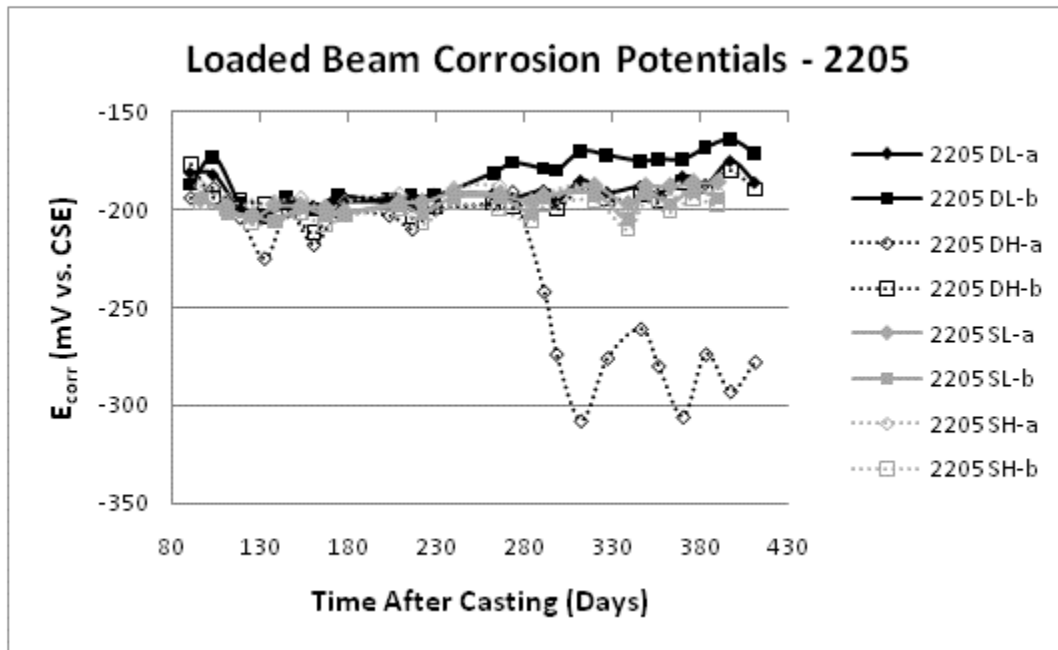


Figure 68: Corrosion potentials of the 2205 steel type loaded beams

As with the loaded beam corrosion current densities, the corrosion potentials showed little variation among the different loading types and concrete strengths. One noticeable trend is that the dynamic beams tended to exhibit greater fluctuations, suggesting that the steel’s passive surface characteristics may be somewhat less stable from the micro-motion of the concrete at the crack-steel interface. The corrosion potentials for 2205 and 316 steel types were in the range of -150 to -200 mV vs. CSE and -200 to -250 mV vs. CSE, respectively, and similar to those measured for the G109 top bars. A noticeable outlier, 2205 DHa, exhibited an abrupt and sustained drop in corrosion potential at ~250 days which is attributed to an erroneous cyclic polarization scan performed at that time where a large cathodic potential (-250 mV vs. E_{corr}) was applied to the bar. Despite this significant drop in corrosion potential, its corrosion current density, shown in Figure 66, has remained stable and similar in value to the other 2205 specimens.

4.2.4 Cyclic Polarization

Cyclic polarization scans performed on one specimen of each loading/concrete type are plotted for the 316 and 2205 steels in Figure 69 and Figure 70, respectively.

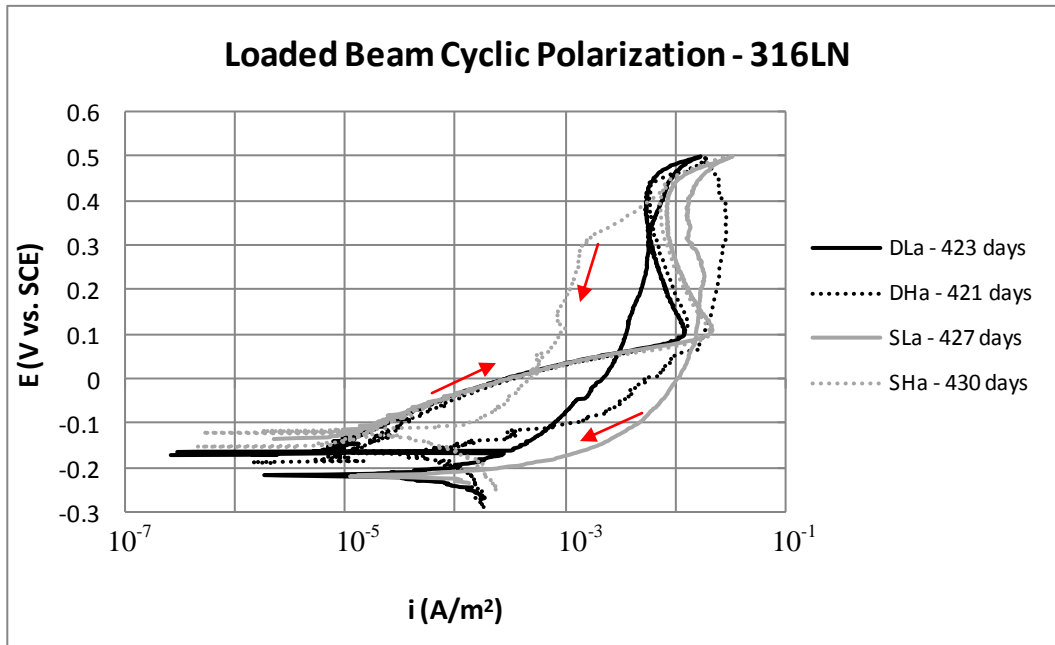


Figure 69: Cyclic polarization curves for 316 steel type loaded beams

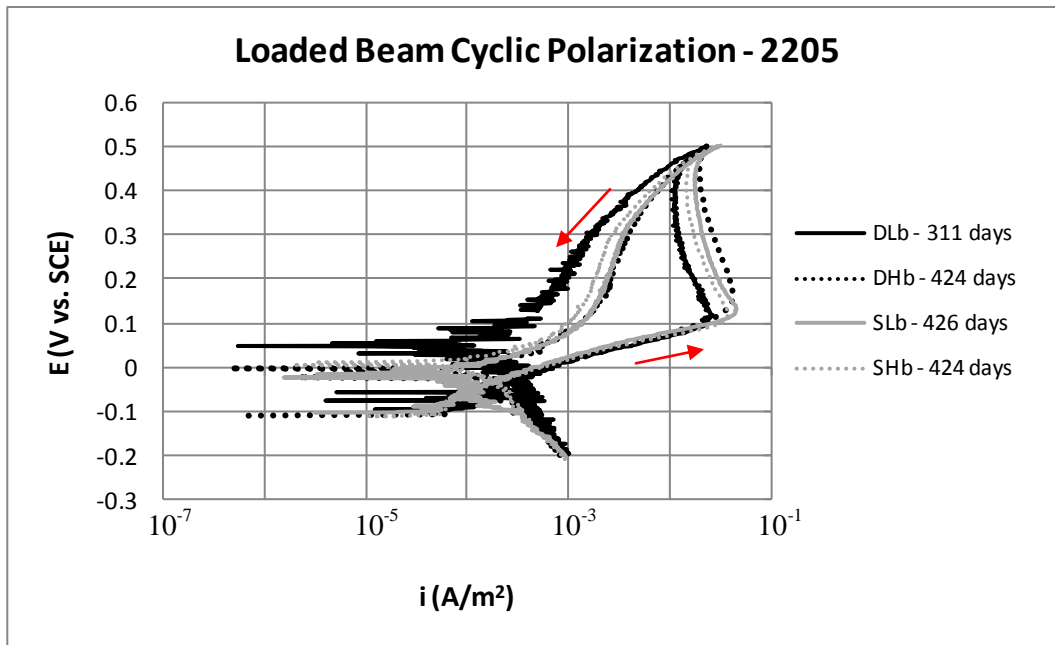


Figure 70: Cyclic polarization curves for 2205 steel type loaded beams

All CP curves exhibited consistent corrosion current densities at E_{corr} with those measured via LPR, and corrosion potentials corresponding to the upper limit of thermodynamic stability of Cr_2O_3 . As an increasing anodic potential is applied, the Cr_2O_3 dissolves and the Fe/Ni spinel Fe_2NiO_4 is probably

the protective species. The CP curves of the 316 show a mixed behaviour: the bars in the DLa, DHa and SLa beams all exhibited more positive currents on the downward scan, more negative anodic to cathodic corrosion potentials, and, thus, a breakdown of the surface film; in contrast, the SHa exhibited a decrease in current on the downward scan, representing an increase in protection of the surface film. The CP curves for the 2205 were much more consistent, showing for all specimens a decrease in currents on the downward scan and thus a more protective surface film. Neither set of CP curves provided any evidence suggesting the dynamically loaded beams are inferior to the statically loaded beams in terms of corrosion resistance.

4.2.5 Electrochemical Noise

Electrochemical current noise (ECN) measurements between the loaded beam pairs were performed at 150 days after casting during the ponding cycle to provide an electrically conductive path between the two beams. Measurements for the dynamically loaded beams were taken while cyclic loading was off, and the results for the 316 and 2205 steel types under both loading conditions are shown in Figure 71 and Figure 72, respectively. The standard deviations of the noise measurements obtained over the ~350 second time interval were plotted in Figure 73.

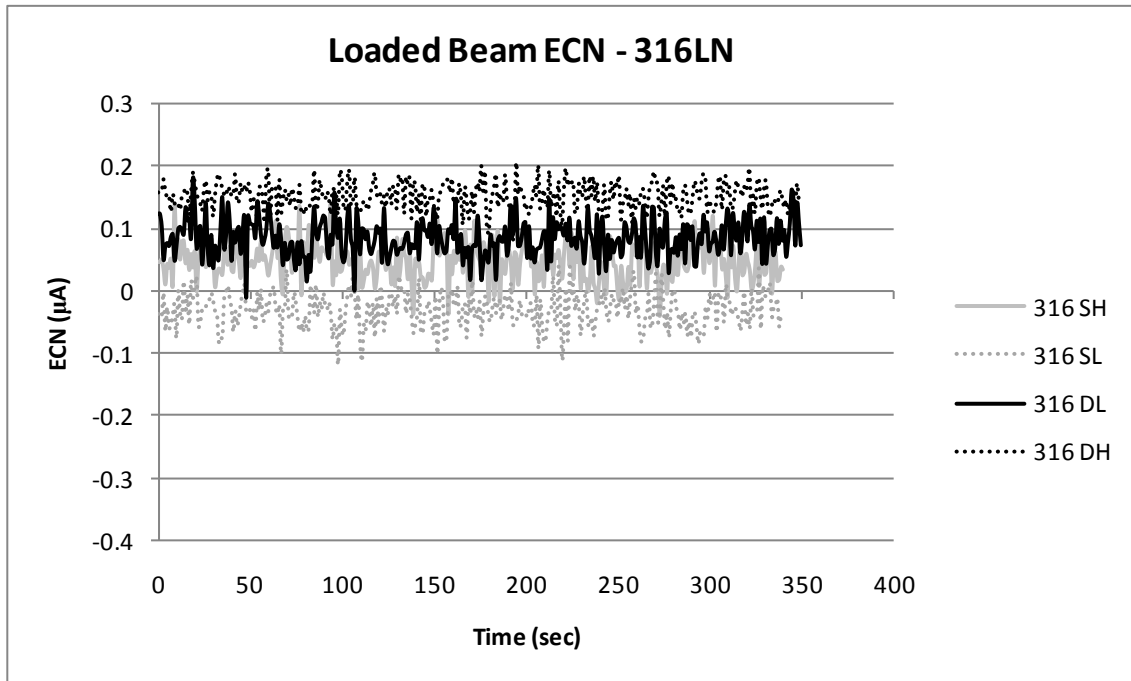


Figure 71: ECN measurements for 316 steel type loaded beams at 150 days after casting

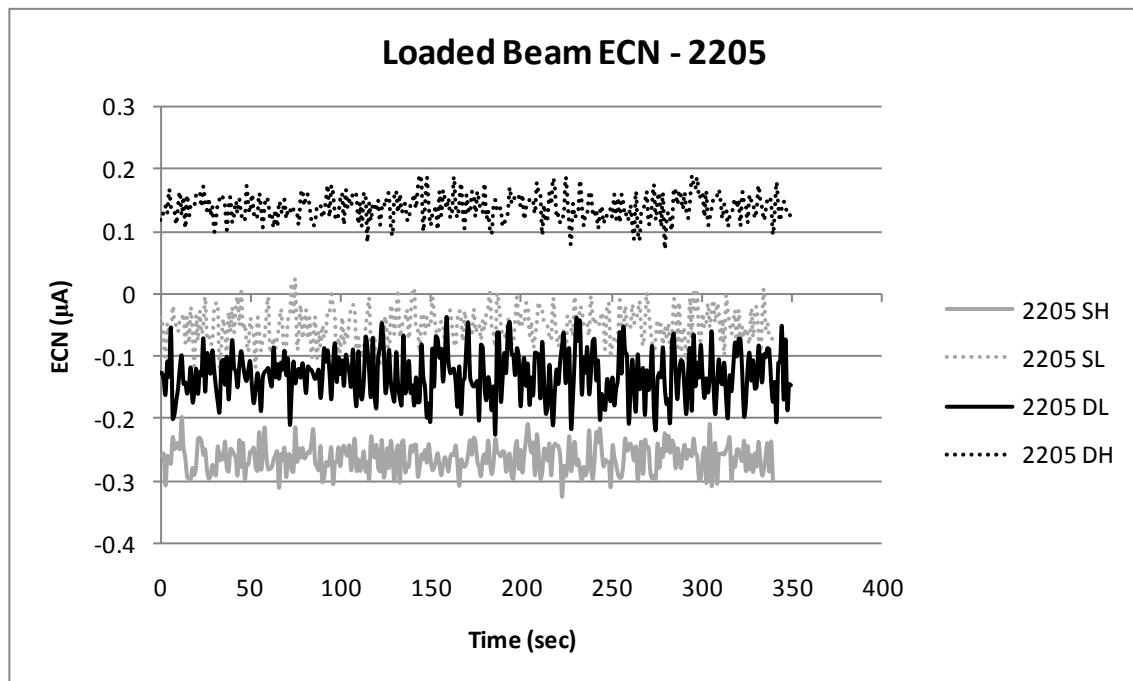


Figure 72: ECN measurements for 2205 steel type loaded beams at 150 days after casting

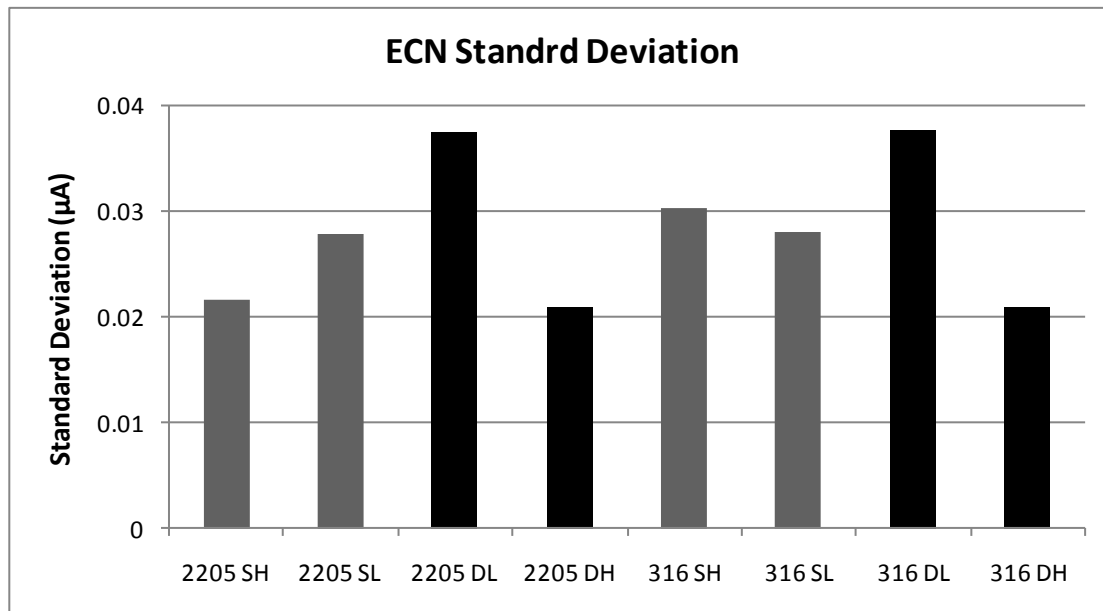


Figure 73: Standard deviation of ECN noise measurements at 150 days after casting

ECN results showed no trend between the different loading types, and the steel types themselves exhibited similar ranges in values. The only noticeable trend is the higher overall ECN fluctuations for the lower strength beams. This could be the result of lower ionic resistivity of the more porous, low strength concretes, as well as the more extensive cracking in concretes of lower strength attributed to their greater interconnected porosity at the interfacial zone between the aggregate and cement paste (Nemati, Monteiro et al., 1998).

At 200 days after casting, ECN measurements were taken on the dynamically loaded beams while cyclic loading was on, in case there were differences in the corrosion performance of the dynamically loaded beams present only at the time of loading that did not remain when cyclic loading was off. A plot of the ECN measurements, their standard deviations, and a magnification of the ECN plot are shown in Figure 74, Figure 75 and Figure 76, respectively.

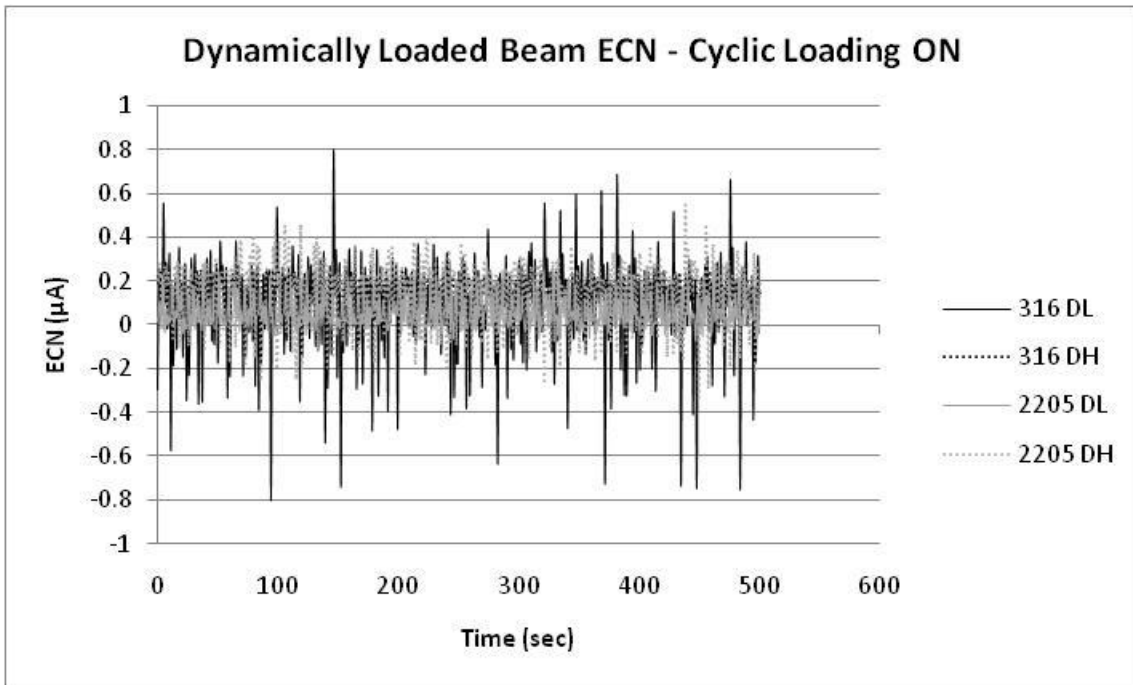


Figure 74: ECN measurements of dynamically loaded beams with cyclic loading applied at 200 days after casting

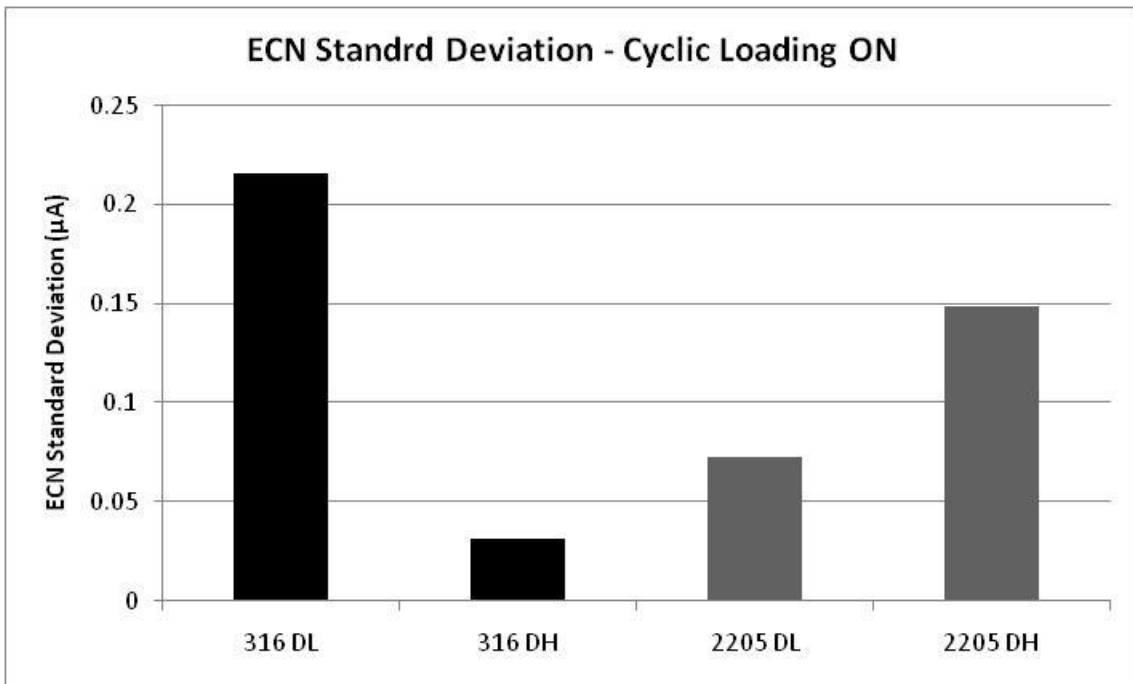


Figure 75: Standard deviation of dynamically loaded beam ECN measurements at 200 days with cyclic loading applied

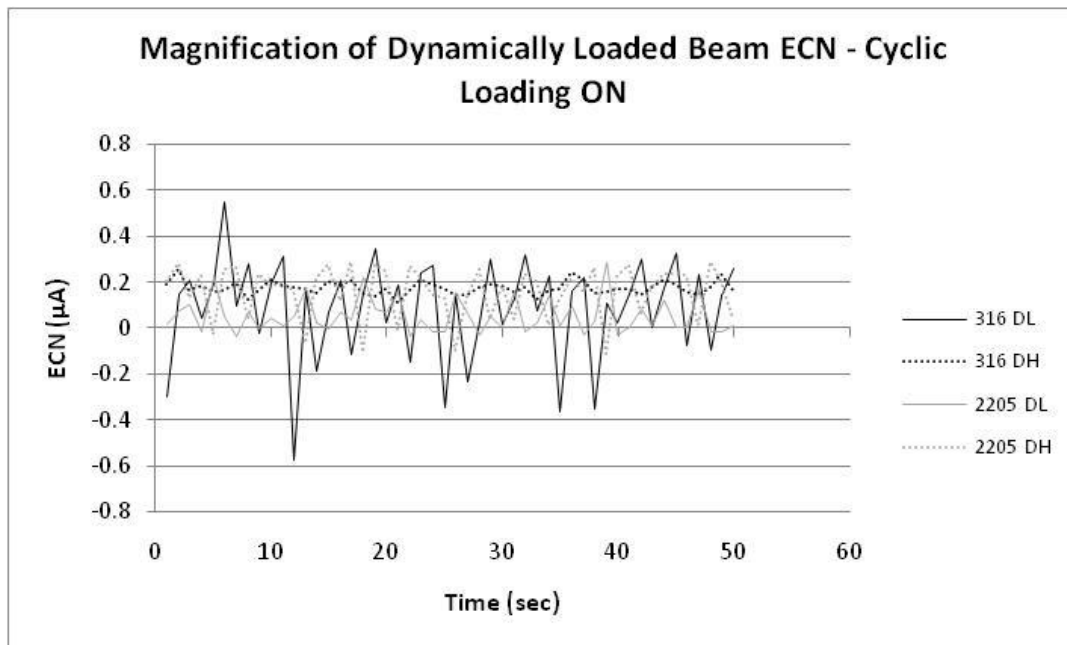


Figure 76: Magnification of ECN measurements of dynamically loaded beams with cyclic loading applied at 200 days after casting

ECN measurements of the dynamically loaded beam with cyclic loading on revealed on average much larger current activity, exhibiting fluctuations reaching as high as $0.8 \mu\text{A}$ compared those consistently $< 0.1 \mu\text{A}$ exhibited with cyclic loading off. Accordingly, this translated into much higher standard deviations of the noise values as well, shown in Figure 75. These higher values suggest that dynamic loading does have some effect on the corrosion performance of the bar at the time of loading, though it is difficult to correlate what effect this increase in noise has on the long-term corrosion resistance of the structure. The magnified image of the ECN measurements in Figure 76 shows a random, sporadic current profile rather than isolated current transients typically found in ECN measurements of pitting corrosion, where breakdown and subsequent repair of passive film are represented by distinct peaks that gradually decreases to the mean current noise values (Weiermair, Hansson et al., 1996; Jaffer and Hansson, 2008). The shape of the ECN profile in Figure 76 may be accounted for by an erosion corrosion mechanisms rather than pitting corrosion, where the passive film is essentially absent during the load cycling due to the constant micro-motion of the concrete causing abrasion of the steel surface at the crack region, leaving the unprotected steel layer beneath vulnerable to uniform corrosion attack. It is only when cyclic loading is off, as shown by the passive, non-distinct results of the LPR, corrosion potential, and cyclic polarization measurements, where the protective surface film becomes stable once again and the passive characteristics are restored.

Chapter 5

Summary, Conclusions & Recommendations

5.1 Summary & Conclusions

5.1.1 Surface Conditions

- After >600 days exposure to concrete admixed with 7.5% Cl⁻ by weight of cement, the as-rolled stainless steel rebars exhibited higher macrocell and microcell corrosion current densities of 10⁻⁴ and 10⁻³ A/m², respectively, compared to those of the pickled stainless steel in the range of 10⁻⁶ – 10⁻⁵ and 10⁻⁵ – 10⁻⁴ A/m², respectively. However, no increase was observed in either values, with a decrease in macrocell current densities in the as-rolled bars, and all remaining well below the 10⁻² A/m² typically found for actively corroding plain carbon-steel reinforcement.
- Corrosion current densities measured when polarized by connection to the bars in chloride-free concrete (macrocell connected), a possible state of rebar in a concrete bridge deck, resulted in a relative increase in microcell corrosion current densities only for the austenitic pickled stainless steels. This reduces the difference in microcell corrosion rates between the pickled and as-rolled bars from ~50× (obtained in the depolarized state) to only ~10×, indicating that as-rolled stainless steels rebar microcell corrosion rates would be even closer to those of pickled stainless steel in structures where macrocell connections are present.
- No dramatic fluctuations in corrosion potentials for both the top and bottom bars were observed over the 100-600 day measurement period, indicating no significant/detectable changes in corrosion states occurred during this time. Plain carbon-steel bottom bars exhibited corrosion potentials more positive than the stainless steel bottom bars, indicating that insufficient chlorides had diffused down to the bottom bars to disrupt their passive state.
- Cyclic polarization (CP) curves on all depolarized top bars exhibited corrosion current densities consistent with those found by LPR. The CP curves for the pickled bars generally showed the buildup of a more protective surface film, except for initial CP curves on 316P specimens where surface film breakdown was observed. CP curves for the as-rolled bars showed steady increases in current densities with increasing anodic potential, characteristic of uniform corrosion, with even higher current densities on the downward scan. CP scans had no

apparent long term detrimental effect on corrosion potential, macrocell current densities or LPR measurements of any top bars, indicating initial passive surface characteristics at equilibrium were restored; however, there was a long-term effect on the future cyclic polarization behaviour for the 316 specimens: pickled 316 bars that were scanned a second time exhibited a more protective surface film on the second scan that was strengthened from the applied anodic potential; in contrast, consecutive scans of as-rolled 316 bars showed current densities increasing at higher rates on the upward scan. Pickled 304 and 2205 bars showed consistent behaviour for multiple CP scans, forming a more protective surface film from the applied anodic potential.

- The pickled 316LN bars had slightly inferior corrosion performance than the pickled 304LN bars, showing a less protective surface film from cyclic polarization curves, greater fluctuations in macrocell current densities, and initially more negative corrosion potentials. This is counter-intuitive to its higher alloying content (higher PREN value) and conventionally superior corrosion performance found in most other studies/applications. The cause of this behaviour is speculated to be either from the presence of pit initiating sulphide inclusions due to its higher sulphur content, differences in chromium profiles at the mill-scale/base-metal interface due its smaller grain size, different pickling procedures employed (i.e. over-pickling, lack of final passivation in mild oxidizing solution), or an interplay of all these factors.
- Examination of autopsied G109 specimens broken open after 500-600 days of exposure revealed the presence of superficial rusting on the top surface of the as-rolled stainless steel top bars, while the bottom surfaces of the same bars were free of rust despite being embedded in the same concrete. The rust appeared brown immediately upon removal, unlike the characteristic black to green to brown transition that corrosion products typically undergo on actively-corroding plain carbon-steel rebar upon being extracted from concrete and undergoing oxidation in the atmosphere. This suggests the corrosion products formed at much earlier stages, and growth of the corrosion products slowed down or ceased with time. This is consistent with the diminishing nature of the macrocell current densities exhibited over the measurement period, with maximum values measured within 5 days of casting that gradually decreased over an order of magnitude by 400 days. Examination of the pickled stainless steel top bars revealed very little corrosion except for a few isolated spots

originating at the ribs. These spots were more prevalent on the pickled 316 specimens than on the pickled 304 and 2205 bars, and may be the result of the processing factors described in the previous paragraph.

- Upon removing the corrosion products and examining the damaged areas of one as-rolled specimen, only a few isolated regions along the bar's mid-section showed visible depth loss (100 - 300 μ m), with the majority of the observable damage occurring at the bar ends. This damage had resulted from the formation of crevice cells between the epoxy-covering and steel interface, as well as from residual knife markings left over from applying the epoxy coating. Given the large influence these crevice cells would have on the measured microcell corrosion current densities of the as-rolled bars, these values would be much lower in the absence of crevices, possibly approaching those of pickled stainless steel. Real structures would, however, introduce crevice cells of their own at the contacts between transverse and longitudinal bars, which are a possible concern.
- EDS analysis of the mill scale/base metal interface found inconsistent composition profiles along this region, though the magnitude of chromium depletion in this region for both the as-rolled 316 and 304 stainless steels reached no lower than 14 wt%, versus the ~18 wt% base metal values measured for both steels. The depth of chromium depletion was 100-500 nm. The amount of chromium depletion found here is less than that reported in research (Stott and Wei, 1989) of stainless steel exposed to high temperatures for prolonged periods of time often cited by others (Li and Celis, 2003; Scully and Hurley, 2007) to justify the pickling process.
- The mill scale varied in composition and thickness at the different areas analyzed, and the predominant constituents were iron and oxygen, with small amounts nickel and chromium present. The mill scale thickness was in the range of 2-9 μ m. Certain regions of mill scale exhibited high chromium contents (up to 36 wt%) near the inner mill scale over distances ~1 μ m, which would account for the chromium depletion found at the mill scale base/metal interface.

5.1.2 Loading Conditions

- Despite identical deflection magnitudes applied, dynamically loaded beams exhibited larger observable crack widths, up to 1.0 mm, whereas statically loaded beams had maximum crack

widths of only 3.0 mm. A combination of crack healing in the statically loaded beams as well as the enhanced development of microcracks in the dynamically loaded beams that enable the formation of larger cracks, are both believed account for the difference in crack sizes.

- Corrosion current densities and potentials of the beams are consistent with those obtained for the same steel types in the G109 prisms, with loading having little effect on these values and exhibiting no clear distinction between those loaded dynamically and those loaded statically.
- CP curves showed an increase in protection of the surface film for the pickled 2205 bars and a mixed behaviour for the pickled 316 bars of both increased and decreased protection of the surface films from the applied anodic potential. Despite a clear distinction in behaviour between the two steel types, no distinction was observed between the different loading types.
- ECN data shows the dynamically loaded beams to exhibit similar noise fluctuation to statically loaded beams when cyclic loading is off. However, when cyclic loading is on, noticeably larger fluctuations are observed for the majority of the dynamically loaded beam pairs, indicating that, while it may recover when cyclic loading is off, the stainless steel's protective film is susceptible to breakdown and general corrosion at the time of cyclic loading, probably attributed to erosion corrosion occurring at the concrete/steel interface due to abrasion from the micro-motion of the concrete crack.

5.2 Recommendations

5.2.1 Surface Conditions

- While the as-rolled stainless steel bars exhibited higher microcell corrosion rates than the pickled stainless steel bars, by a factor of 10-50x depending on the whether the bars were polarized by the bottom bars or depolarized, their values are similar to those typically measured for passive black steel in chloride-free concretes, and at least an order of magnitude less than the corrosion rates of actively corroding black steel in concrete. This is despite being exposed to extremely high chloride concentrations of 7.5% Cl by weight of cement, which is well beyond the upper levels typically encountered in structures exposed to de-icing salts (McCormick_Rankin_Corporation, 2008). Furthermore, a large contribution to the measure of corrosion rates was the result of crevice corrosion at the bar ends induced by the

epoxy-cover/steel interface, meaning the corrosion rates of as-rolled stainless steel bars in the absence of these crevices would be even less. In light of these factors, the use of as-rolled stainless steel rebar in aggressive environments should provide sufficient corrosion resistance for the 75 year lifespan currently specified by the Canadian Bridge Code (CAN/CSA-S6-06, 2006).

- Monitoring of G109 specimen corrosion rates should be continued to ensure that current densities of as-rolled specimens do not increase and that the superficial surface rust found from the autopsied G109s does not expand further and cause concrete cracking.
- Further analysis of the corrosion products on the as-rolled bars should be done by autopsying another prism without exposing the rebar surface to the atmosphere, and performing Raman spectroscopy on the corrosion products in a vacuum. This would provide information on compounds present and confirm whether they had formed earlier and had already oxidized, or were in fact formed fairly recently in which case the risk of concrete cracking would be more of a concern.
- Sources of crevice corrosion for concrete reinforcement that would be present under real service conditions (i.e. rebar joints, stirrups), as well as the corresponding corrosion resistance of as-rolled stainless steel bar under such conditions should be evaluated, since it does exhibit higher susceptibility than pickled stainless steel to crevice corrosion.
- Further study should be done on the maximum chloride contents typically found in concrete structures in aggressive environments, as well as magnitude of localized corrosion capable of inducing concrete cracking.
- In light of the pickled 316's slightly inferior corrosion performance to pickled 304 (though still exhibiting very low corrosion rates), the effect of sulphur content and/or grain size on the pickling and/or corrosion performance characteristics of austenitic stainless steel rebar should be investigated.
- In light of the as-rolled stainless steel rebar's positive results, investigation of the corrosion performance of lower alloyed stainless steels in the as-rolled conditions for concrete reinforcement would be beneficial. Candidates include low-nickel types that have demonstrated relatively strong performance in the pickled condition in previous studies (Bautista, Blanco et al., 2006; García-Alonso(a), M.L.Escudero et al., 2007), as well as

ferritic 430 which has shown very high resistance to pickling in the as-rolled condition (Fernando and Zaremski, 1986) due to the strong continuity of its mill scale.

- Applying the ASTM C876 corrosion probability guidelines to stainless steels in concrete is not suitable since the outliers 316PB4 and 304PB4 in this project exhibited consistently low corrosion potentials below -350 mV vs. CSE while maintaining passive corrosion rates. Similar behaviour has been found for stainless steel in chloride contaminated concrete in other studies (Mammoliti and Hansson, 2007). A database of stainless steel rebar corrosion potentials and corresponding corrosion states should be established to develop corrosion probability guidelines, however a challenge remains in finding values for stainless steels in the actively corroding state.

5.2.2 Loading Conditions

- Despite the presence of larger cracks easily able to facilitate chloride penetration to the rebar and exposure to aqueous solution of >7 wt% Cl⁻, dynamically loaded beams, when cyclic loading is off, exhibit no increased risk of corrosion compared to statically loaded beams, with both exhibiting low corrosion rates below that of passive black steel in concrete. No significant evidence was thus found to suggest that the use of pickled stainless steel rebar in dynamically loaded concrete structures would be particularly detrimental, and it should therefore be specified in such structures if all other factors permit.
- Given that higher electrochemical noise fluctuations were measured on the dynamically loaded beams when cyclic loading was on, the corrosion risk posed by dynamically loaded beams may be strongly influenced by the time duration over which it is applied. In the case of applications exposed to more extreme loading regimens where dynamic loading is constantly repeated, further testing would be recommended.

Appendix A

Admixed Chloride for Saturated Pore Solution

The admixed chloride analysis, conducted with the assistance of colleague Brad Bergsma, was carried out in order to determine the minimum amount of NaCl that was required for admixing into cement in order to achieve pore solution in the mature cement that is saturated with chlorides. This admixed chloride concentration was then used for the upper concrete layer mix design of the G109 specimens surrounding the top rebar.

Cylinders of cement paste, 50 mm by 100 mm, having a water/cement ratio of 0.5 (the same ratio used for the G109 specimens) and with varying amounts of admixed chloride in the form of NaCl were prepared in accordance with standard mixing schedule: mixing for 3 minutes, followed by 3 minutes of rest, then an additional 2 minutes of mixing (ASTM-C192, 2005). The admixed chloride contents used were 0.1, 0.5, 1.0, 2.5, 5, 7.5 and 10% Cl^- by mass of cement, and the cement and salt were mixed together before adding the water. Three to four cylinders of each admixed chloride concentration were cast, capped and rotated for 24 hours to avoid bleeding (separation of water from the cement paste), then placed in a humidity room for 27 days.

Once cured, approximately 4 ml of the pore solution from each specimen was extracted by loading the specimen into a cylindrical stainless steel chamber sitting on a base plate containing a small ejection hole where a syringe is attached to collect the pore fluid. The specimen is then compressed by a piston for a series of loads increasing from 300→450→600→750 kN at five minutes each, until sufficient fluid is extracted into the syringe in order to exclude air and prevent carbonation. A schematic diagram and photograph of the pore solution extraction chamber are shown in Figure 77 (a) and (b), respectively.

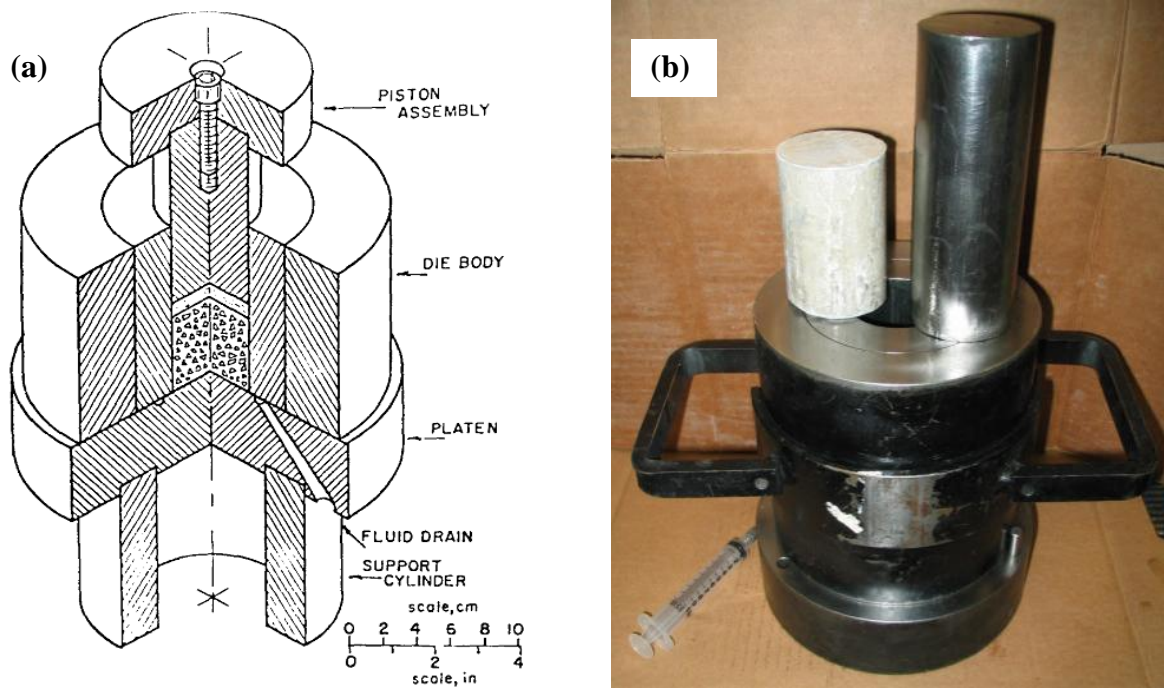


Figure 77: (a) Schematic diagram (Barneyback and Diamond, 1981) and (b) photograph of pore solution extraction chamber

Chloride analysis of the extracted pore solution was then performed using an auto-titrator (model: TIM800 Titration Manager and ABU901 Autoburette from Radiometer-Copenhagen). After calibrating the titration system with aqueous solutions of known chloride concentrations, 50 μ L of pore solution was diluted in 50mL of distilled water, buffered with one drop of HNO₃, and stirred for 5 minutes with a magnetic stirrer. The solution was then titrated against a 0.01 M silver nitrate (AgNO₃) solution, and, as shown in Table 15 and Figure 78, a minimum of 7.5% Cl⁻ by mass of cement was needed to yield the maximum concentration of Cl⁻ in pore solution of ~ 16% by mass.

Table 15: Chloride analysis data from extracted pore solution

%Admixed Cl⁻ by mass of cement:	0.1	0.5	1.0	2.5	5.0	7.5	10
				6.345	11.061	15.193	14.893
Trials – Mass % Cl ⁻ in Pore Solution:	0.224	0.296	1.735	5.450	12.300	15.523	15.006
	0.224	0.296	1.481	6.479	11.963	16.342	15.009
				6.708			15.302
Average – Mass %Cl⁻ in Pore Solution:	0.224	0.296	1.61	6.25	11.8	15.7	15.1

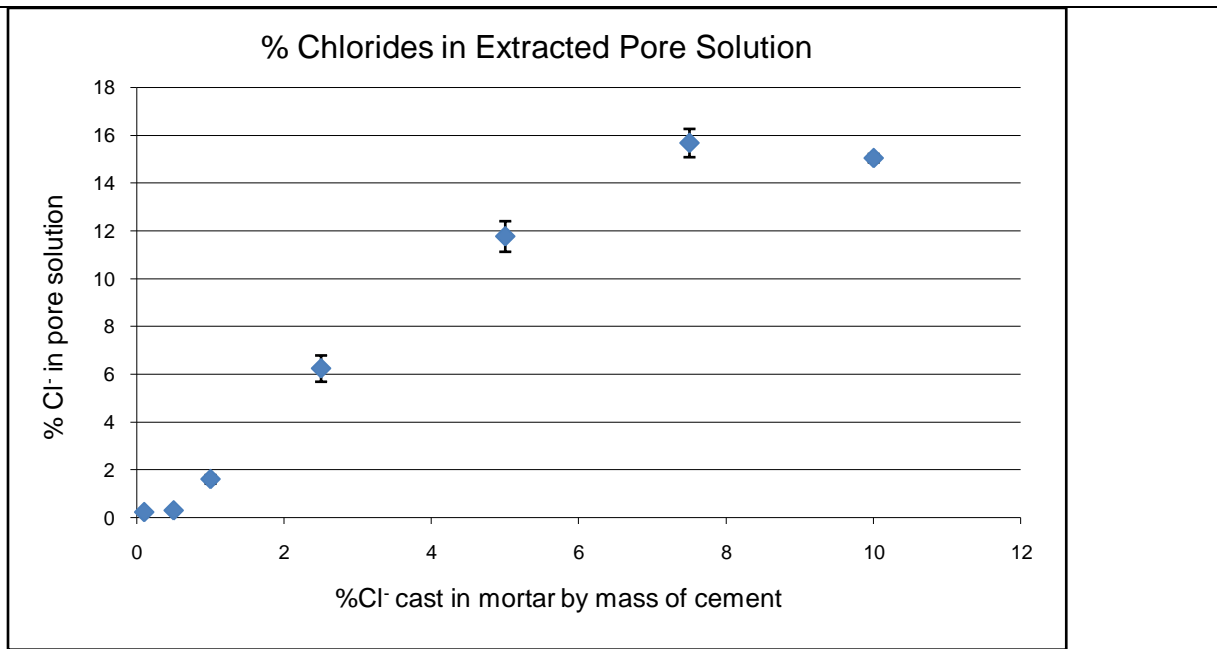


Figure 78: Chloride content in pore cement paste pore solution with varying amounts of admixed chlorides.

Appendix B

G109 Specimen Cast Dates and Engraving Identification

Specimen Type	Engraving Identification	Cast Date
2205P B	I	Dec. 15/06
2205P S	SI	
316P B	II	Dec. 18/06
316P S	SII	
316A B	III	Feb. 15/07
316A S	SIII	
304P B	IV	Mar. 9/07
304P S	SIV	
304A B	V	Mar. 22/07
304A S	SV	

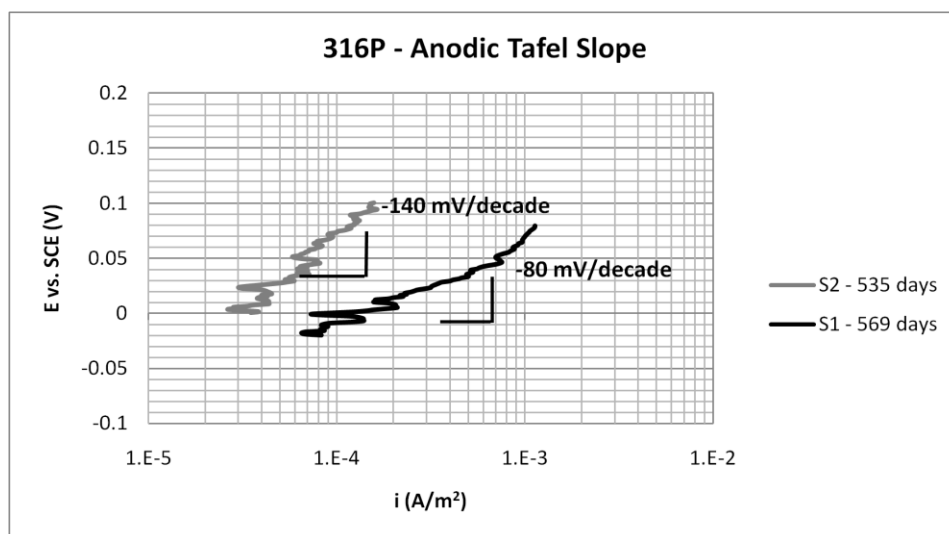
Appendix C
G109 As-Cast Concrete Data

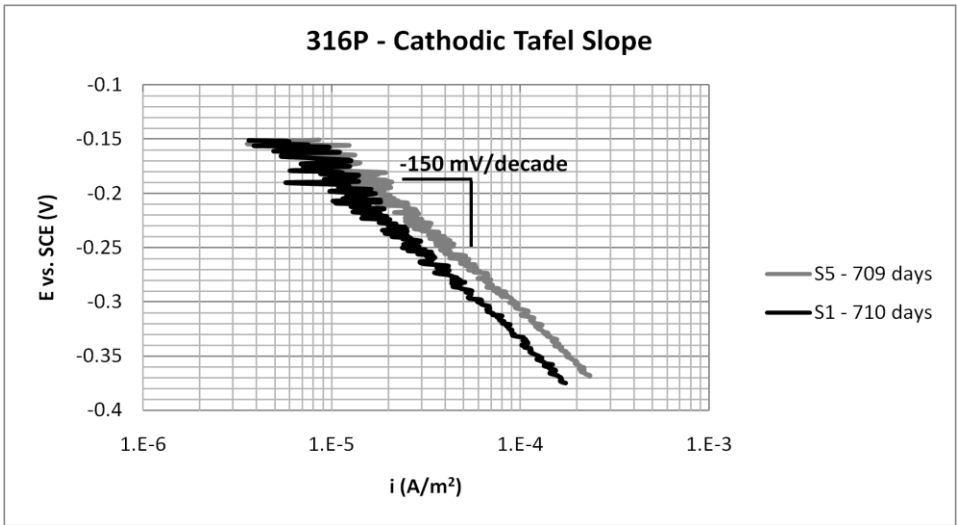
Steel Type	Cl Admixed	Slump Loss (cm)	Air Content (Vol. %)	Compression Strength (MPa)		
				Trials	Average	
2205P	Yes	12	5.1	29.9	30.6	
				31.5		
				30.4		
316P		18	4.5	4.5	24.8	24.0
					21.6	
					25.5	
316A		17	5.7	5.7	26.6	28.5
					29.2	
					29.5	
304P		20	6.7	6.7	21.0	23.4
					25.7	
					23.6	
304A	18	7	7	23.4	22.7	
				23.8		
				21.0		
2205P	No	10	12	14.4	14.6	
				13.8		
				15.6		
316P		10	10.4	10.4	15.9	21.6
					23.6	
					25.5	
316A		12	11.2	11.2	18.1	18.4
					16.7	
					20.4	
304P		10	11.6	11.6	19.7	19.7
					19.5	
					19.9	
304A		10	9.7	9.7	13.6	14.7
					15.1	
					15.4	

Appendix D

Derivation of B Constants from Tafel Slopes

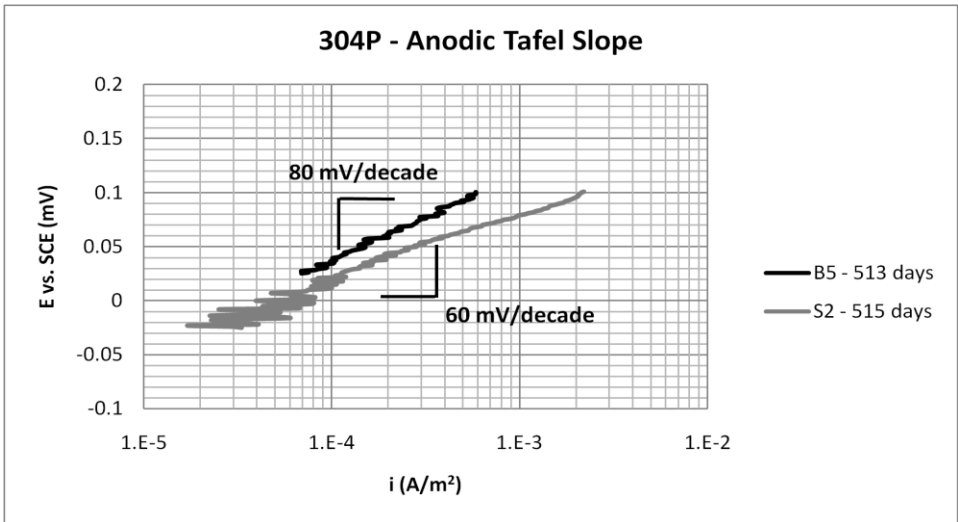
B constants of all steel types for use in the calculating corrosion rates from the LPR measurements were determined from the Tafel slopes of their respective potentiodynamic polarization curves using Equation 4. Two cathodic and two anodic Tafel slopes were averaged, and the resulting values were used to calculate B using Equation 4. Each of the potentiodynamic curves shown represent scans beginning at the corrosion potential and either increasing or decreasing in potential at a scan rate of 0.025 mV/s.

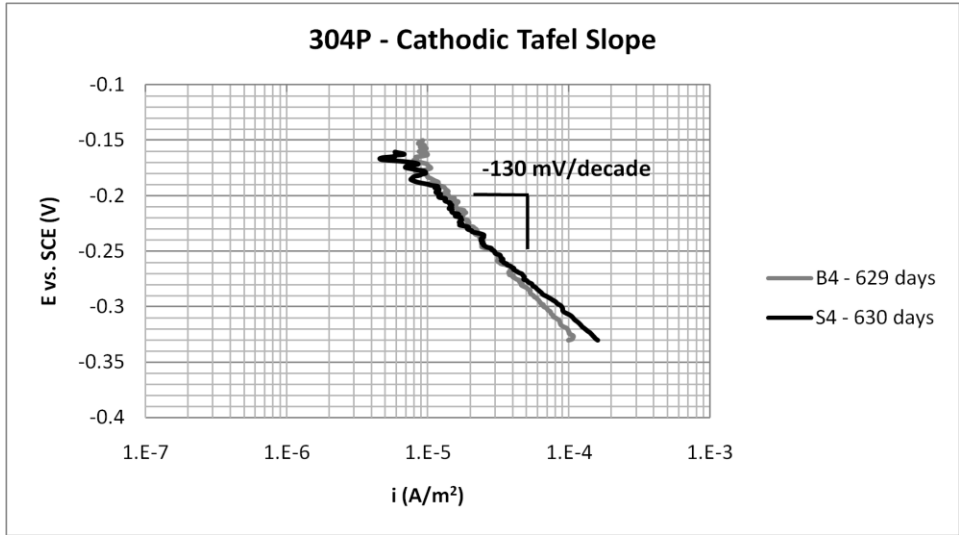




316P B Value:

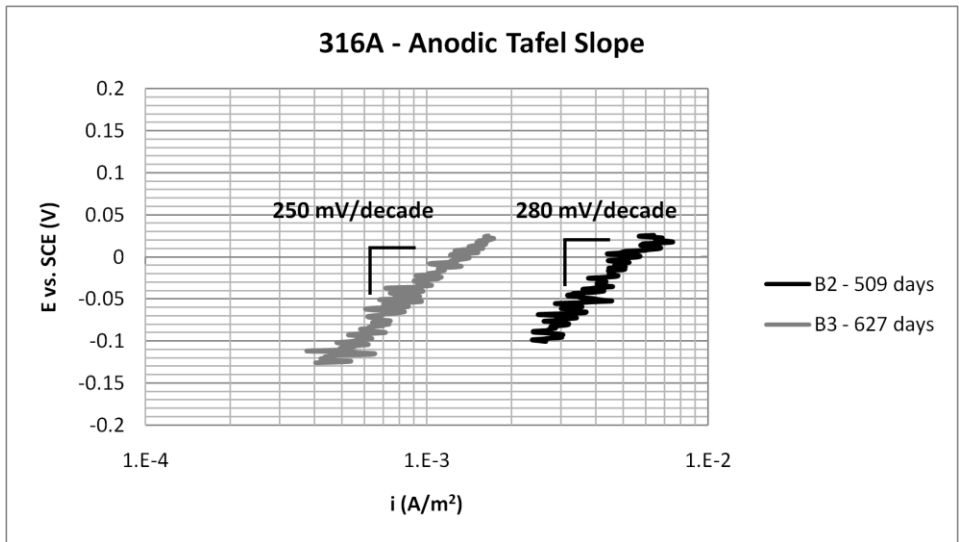
Specimen	β_a (mV/decade)	β_c (mV/decade)	B (mV)
S2 - 535 days	140		
S1 - 569 days	88		
S5 - 709 days		150	
S1 - 710 days		150	
Average:	114	150	28.2

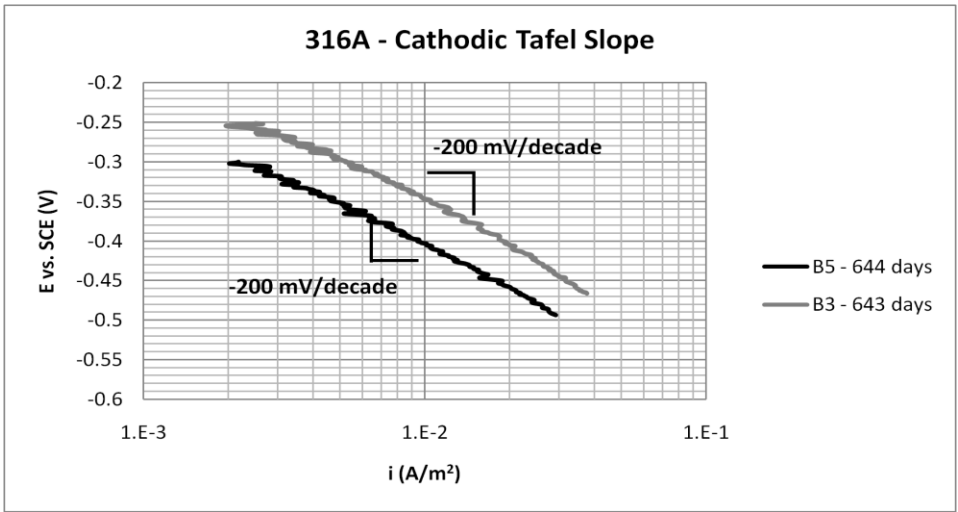




304P B Value:

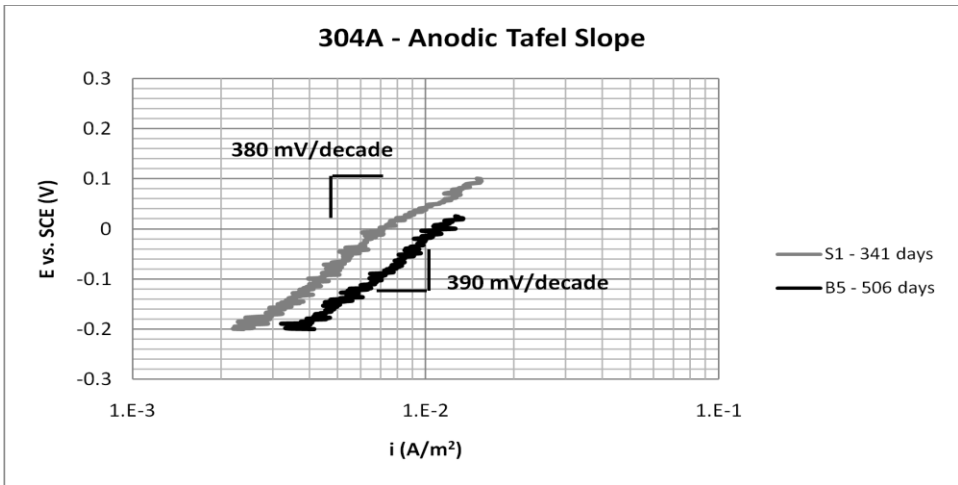
Specimen	β_a (mV/decade)	β_c (mV/decade)	B (mV)
B5 - 513 days	80		
S2 - 515 days	60		
B4 - 629 days		130	
S4 - 630 days		130	
Average:	70	130	19.8

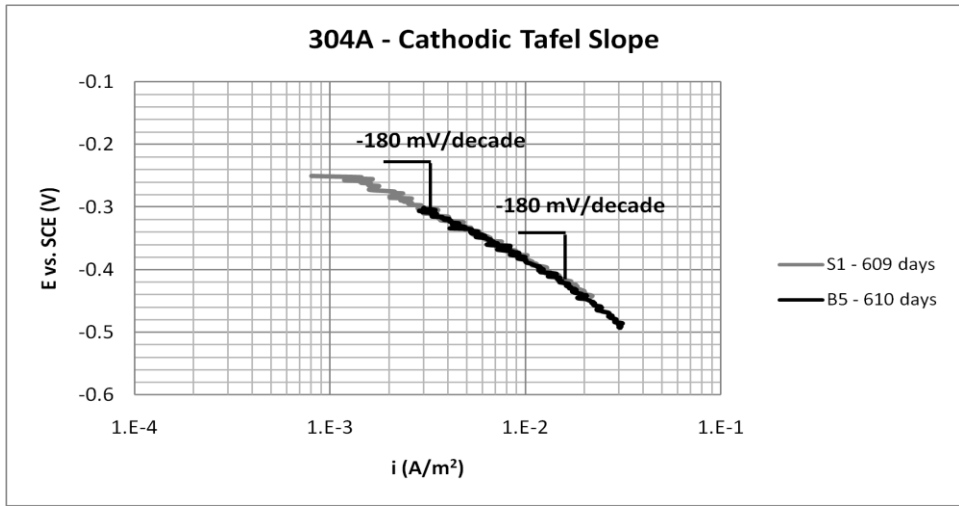




316A B Value:

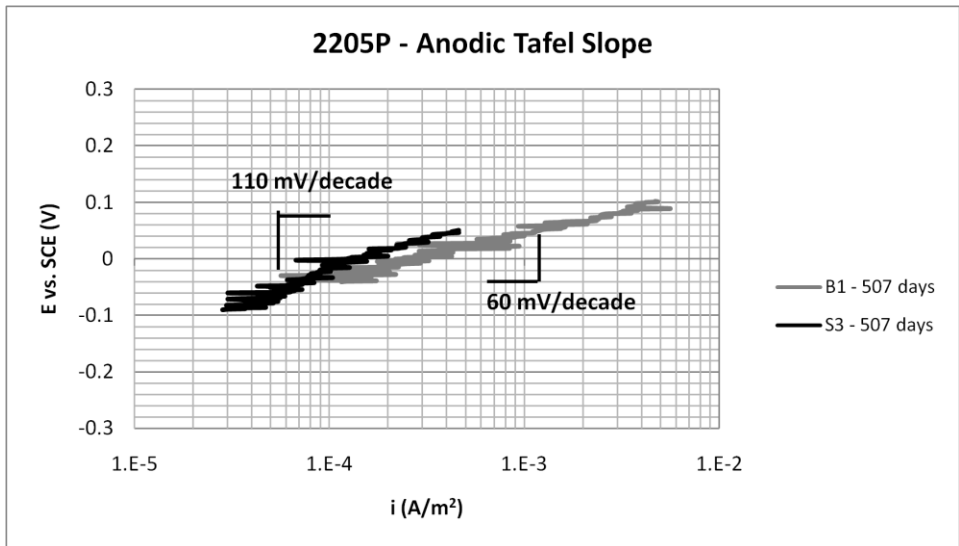
Specimen	β_a (mV/decade)	β_c (mV/decade)	B (mV)
B2 - 509 days	250		
B3 - 627 days	280		
B5 - 644 days		200	
B3 - 643 days		200	
Average:	265	200	49.6

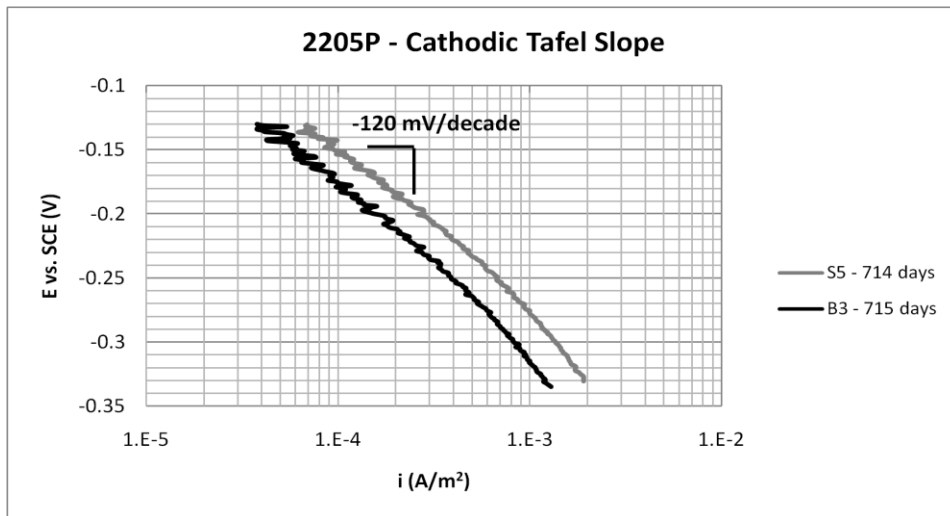




304A B Value:

Specimen	β_a (mV/decade)	β_c (mV/decade)	B (mV)
S1 - 341 days	380		
B5 - 506 days	390		
S1 - 609 days		180	
B5 - 610 days		180	
Average:	385	180	53.3





2205P *B* Value:

Specimen	β_a (mV/decade)	β_c (mV/decade)	<i>B</i> (mV)
B1 - 507 days	60		
S3 - 507 days	110		
S5 - 714 days		120	
B3 - 715 days		120	
Average:	85	120	21.6

Appendix E

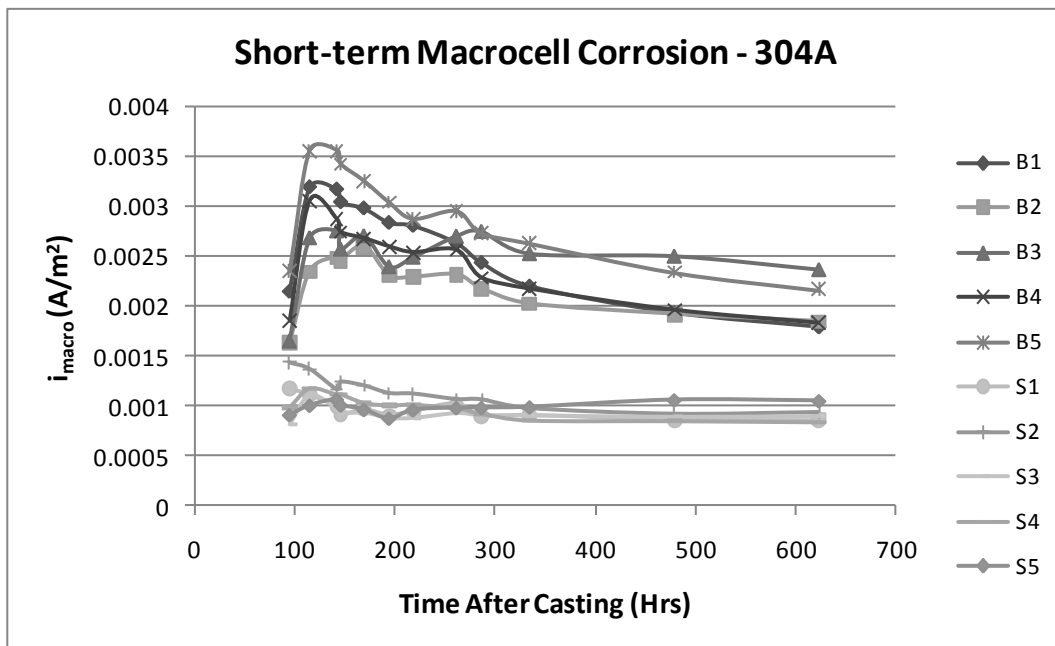
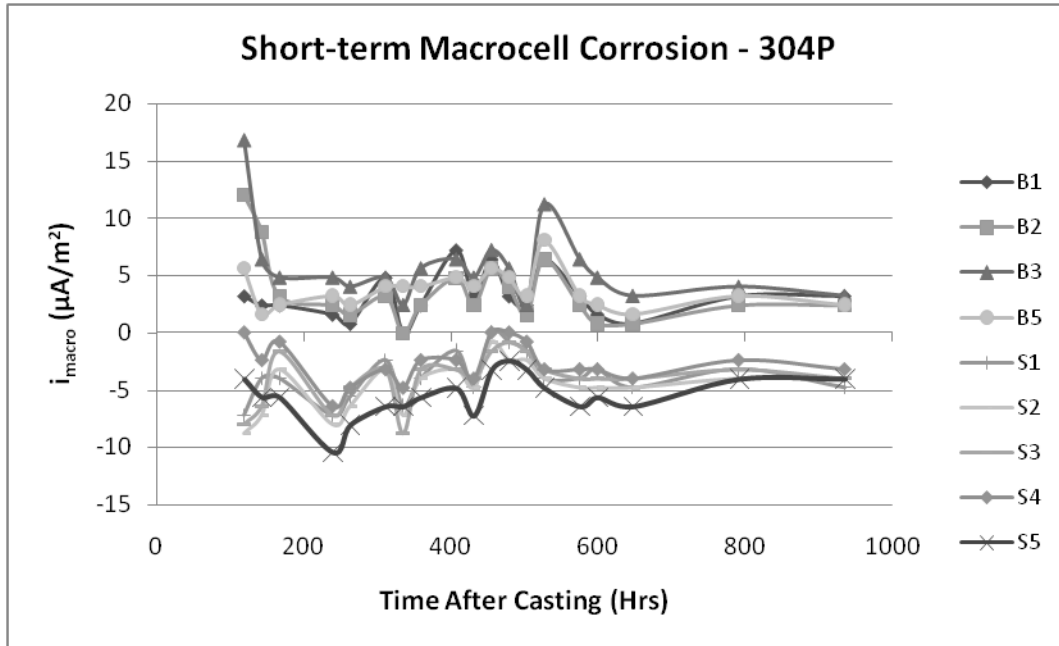
Loaded Beam Casting Data

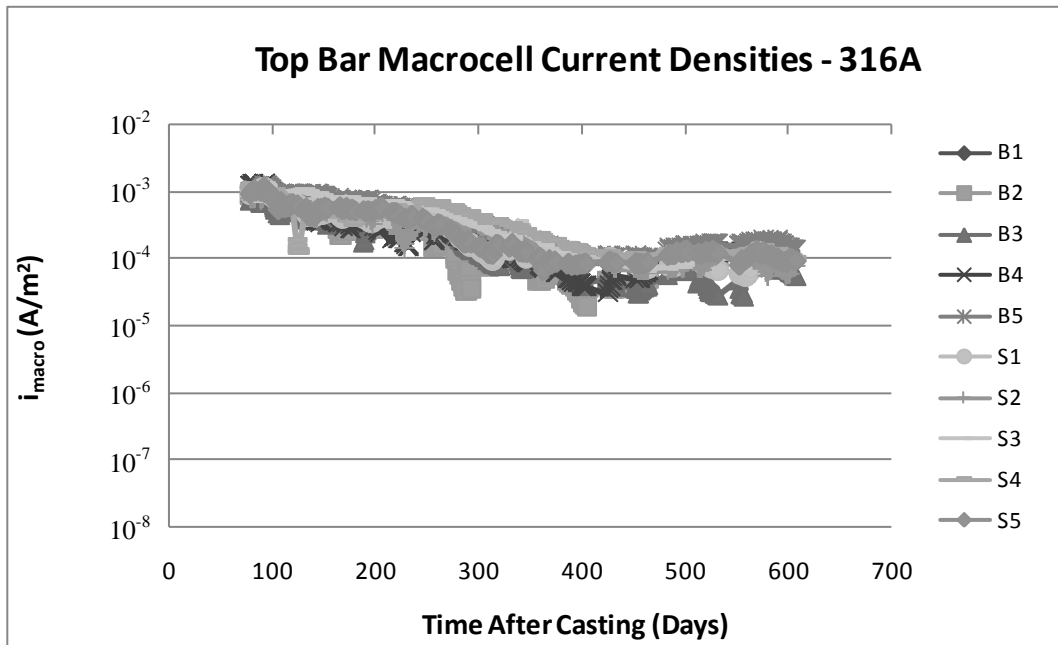
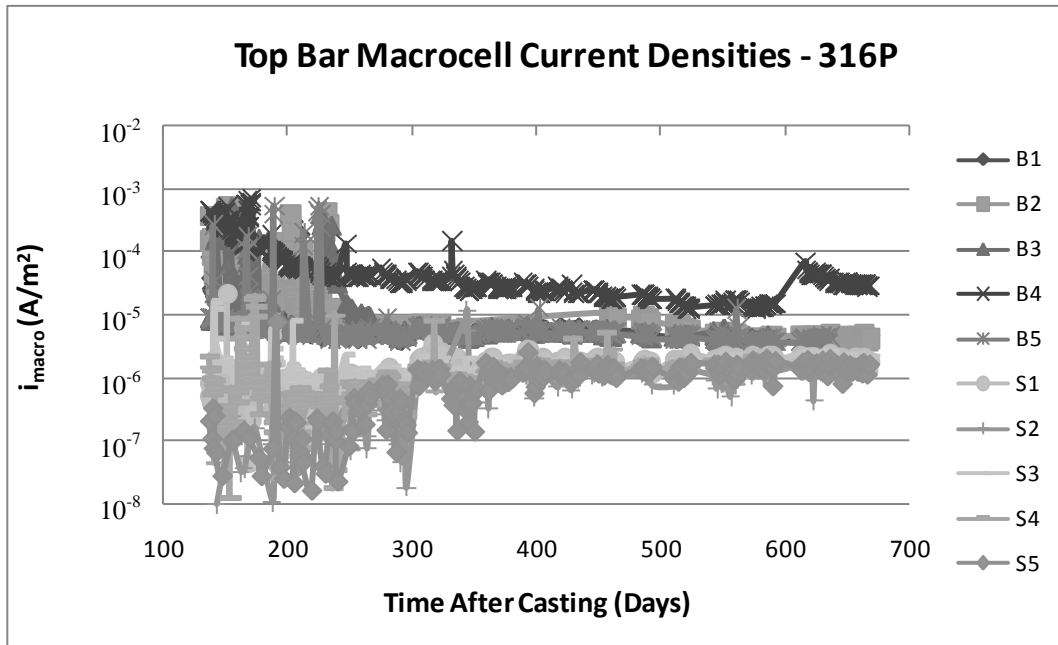
Concrete Batch	Casting Date	Slump (cm)	Air Content (%)	28-Day Compression Strength (MPa)		Loading Type
				Trial	Average	
1	23-Aug-07	8.9	12	21.27	20.7	Dynamic
				20.71		
				20.12		
2	23-Aug-07	2.1	8	33.30	33.5	Dynamic
				34.47		
				32.61		
3	30-Aug-07	3.1	8.5	26.81	26.6	Static
				25.29		
				27.68		
4	30-Aug-07	5.5	10	23.75	23.5	Static
				23.99		
				22.64		

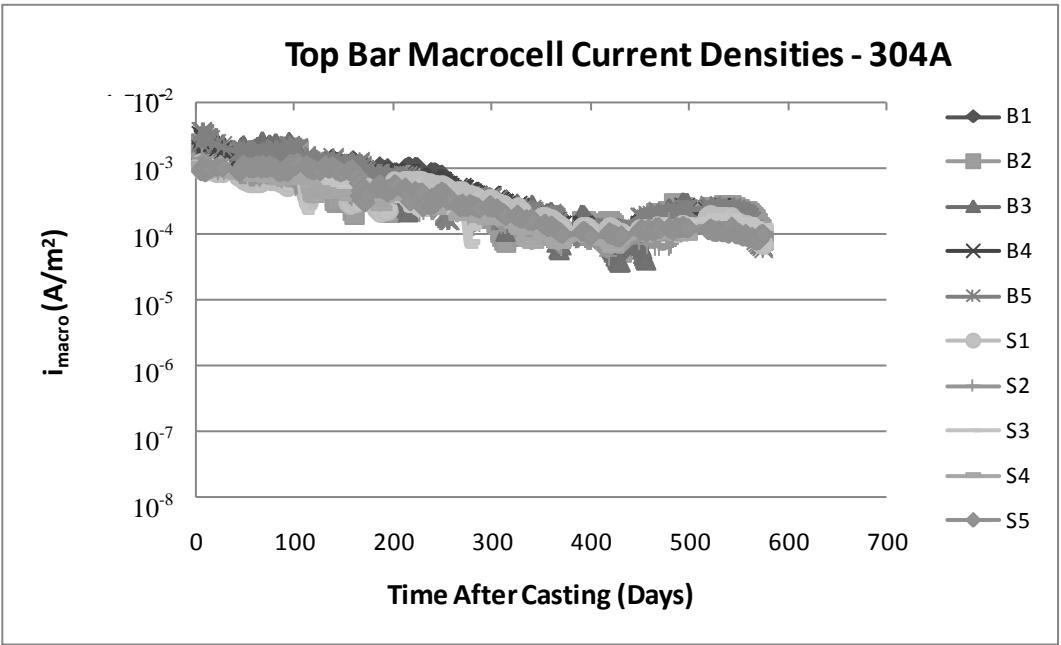
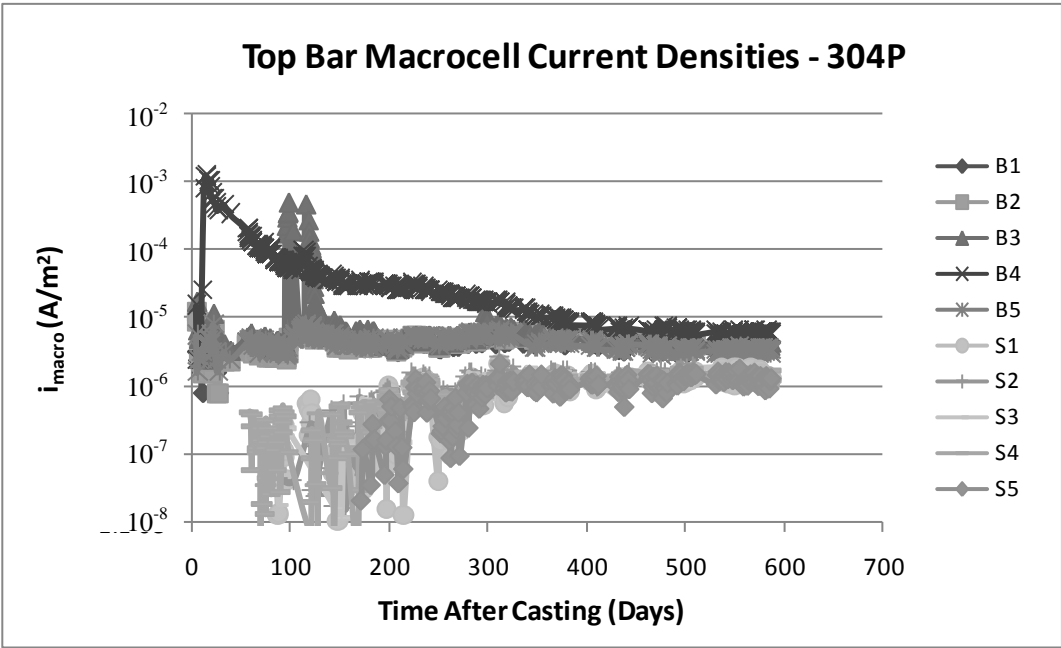
Appendix F

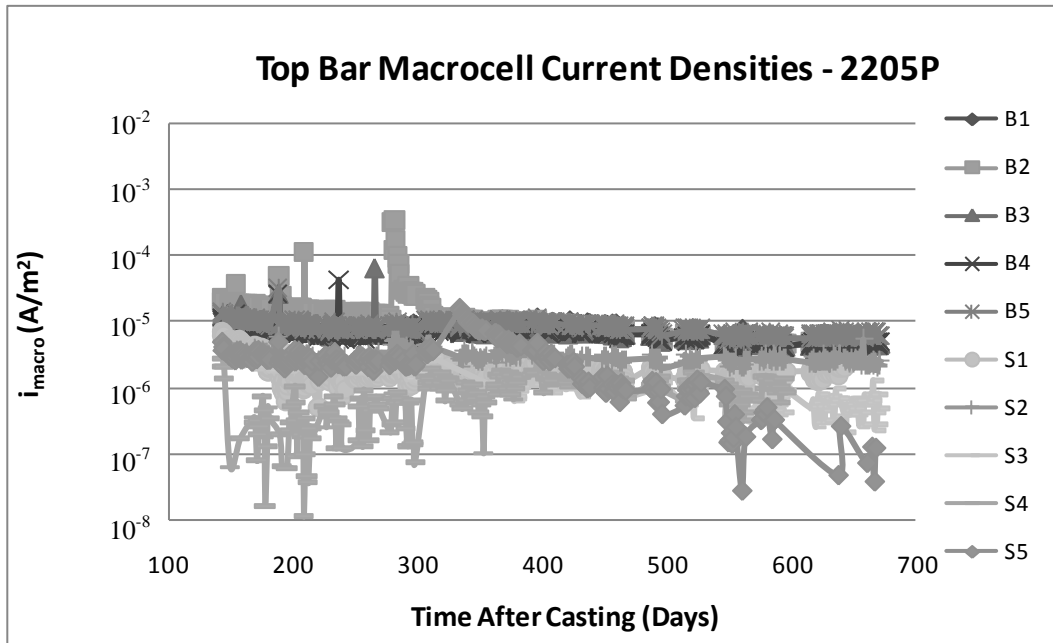
Macrocell Current Densities for Individual G109 Specimens

*Note: Specimen 304P B4 was not shown here since its values were much higher, as discussed in Section 4.1.1.2, and was thus excluded as an outlier.







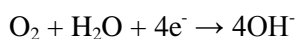


Appendix G

G109 Bottom Bar Cathodic Exchange Current Densities

The oxygen redox reaction exchange current densities of the G109 bottom bars at a pH of 13.5 were determined in order to correlate trends in macrocell corrosion rates with the bottom bar steel types. This meant determining the standard potential for the oxygen redox reaction in concrete, Equation 6, using the Nernst equation for an alkaline solution of unit oxygen activity at 25°C, Equation 7.

Equation 6:



Equation 7:

$$e_{\text{O}_2/\text{H}_2\text{O}} = e_{\text{O}_2/\text{H}_2\text{O}}^\circ - 0.059 \text{ pH}$$

For pH = 0, $e_{\text{O}_2/\text{H}_2\text{O}}^\circ = 1.229 \text{ V vs. SHE}$ (Pourbaix, 1966); therefore, in concrete with pH of ~13.5, the redox potential is ~0.430 V vs. SHE, or ~0.190 V vs. SCE. This value can be double-checked by looking at the E vs. pH diagram in Figure 2 where the top dashed line denoting the oxygen evolution line crosses a pH of 13.5.

Oxygen exchange current densities were obtained for three bottom bars of different steel-surface type characteristics: a SS316 pickled, a SS316 as-rolled, and a black steel rebar. Cyclic polarization scans were performed on each (starting in the depolarized state), and the resulting cathodic Tafel slopes, shown in Figure 79, were mathematically extrapolated using the Excel[®] derived trendlines towards the oxygen evolution potential of 0.190 V vs. SCE to give the oxygen exchange current densities, i_o , listed in Table 16. The as-rolled SS316 and black steel had similar oxygen exchange current densities of $\sim 10^{-6} \text{ A/m}^2$, about an order of magnitude higher than the $\sim 10^{-7} \text{ A/m}^2$ found for pickled SS316. This is consistent with the similar effects of black steel and as-rolled stainless bottom bars on macrocell current densities, as well as the higher macrocell current densities exhibited by specimens with black steel bottom bars compared with pickled stainless steel bottom bars.

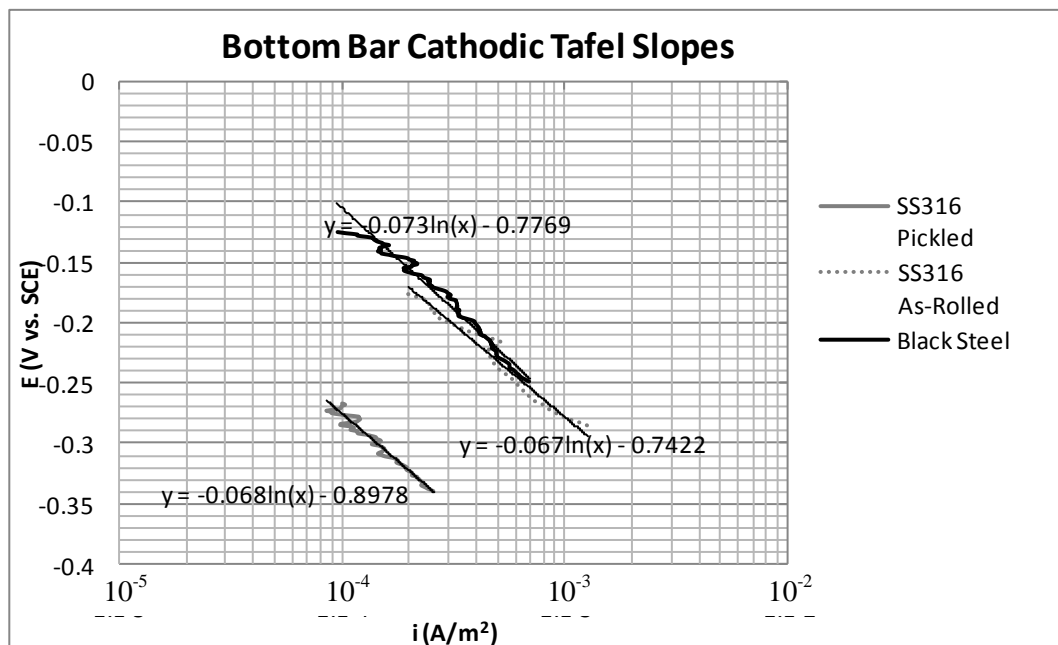


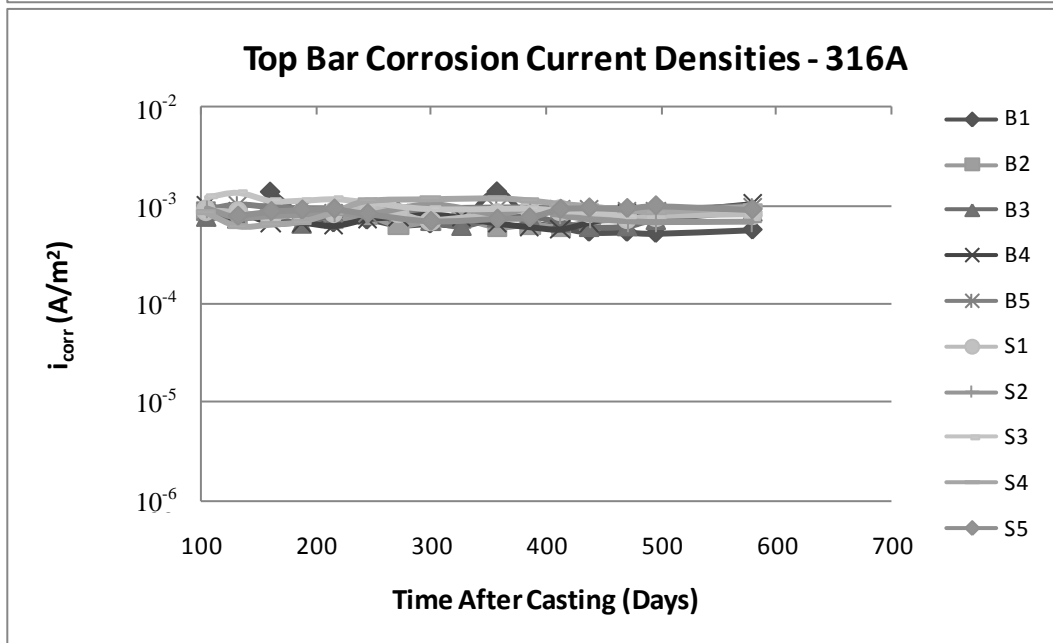
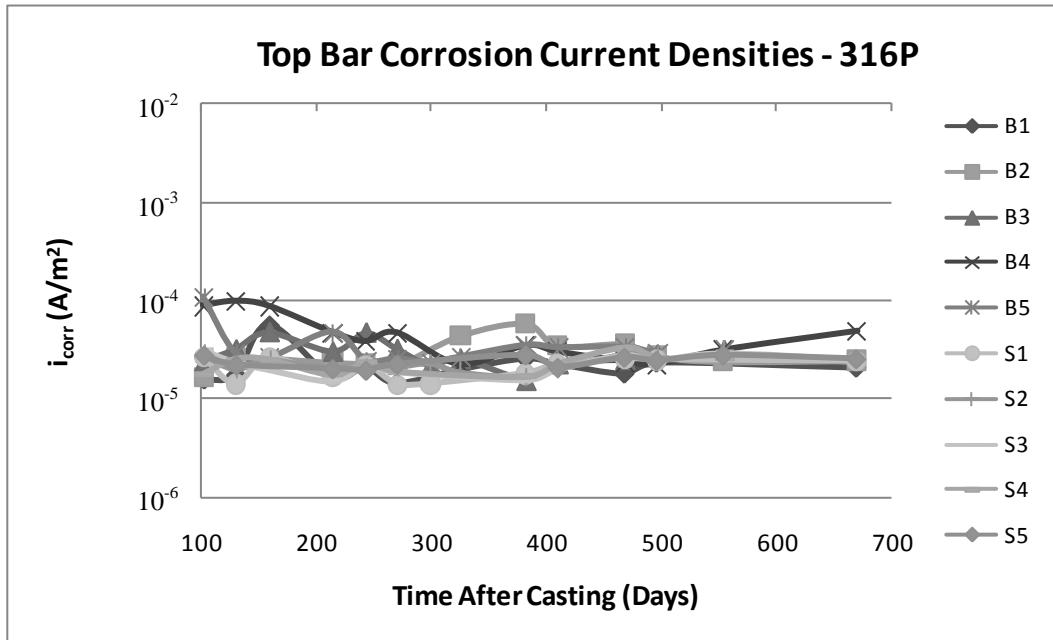
Figure 79: Tafel slopes and trendlines for select G109 bottom bars

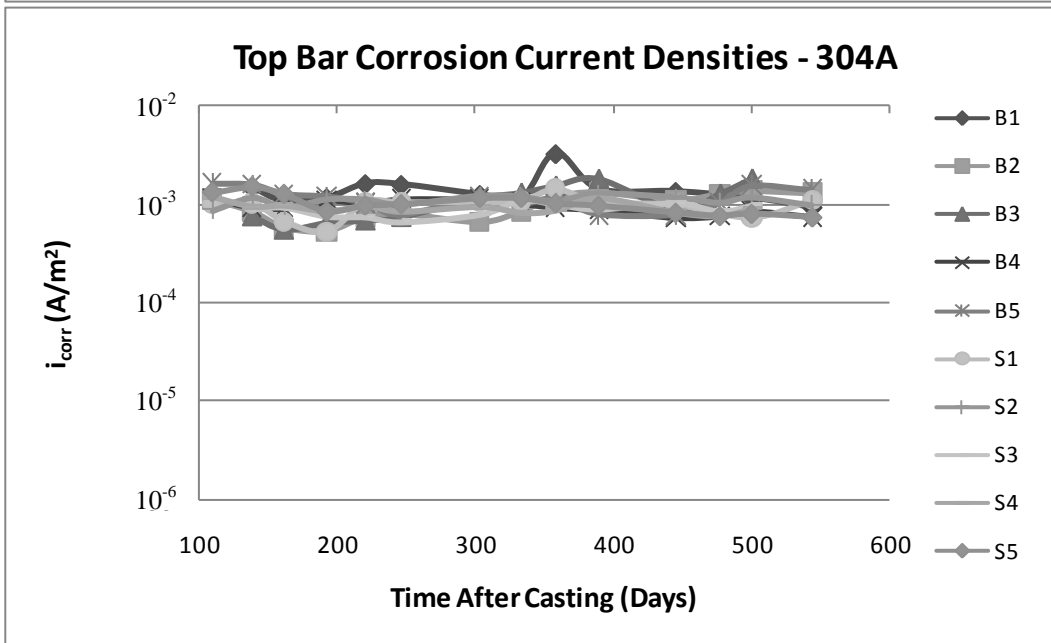
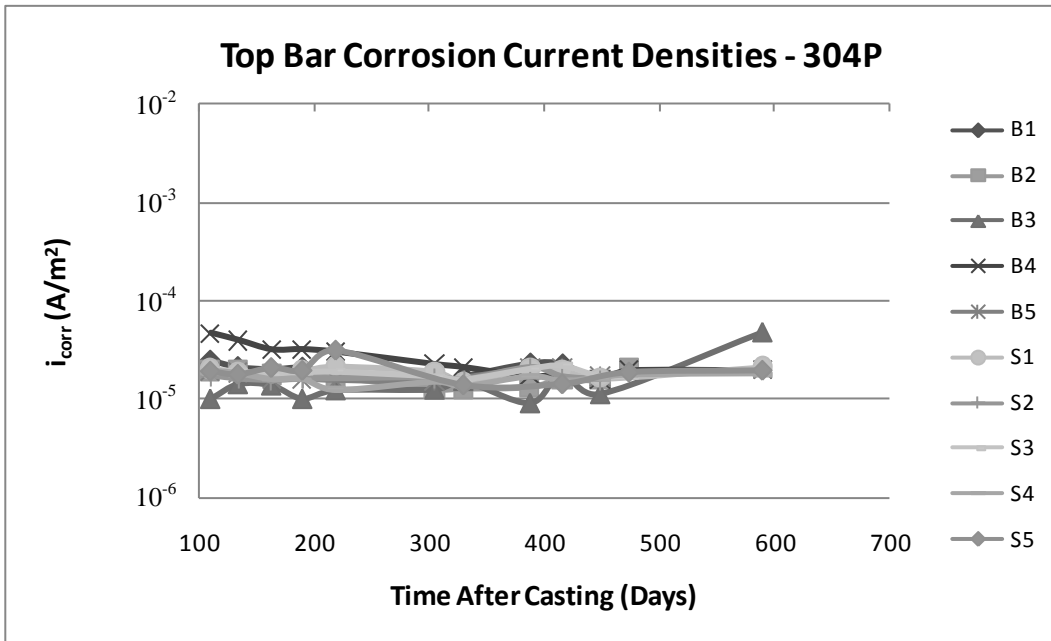
Table 16: Oxygen exchange current densities of different G109 bottom bar types

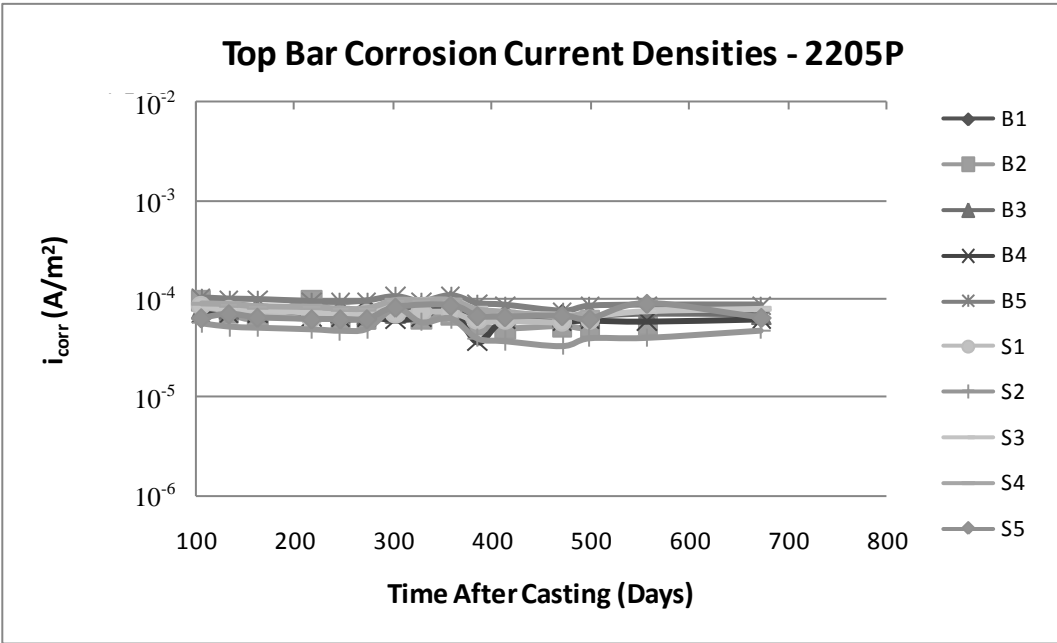
Bottom Bar	i_o (A/m ²)
SS316 Pickled	1.1×10^{-7}
SS316 As-Rolled	8.9×10^{-7}
Black Steel	1.7×10^{-6}

Appendix H

Microcell Corrosion Current Densities of Individual G109s

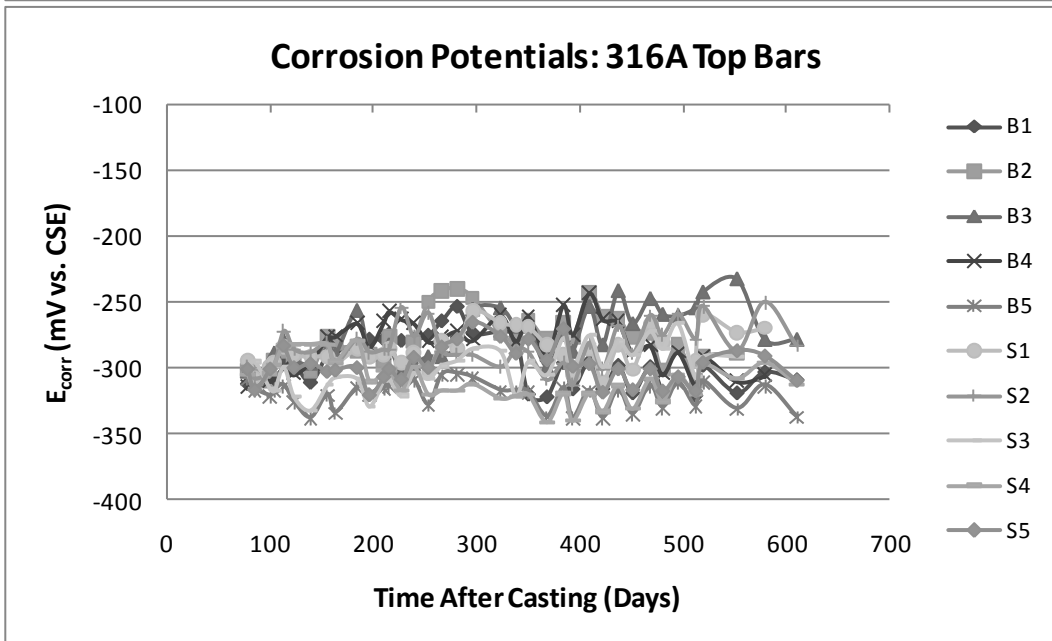
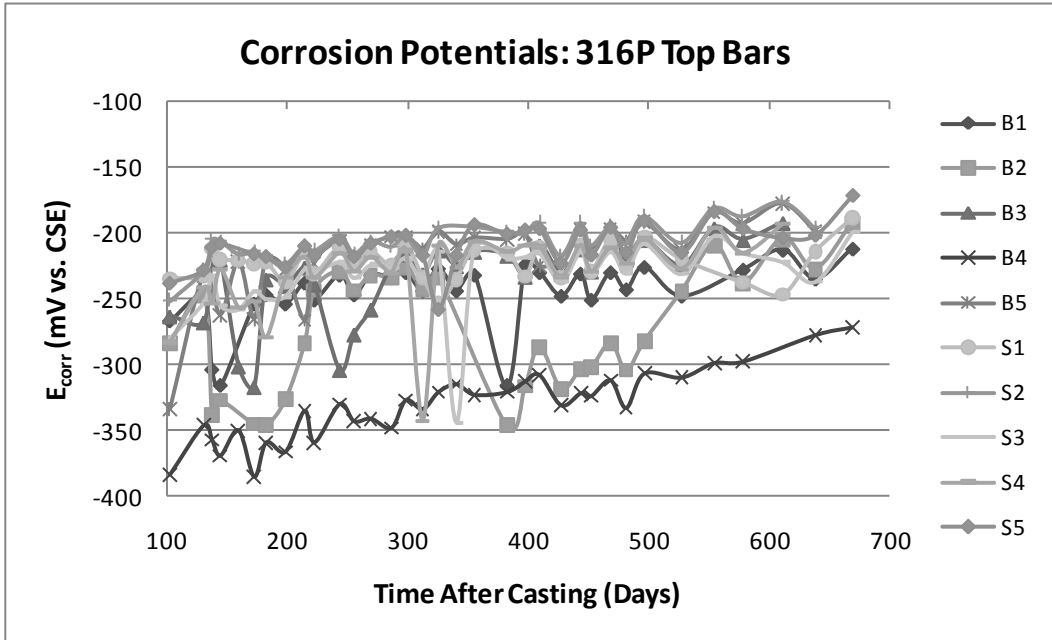


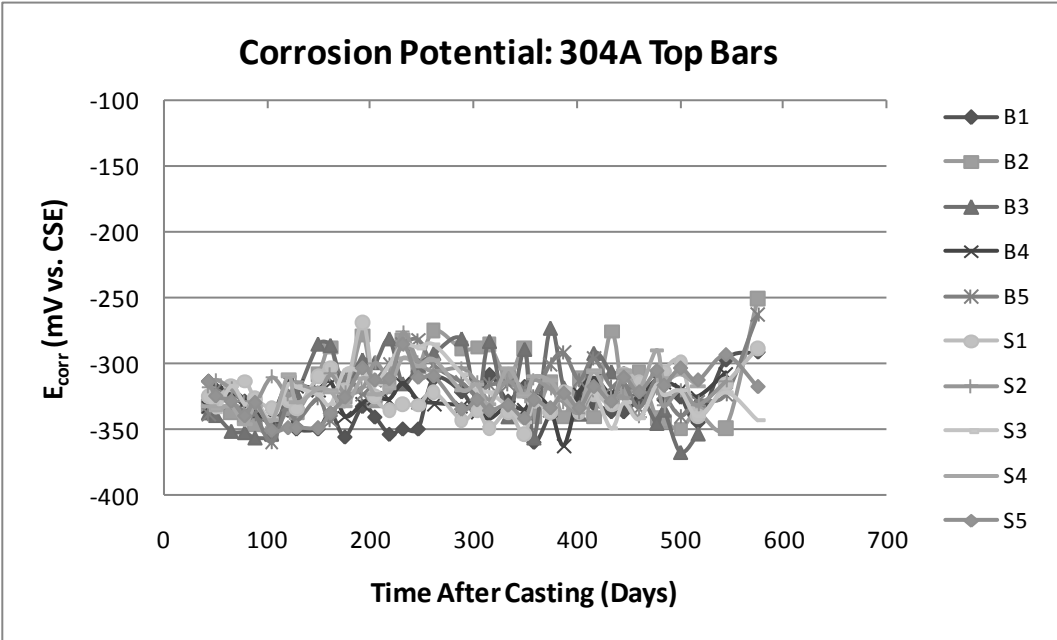
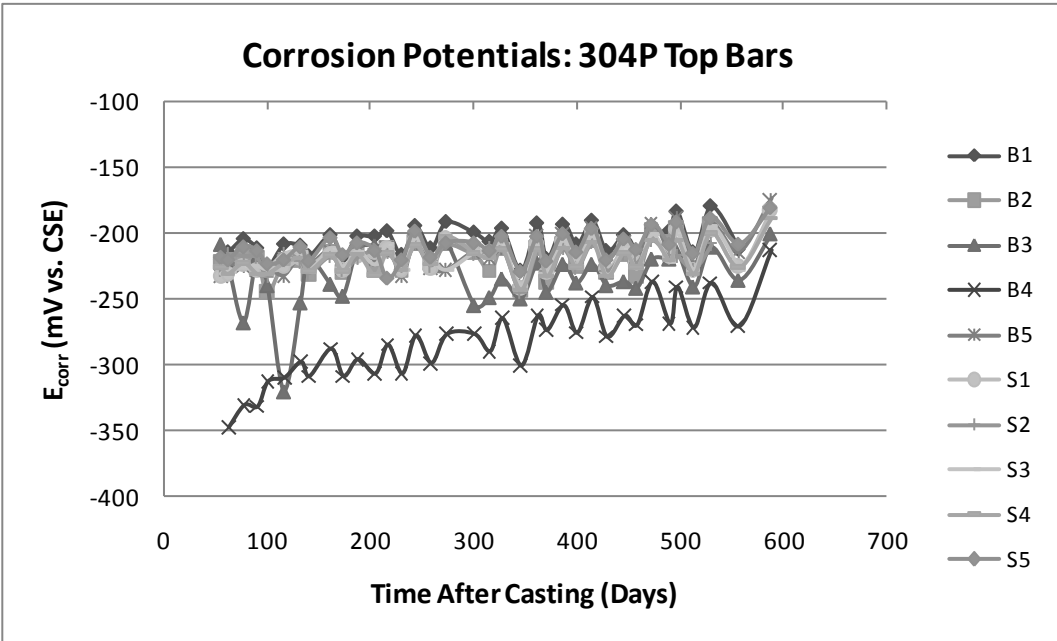


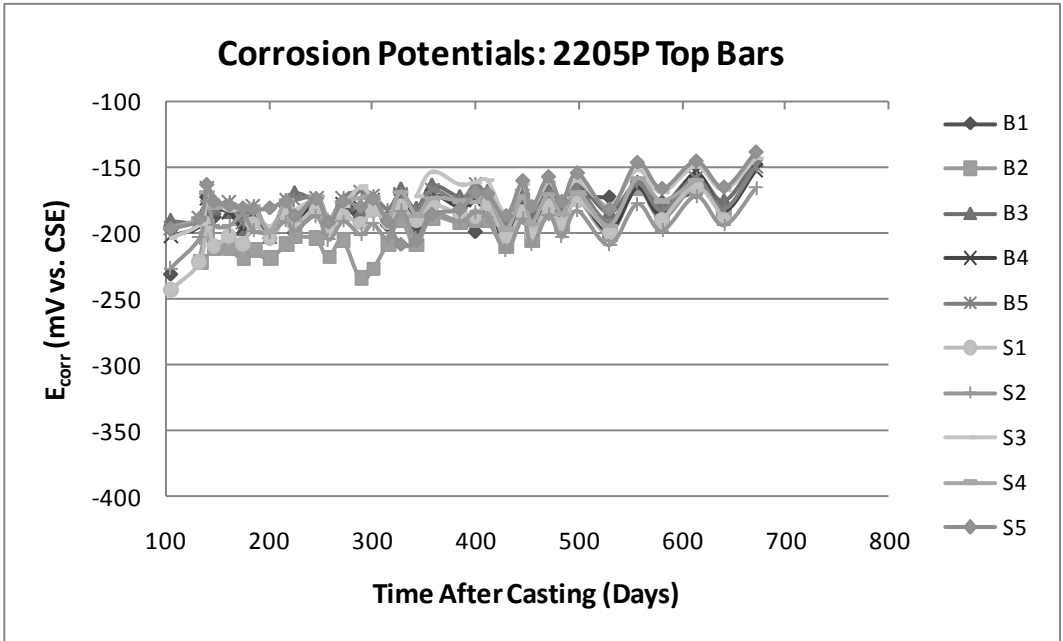


Appendix I

Corrosion Potentials of Individual G109s







Appendix J

Additional Top Bar 316P Cyclic Polarization

The variable behaviour of the 316P cyclic polarization curves in Figure 44 (a) prompted additional CP scans of 316P specimens, shown in Figure 80, to confirm the trend of decreasing current densities on the second scan of a single specimen, shown by the dashed curves, after running an initial scan, shown by the solid curves. The two curves plotted for both 316P S1 and S3 show this trend to be consistent.

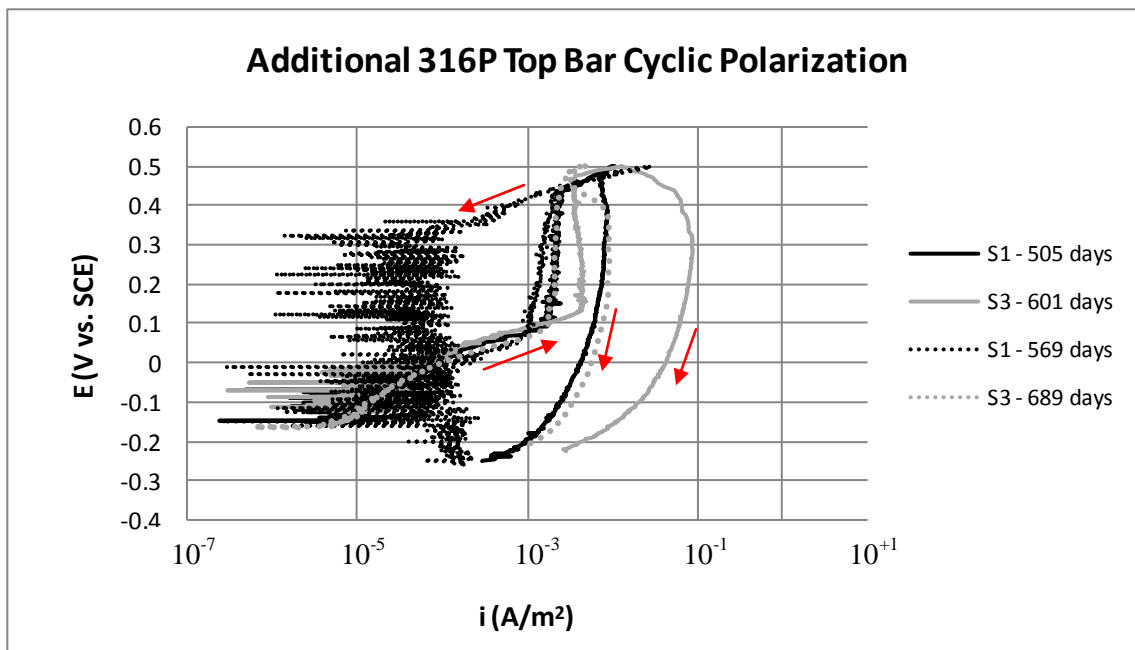


Figure 80: Additional potentiodynamic cyclic polarization curves for 316P top bars

Appendix K

Energy Dispersive X-ray Spectroscopy of Pickled Rebar

In order to validate the quantitative results obtained from the EDS chemical analysis of the as-rolled bars in Section 4.1.4.3, it was useful to analyze the pickled specimens using EDS in order to obtain comparable bulk metal chromium contents that would factor out any bias or calibration error inherent in the EDS equipment. Cross-sectional images of the regions analyzed as well as the chemical content profiles are shown below for 316P and 304P in Figure 81 (a) and (b), respectively. The Cr bulk content, determined by averaging all Cr values at points where oxygen was $\leq 1\%$ by weight, was found to be approximately 18.8% and 18.3% by weight for 316P and 304P, respectively.

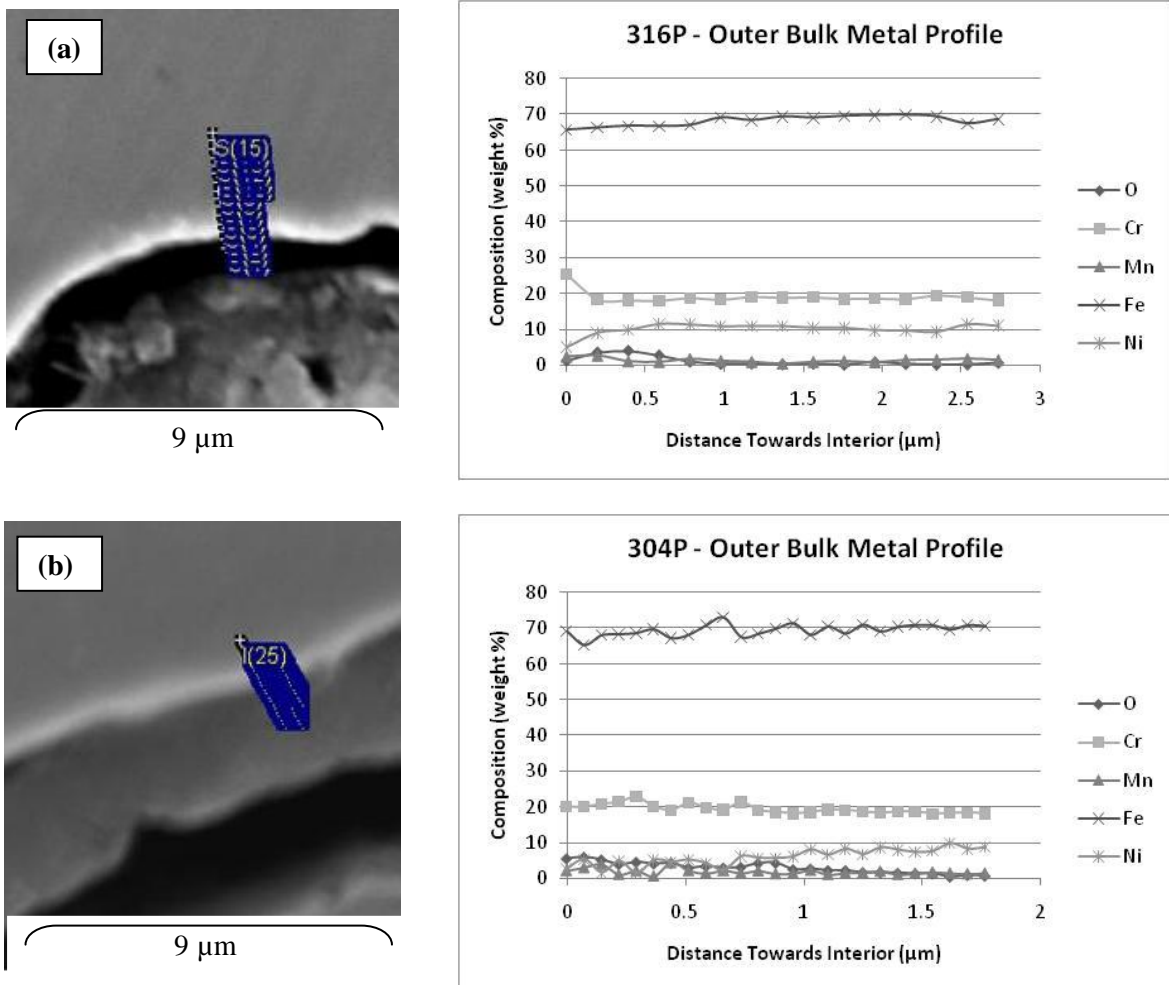


Figure 81: Energy dispersive x-ray spectroscopy of outer bulk metal of (a) 316P and (b) 304P

Appendix L

Loaded Beam Polarized Area

The polarized area of three loaded beams was determined by applying a potential of 20 mV to the beam's mid-section and determining the length along the bar away from the mid-section at which the bar stays polarized. Corrosion potentials along the bar at ~3.2 cm increments were taken before applying the potential, and upon applying the 20mV, if those original values differed by less than 5 mV from the difference experienced at the beam's mid-section, than that length of the beam was not considered polarized and as such should not be included in the corrosion current density calculations. The data for the polarized area measurements of three beams is shown in Table 17, and among the three beams an average polarized length ~66 cm was found (out of the 100cm of exposed length), which translates to a polarized area of 0.033 cm². Measurements were not obtained for the entire length of the beam due to the obstruction created by the steel braces joining the beam pairs together.

Table 17: Loaded Beam Polarized Area Data

<u>Loaded Beam Polarized Area Measurements:</u>																										
	Increments = 3.2 cm																									
316 SLb																										
Position from Center	-14	-12	-11	-10	-9	-8	-7	-6	-5	-4	-3	-2	-1	0	1	2	3	4	5	6	7	8	9	10	11	12
Pos. from Center (cm)	-45	-38	-35	-32	-29	-25	-22	-19	-16	-13	-9.5	-6.4	-3.2	0	3.2	6.4	9.5	13	16	19	22	25	29	32	35	38
Unpolarized (mV):	-144	-144	-145	-155	-157	-158	-161	-162	-153	-156	-157	-157	-154	-156	-158	-152	-151	-152	-154	-154	-153	-154	-151	-157	-142	-147
Polarized w/+20 mV	-130	-128	-129	-139	-138	-139	-142	-142	-132	-136	-136	-138	-136	-136	-139	-133	-133	-134	-136	-135	-134	-134	-132	-139	-116	-118
Difference (mV):	14	16	16	16	19	19	19	20	21	20	21	19	18	20	19	19	18	18	18	19	19	20	19	18	26	29
Polarized length =	67 cm																									
2205 SHb																										
Position from Center	-14	-12	-11	-10	-9	-8	-7	-6	-5	-4	-3	-2	-1	0	1	2	3	4	5	6	7	8	9	10	11	12
Pos. from Center (cm)	-45	-38	-35	-32	-29	-25	-22	-19	-16	-13	-9.5	-6.4	-3.2	0	3.2	6.4	9.5	13	16	19	22	25	29	32	35	38
Unpolarized (mV):	-121	-115	-115	-112	-116	-118	-120	-112	-119	-120	-120	-117	-120	-121	-123	-121	-108	-109	-109	-113	-103	-109	-103	-101	-103	-98
Polarized w/+20 mV	-106	-100	-99	-99	-103	-104	-105	-97	-106	-106	-105	-102	-105	-93	-105	-93	-87	-88	-97	-96	-100	-101	-97	-98	-92	-96
Difference (mV):	15	15	16	13	13	14	15	15	13	14	15	15	15	28	18	28	21	21	12	17	3	8	6	3	11	2
Polarized length =	64 cm																									
316 SLa																										
Position from Center	-14	-12	-11	-10	-9	-8	-7	-6	-5	-4	-3	-2	-1	0	1	2	3	4	5	6	7	8	9	10	11	12
Pos. from Center (cm)	-45	-38	-35	-32	-29	-25	-22	-19	-16	-13	-9.5	-6.4	-3.2	0	3.2	6.4	9.5	13	16	19	22	25	29	32	35	38
Unpolarized (mV):	-144	-142	-144	-146	-142	-145	-150	-151	-149	-150	-149	-145	-143	-149	-142	-143	-140	-139	-148	-140	-139	-128	-111	-110	-101	-112
Polarized w/+20 mV	-124	-119	-121	-126	-129	-122	-129	-129	-127	-128	-127	-122	-121	-129	-121	-117	-119	-114	-127	-121	-121	-116	-102	-96	-105	-114
Difference (mV):	20	23	23	20	13	23	21	22	22	22	22	23	22	20	21	26	21	25	21	19	18	12	9	14	4	2
Polarized length =	67 cm																									
Average Polarized	66 cm																									

References

- Abreu, C. M., M. J. Cristobal, et al. (2002). "Galvanic coupling between carbon steel and austenitic stainless steel in alkaline media." Electrochimica Acta **47**(13-14): 2271-2279.
- Aguilar, A., A. A. Sagues, et al. (1990). Corrosion Measurements of Reinforcing Steel in Partially Submerged Concrete Slabs. Philadelphia, U.S.A., American Society for Testing and Materials.
- Alonso, C., C. Andrade, et al. (2000). "Chloride threshold values to depassivate reinforcing bars embedded in a standardized OPC mortar." Cement and Concrete Research **30**(7): 1047-1055.
- Andrade, C., V. Castelo, et al. (1986). The Determination of the Corrosion Rate of Steel Embedded in Concrete by the Polarization Resistance and AC Measurements Impedance Methods. Philadelphia, American Society for Testing and Materials.
- Andrade, C., J. D. Holst, et al. (1991). "Protection Systems for Reinforcement." Task Group VII/8 of Permanent Commission VII: 'Reinforcement: Technology and Quality Control'.
- Arminox (1999). Pier in Progreso, Mexico: Inspection Report Evaluation of the Stainless Steel Reinforcement. Viborg, Denmark.
- ASSDA. (2008). "Pickling and Passivation." Retrieved October 13, 2008, from http://www.assda.asn.au/index.php?option=com_content&task=view&id=78&Itemid=103.
- ASTM-A615 (2007). Standard Specifications for Deformed Plain Carbon-Steel Bars for Concrete Reinforcement. A. International. West Conshohocken, PA, USA, ASTM International.
- ASTM-A955 (2004). Standard Specification for Deformed and Plain Stainless Steel Bars for Concrete Reinforcement. West Conshohocken, PA, USA, ASTM International.
- ASTM-C39 (2003). Standard Test Method for Compressive Strength of Cylindrical Concrete Specimens. A. International. West Conshohocken, PA, USA, ASTM International.
- ASTM-C143 (2005). Standard Test Method for Slump of Hydraulic-Cement Concrete. A. International. West Conshohocken, PA, USA, ASTM International.
- ASTM-C192 (2005). Standard Practice for Making and Curing Concrete Test Specimens in the Laboratory. A. International. West Conshohocken, PA, USA, ASTM International.
- ASTM-C876-91 (1991). Standard Test Method for Half-Cell Potentials of Uncoated Reinforcing Steel in Concrete. A. International. West Conshohocken, PA, USA, ASTM International.
- ASTM-G1-03 (2003). Standard Practice for Preparing, Cleaning, and Evaluating Corrosion Test Specimens. A. International. West Conshohocken, PA, USA, ASTM International.
- ASTM-G61-86 (2003). Standard Test Method For Conducting Cyclic Potentiodynamic Polarization Measurements for Localized Corrosion Susceptibility of Iron-, Nickel-, or Cobalt-Based Alloys. A. International. West Conshohocken, PA, USA, ASTM International.
- ASTM-G109-99a (2005). Standard Test Method for Determining the Effects of Chemical Admixtures on the Corrosion of Embedded Steel Reinforcement in Concrete Exposed to Chloride Environments. A. International. West Conshohocken, PA, USA, ASTM International.
- Barneyback, R. S. and S. Diamond (1981). "Expression and analysis of pore fluids from hardened cement pastes and mortars." Cement and Concrete Research **11**(2): 279-285.
- Bautista, A., G. Blanco, et al. (2006). "Corrosion behaviour of low-nickel austenitic stainless steels reinforcements: A comparative study in simulated pore solutions." Cement and concrete research **36**: 1922-1930.
- Beattie, I. R. and T. R. Gilson (1970). "Single-Crystal Raman Spectra of Nearly Opaque Materials - Iron (III) Oxide and Chromium (III) Oxide." Journal of the Chemical Society A - Inorganic Physical Theoretical(6): 980-986.

- Berke, N. S., D. F. Shen, et al. (1990). Comparison of the Polarization Resistance Technique to the Macrocell Corrosion Technique. Philadelphia, PA, American Society for Testing and Materials.
- Betz, G., G. K. Wehner, et al. (1974). "Composition-vs-depth profiles obtained with auger electron spectroscopy of air-oxidized stainless-steel surfaces." Journal of Applied Physics **45**(12): 5312-5316.
- Beverkog, B. and I. Puigdomenech (1999). "Pourbaix Diagrams for the Ternary System of Iron-Chromium-Nickel." Corrosion **55**(11): 1077-1087.
- Binder, W. D. and C. M. Brown (1946). Proceedings of the American Society for Testing and Materials **46**: 593.
- Boucherit, N., P. Delichere, et al. (1989). "Passivity of Iron and Iron Alloys Studied by Voltammetry and Raman Spectroscopy." Materials Science Forum **44&45**: 51-52.
- BSSA. (2007). "Calculation of Pitting Resistance Equivalent Numbers." Retrieved August 22, 2008, from <http://www.bssa.org.uk/topics.php?article=111>.
- Byfors, K., C. M. Hansson, et al. (1986). "Pore solution expression as a method to determine the influence of mineral additives on chloride binding." Cement and Concrete Research **16**(5): 760-770.
- CAN/CSA-S6-06 (2006). Canadian Highway Bridge Design Code - A National Standard of Canada, Canadian Standards Association: 17.
- Clayton, C. R. and I. Olefjord (1995). Passivity of Austenitic Stainless Steels. Corrosion Mechanisms in Theory and Practice. P. Marcus and J. Oudar. 270 Madison Avenue, New York, New York, Marcel Dekker: 175-199.
- Cleland, J. H. (1996). "What Does the Pitting Resistance Equivalent Really Tell Us." Engineering Failure Analysis **3**(1): 65-69.
- Cochrane, D. J. (1995). European developments in the application of structural austenitic and duplex stainless steels. Proceedings of the International Symposium on High Performance Steels for Structural Applications, ASM International, Cleveland, Ohio.
- Corrosion_Doctors. (1999). "Ideal Linear Polarization Curve." 2008, from <http://www.corrosion-doctors.org/Electrochem/linear.htm>.
- Covino, B. S., J. V. Scalera, et al. (1984). Pickling of Stainless Steels - A Review, Information Circular 8985, United States Department of Interior, Bureau of Mines.
- Esmailpoursaee, A. (2007). An Analysis of the Factors Influencing Electrochemical Measurements of the Condition of Reinforcing Steel in Concrete Structures. Mechanical Engineering. Waterloo, Ontario, University of Waterloo. **Doctor of Philosophy**: 298.
- Evans, H. E., D. A. Hilton, et al. (1976). "Chromium-depleted zones and the oxidation process in stainless steels." Oxidation of Metals **10**(3): 149-161.
- Evans, H. E., D. A. Hilton, et al. (1980). "The development of localized pits during stainless steel oxidation." Oxidation of Metals **14**(3): 235-247.
- Evans, H. E. and R. C. Lobb (1984). "Conditions for the initiation of oxide-scale cracking and spallation." Corrosion Science **24**(3): 209-222.
- Feliu, S., J. A. Gonzalez, et al. (1996). Electrochemical Methods for on-site Determination of Corrosion Rates of Rebars. West Conshohocken, PA, American Society for Testing Materials.
- Fernando, L. A. and D. R. Zaremski (1986). "Some fundamental aspects of annealing and pickling stainless steels." Metallurgical Transactions A (Physical Metallurgy and Materials Science) **19A**(4): 1083-1100.
- Fontana, M. G. (1986). Corrosion Engineering. New York, McGraw-Hill.

- García-Alonso(a), M. C., M.L.Escudero, et al. (2007). "Corrosion behaviour of new stainless steels reinforcing bars embedded in concrete." Cement & Concrete Research **37**(10): 1463-1471.
- García-Alonso(b), M. C., J. A. González, et al. (2007). "Corrosion behaviour of innovative stainless steels in mortar." Cement and Concrete Research **37**(11): 1562-1569.
- Glass, G. K. and N. R. Buenfeld (1997). "Presentation of the chloride threshold level for corrosion of steel in concrete." Corrosion Science **39**(5): 1001-1013.
- Glasser, F. G. and K. K. S. Crentsil (1989). Steel in Concrete: Part II - Electron Microscopy Analysis. Magazine of Concrete Research. **41**: 213-220.
- Gu, P. and J. J. Beaudoin (1998). "Obtaining Effective Half-Cell Potential Measurements in Reinforced Concrete Structures." Construction Technology Update **18**.
- Gu, P., S. Elliott, et al. (1996). "Corrosion resistance of stainless steel in chloride contaminated concrete." Cement and Concrete Research **26**(8).
- Hansson, C., S. Jaffer, et al. (2008). The Corrosion Behaviour of 2101 Lean Duplex Stainless Steel Reinforcing Bar in Solution Corresponding to the Pore Solution of Ordinary Portland Cement Contaminated with Deicing Salts. Waterloo, Ontario, University of Waterloo & Outokumpu Stainless Bar Products.
- Hansson, C. M. (1984). "Comments on Electrochemical Measurements of the Rate of Corrosion of Steel in Concrete." Cement and Concrete Research **14**: 574-584.
- Hansson, C. M., T. Froelund, et al. (1985). "The Effect of Chloride Cation Type on the Corrosion of Steel in Concrete by Chloride Salts." Cement and Concrete Research **15**(1): 65-73.
- Hansson, C. M., A. Poursaei, et al. (2006). "Macrocell and microcell corrosion of steel in ordinary Portland cement and high performance concretes." Cement and Concrete Research **36**(11): 2098-2102.
- Hansson, C. M. and B. Soerensen (1990). Threshold concentration of chloride in concrete for the initiation of reinforcement corrosion. Philadelphia, Pa., American Society for Testing and Materials.
- Higginson, R. L., M. A. E. Jepson, et al. (2006). "Use of EBSD to characterise high temperature oxides formed on low alloy and stainless steels." Materials Science and Technology **22**(11).
- Hilden, J., J. Virtanen, et al. (2001). "Electrolytic pickling of stainless steel studied by electrochemical polarisation and DC resistance measurements combined with surface analysis." Electrochimica Acta **46**.
- Hoar, T. P. (1959). Modern Aspects of Electrochemistry, No. II. London, Butter-worths.
- Hobby, M. G. and G. C. Wood (1969). "Role of nickel in the high-temperature oxidation of Fe-Cr-Ni alloys in oxygen." Oxidation of Metals **1**(1): 23-54.
- Holly, R., E. J. Reardon, et al. (2007). "Proton Spin-Spin Relaxation Study of the Effect of Temperature on White Cement Hydration." Journal of the American Ceramic Society **90**(2): 570-577.
- Hope, B. (2001). Some Corrosion Aspects of Stainless Steel Reinforcement in Concrete Ministry of Transportation Ontario, Kingston, Ontario, Queen's University.
- Hope, B. B., A. K. Ip, et al. (1985). "Corrosion and electrical impedance in concrete." Cement and Concrete Research **15**(3): 525-534.
- Hunkeler, F. (2005). Corrosion in Reinforced Concrete: Processes and Mechanisms. Corrosion in Reinforced Concrete Structures. H. Bohni. Boca Raton, Florida, CRC Press: 1-45.
- Hussain, S. E., Rasheeduzzafar, et al. (1995). "Factors affecting threshold chloride for reinforcement corrosion in concrete." Cement and Concrete Research **25**(7): 1543-1555.
- Ismail, M., A. Toumi, et al. (2004). "Effect of crack opening on the local diffusion of chloride in inert materials." Cement and Concrete Research **34**(4): 711-716.

- Jacobsen, S., J. Marchand, et al. (1996). "Effect of cracking and healing on chloride transport in OPC concrete." Cement and Concrete Research **26**(6): 869-881.
- Jaffer, S. J. (2007). Influence of loading on the corrosion of steel in cracked ordinary portland cement and high performance concretes. Waterloo, Ont., University of Waterloo.
- Jaffer, S. J. and C. M. Hansson (2008). "The Influence of Cracks on Chloride-Induced Corrosion of Steel in Ordinary Portland Cement and High Performance Concretes Subjected to Different Loading Conditions." Corrosion Science.
- Klinghoffer, O. "Embeddable Reference Electrode for Potential Reading." Retrieved October 7, 2008, from <http://www.force.dk/NR/rdonlyres/6A6873F7-1A84-426B-B078-C4EF284D2ACE/1805/19192en.pdf>.
- LeClaire, A. B., P. J. Zoob, et al. (1985). Corrosion Test on Concrete with Solid Stainless Steel Reinforcing Bars for Joslyn Stainless Steels. Northbrook Illinois.
- Legat, A. and V. Dolecek (1995). "Corrosion Monitoring System Based on Measurement and Analysis of Electrochemical Noise." Corrosion **51**(4): 295-300.
- Li, L.-F., P. Caenen, et al. (2005). "Mechanism of single and multiple step pickling of 304 stainless steel in acid electrolytes." Corrosion Science **47**: 1307-1324.
- Li, L.-F. and J.-P. Celis (2003). "Pickling of Austenitic Stainless Steels (A Review)." Canadian Metallurgical Quarterly **42**(3): 365-376.
- Locke, C. E. (1986). Corrosion of Steel in Portland Cement Concrete: Fundamental Studies. Philadelphia, American Society for Testing and Materials.
- Mahallati, E. and M. Saremi (2006). "An assessment on the mill scale effects on the electrochemical characteristics of steel bars in concrete under DC-polarization." Cement and Concrete Research **36**(7): 1324-1329.
- Mammoliti, L. and C. M. Hansson (2007). The Effect of Mill Scale on Corrosion of Stainless Steel in Concrete, Report to the Ministry of Transportation of Ontario.
- Mammoliti, L. T., L. C. Brown, et al. (1996). "The influence of surface finish of reinforcing steel and pH of the test solution on the chloride threshold concentration for corrosion initiation in synthetic pore solutions." Cement and Concrete Research **26**(4): 545-550.
- Mansfeld, F. (1976). The Polarization Resistance Technique for Measuring Corrosion Currents. Advances in Corrosion Science and Technology. M. G. Fontana and R. W. Staehle. New York, Plenum Press. **6**: 163-262.
- Mansfeld, F. and M. Kendig (1981). "Concerning the Choice of Scan Rate in Polarization Measurements." Corrosion **37**(9): 545-546.
- Marcotte, T. D. and C. M. Hansson (2007). "Corrosion products that form on steel within cement paste." Materials and Structures/Materiaux et Constructions **40**(3): 325-340.
- Markeset, G., S. Rostam, et al. (2006). Guide for the Use of Stainless Steel Reinforcement in Concrete Structures. Nordic Innovation Centre Project - 04118: Corrosion Resistant Steel Reinforcement in Concrete Structures: 68.
- McCormick_Rankin_Corporation (2008). High end chloride contents of abutment walls in Ontario. K. Anders, Frank Pianca.
- Mendoza, A. R. (2003). Corrosion of reinforcing steel in loaded cracked concretes exposed to de-icing salts. Mechanical Engineering. Waterloo, Ontario, Canada, University of Waterloo. **Master of Applied Science**: 138.
- MTO. (2001). "Guidelines for Inspection and Acceptance of Stainless Steel Reinforcement on the Contract Site." Retrieved October 14, 2008, from <http://www.mto.gov.on.ca/english/pubs/research/stainless/stainless.htm>.
- Nemati, K. M., P. J. M. Monteiro, et al. (1998). "Analysis of Compressive Stress-Induced Cracks in Concrete." ACI Materials Journal **95**(5): 617-630.

- Newhouse, C. D. and R. E. Weyers (1996). Modeling the measured time to corrosion cracking, SAE, Warrendale, PA, USA.
- NIDI. (2004). "Stainless Steel Rebar Guidelines for Shipping, Handling, Fabrication and Placement." Retrieved August 14, 2008, from http://www.ssina.com/view_a_file/rebarbroc.pdf.
- Nuernberger, U. (1996). Stainless Steel in Concrete - State of the Art Report. London, The Institute of Materials.
- Nuernberger, U. (2005). "Stainless steel reinforcement-a survey." Otto Graf Journal **16**: 111-138.
- Nuernberger, U., W. Beul, et al. (1993). "Corrosion Behaviour of Welded Stainless Reinforced Steel in Concrete." Otto Graf Journal **4**: 225-259.
- Nürnberg, U. and W. Beul (1999). "Corrosion of Stainless Steel Reinforcement in Cracked Concrete." Otto Graf Journal **10**: 23-37.
- Oh, B. H., S. Y. Jang, et al. (2003). Experimental investigation of the threshold chloride concentration for corrosion initiation in reinforced concrete structures. Magazine of Concrete Research. [London], Thomas Telford Services. **55**: 117-124.
- Oh, S. J., D. C. Cook, et al. (1998). "Characterization of Iron Oxides Commonly Formed as Corrosion Products on Steel." Hyperfine Interactions **112**(1-4): 59-66.
- Ohtsuka, T. (1996). "Raman Spectra of Passive Films of Iron in Neutral Borate Solution." Materials Transactions, JIM **37**(1): 67-69.
- Olefjord, I., B. Brox, et al. (1985). "Surface Composition of Stainless Steels During Anodic Dissolution and Passivation Studied by ESCA." Journal of the Electrochemical Society **132**(12).
- Ostwald, C. and H. J. Grabke (2004). "Initial oxidation and chromium diffusion. I. Effects of surface working on 9-20% Cr steels." Corrosion Science **46**: 1113-1127.
- PAR. (1982). "Basics of Corrosion Measurements, Application Note Corr-1." Princeton Applied Research Retrieved October 29, 2008, from <http://new.ametek.com/content-manager/files/PAR/087.pdf>.
- PAR. (2008). "Electrochemistry and Corrosion Overview and Techniques, Application Notes Corr-4." Princeton Applied Research Retrieved October 29, 2008, from <http://new.ametek.com/content-manager/files/PAR/088.pdf>.
- PCA. (1998). "Control of Air Content in Concrete." Concrete Technology Today, Portland Cement Association Retrieved October 30, 2008, from <http://www.cement.org/tech/pdfs/PL981.pdf>.
- PCA. (2008). "Concrete Technology: Air-Entraining Admixtures." Retrieved October 15, 2008, from http://www.cement.org/tech/cct_admixtures_AEA.asp.
- Pianca, F. (2005). Cheaper and Greener Stainless Steel Processing. Road Talk. Ontario, Canada, Ontario Ministry of Transportation. **11**: 3.
- Pillai, R. G. and D. Trejo (2005). "Surface Condition Effects on Critical Chloride Threshold of Steel Reinforcement." ACI Materials Journal **102**(2): 103-109.
- Pourbaix, M. (1966). Atlas of Electrochemical Equilibria in Aqueous Solutions. Oxford, Pergamon Press.
- Pozansky, A., C. S. Nalborne, et al. (1983). Duplex Stainless Steel. Materials Park, OH, ASM International.
- Price, D. M. and G. L. Horter (1994). "Waste minimization in stainless steel pickling solutions. A study to model dissolution kinetics of the chromium-depleted surface." Metal Finishing **92**(2): 60-65.
- Qian, S., D. Qu, et al. (2006). "Galvanic Coupling Between Carbon Steel and Stainless Steel Reinforcements." Canadian Metallurgical Quarterly **45**(4).
- Raju, N. K. (1970). "Microcracking in concrete under repeated compressive loads." Building Science **5**(1): 51-56.

- Rasheeduzzafar, F. H. Dakhil, et al. (1992). "Performance of Corrosion Resisting Steels in Chloride-Bearing Concrete." ACI Materials Journal **89**(5): 439-448.
- Rau, R. H. G. (1988). "Rapid electrolytic descaling process for stainless steel wire rods." Ironmaking Steelmaking **15**(4): 202.
- Ritter, K., M. S. Odziemkowski, et al. (2002). "An In situ Study of the Role of Surface Films on Granular Iron in the Permeable Iron Wall Technology." Journal of Contaminant Hydrology **55**: 87-111.
- Saremi, M. and E. Mahallati (2002). "A study on chloride-induced depassivation of mild steel in simulated concrete pore solution." Cement and Concrete Research **32**(12): 1915-1921.
- Scully, J. R. and M. F. Hurley (2007). Investigation of the Corrosion Propagation Characteristics of New Metallic Reinforcing Bars. Commonwealth of Virginia, Charlottesville, Virginia, University of Virginia.
- Sedriks, A. J. (1983). "Role of Sulfide Inclusions in Pitting and Crevice Corrosion of Stainless Steels." International Metals Review **28**(5): 295-307.
- Sedriks, A. J. (1996). Corrosion of Stainless Steels. New York, John Wiley & Sons.
- Silverman, D. "Tutorial on Polexpert and the cyclic potentiodynamic polarization technique." Retrieved October 15, 2008, from http://www.argentumsolutions.com/tutorials/polexpert_tutorialpg4.html.
- Smith, F. N. and M. Tullmin (1999). Using Stainless Steel as Long-Lasting Rebar Material. Materials Performance. Houston, TX, USA, NACE International: 72-76.
- Steel, S. (2008). Relative Cost of Stainless Steel. C. Hansson, Frank Pianca.
- Stern, H. and E. D. Weisert (1959). "Proc. ASTM." **32**: 1280.
- Stern, M. (1957). "Electrochemical Polarization II. Ferrous and Ferric Electrode Kinetics on Stainless Steel." Journal of the Electrochemical Society **104**(9): 559-563.
- Stern, M. and A. L. Geary (1957). "Electrochemical Polarization: A Theoretical Analysis of the Shape of Polarization Curves." Journal of Electrochemical Society **104**(1): 56-63.
- Stott, F. H. and F. I. Wei (1989). "High temperature oxidation of commercial austenitic stainless steels." Materials Science and Technology **5**(11): 1140-1147.
- Stratfull, R. F. (1957). "The Corrosion of Steel in Reinforced Concrete Bridge." Corrosion **13**: 43-48.
- Suleiman, M. I. and R. C. Newman (1994). "Use of very weak galvanostatic polarization to study localized corrosion stability in stainless steel." Corrosion science **36**(9): 1657-1655.
- Thibeau, R. J., C. W. Brown, et al. (1978). "Raman Spectra of Possible Corrosion Products of Iron." Applied Spectroscopy **32**(6): 532-535.
- Thierry, D., D. Persson, et al. (1991). "Raman Spectroscopy and XPS Investigations of Anodic Corrosion Films Formed on Fe-Mo Alloys in Alkaline Solutions." Corrosion Science **32**(3): 273-284.
- Tran, K. A. (2007). The Durability of Concrete Using Concrete Plant Wash Water. Civil Engineering. Waterloo, Ontario, Canada, University of Waterloo. **Master of Applied Science**: 157.
- Treadway, K. W. J., R. N. Cox, et al. (1989). Durability of Corrosion Resisting Steels in Concrete. Proc. Instn Civ. Engrs, Part 1,.
- Trejo, D. and R. G. Pillai (2003). "Accelerated Chloride Threshold Testing: Part I - ASTM A 615 and A 706 Reinforcement." ACI Materials Journal **100**(6): 519-527.
- Trejo, D. and R. G. Pillai (2004). "Accelerated Chloride Threshold Testing - Part II: Corrosion-Resistant Reinforcement." ACI Materials Journal **101**(1).
- Tullmin, M. (2006). "Stainless Steel Rebar News Bulletin." Retrieved October 21, 2008, from <http://www.stainless-rebar.org/index.html>.
- Virmani, Y. P. and G. G. Clemena (1998). Corrosion Protection: Concrete Bridges. U.S. Department of Transportation, McLean, VA, US Federal Highway Administration.

- Vuurman, M. A., D. J. Stufkens, et al. (1990). "Raman Spectra of Chromium Oxide Species in $\text{Cr}_2\text{O}_3/\text{Al}_2\text{O}_3$ Catalysts." Journal of Molecular Catalysis **60**(1): 83-98.
- Waids, N. (2008). "Crevice Corrosion and Pitting Corrosion." Retrieved August 27, 2008, from <http://octane.nmt.edu/waterquality/corrosion/crevice.htm>.
- Wang, K., D. C. Jansen, et al. (1997). "Permeability study of cracked concrete." Cement and Concrete Research **27**(3): 381-393.
- Washko, S. D. and G. Aggen (2002). Properties and Selection: Irons, Steels, and High-Performance Alloys. ASM Handbook. United States of America, ASM International. **1**.
- Weiermair, R., C. M. Hansson, et al. (1996). Corrosion Measurements on Steel Embedded In High Performance Concrete Exposed to a Marine Environment. Third CANMET/ACI International Conference on Concrete in Marine Environment, St. Andrews by-the-Sea, N.B., Canada.
- Weyers, R. E., W. Pyc, et al. (1998). "Estimating the service life of epoxy-coated reinforcing steel." ACI Materials Journal **95**(5): 546-557.
- Whiting, D. (1978). Concrete Materials, Mix Design, Construction Practices, and Their Effects on the Corrosion of Reinforcing Steel. Corrosion/78, Paper No. 73, Houston, Texas, National Association of Corrosion Engineers.
- Whittle, D. P., G. C. Wood, et al. (1967). "Concentration profiles in the underlying alloy during the oxidation of iron-chromium alloys." Acta Metallurgica **15**(11): 1747-1755.
- Wood, G. C. (1962). "Some observations on break-through of protective oxide films on iron-chromium alloys." Corrosion Science **2**: 255-268.
- Yonezawa, T., V. Ashworth, et al. (1988). "Pore Solution Composition and Chloride Effects on the Corrosion of Steel in Concrete." Corrosion **44**(7): 489-499.
- Yunovich, M., N. G. Thompson, et al. (2001). Appendix D - Highway Bridges. Corrosion Costs and Preventive Strategies in the United States. G. H. Koch, M. P.H.Brongers, N. G. Thompson, Y. P. Virmani and P. D. Joe H. Payer. CC Technologies Laboratories Inc, Dublin, Ohio, Federal Highway Administration.